

博士論文

**Novel Design and Fabrication of Metal Face
/ 3D CFRP Composite Hybrid Structure**
(メタルフェースと 3D CFRP コアからなる
複合材料の新たな構造設計と評価)

張 敬偉

Novel Design and Fabrication of Metal Face / 3D CFRP Composite Hybrid Structure

(メタルフェースと 3D CFRP コアからなる
複合材料の新たな構造設計と評価)

A thesis submitted for the degree of
DOCTOR OF ENGINEERING

by **Jingwei ZHANG**

Supervisor: Prof. Jun YANAGIMOTO

**Department of Mechanical Engineering
The University of Tokyo**

March 2022

Contents

Chapter 1	Background.....	1
1.1	Demand for lightweight materials.....	1
1.2	Current answers for high demand for lightweight materials.....	6
1.2.1	Carbon fiber reinforced plastic (CFRP).....	7
1.2.1.1	Common intermediate substrates of CFRP.....	7
1.2.1.2	Stampable CFRP sheet.....	9
1.2.2	Hybrid structures.....	11
1.2.2.1	Laminates.....	12
1.2.2.2	3D hybrid sandwich sheet.....	18
1.2.3	Lightweight structures produced by additive manufacturing.....	25
1.2.3.1	Introduction of additive manufacturing.....	25
1.2.3.2	Additive manufacturing of lightweight structures.....	29
1.3	Motivation and research purpose.....	42
1.3.1	Key engineering issues to be resolved.....	42
1.3.1.1	Production efficiency and manufacturing cost.....	42
1.3.1.2	Formability.....	45
1.3.1.3	Mechanical property and functionality.....	50
1.3.2	Research objectives.....	52
1.4	Proposed solutions in this thesis.....	56
1.4.1	Proposal of formable metal face /CFRP core hybrid sandwich sheet.....	56
1.4.2	Shape design for the improvement of mechanical property and formability of metal face/CFRP core sandwich sheet.....	57

1.4.3 Synergy of topology optimization and additive manufacturing for the design and fabrication of formable sandwich sheets with superior mechanical property.....	58
1.5 Research framework.....	62
1.6 References	65
Chapter 2 Shape design and conventional fabrication of formable sandwich sheet	72
2.1 Research background and literature review	73
2.2 Basic knowledge about failure characteristics of sandwich sheets	76
2.2.1 Failure modes of sandwich structure	76
2.2.2 Failure constraints	77
2.3 Structures and materials	81
2.3.1 Selection of core structure	81
2.3.2 Materials	84
2.4 Determination of optimal structural parameters.....	86
2.4.1 Evaluation of core shear strength.....	86
2.4.2 Evaluation of bending stiffness by CAE.....	88
2.4.3 Evaluation of face buckling degree and shear modulus.....	89
2.4.4 Comparison of mechanical properties of various types of core structures	93
2.5 Production of sandwich sheets	95
2.5.1 Optimal forming conditions of CFRTP.....	95
2.5.2. Piecewise sectional forming and bonding.....	96
2.6 Property evaluation.....	98
2.6.1 Evaluation of bending stiffness by three-point bending test.....	98
2.6.2 Formability test.....	100
2.6.2.1 Forming tools	100

3.2.5.1	Materials	141
3.2.5.2	Fabrication of the sandwich sheet	141
3.2.5.3	Three-point bending and L-bending tests	142
3.2.6	Results and discussion	143
3.2.6.1	Produced sandwich sheets	143
3.2.6.2	Mechanical properties	147
3.2.6.3	Bendability	154
3.2.7	Conclusion of section 3.2.....	164
3.3	Summary	166
3.4	References	168
Chapter 4	Design and fabrication of inner macrostructure with enhanced stiffness via topology optimization and additive manufacturing	170
4.1	Topology optimization of microlattice dome with enhanced stiffness.....	172
4.1.1	Research background and literature review	172
4.1.2	Introduction to the microlattice dome structure.....	175
4.1.3	Design flowchart.....	178
4.1.4	Topology optimization	179
4.1.4.1	Mathematical formulation of topology optimization problem	179
4.1.4.2	Updating scheme for design variables.....	181
4.1.4.3	Integrating topology optimization with microlattice structure	182
4.1.4.4	Topology optimization models	184
4.1.4.5	Topology optimization results	185
4.1.5	3D construction of microlattice dome.....	186
4.1.5.1	Construction method	186

4.1.5.2 Constructed 3D models	188
4.1.6 Numerical and experimental validation	190
4.1.6.1 CAE simulation	191
4.1.6.2 additive manufacturing and experimental setup.....	193
4.1.7 Results and discussion	195
4.1.7.1 Comparison between optimal density map with stress distribution contour...	195
4.1.7.2 Stiffness and energy absorption.....	196
4.1.8 Conclusion of section 4.1.....	201
4.2 Homogenization-based topology optimization integrated with elastically isotropic lattices for additive manufacturing of ultralight and ultrastiff structures.....	203
4.2.1 Research background and literature review	203
4.2.2 Evaluation of mechanical properties and elastic isotropy.....	206
4.2.2.1 Selection of lattice structures	206
4.2.2.2 Effective mechanical properties and elastic isotropy	207
4.2.3 Topology optimization	210
4.2.3.1 Integration of isotropic lattices with HMTO.....	210
4.2.3.2 Topology optimization examples	211
4.2.3.3 Numerical validation and experimental tests	211
4.2.4 Results and discussion	212
4.2.4.1 Topology optimization results	212
4.2.4.2 Stiffness and energy absorption capability.....	213
4.2.5 Conclusion of section 4.2.....	214
4.3 Summary	215
4.4 References	217

Chapter 5	Concurrent topology optimization of formability and bending stiffness of sandwich sheets	219
5.1	Research background and literature review	220
5.2	Topology optimization method.....	223
5.2.1	Introduction of topology optimization strategy	223
5.2.2	Potential failure modes and corresponding constraints	224
5.2.2.1	Core shear failure constraint.....	225
5.2.2.2	Face buckling constraint.....	225
5.2.2.3	Core–face sheet delamination constraint.....	227
5.2.3	FEM simulation of macroscopic core shear strength and equivalent bending stiffness	228
5.2.4	Formulation of topology optimization problem.....	229
5.2.4.1	Topology optimization schemes	229
5.3	Materials and experiments.....	235
5.3.1	Materials and fabrication of prototypes	235
5.3.2	Experimental tests of mechanical properties and formability.....	236
5.4	Results and discussion.....	237
5.4.1	Topology optimization results.....	237
5.4.1.1	Evolution of objective functions	237
5.4.1.2	Evolution of core topology.....	241
5.4.1.3	Generation of 3D models for additive manufacturing.....	246
5.4.2	Experimental validation	249
5.4.2.1	Additively manufactured prototypes	249
5.4.2.2	Three-point bending results	251

5.4.2.3 L-bending results	254
5.4.2.4 Draw-bending results	256
5.5 Summary	259
5.6 References	260
Chapter 6 Concluding remarks	262
Appendix.....	273
Appendix A Periodic boundary conditions for pure bending.....	273
Appendix B Implementation of periodic boundary conditions for pure bending by MPC User Subroutine incorporated in ABAQUS	276
Publications.....	278
Acknowledgement	282

Figure 1-1. China’s petroleum consumption from 1993 to 2019.....	2
Figure 1-2. Global carbon emissions from 1990-2018.	3
Figure 1-3. Fuel consumption (FC) in function of mass (M) with the relative regression line.	3
Figure 1-4. Material usage composition in Boeing 787 Dreamliner™.	4
Figure 1-5. Aerospace advanced composite usage rate in the past few decades.	5
Figure 1-6. BMW i3 body structure part weight composition.	5
Figure 1-7. Flying car developed by Boeing.	6
Figure 1-8. Specific strength and stiffness of main engineering materials.	7
Figure 1-9. Common intermediate substrates of CFRP.	8
Figure 1-10. Processes of intermediate substrates of CFRP.	9
Figure 1-11. SCFRTP and UTCTT used for the fabrication of the core structure: (a) illustration of SCFRTP; (b) cross-sections of SCFRTP; (c) illustration of UTCTT and (d) randomly oriented tapes in UTCTT.	10
Figure 1-12. Illustration of hybrid structures reviewed in this thesis: (a) laminates; (b) 3D hybrid sandwich sheet.....	11
Figure 1-13. Mechanism illustration for the enhancement of formability of multilayer sheets.	14
Figure 1-14. General classification of the FMLs.	16
Figure 1-15. Heat-assisted forming strategy of thermoplastic matrix based FML.	17
Figure 1-16. Process of FMLs parts via combination of forming and joining in one step.	17
Figure 1-17. Some representative sandwich structures.....	19
Figure 1-18 Sandwich structures with various cellular cores.	20
Figure 1-19. Sandwich structures with folded cellular cores.....	20
Figure 1-20. Fabrication processes of pyramidal truss core sandwich structure	22
Figure 1-21. Fabrication processes of honeycomb core sandwich structure	22
Figure 1-22. Manufacturing processes of Y-frame core	22
Figure 1-23. CFRP honeycomb and pyramidal core sandwich structures: (a) honeycomb structure; (b) pyramidal structure.....	23
Figure 1-24. CFRP pyramidal truss core sandwich structure.	24

Figure 1-25. Sandwich structure with a hybrid carbon fiber lattice foam core.	24
Figure 1-26. CFRP Kagome lattice sandwich structure.....	25
Figure 1-27. Additive manufacturing processes classified by ASTM Committee F42. Source: Boeing/ASTM.....	27
Figure 1-28. Outboard landing gear rib fabricated by Wire + Arc Additive Manufacturing: CAD model (left) and produced part before machining (right).	28
Figure 1-29. Injection molding tools manufactured by hybrid gas metal arc welding and CNC machining: CAD model (left), near net shape molds (center), and final parts (right).....	28
Figure 1-30. Conformal cooling channels embedded in an injection molding die.....	29
Figure 1-31. Classification of metal AM processes based on heat sources utilization.	31
Figure 1-32. Examples of FDA-approved Ti-6Al-4V lattice implants.	31
Figure 1-33. Fabrication of polymer lattice structures via the combination of snap-fit method with the PolyJet technology.	36
Figure 1-34. (a) Printing of lightweight cellular composites with controlled alignment of multiscale, high-aspect ratio fiber reinforcement; (b) printing of continuous carbon fiber reinforced plastic.....	36
Figure 1-35. A free-hanging method for the printing of 3D lattice structure using continuous carbon fiber reinforced composites.....	37
Figure 1-36. A typical topology optimization example.	38
Figure 1-37. Comparison of conventional density based TO and HMTTO integrated with lattice.	40
Figure 1-38. Topologically optimized nacelle hinge brackets for Airbus A320 (left) and Airbus A380 (right).	41
Figure 1-39. Digital design of soft lattices for multifunctional applications.	41
Figure 1-40. Octet lattice structures manufactured using CFRP hollow cylindrical struts.....	43
Figure 1-41. 3D double-arrow-head (DAH) auxetic structure fabricated using CFRP laminates.	44
Figure 1-42. CFRP lattice core made up of orthogonal corrugated lattice trusses (CLTs).	44
Figure 1-43. Fabrication process of all-CFRP tetrahedral truss core sandwich panel.....	45

Figure 1-44. Forming of AA5052/PP/AA5052 sandwich sheets by Nakajima tests.	46
Figure 1-45. Thin metallic sandwich sheet with fiber core (side view, left) and perforated core (top view, right).....	47
Figure 1-46. Shear failure of the sandwich cross section: (a) fiber core; (b) perforated core.	48
Figure 1-47. Fabrication process of sandwich sheets with a sheared dimple core by piecewise sectional forming technology and its secondary bending.	49
Figure 1-48. Summary of formability degree of sandwich sheets investigated in the past.	50
Figure 1-49. The research route from multilayer metallic sheets to metal face/CFRP core hybrid sandwich sheet.	57
Figure 1-50. Flowchart of shape optimization, fabrication and property evaluation of sandwich sheets.....	58
Figure 1-51. Development map of topology optimization for the design and fabrication of formable sandwich sheets with superior mechanical property.	60
Figure 1-52. Research framework of this dissertation.	64
Figure 2-1. (a) Delamination; (b) Core shear failure	76
Figure 2-2. (a) Face fracture; (b) Face buckling	77
Figure 2-3. Illustration of potential failure modes of sandwich sheets during bending.	80
Figure 2-4. Free body diagram of sandwich sheets during bending.	80
Figure 2-5. Metallic core sandwich sheets characterized in two-dimensional plane with ‘relative bendable radius’ and ‘relative density’ axes.	82
Figure 2-6. Geometrical characteristics of dome-like structures.	84
Figure 2-7. Short carbon fiber reinforced thermoplastic.	85
Figure 2-8. Schematics of truncated dome core and repeated unit cell	86
Figure 2-9. The effects of the bending radius and the dome radius on the ratio of τ_c to τ_{re}	87
Figure 2-10. Bending moment-curvature curves at different radius ratios and different bending directions.....	89
Figure 2-11. Illustration of the implementation of periodic boundary conditions for pure bending.....	90
Figure 2-12. Illustration of boundary conditions for the pure shear analysis.	90

Figure 2-13. Pure bending deformation and face buckling of sandwich sheets with different relative densities.....	92
Figure 2-14. Specific shear modulus and bending stiffness with the relative density.	93
Figure 2-15. Comparison of mechanical properties of sandwich sheets with different types of core structures.	94
Figure 2-16. Surface condition observation and dome height measurements.	95
Figure 2-17. Forming dies and piecewise sectional forming process.....	96
Figure 2-18. Bonding conditions in autoclave.....	97
Figure 2-19. Servopulser material testing machine.	98
Figure 2-20. Three-point bending test configuration.....	99
Figure 2-21. Bending load-displacement curves.	100
Figure 2-22. Forming tools for draw-bending and L-bending tests.....	101
Figure 2-23. Configuration of warm forming apparatus.....	102
Figure 2-24. L-bending test of sandwich sheets with A2017P faces at clearance of 8 mm...	102
Figure 2-25. Deformed sandwich sheets with A2017P faces at clearance of 8 mm.	103
Figure 2-26. L-bending test of sandwich sheets with A2017P faces at clearance of 15 mm.	103
Figure 2-27. Deformed sandwich sheets with A2017P faces at clearance of 15 mm.	103
Figure 2-28. L-bending test of sandwich sheets with CFRTP faces at clearance of 8 mm...	104
Figure 2-29. Deformed sandwich sheets with CFRTP faces at clearance of 8 mm.	104
Figure 2-30. L-bending test of sandwich sheets with CFRTP faces at clearance of 15 mm..	104
Figure 2-31. Deformed sandwich sheets with CFRTP faces at clearance of 15 mm.	105
Figure 2-32. L-bending of sandwich sheet with SUS304 faces at clearance of 15 mm.	105
Figure 2-33. Secondarily formed sandwich sheets with a CFRTP core formed at 25 °C: (a) A2017P–CFRTP; (b) SUS304–CFRTP; (c) CFRTP–CFRTP.	106
Figure 2-34. Secondarily formed sandwich sheets with a CFRTP core formed at 100 °C: (a) A2017P–CFRTP; (b) SUS304–CFRTP; (c) CFRTP–CFRTP.	107
Figure 2-35. Secondarily formed sandwich sheets with a CFRTP core formed at 150 °C: (a) A2017P–CFRTP; (b) SUS304–CFRTP; (c) CFRTP–CFRTP.	108
Figure 2-36. Explanation models of failure behaviors of sandwich sheets during cold and warm	

forming.....	110
Figure 3-1. Illustration of the sandwich sheet with the truncated dome core.....	120
Figure 3-2. Shear failure mode of the truncated dome core.....	122
Figure 3-3. Illustration of the face buckling mode of the sandwich sheet with the truncated dome core.....	124
Figure 3-4. Design map for the sandwich sheet with the A2017P face sheet.....	126
Figure 3-5. Design map for the sandwich sheet with the SUS304 face sheet.....	127
Figure 3-6. Piecewise sectional forming process and produced core structures.....	128
Figure 3-7. Experimental configuration of the L-bending test.....	129
Figure 3-8. L-bending tests of sandwich sheets with A2017P face sheets: (a) bending radius of 30 mm; (b) bending radius of 60 mm.....	130
Figure 3-9. L-bending tests of sandwich sheets with SUS304 face sheets: (a) bending radius of 30 mm; (b) bending radius of 60 mm.....	131
Figure 3-10. Sandwich designs inspired by biological structures: (a) CFRP face/metal honeycomb core sandwich panel and grass leaf stem; (b) CFRP face/metal foam core sandwich plate and hornbill beak.....	136
Figure 3-11. Representative lattice structures originating from basic topologies of shell, strut and plate: (a) spherical shell; (b) tetrahedral truss; (c) tetrahedral plate; (d) bilayered dome composed of spherical shell; (e) octet truss composed of tetrahedral truss; (f) octet plate composed of tetrahedral plate.....	137
Figure 3-12. Lattice constant L_e and lattice thickness t of representative lattice structures: (a) bilayered dome structure; (b) octet truss structure; (c) octet plate structure.....	138
Figure 3-13. Lattice relative density corresponds to lattice thickness ratio.....	138
Figure 3-14. Boundary conditions for FEM analyses and determination of flexural rigidity and macroscopic shear strength: (a) pure bending analysis; (b) determination of flexural rigidity from bending moment–curvature curve; (c) shear analysis; (d) determination of shear strength from shear stress–strain curve.....	139
Figure 3-15. Face buckling modes of sandwich sheets with bilayered dome, octet truss and octet plate cores: (a) unsupported regions of face sheet bonded to the bilayered dome, octet	

truss and octet plate cores indicated by the grey section; (b) repeated unit cell of unsupported face sheet; (c) face buckling mode decomposed into biaxial compression and shear modes.	140
Figure 3-16. Experimental configuration of three-point bending and L-bending tests: (a) three-point bending test; (b) L-bending test.	143
Figure 3-17. Produced bilayered dome, octet truss and octet plate core structures with relative densities of 40% and 50% and core heights of 6 and 8 mm: (a) bilayered dome; (b) octet truss; (c) octet plate.....	144
Figure 3-18. Sandwich sheets with bilayered dome, octet truss and octet plate core structures of relative densities of 40% and 50% and core heights of 6 and 8 mm: (a) sandwich sheets with bilayered dome core; (b) sandwich sheets with octet truss core; (c) sandwich sheets with octet plate core.	145
Figure 3-19. Lattice structures observed at a magnification 12 ×: (a) bilayered dome; (b) octet truss; (c) octet plate.	146
Figure 3-20. Comparison of lattice thicknesses of printed models and 3D models built by CAD programs.	146
Figure 3-21. Specific bending moment–curvature curves of bilayered dome, octet truss and octet plate structures.	148
Figure 3-22. Specific flexural rigidity of bilayered dome, octet truss and octet plate structures.	148
Figure 3-23. Specific bending moment–curvature curves: (a) sandwich sheets with bilayered dome core; (b) sandwich sheets with octet truss core; (c) sandwich sheets with octet plate core.	149
Figure 3-24. Specific flexural rigidity of sandwich sheets with bilayered dome, octet truss and octet plate cores.....	150
Figure 3-25. Comparison of specific flexural rigidity between sandwich sheets and cores..	150
Figure 3-26. Stress distribution contours of the core structures and sandwich sheets: (a) core structures; (b) sandwich sheets.	151
Figure 3-27. Dominant failure modes during three-point bending process.	152

Figure 3-28. Results of three-point bending tests.	153
Figure 3-29. Stiffness and absorbed energy from three-point bending tests.	154
Figure 3-30. Shear stress–strain curves of bilayered dome, octet truss and plate lattice structures at various relative densities: (a) bilayered dome; (b) octet truss; (c) octet plate; (d) macroscopic shear strength.	154
Figure 3-31. Shear strength ratios (τ_c/τ_{re}) calculated for 30 and 60 mm bending radii, 0.3 and 0.5 mm face sheet thicknesses, 6 and 8 mm core heights and 10% to 90% core relative densities for the judgement of core shear failure.	156
Figure 3-32. Gap ratios (d/d_{cr}) calculated for 30 and 60 mm bending radii, 0.3 and 0.5 mm face sheet thicknesses, 6 and 8 mm core heights and 10% to 90% core relative densities for the evaluation of face buckling.	157
Figure 3-33. Deformation of specimens having the bilayered dome core.	158
Figure 3-34. Deformed specimens having the bilayered dome core after L-bending.	159
Figure 3-35. Deformation of specimens having the octet truss core during L-bending.	160
Figure 3-36. Deformed specimens having the octet truss core after L-bending.	161
Figure 3-37. Deformation of specimens having the octet plate core during L-bending.	162
Figure 3-38. Deformed specimens having the octet plate core after L-bending.	163
Figure 3-39. Summarized failure modes in theoretical predictions and experimental tests. .	164
Figure 4-1. Commonly used core structures of sandwich sheets characterized by relative density, relative modulus and failure resistance.	175
Figure 4-2. Polyhedral cells categorized as the stretch-dominated or bending-dominated following the Maxwell stability criterion.	176
Figure 4-3. Basic cell topology of the bidirectional dome and its structural parameters.	178
Figure 4-4. Illustration of the microlattice dome.	178
Figure 4-5. Design flowchart.	179
Figure 4-6. Hexahedral unit cell composed of tetrahedra.	184
Figure 4-7. Boundary conditions for topology optimization models.	185
Figure 4-8. Optimal density distribution of lattices for compression models obtained from topology optimization.	185

Figure 4-9. Optimal density distribution of lattices for three-point bending models obtained from topology optimization.	186
Figure 4-10. Illustration of the basic structure of tetrahedral lattice.....	188
Figure 4-11. Hexahedral unit with different volume fractions generated using the proposed construction method.....	188
Figure 4-12. Constructed compression models with different cell sizes before and after topology optimization.	189
Figure 4-13. Comparison of top views of constructed compression models.	190
Figure 4-14. Constructed three-point bending models with different cell sizes before and after topology optimization.	190
Figure 4-15. Tensile test configuration and results.	192
Figure 4-16. Illustration of boundary conditions for CAE models.	193
Figure 4-17. Additively manufactured optimized and unoptimized microlattice domes for compression tests.	194
Figure 4-18. Additively manufactured optimized and unoptimized microlattice domes for three-point bending tests.	194
Figure 4-19. Experimental configuration for compression test.	195
Figure 4-20. Experimental configuration for three-point bending test.	195
Figure 4-21. Stress distribution maps obtained from the compression simulation.....	196
Figure 4-22. Stress distribution maps obtained from the three-point bending simulation....	196
Figure 4-23. Fractured microlattice domes and solid dome after compression tests.....	197
Figure 4-24. Fractured microlattice domes and solid dome after three-point bending tests..	198
Figure 4-25. Compressive load–displacement curves obtained from numerical simulation and experiments.	199
Figure 4-26. Three-point bending load–displacement curves obtained from numerical simulation and experiments.	199
Figure 4-27. Specific compressive and bending stiffnesses obtained from FEA and experiments.	200
Figure 4-28. Specific energy absorption obtained from experiments.....	200

Figure 4-29. Comprehensive evaluation of some representative topology optimization methods.	205
Figure 4-30. Basic topologies of truss–lattices and plate–lattices and their combinations. ..	207
Figure 4-31. Stress distribution of truss–lattices and plate–lattices with relative density of 30% under axial compression strain of 0.2 and shear strain of 0.4.....	208
Figure 4-32. Effective mechanical properties at different relative densities for representative truss–lattices and plate–lattices.....	209
Figure 4-33. Elastic moduli and Zener anisotropy ratios of lattice structures: (a) normalized elastic moduli and (b) Zener anisotropy ratios.	210
Figure 4-34. Dimensions and boundary conditions of topology optimization models subjected to three-point bending and out-of-plane compression.	211
Figure 4-35. Topology optimization results and constructed 3D models.	212
Figure 4-36. Optimized and unoptimized rectangular beams obtained by AM.	213
Figure 4-37. Three-point bending and out-of-plane compression results.....	214
Figure 5-1. Illustration of topology optimization strategy.	223
Figure 5-2. Illustration of typical failure modes of sandwich sheets during bending: (a) typical failure modes including core shear failure, face buckling, face fracture and core-face sheet delamination and (b) experimentally observed failure modes of sandwich sheets during bending.	224
Figure 5-3. Determination of gap between attachment points and bonding length: (a) Calculation of gap between attachment points and (b) Determination of bonding length. ...	227
Figure 5-4. Setup of FEM models: (a) Determination of macroscopic core shear strength and (b) Determination of equivalent bending stiffness and (c) Material properties assigned to design elements.	229
Figure 5-5. Flowchart of the optimization scheme 1 (case 1).....	230
Figure 5-6. Flowchart of the optimization scheme 2 (case 2).....	232
Figure 5-7. Design map of the density-based topology optimization integrated with multi-stage GA.....	234
Figure 5-8. Experimental setups for three-point bending, L-bending and draw-bending tests.	

.....	236
Figure 5-9. The objective function value and core shear strength with the update of the iteration step in case 1: (a) Volume fraction constraint of 50% and (b) Volume fraction constraint of 62.5%.	238
Figure 5-10. The objective function value, core shear strength and bending stiffness with the update of the iteration step in case 2: (a) Volume fraction constraint of 50% and (b) Volume fraction constraint of 62.5%.....	240
Figure 5-11. Evolution processes of core topologies under volume fraction constraint of 50% in case 1.....	242
Figure 5-12. Evolution processes of core topologies under volume fraction constraint of 62.5% in case 1.....	243
Figure 5-13. Evolution processes of core topologies under volume fraction constraint of 50% in case 2.....	244
Figure 5-14. Evolution processes of core topologies under volume fraction constraint of 62.5% in case 2.....	245
Figure 5-15. The optimal topologies obtained by proposed topology optimization schemes.	246
Figure 5-16. 2D and 3D models converted from optimal topologies for additive manufacturing.	247
Figure 5-17. Stress distributions of the optimal topologies (TO models) and converted 2D models in case 1: (a) Relative density of 50% and (b) Relative density of 62.5%.	248
Figure 5-18. Stress distributions at a bending curvature of 0.001 rad/mm and a shear strain of 5% for TO and 2D models in case 2: (a) Pure bending at relative density of 50%; (b) Shear at relative density of 50%; (c) Pure bending at relative density of 62.5% and (d) Shear at relative density of 62.5%.	248
Figure 5-19. Additively manufactured prototypes: (a) Core structures optimized in case 1 and (b) Core structures optimized in case 2.....	250
Figure 5-20. Produced sandwich sheets after adhesive bonding.	250
Figure 5-21. Sandwich topologies observed by a wide-area 3D measurement system controller	

with a magnification on a 15" monitor 12×.	251
Figure 5-22. Deformation processes during three-point bending experiments and simulations for sandwich sheets with the core density of 50% in case 1.	252
Figure 5-23. Deformation processes during three-point bending experiments and simulations for sandwich sheets with the core density of 50% in case 2.	253
Figure 5-24. Three-point bending properties: (a) Load-displacement curves and (b) Specific bending stiffness and absorbed energy.	253
Figure 5-25. Deformation processes of sandwich sheets during L-bending tests.	255
Figure 5-26. Deformed sandwich sheets and highlighted failure modes after L-bending.	256
Figure 5-27. Deformation processes and failure modes of sandwich sheets during draw-bending tests.	257
Figure 5-28. Deformed sandwich sheets and highlighted failure modes after draw-bending.	258

Table 1-1. Metal lattice structures produced by AM processes summarized by Zhang et al. (2018b).....	32
Table 1-2. Particle reinforced polymer composites manufactured by AM processes with enhanced property.	34
Table 2-1. Mechanical properties of A2017P, SUS304 and CFRTP.	85
Table 2-2 Structural parameters in design.....	87
Table 2-3. Bending stiffness at different radius ratios and bending directions.....	89
Table 2-4. Relative densities and corresponding dome radii.	89
Table 2-5. Optimal structural parameters in design.	93
Table 2-6. Multi stroke press forming conditions and results.....	96
Table 2-7. Flexural properties of sandwich sheets.....	100
Table 3-1. Mechanical properties of A2017P, SUS304 and the CFRTP.	119
Table 3-2. Structural parameters in design.....	120
Table 3-3. Comparison of failure modes between theoretical predictions and experimental results.	132
Table 3-4. Mechanical properties of SUS304 and Onyx.	141
Table 3-5. Process parameters for additive manufacturing of carbon fibre reinforced nylon.	142
Table 4-1. Structural parameters of models for topology optimization.	184
Table 4-2. Process parameters.....	191
Table 4-3. Material properties of 3D-printed PLA.	191
Table 4-4. The numbers of elements and nodes of CAE models.	193
Table 5-1. Mechanical properties of SUS304 and Onyx.	235
Table 5-2. Process parameters for additive manufacturing.....	235
Table 5-3. Core shear strength, gap between attachment points and bonding length ratio of optimal topologies.....	246
Table 5-4. Comparison of TO and 2D models in terms of core shear strength and bending stiffness.	249
Table 5-5. Specific bending stiffness and absorbed energy for different sandwich topologies.	

Chapter 1 Background

1.1 Demand for lightweight materials

With the rapid economic development, more daily necessities, electronic products and transportation tools are needed, which results in increasing amount of energy consumption and greenhouse gas emissions. Taking the amount of petroleum consumption in China as an example, it can be seen in the [Figure 1-1](#) (data from [U.S. Energy Information Administration](#)) that the energy consumptions have shown a continuously increasing trend in the past few decades. It can be expected that the energy consumption would keep increasing in the future, which would be a critical and thorny issue for the sustainable development. The increasing energy consumption year by year has also led to an increase in carbon emissions. The trend of global total carbon emissions is shown in [Figure 1-2](#). It can be found that carbon emissions are increasing year by year, and will continue to increase in the future, which will lead to serious environmental problems and global warming. Mitigating the increase in energy consumption and carbon emissions to achieve sustainable development has become a powerful driving force to stimulate the rapid development of materials, design, manufacturing and assembly technologies to promote more applications of lightweight components in the military and commercial engineering fields. It is reported by [Del Pero et al. \(2017\)](#) that the fuel consumption can be considered to be proportional to the mass of vehicles as shown in [Figure 1-3](#). With the prerequisite of the maintained product performance and safety, the reduction in weight in transportation would effectively decrease the fuel consumption and gas emission. The Japanese Aluminum Society has reported that the gas emission is reduced from 300 g-CO₂/km to 100 g-CO₂/km if the mass of the vehicles reduces from 2000 kg to 750 kg. The strategies to realize the weight reduction include fabricating miniaturized products, designing more reasonable internal structures and using lightweight materials, among which the flexible application of lightweight materials is considered as the most effective approach. In recent decades, a lot of lightweight materials, such as aluminum alloys, magnesium alloys, titanium alloys, polymer, composites, etc., have found widespread applications in aeronautics, astronautics, express

trains, automobiles and other industrial areas.

China's petroleum and other liquids production and consumption, 1993-2019

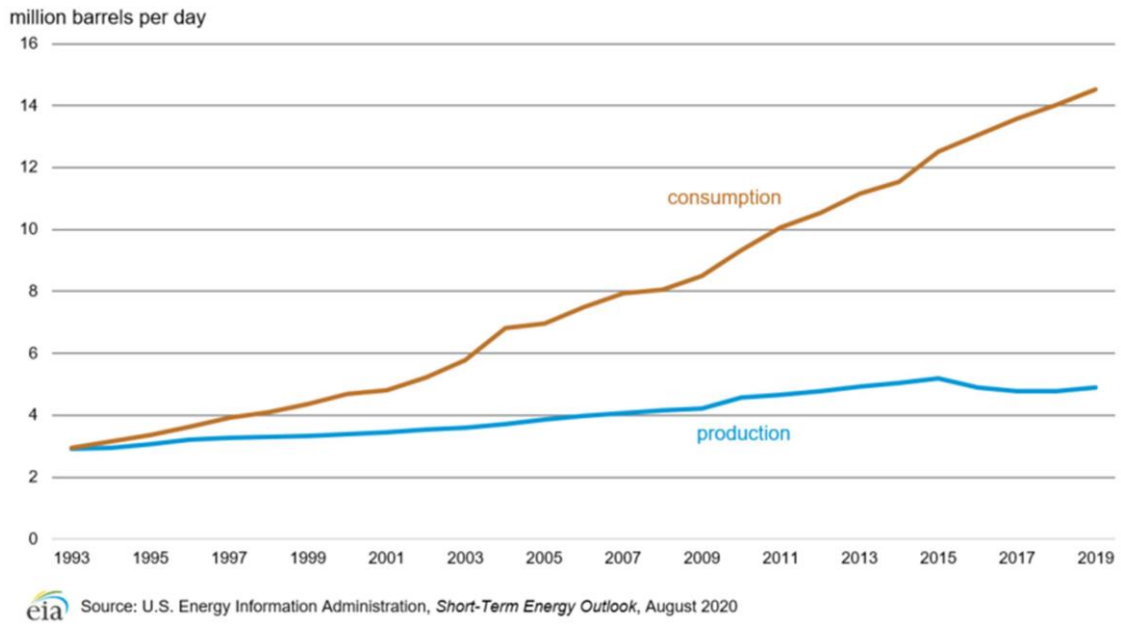
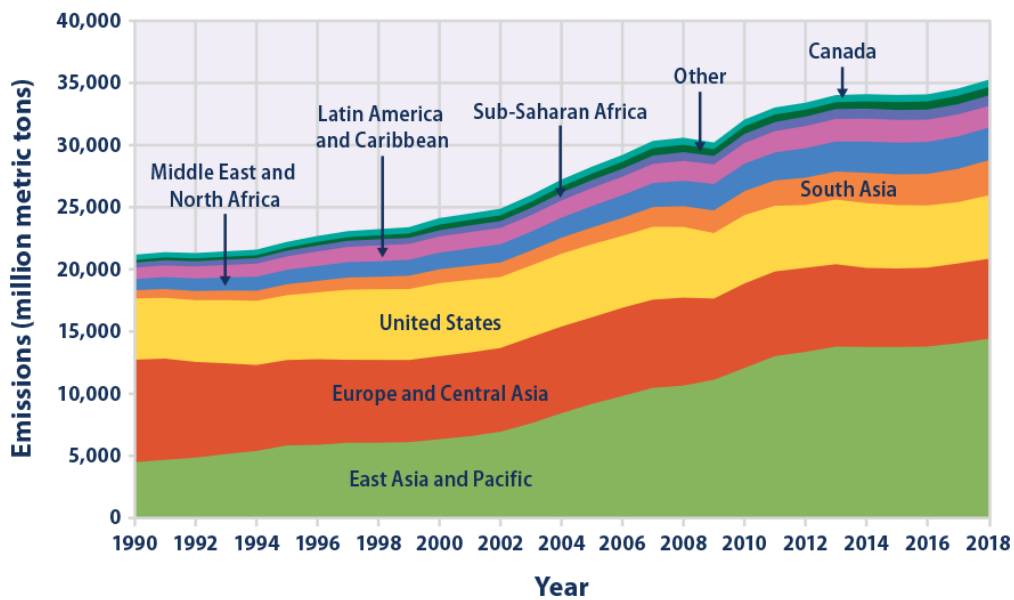


Figure 1-1. China's petroleum consumption from 1993 to 2019 (data from U.S. Energy Information Administration).

Global Carbon Dioxide Emissions by Region, 1990–2018



Data source: WRI (World Resources Institute). 2021. Climate Watch historical GHG emissions. Accessed March 2021. www.climatewatchdata.org/ghg-emissions.

For more information, visit U.S. EPA's "Climate Change Indicators in the United States" at www.epa.gov/climate-indicators.

Figure 1-2. Global carbon emissions from 1990-2018.

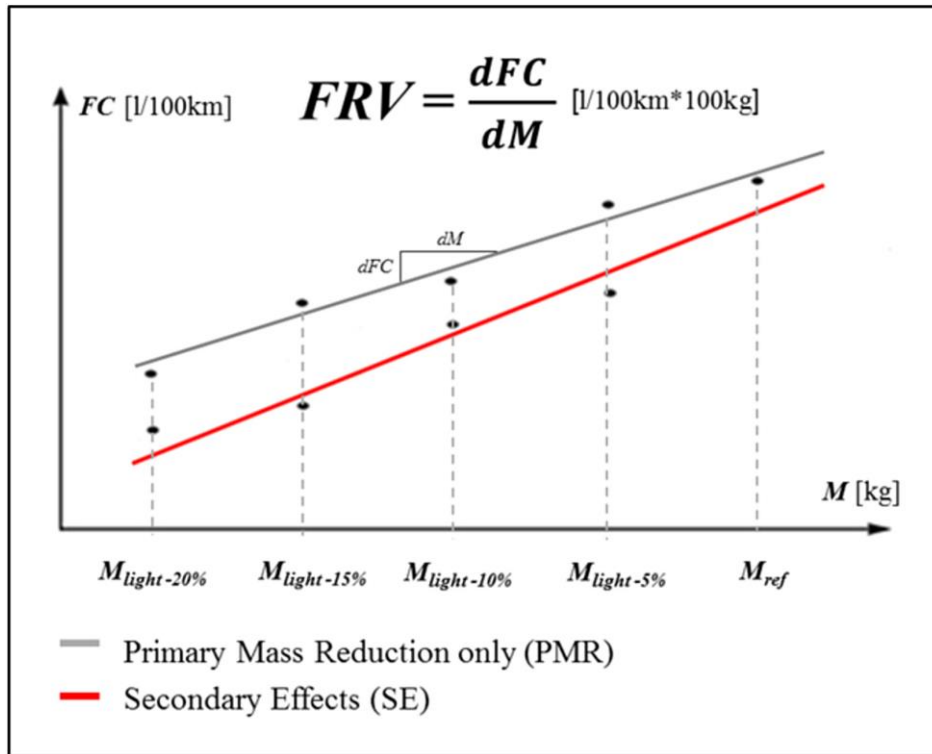


Figure 1-3. Fuel consumption (FC) in function of mass (M) with the relative regression line
Del Pero et al. (2017).

Advanced composite materials have been increasingly used in aircraft and automobile manufacturing to reduce fuel consumption and increase passenger capacity. The recently released Boeing 787 Dreamliner™ uses carbon fiber reinforced plastic (CFRP), which forms half of its airframe as shown in Figure 1-4. The use of advanced composites, specifically carbon fiber reinforced polymers (CFRP), has skyrocketed since the introduction of the Boeing 787 Dreamliner and, more recently, the Airbus A350. Figure 1-5 shows the advanced composites usage rate in aerospace industries in the past few decades, a continuous growing trend is seen and can be expected to further increase in the future. Increased usage of composite materials is also mirrored in automotive industries. Italian car manufacturer Lamborghini launched the Lamborghini Sesto Elemento™ weighing 999 kilograms. The chassis, body, drive shaft and suspension components are all made of carbon fiber reinforced composite materials. CFRP has also been widely used in BMW i3 and i8 series. As shown in the weight composition pie chart in Figure 1-6, CFRP accounts for 68.5 kg, nearly a half of the total weight of the BMW i3 body

structure. The BMW i3 has the body weight of 138.1kg, which is 90 kg (39%) lighter than that of a Mazda2-based steel-made vehicle of the same size. Especially in recent years, the development of electric vehicles has been extremely rapid. However, due to the limitation of battery energy density, the cruising range of electric vehicles is generally below 1,000 kilometers, which still cannot meet people's requirements for travel. The cruising range of electric vehicles is obviously negatively correlated with the weight of the vehicle. Therefore, the use of lightweight materials to manufacture the car body is undoubtedly an effective way to increase the cruising range of electric vehicles. The electric flying car, as shown in Figure 1-7, has been widely concerned in recent years. Its demand for lightweight structural materials is more urgent because of its flexible take-off, landing and flight. The development of flying car is of great significance to make up for the shortcomings of land vehicles and can realize flexible transportation in areas that cannot be reached by land vehicles.

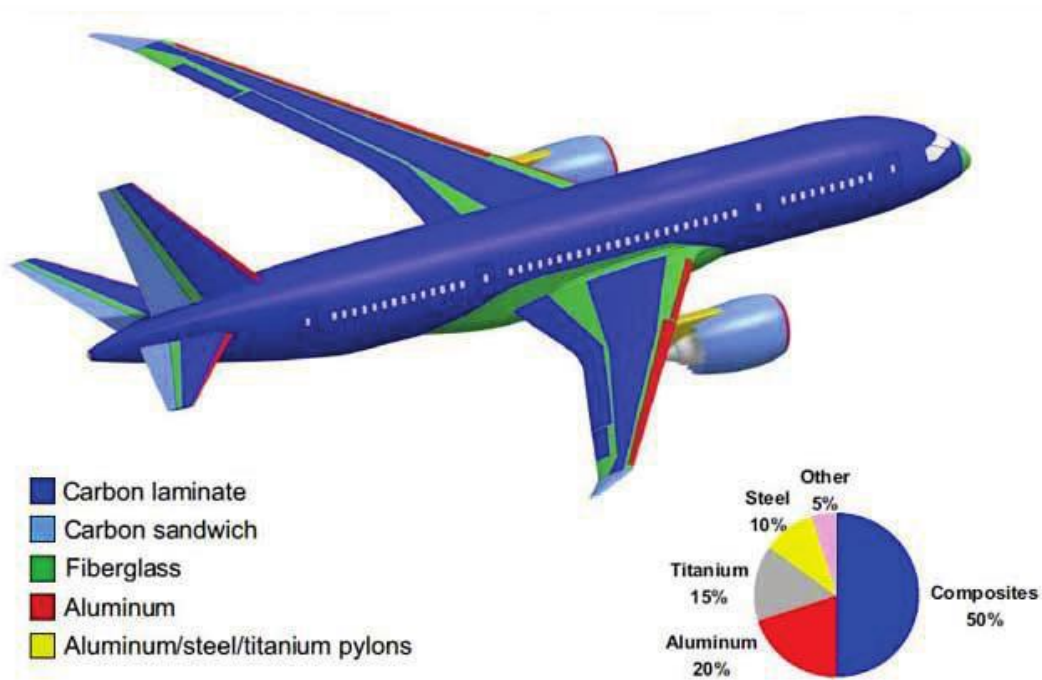


Figure 1-4. Material usage composition in Boeing 787 Dreamliner™.

Aerospace Advanced Composite Usage

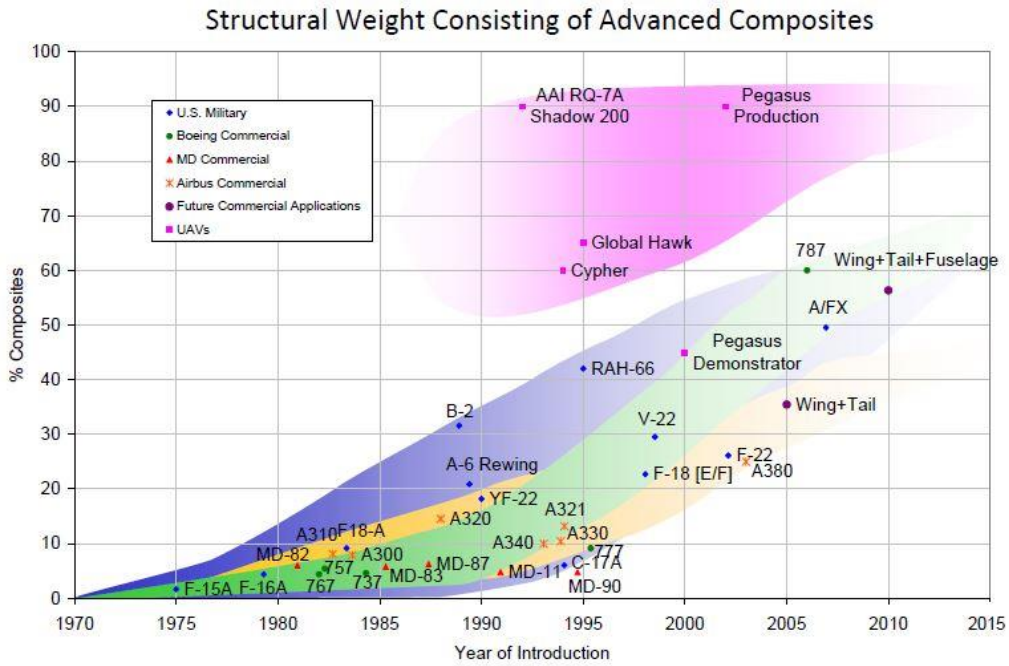


Figure 1-5. Aerospace advanced composite usage rate in the past few decades.

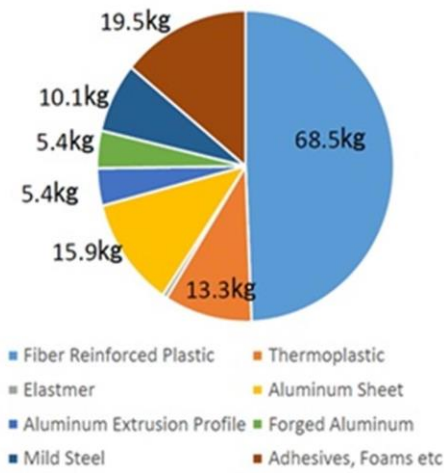


Figure 1-6. BMW i3 body structure part weight composition.



Figure 1-7. Flying car developed by Boeing.

1.2 Current answers for high demand for lightweight materials

In recent decades, with the improvement of industrial production capacity, many lightweight materials, such as aluminum alloy, magnesium alloy, titanium alloy, engineering plastics, structural ceramics, and composite materials of polymer, ceramic and metal matrix etc., are increasingly used in aircraft, automobiles, railways, electronic products and other fields to meet the needs of sustainable social development. These lightweight materials have a lower density than conventional steels and are promising for the future lightweight applications. The specific strength and stiffness of main engineering materials are compared in [Figure 1-8](#), in which the carbon fiber-reinforced thermosetting plastic with fiber volume fraction (V_f) of 0.6 has much higher specific strength and stiffness than other lightweight metallic materials, such as aluminum, magnesium and titanium. Increasing demand for lightweight material to decrease greenhouse gas emissions and energy consumption leads to growing application of CFRP components.

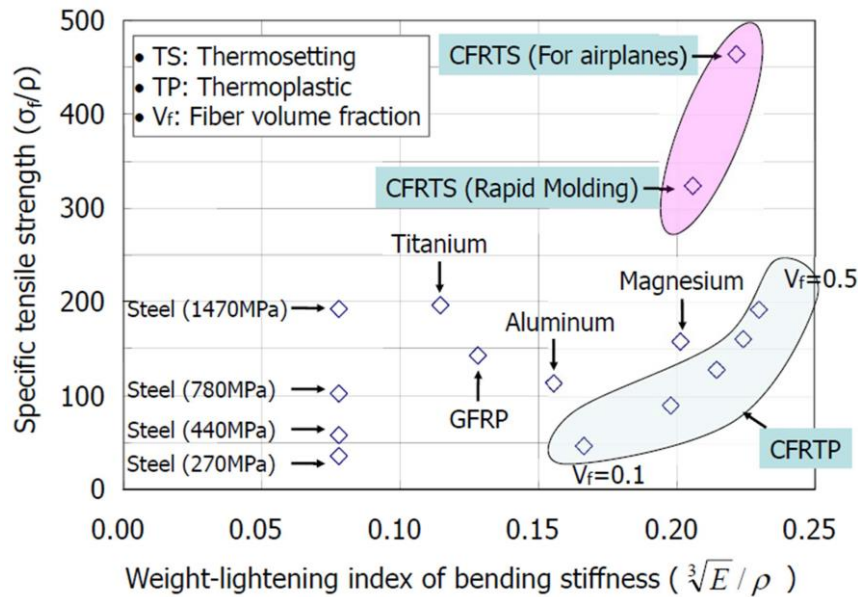


Figure 1-8. Specific strength and stiffness of main engineering materials Miura (2008).

1.2.1 Carbon fiber reinforced plastic (CFRP)

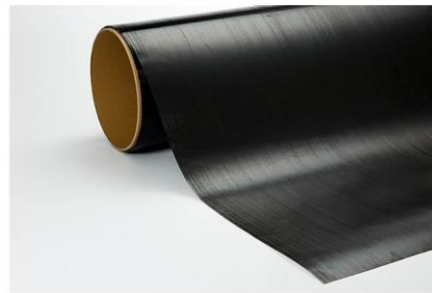
1.2.1.1 Common intermediate substrates of CFRP

CFRP is a composite material made by mixing a certain amount of carbon fibers into matrix. Depending on fiber lengths, CFRP can be divided into short fiber reinforced, long fiber reinforced and continuous fiber reinforced types. The ranges of short and long fiber lengths are less than 1 mm and 5-25mm, respectively. Generally, with the same fiber content, the mechanical properties of CFRP are proportional to the fiber length, but its plasticity is inversely proportional to the fiber length. Therefore, it is often necessary to comprehensively consider the mechanical properties and plasticity to seek a balance between the two for the selection of proper materials for industrial products. The forming methods of CFRP are not only related to fiber lengths, but matrix also affects the formability. The matrix in CFRP can be divided into two types: thermoplastic (PA (Polyamide), PP (Polypropylene), ABS (Acrylonitrile Butadiene Styrene), etc.) and thermosetting (epoxy) resins. Since the curing process of the thermoplastic resin is a reversible physical change (the softening and curing can be repeated), so the softening and forming of CFRP with thermoplastic resins can be achieved by increasing the temperature. The curing of thermosetting resin is an irreversible chemical cross-linking reaction, once cured, it is difficult to be softened again even if the temperature is increased and thus the processing

of thermoset CFRP is more difficult. Although the processability of thermoset CFRP is worse than that of thermoplastic CFRP, its mechanical properties are reported to be better as shown in [Figure 1-8](#), in which the strength of thermoset CFRP is higher than that of thermoplastic CFRP at 60% fiber content. Based on the type of resin and carbon fiber length, common intermediate substrates of CFRP are woven cloth, prepreg, carbon fiber mat and pellet as shown in [Figure 1-9](#).



Woven cloth



Prepreg



Carbon fiber mat



Pellet

[Figure 1-9](#). Common intermediate substrates of CFRP.

As shown in [Figure 1-10](#) (a), CFRP woven cloth is usually processed by Resin Transfer Molding (RTM), in which the woven cloth is firstly preformed in the closed mold and then liquid resin is injected into the closed mold, followed by applying high pressure and heat to cure the resin. Prepreg is pre-impregnated soft composite sheet in which carbon fibers are mixed with thermosetting epoxy resin, which is commonly preformed into desired shape and then placed in an autoclave with certain heat and pressure to get the cured parts. Compression molding is generally used to form carbon fiber mat as shown in [Figure 1-10](#) (b), the carbon fiber mat material is firstly heated and softened followed by closing the molds, and pressure and heat are kept to cure the part. Pellets are small granules in which short or long fibers are

infiltrated in resin as illustrated in Figure 1-10 (c). CFRP parts obtained from long fiber pellets have better tensile strength and impact properties compare to those made from short fiber pellets. As shown in Figure 1-10 (d), pellets are usually used for injection molding, in which pellets are firstly fed into a heated barrel, then mixed by a helical shaped screw, and finally injected into a closed mold until they are hardened to the shape of the cavity.

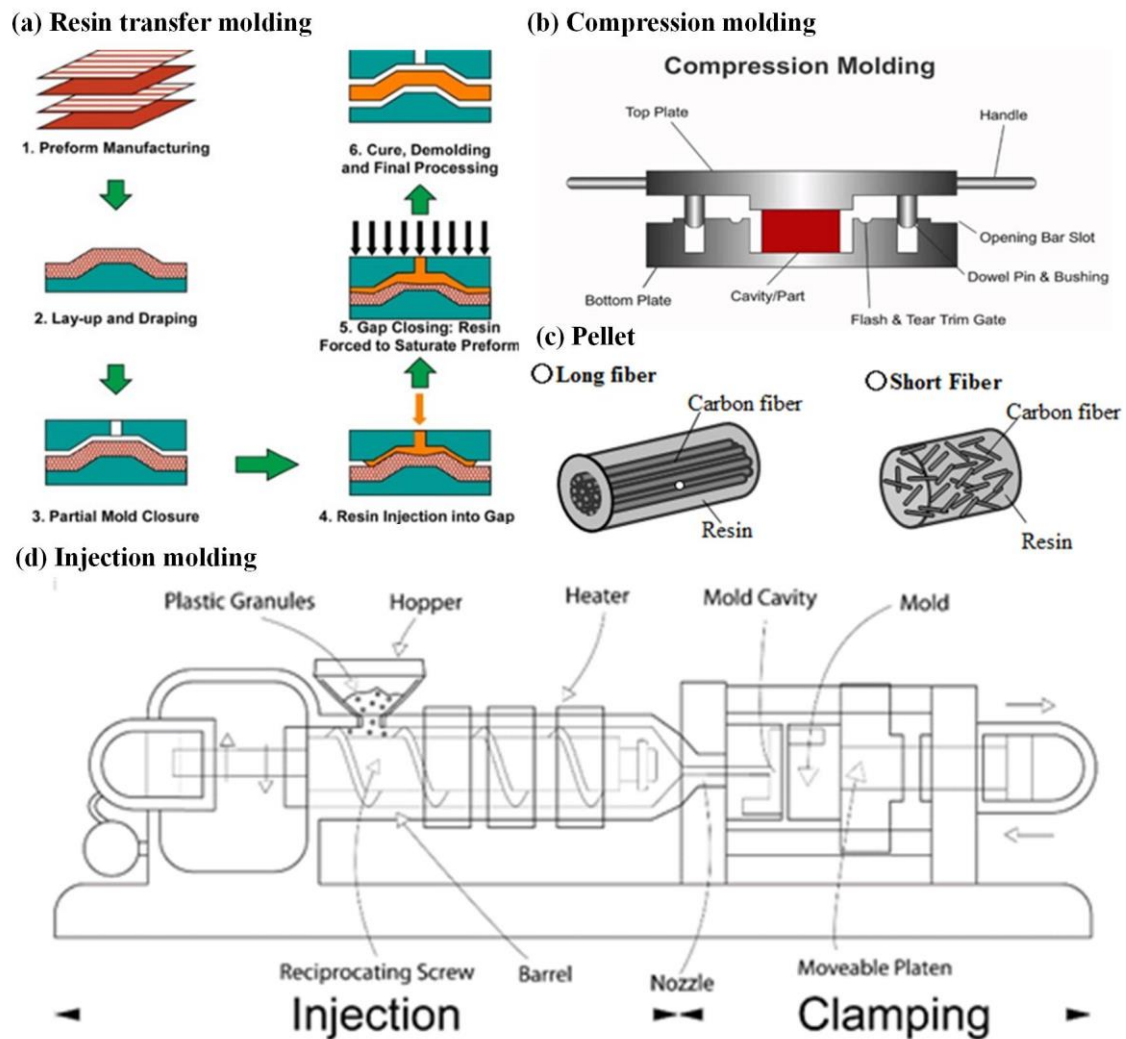


Figure 1-10. Processes of intermediate substrates of CFRP.

1.2.1.2 Stampable CFRP sheet

The long curing time of the thermosetting resin during aforementioned forming processes such as RTM, compression molding and injection molding indicates that they are not suitable for mass production. Furthermore, limited by the size of the molding equipment, the dimension of the produced CFRP part cannot be too large, which limits the produced parts to small or

medium-size components. Different from thermosetting resins, thermoplastic resins can be softened again at elevated temperatures and thus exhibiting better formability. To increase productivity and manufacture large components, stampable CFRP sheet have been developed. One kind of stampable CFRP sheet is carbon fiber mat reinforced thermoplastic (CFRTP) as shown in Figure 1-11 (a), in which chopped carbon fibers are randomly dispersed in thermoplastic resin. The other one is ultra-thin chopped carbon fiber tape reinforced thermoplastics (UTCTT) as shown in Figure 1-11 (c), where chopped unidirectional continuous carbon fiber tapes are randomly dispersed in thermoplastic matrix such as PA6 and PP. Different from CFRP with unidirectional carbon fibers, CFRTP and UTCTT sheets exhibit transverse isotropic mechanical properties due to randomly dispersed reinforcements. Fiber volume fraction of CFRTP is generally 10%-30% while that of UTCCT is higher to be 40%-60%. Therefore, UTCTT with higher fiber volume fraction displays higher strength but relatively worse formability. In this thesis, for the mass production of 3D macro inner structures of the sandwich sheets, CFRTP was selected owing to its better formability.

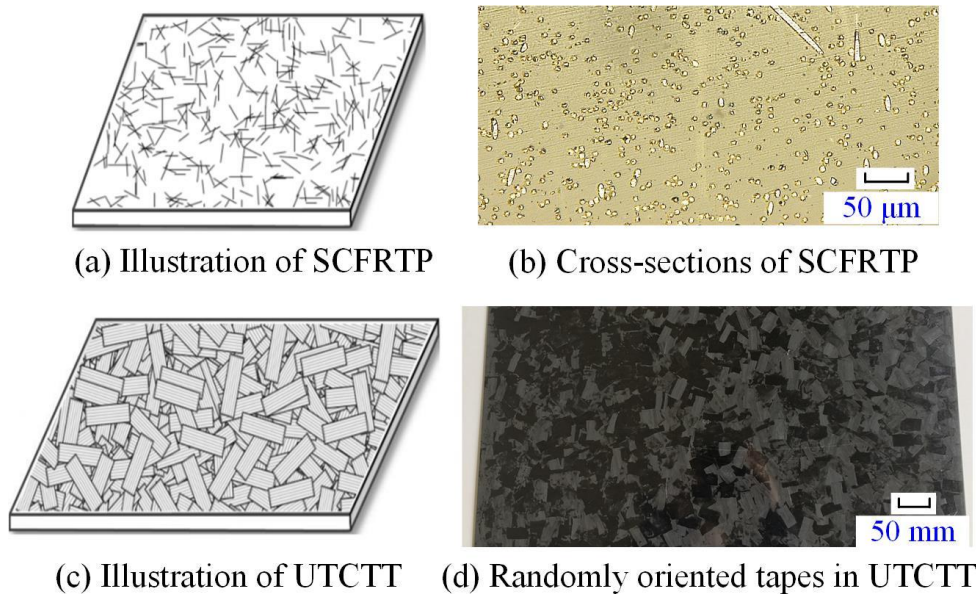


Figure 1-11. SCFRTP and UTCTT used for the fabrication of the core structure: (a) illustration of SCFRTP; (b) cross-sections of SCFRTP; (c) illustration of UTCTT and (d) randomly oriented tapes in UTCTT.

1.2.2 Hybrid structures

As is well-known, the observation of natural composite materials such as wood has promoted the idea of combining two or more materials with different characteristics to obtain new materials with enhanced and unique characteristics that cannot be achieved by any of the single constituent when standing alone. The first development of engineering composite materials and related manufacturing technologies can be traced back to the beginning of the 20th century, but the widespread use of composite materials in various applications in the engineering field has only occurred in the last few decades. The existing and potential applications of composite materials are particularly abundant in which high specific strength or stiffness is required. As pointed out in the previous section, although CFRP parts have higher weight-specific stiffness and strength than conventional metal materials, their formability is limited. Combining metal and CFRP together could potentially achieve a better balance between mechanical property and formability. The brief review of the composite materials in this section will mainly include the following two types: laminates and 3D hybrid sandwich sheet, illustrated in Figure 1-12 (a) and (b), respectively.

(a) Laminates



(b) Sandwich sheet

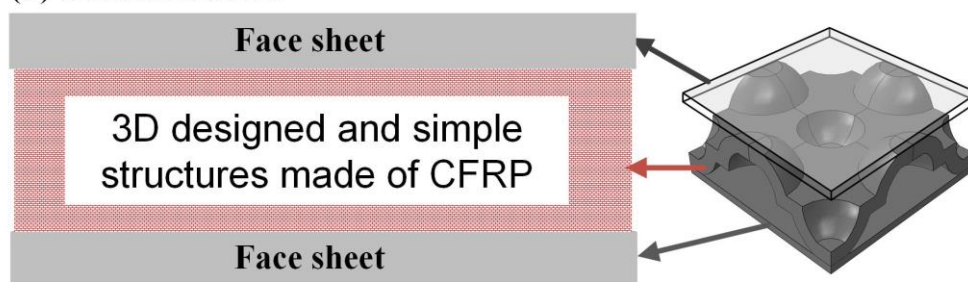


Figure 1-12. Illustration of hybrid structures reviewed in this thesis: (a) laminates; (b) 3D hybrid sandwich sheet.

Based on the definition given by Bruschi et al. (2021), laminates consist of individual

plies that can be metal, polymer, or fiber reinforced polymer of different thickness and properties. Laminates of interest in this section are: (i) alternating sheets of similar or dissimilar nature and thickness, joined together by very thin adhesive layers or diffusion bonding and (ii) high strength metal sheets alternated with fiber reinforced polymer plies, known also as fiber metal laminates (FMLs). The sandwich sheets discussed here refers to the structures in which two thin but stiff face sheets are bonded with a thick and lightweight core of a low strength material that can be metal, low-density polymer, fiber reinforced polymer or cellular material.

1.2.2.1 Laminates

Clad and multilayer sheets

In order to make full use of the physical and functional properties, dissimilar thin metal sheets are often combined together by means of various joining methods to get new clad metal sheets. Common combinations include aluminum/steel [Yahiro et al. \(1991\)](#), aluminum/titanium [Tseng et al. \(2011\)](#) and copper/stainless steel [Dehghani and Salimi \(2016\)](#), in which aluminum/steel clad sheets are adopted for sliding surfaces of sliding bearings in reciprocal engines. More applications of clad sheets can be found in [ISHIO \(1989\)](#). Since the 18th century, bimetallic strips have been used to convert the temperature change into a mechanical displacement and now are widely used in semiconductors, contact springs, magnetic applications, crystal oscillators, etc. As an early representative example, bimetallic strips made of nickel-based and nickel-based invariable steels were designed for thermostatic devices by the Nobel laureate Charles Edouard Guillaume in 1920. Various joining technologies have been adopted to fabricate the clad sheets, among which the representative ones include the cold or hot rolling, explosive cladding and pressure welded hot rolling. Cold rolling was the first method to join two dissimilar metal materials, in which two main procedures are included: (i) surface treatment of clad metal sheets to increase roughness and remove oxide layer and (ii) stacking of two clad sheets and apply pressure to join them together. To improve the joinability and interface property, hot rolling is generally conducted at an elevated temperature. Reported by [Maier et al. \(2012\)](#), a local laser heat treatment was used to improve the local recovery and recrystallization of the AA6016 aluminum sheets and desired formability was

obtained.

The secondary forming of clad sheets can be carried out via different sheet forming technologies such as bending, stamping and drawing. To clarify the limited drawing ratio of copper/stainless steel clad sheets, Nakajima tests and numerical simulations were conducted by [Dehghani and Salimi \(2016\)](#) for the prediction of failure location during stamping. Aluminum/titanium clad sheets were sheet hydroformed by [Tseng et al. \(2011\)](#) for better formability as compared to those obtained by conventional sheet forming methods.

Cold rolling was further developed into accumulative roll-bonding (ARB) by [Saito \(1998\)](#), in which new layers of sheets were added by repeating the rolling operations for the fabrication of multilayer sheets. Multilayer sheets consist of three or more layers of sheets and two or more material combinations based on the special requirement of the mechanical property and functionality of the final product. The formability of multilayer sheets consist of brittle core and ductile skin was investigated by [Yanagimoto et al. \(2010\)](#) using various forming tests, demonstrating that the multilayer sheets exhibit superior formability than the monolithic sheet of same thickness. The mechanism of the enhancement of formability of multilayer sheets was explained by [Figure 1-13](#), in which the necking initiation in the brittle layer can be delayed owing to the relocation of the stress distribution. Based on this mechanism, multilayer sheets made of martensitic stainless steel and ductile 304 stainless steel can be well bent without failure. Furthermore, multilayer sheets consist of stainless steel, aluminum and copper sheets were fabricated using hot rolling by [Lee et al. \(2007\)](#), and the mechanical and interface behaviors were shown to be dependent on the forming temperature.

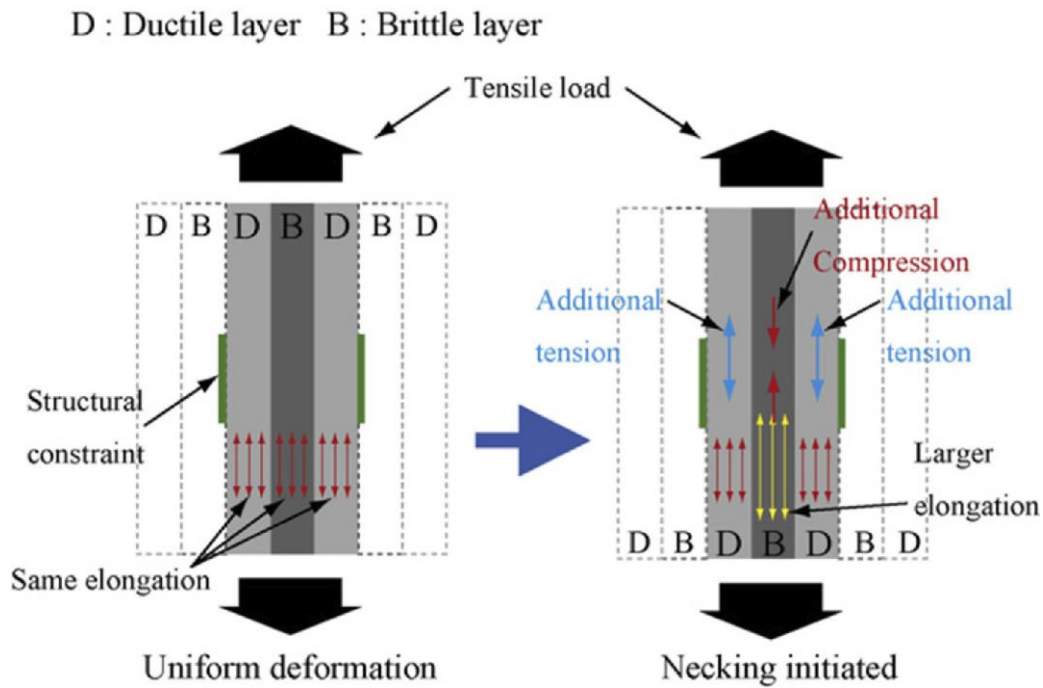


Figure 1-13. Mechanism illustration for the enhancement of formability of multilayer sheets
Yanagimoto et al. (2010).

Except for the full metallic clad sheets and multilayer sheets, the combination of metal and non-metal materials such as polymers have also gained much attention in the past few decades. They are widely used in structural applications relevant to seismic isolation by Kang et al. (2003) or other functional fields by Troch-Nagels et al. (1992). As an example, a consistent amount of polymer-coated tin steels is currently used for beverage cans that are fabricated by multiple drawing and ironing procedures by Kai et al. (2013). The polymer that coats the base metal can act as both anti-corrosive layer and lubrication film as they are cold formed. An inferior formability of steel/polymer laminates was found than that of the monolithic steel sheets of the same thickness owing to the lower shear resistance of the low-strength polymer core. However, for the aluminum/polymer laminates, superior formability than that of the monolithic sheets was shown by Kim and Yu (1997).

Fiber metal laminates (FMLs)

Laminates consist of high-strength metal faces and a fiber reinforced polymer core is well-known as fiber metal laminates (FMLs). Based on the metal face constituent, core material, lamination lay-up and direction of laminate, they were classified by Bruschi et al. (2021) as

shown in [Figure 1-14](#). FMLs have received remarkable success in the past few decades as they are widely used in aerospace and automotive industries. They are made of two similar or dissimilar metallic face layers and a fiber reinforced polymer core of which height is generally no more than 40-60% of the total thickness of the laminate. Very thin adhesive layers are commonly applied to the interface between metallic face sheets and polymer core for better bonding strength. The first FML, called ARALL (Aramid Fiber Reinforced Aluminum Laminate), was born in 1978 at the Delft University of Technology, Denmark, for the purpose of enhancing the fatigue performance of multilayer sheets. To further improve the stiffness of FML, carbon fiber reinforcement was used to replace the aramid ones to get the CARALL (Carbon Fiber Reinforced Aluminum Laminate) and later the GLARE (Glass Laminate Aluminum Reinforced Epoxy) with high-strength glass fiber reinforcement. These early FMLs are all aluminum alloy-based laminates and now they are widely used in aerospace industry. Recently, FMLs that are based on other metals such as titanium, steel and magnesium have been developed for the wider range of applications. Owing to the advantageous including superior mechanical resistance, better recyclability and shorter processing time, thermoplastic matrix based FMLs received much attention in recent years.

FMLs are generally firstly placed in an autoclave, in which the resin is cured under a certain pressure and temperature and simultaneously the metal and polymers are bonded together, followed by a stretching process to remove the residual stress as reviewed by [Sinmazçelik et al. \(2011\)](#). To obtain the optimal interface property, metal surfaces should be firstly treated, such as through mechanical, chemical or physical processes prior to bonding operations. Different from the monolithic sheets, more complex factors affect the process performance of FMLs, especially the interface characteristics except for the fiber orientation and properties of constituted metal and composites.

Fiber Metal Laminates (FMLs)

Based on Metal Constituent	Based on Reinforcement Constituent	Based on Lamination Lay-up	Based on Direction of the Laminate
Stainless Steel	Kevlar	2/1 Lay-up	Unidirectional Hybrid
Titanium	Carbon	3/2 Lay-up	Cross Ply Hybrid
Magnesium	Glass	4/3 Lay-up	
Aluminium	Aramid		

Figure 1-14. General classification of the FMLs [Bruschi et al. \(2021\)](#).

Until 2000, most FMLs structures were mainly produced by simple bending and manual lay-up methods, which only enables the fabrication of components of relatively simple geometries such as the skin panels of aircrafts. To shape FMLs into more complex geometries, die forming technologies were later introduced. Nowadays, more advanced die forming technologies such as hydroforming reported by [Saadatfard et al. \(2020\)](#) and electro-magnetic forming introduced by [Chernikov et al. \(2019\)](#) are adopted for the enhancement of formability. To evaluate the formability of FMLs, tensile and cup drawing tests are commonly used. According to FML composition, formability can be expected to be enhanced compared with the monolithic constituent. FMLs consist of low-ductility aluminum sheets and aramid composite exhibited better formability over the single constituent as shown by [Gonzalez-Canche et al. \(2017\)](#), and FMLs composed of aluminum sheets and PP composite displayed superior ductility to the monolithic sheets as reported by [Sexton et al. \(2012\)](#). The Delamination Forming Limit Curve (D-FLC) was introduced to characterize the delamination path of FML by the Nakajima test as given by [Liewald and Hofmann \(2017\)](#). In the case of thermoplastic matrix based FML, forming at elevated temperatures could be helpful for the improvement of formability. A feasible means of forming thermoplastic matrix based FML is shown in [Figure 1-15](#), and detailed descriptions of such forming strategies are given by [Ding et al. \(2021\)](#).

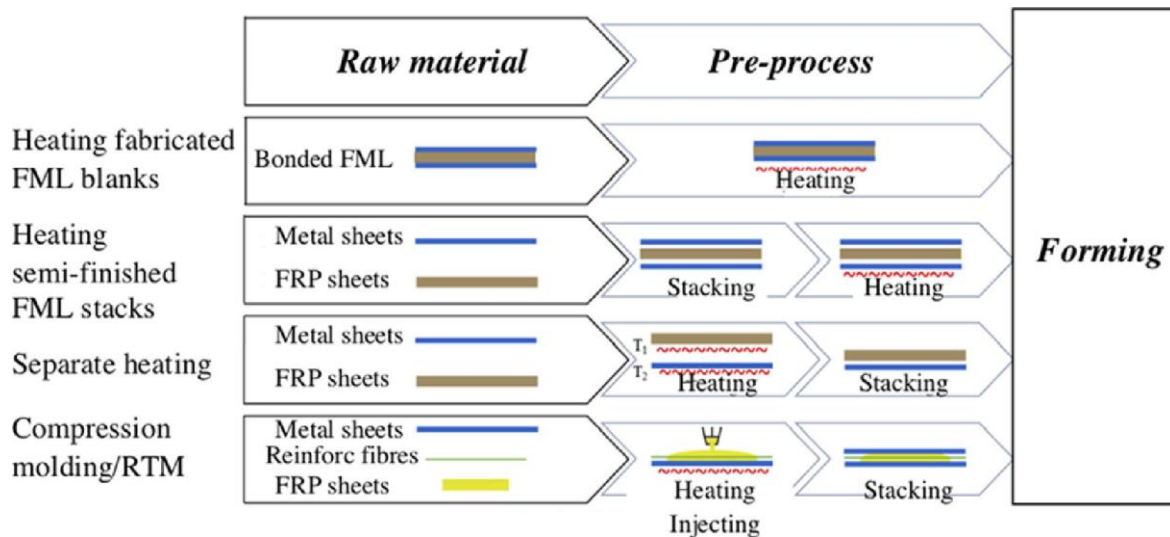


Figure 1-15. Heat-assisted forming strategy of thermoplastic matrix based FML Ding et al. (2021).

The most important factor that affects the forming behavior of thermoplastic matrix based FML during the above process is the forming temperature. The optimal forming temperature of fiber reinforced polymer is generally located between the glass transition and melting temperature of matrix. The combination of forming and joining in one step was proposed to shape FMLs consist of steel and CFRP prepregs at the temperature above the melting point by Bernd-Arno et al. (2017). Following the process chain illustrated in Figure 1-16, the successful forming of FMLs was achieved with a tool temperature of 250 °C. More details about the forming process have been introduced by Bernd-Arno et al. (2017).

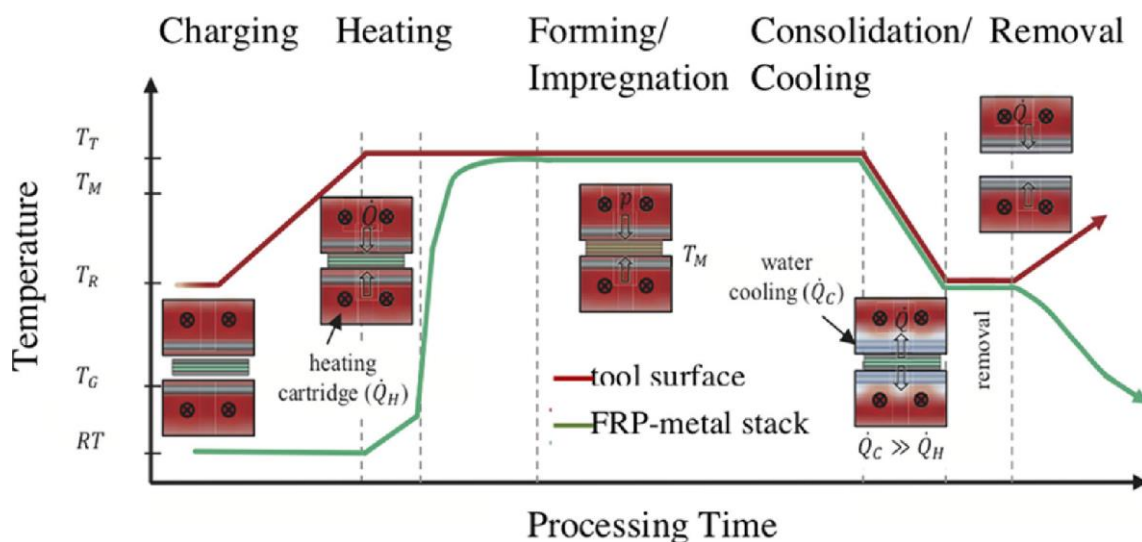


Figure 1-16. Process of FMLs parts via combination of forming and joining in one step

1.2.2.2 3D hybrid sandwich sheet

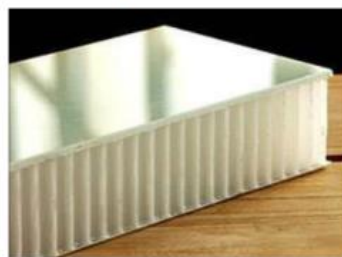
Sandwich structure is generally composed of two thin similar face sheets of high stiffness and a thick low-density core with height several times that of the face sheet. This unique combination enables much higher bending stiffness compared to the monolithic constituent of the same weight. Face sheet materials are commonly made of FRP and Metals (Aluminum, Steel, Titanium, etc.) of high stiffness. A wide range of candidates of different materials or structures are available for the inner macro core structure, which can be metals, polymers, foams (polymer foam, metal foam, etc.), hollow structure (honeycomb, corrugated, truss, pyramidal, etc.), and solid (balsa wood). The most widely used sandwich structure is that with a honeycomb core, which can be seen in many transport vehicles and aircrafts. Besides, some representative sandwich structures are shown in [Figure 1-17](#). The inner macro core structure is generally adhesively bonded to the face sheets, similar to the FMLs, the surface treatment of face sheets should be conducted prior to the bonding process to ensure sufficient bonding strength. Different from FMLs, for sandwich sheets, more design freedom of inner macro core structures exists not only in materials but also in structures (shape, topology, etc.). Namely, the inner macro structure could be 3D and its shape or topology can be optimized to achieve special mechanical and functional properties.



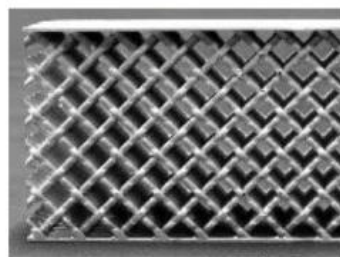
(a) Foam core



(b) Balsa wood



(c) Honeycomb core



(d) Trussed core

Figure 1-17. Some representative sandwich structures.

The production of 3D sandwich sheets includes two steps: (i) fabrication of sandwich sheets and (ii) secondary forming of sandwich sheets into curved shape. Compared with clad sheets, multilayer sheets and FMLs, the relatively poor formability of sandwich sheets limits their applications more to the flat panel types. To design and produce sandwich sheets that not only have superior mechanical properties and good formability is the key to expanding the application ranges of lightweight sandwich materials. It should be noted that the manufacturing of 3D sandwich sheets by sheet forming process is still at an early stage and the purpose of this thesis is to promote the development in this area. Another issue that blocks the widespread usage of sandwich structures is the high cost. The manufacturing process of sandwich structures highly depends on the constituted materials, so the review of the related literatures in this section is based on the sandwich compositions and production methods. To be specific, they are categorized as full metallic sandwich structure, FRP sandwich structure and novel structures produced by additive manufacturing (AM). They are treated as full metallic sandwich structure if both face sheet and core are metallic materials, while at least one constituent is FRP material for FRP sandwich structure. For novel structures produced by AM, no matter the material compositions, they are reviewed separately from the above two categories.

Full metallic sandwich structure

As shown in Figure 1-18, various 3D core structures have been designed for full metallic sandwich sheets including but not limited to pyramidal truss, tetrahedral truss, straight kagome, woven wire, honeycomb, corrugated, Y-frame, etc. Among aforementioned structures, owing to the largest volume empty, truss core type is generally considered to be the most lightweight. Woven wire core was found to have better specific stiffness, while honeycomb, corrugated and y-frame cores display excellent out-of-plane compressive performance. As shown in Figure 1-19, to increase the bonding area and keep sufficient bonding strength, folded unidirectionally corrugated and pyramidal truss cores were designed by Wadley (2006) and Kooistra and Wadley (2007), respectively. Face buckling may also be delayed by increasing the bonding area as the face sheets can receive more support from the core structure during bending or

compression.

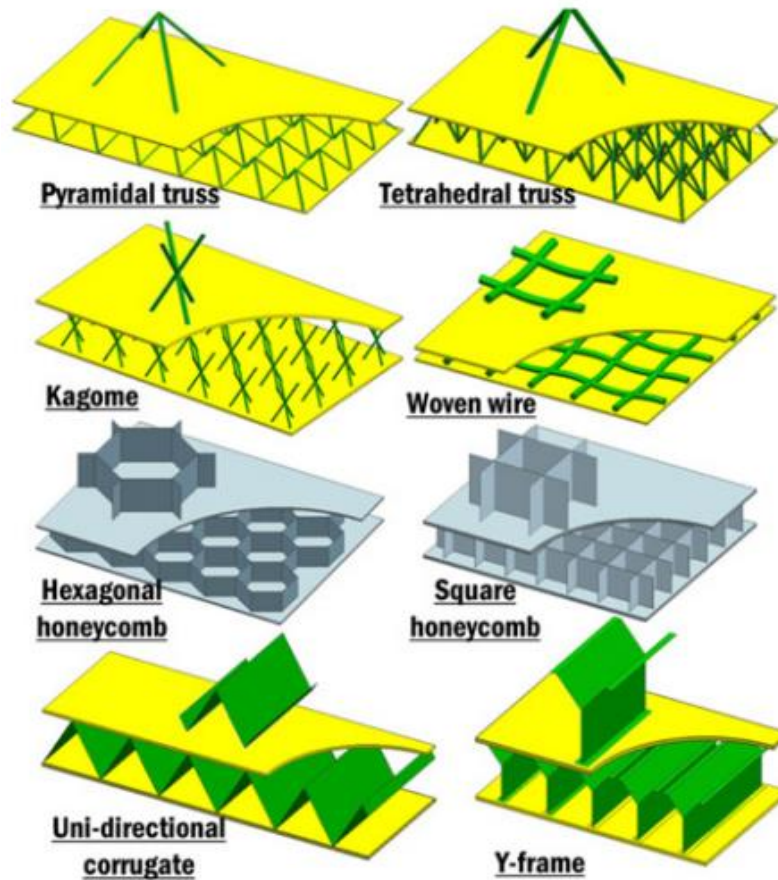


Figure 1-18 Sandwich structures with various cellular cores.

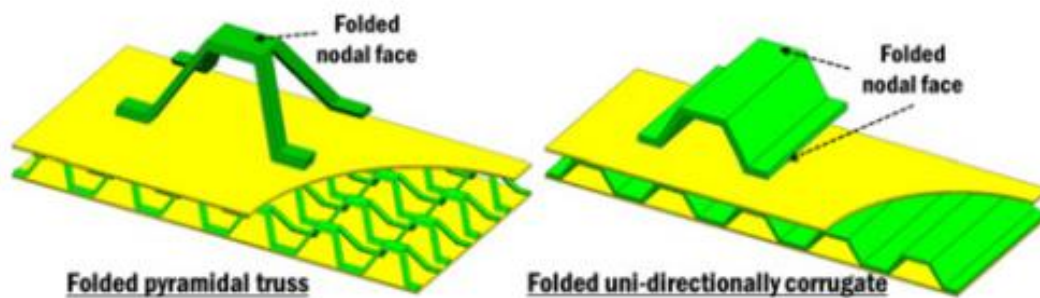


Figure 1-19. Sandwich structures with folded cellular cores Wadley (2006) and Kooistra and Wadley (2007).

Owing to the geometry and topology differences, suitable manufacturing technologies should be specially designed for each corresponding structure. Production chain of pyramidal truss core sandwich structure included multiple steps including slitting, expanding, roll flattening, folding and brazing as given by Kooistra and Wadley (2007) in Figure 1-20(a). As

introduced by [Queheillalt et al. \(2008\)](#) in [Figure 1-20\(b\)](#), another approach included extrusion and electrical discharge machining (EDM) for the fabrication of pyramidal truss core sandwich structure. Initial flat metal sheet was firstly perforated followed by elongation and crimping of elongated-perforated sheet to produce the tetrahedral truss as proposed by [Sypeck and Wadley \(2002\)](#). Crossly twisted helical wires were connected by soldering and brazing for the production of woven-wire structure as proposed by [Kang \(2009\)](#). Metal sheet was firstly stamped to get corrugated structure and then joined them together to fabricate corrugated honeycomb as introduced by [Bitzer \(1997\)](#) in [Figure 1-21](#). As illustrated in [Figure 1-22](#), webs and legs were firstly produced by cold folding and CNC cutting, respectively, followed by brazing and laser welding together to get the Y-frame structure as described by [Rubino et al. \(2009\)](#). It can be found that the production of sandwich structures generally includes multiple steps, which induces a high manufacturing cost and a low production efficiency and thus preventing their mass production.

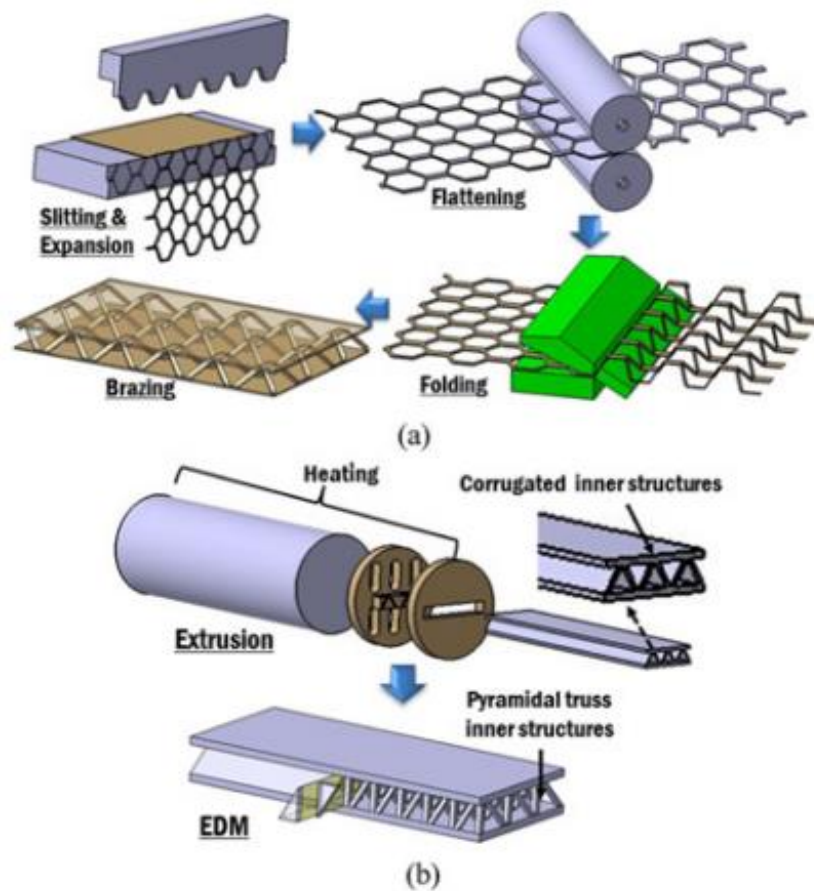


Figure 1-20. Fabrication processes of pyramidal truss core sandwich structure Kooistra and Wadley (2007) and Queheillalt et al. (2008).

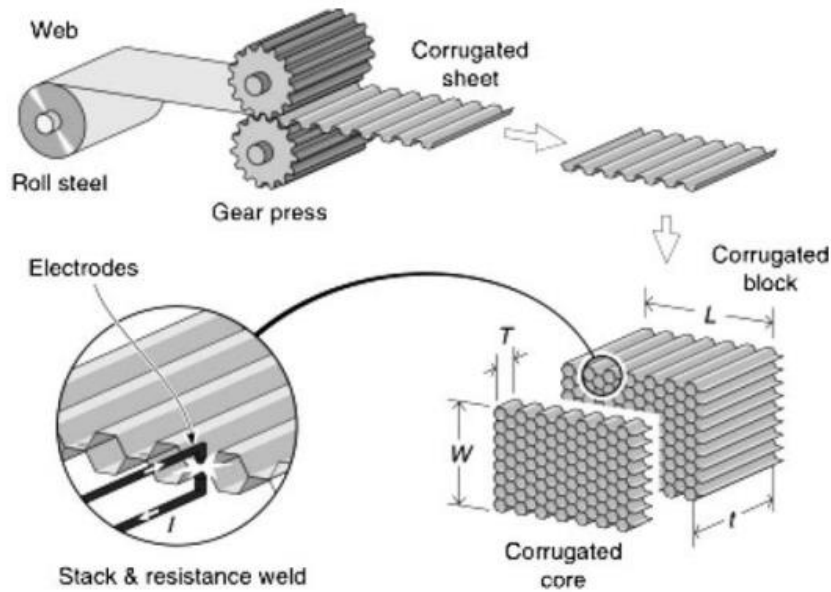


Figure 1-21. Fabrication processes of honeycomb core sandwich structure Bitzer (1997).

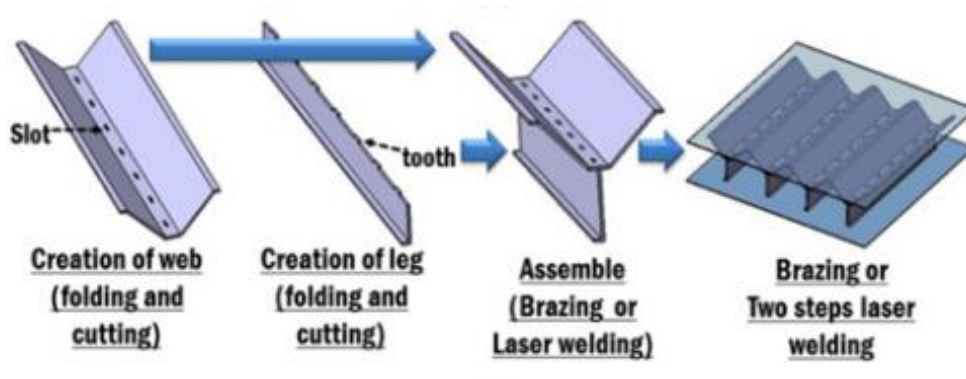


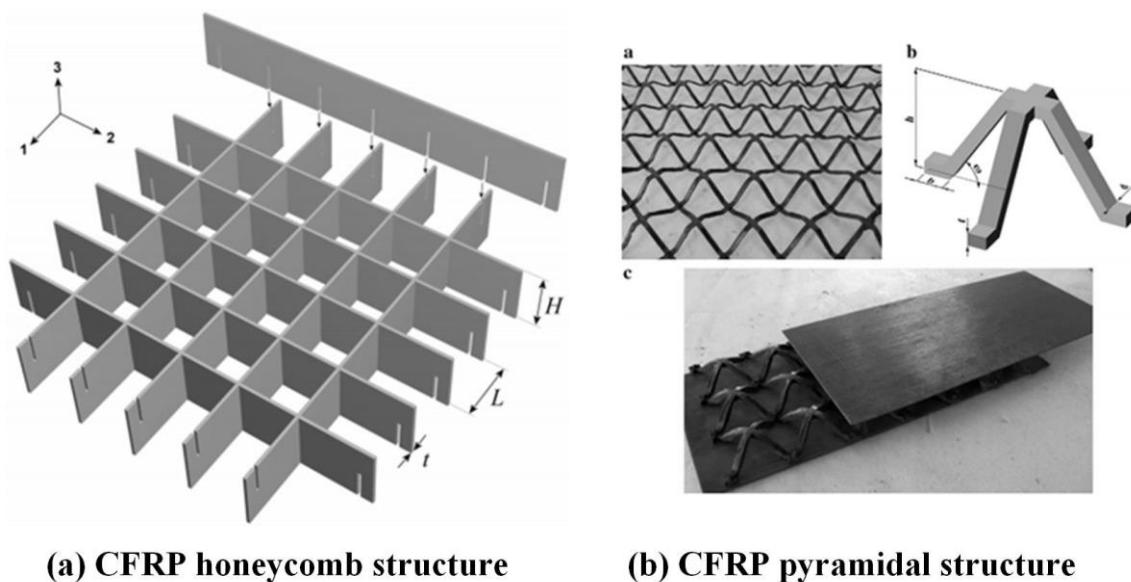
Figure 1-22. Manufacturing processes of Y-frame core Rubino et al. (2009).

FRP sandwich structure

To further improve weight-specific structural efficiency, fiber reinforced plastic (FRP) has been more and more adopted in manufacturing sandwich structure in the past two decades. Glass fiber reinforced plastic (GFRP), CFRP and AFRP (aramid fiber reinforced plastic) laminates usually act as face sheets of sandwich structure, among which GFRP is most popular owing to its cheap price. Combination of metallic honeycomb core especially aluminum based honeycomb core and GFRP face sheets is now widely mirrored in engineering structures. As reviewed by Russo and Zuccarello (2007), GFRP skin/PVC foam gained widespread use in

marine ships. Polyvinyl chloride (PVC) and polyurethane (PU) are generally selected as foam cores to be integrated with FRP faces. In addition, recyclable thermoplastic materials such as polyethylene terephthalate (PET) has also been widely used as foam cores. Due to high weight-specific mechanical properties including shear and bending stiffness, balsa wood is also a good option for core material. To improve failure resistance such as to prevent face wrinkling and core indentation, end-grain balsa made of small blocks can be used as core material as demonstrated by [Tagarielli et al. \(2008\)](#).

3D honeycomb structure was made from CFRP laminates through slotting followed by adhesive bonding process as described by [Russell et al. \(2008\)](#) in [Figure 1-23\(a\)](#). As introduced by [Xiong et al. \(2010\)](#) in [Figure 1-23\(b\)](#), pyramidal truss structure was fabricated by hot-press molding of carbon fiber/epoxy prepregs or it can be produced by a mechanical “snap-fit” process as proposed by [George et al. \(2013\)](#) in [Figure 1-24](#). As shown in [Figure 1-25](#), to improve compressive strength and energy absorption characteristics, carbon fiber lattice was combined with foam material to get a hybrid core structure and then stitched to CFRP faces, and finally epoxy resin was injected to cure the whole structure, as proposed by [George et al. \(2014\)](#). An interlock method, as shown in [Figure 1-26](#), was proposed by [Fan et al. \(2006\)](#) to produce the Kagome lattice structure using CFRP.



(a) CFRP honeycomb structure **(b) CFRP pyramidal structure**

[Figure 1-23](#). CFRP honeycomb and pyramidal core sandwich structures: (a) honeycomb structure [Russell et al. \(2008\)](#); (b) pyramidal structure [Xiong et al. \(2010\)](#).

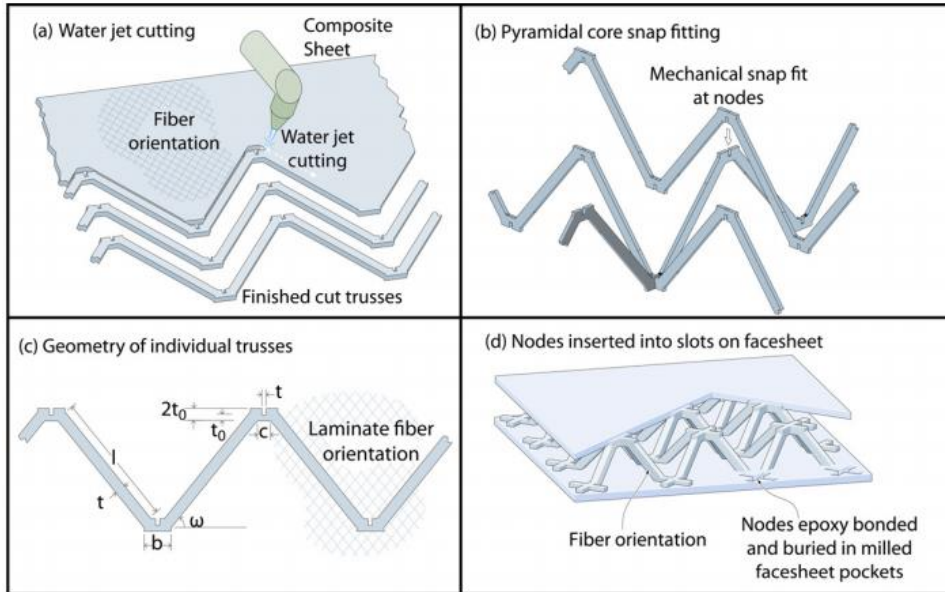


Figure 1-24. CFRP pyramidal truss core sandwich structure George et al. (2013).

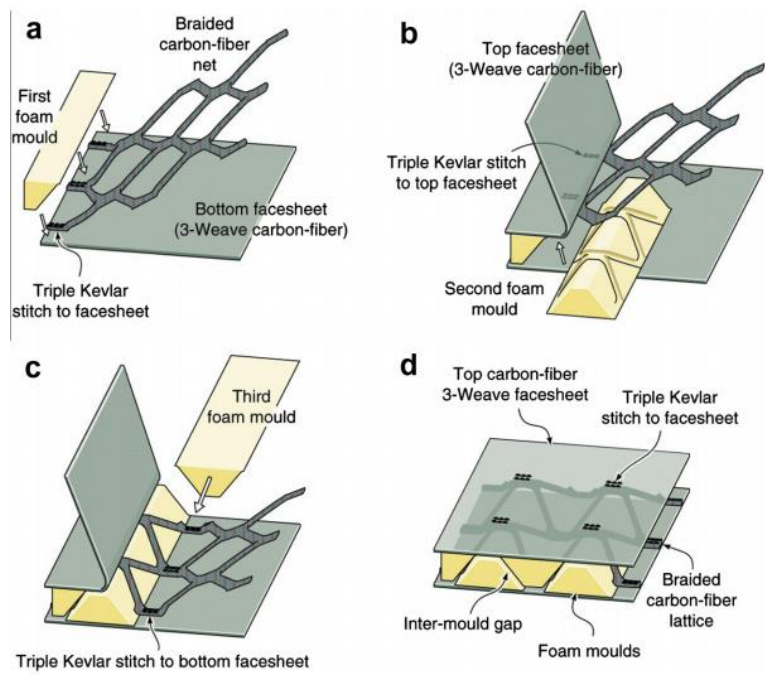


Figure 1-25. Sandwich structure with a hybrid carbon fiber lattice foam core George et al. (2014).

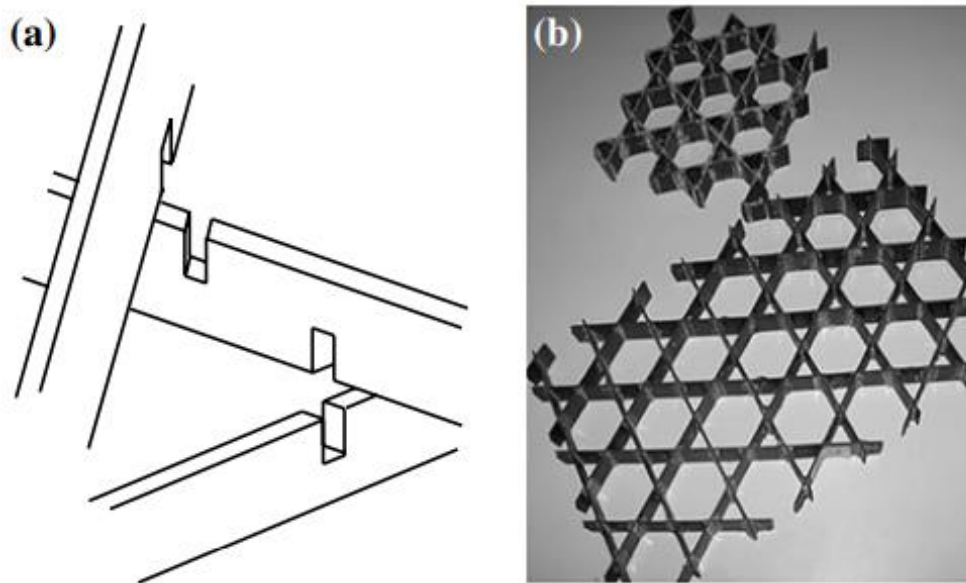


Figure 1-26. CFRP Kagome lattice sandwich structure [Fan et al. \(2006\)](#).

1.2.3 Lightweight structures produced by additive manufacturing

1.2.3.1 Introduction of additive manufacturing

History of additive manufacturing

The first development of additive manufacturing can be traced back to almost 150 years, with inventions to generate freeform topographical maps and photo sculptures from 2D layers as reviewed by [Beaman et al. \(1997\)](#). Later in 1960s and 70s, photopolymerization, powder fusion and sheet lamination additive approaches were invented one after another owing to the emergence of computer in the late 1940s, photopolymer resins by Dupont in the 1950s, and commercialization of lasers in the 1960s. The development of additive technologies in this period highly relies on the advancement of computer aided design (CAD), including the numerical control machine tools in the 1950s, computer graphics and CAD tools and CAD systems in the 1960s, and the low-cost computer monitors in early 1970s. However, the development of additive manufacturing was still in its infancy without commercial market and support for research activities.

An increase in the number of patents and publications on additive manufacturing was seen in the 1980s and early 1990s, such as the MIT's 3D printing process in 1989 as reviewed by [Mueller \(2012\)](#) and laser beam melting (LBM) process in early 1990s as introduced by

Shellabear and Nyrhilä (2004). Some additive manufacturing technologies invented during this period gained successful commercialization such as the stereolithography (SL), fused deposition modelling (FDM) and laser sintering as reviewed by Wohlers and Gornet (2014). The development of additive manufacturing in this period attributed to the advancement in geometric modelling capability and programmable logic controllers in the 1960s and 70s as stated by Chua et al. (2010) and Mueller (2012). However, the development during this period was still slow owing to the high cost, limited printable material and low accuracy of the equipment.

A rapid growth of AM happened in the 1990s and 2000s, new process such as electron beam melting (EBM) process was commercialized, existing AM processes were improved, and attention began to move to the development of relevant software. AM-specific file formats including STL (stereolithography), LMI (Layer Manufacturing Interface) and LEAF (Layer Exchange ASCII Format) were developed. In addition, AM-specific software programs such as Clemson's CIDES (1990) and Materialise's Magics (1992) were introduced. New software provided improved function and features, which enabled AM of patterns, tooling and final parts. At the same time, cheap but powerful desktop computers made AM equipment affordable and smaller. The advances in modelling software enabled students and professionals to create 3D models by themselves more easily and inexpensively. The Internet also promoted the knowledge sharing and speeded up the updating of hardware and software, which enabled the born of the first hobby AM machine by RepRap in 2005.

The attention paid to metal-based AM processes showed a growing trend in the late 2000s, with the competitive commercialization of some old metal AM processes invented in 1980s. This, together with promoted innovation with the growing AM hobby community, opening the door to a wide range of market supply and demand. Nowadays, AM technologies provide huge support for a load of activities, including but not limited to manufacturing, art, architecture, energy, hobbies, space exploration, transportation, education, and military. AM processes now enables the direct fabrication of final products in the medical, automotive and aerospace industries. Meanwhile, commercial amateur printers and entry-level professional machines have made additive manufacturing technology available to the general public.

Additive manufacturing processes and workflow

Additive manufacturing processes can be generally classified into seven groups by ASTM as shown in Figure 1-27: vat polymerization, material jetting, material extrusion, binder jetting, powder bed fusion, sheet lamination, and directed energy deposition. The physical workflow of AM technologies begins with one of the above seven families.

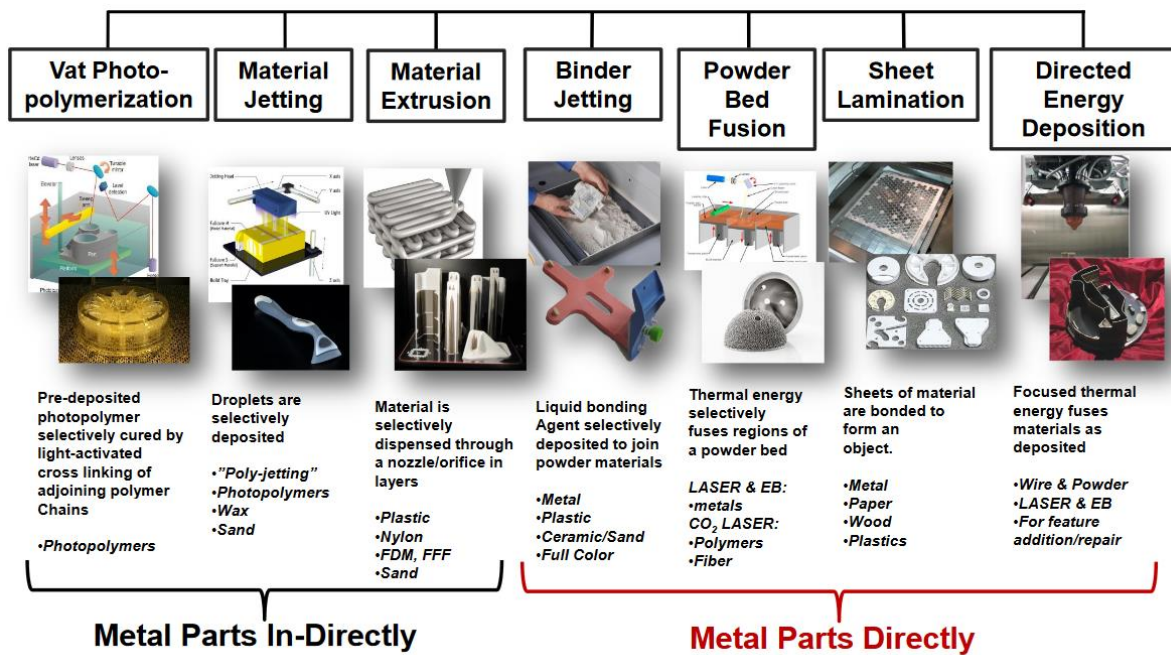
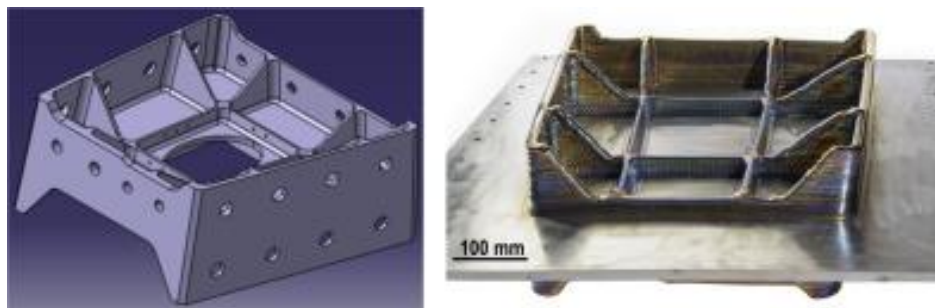


Figure 1-27. Additive manufacturing processes classified by ASTM Committee F42. Source: Boeing/ASTM.

Direct fabrication of prototypes, models, assemblies, and end-use parts, as well as those for indirect production such as patterns, fixtures, and tools can be achieved by AM processes as introduced in VDI-Guideline (2009). Hybrid processes were created by integrating AM processes together as proposed by Keating and Oxman (2013) and longer multi-stage process chains were formed by combining AM technologies with conventional production methods as introduced by Thompson et al. (2016b). For instance, outboard landing gear rib of near net shape was firstly produced using Ti-6Al-4V by Wire + Arc Additive Manufacturing (WAAM) and then post-machined as shown in Figure 1-28, in which left one is the CAD model and right one is the printed part before machining, as discussed by Williams et al. (2016). In addition, by alternating AM and machining operations, as shown in Figure 1-29, injection molding tools

were produced by 3-axis hybrid layered manufacturing (Gas Metal Arc Welding plus CNC machining), in which left one is the CAD model, middle one is the near net shape molds, and right one is final molds as described by [Suryakumar et al. \(2011\)](#). And features can also be added onto the top of formed components by AM processes as introduced by [Ahuja et al. \(2015\)](#). Furthermore, components can be embedded within printed parts, as shown in [Figure 1-30](#), in which the left one shows the cooling tubes inserted into the substrate mold, and the middle one indicates that the tubes were ‘buried’ and the die was completed using a laser-aided metal-based AM process, and the right one is post-machined final tool, as introduced by [Campbell et al. \(2013\)](#).



[Figure 1-28](#). Outboard landing gear rib fabricated by Wire + Arc Additive Manufacturing: CAD model (left) and produced part before machining (right) [Williams et al. \(2016\)](#).

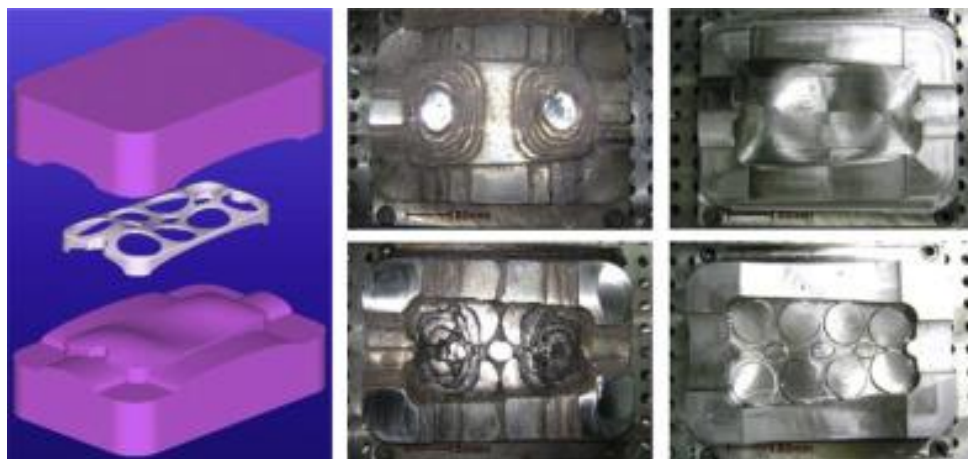


[Figure 1-29](#). Injection molding tools manufactured by hybrid gas metal arc welding and CNC machining: CAD model (left), near net shape molds (center), and final parts (right) [Suryakumar et al. \(2011\)](#).

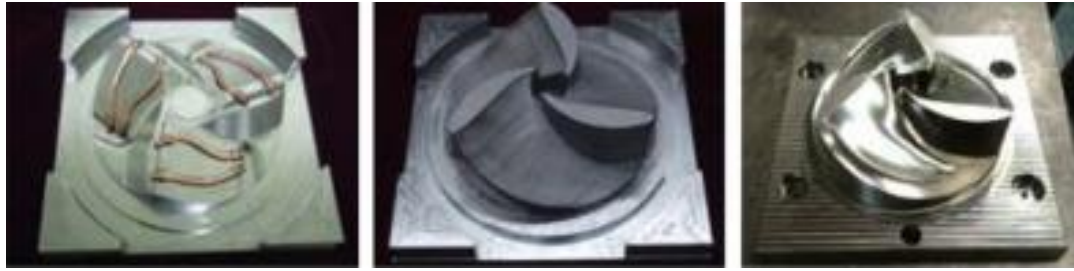


Figure 1-30. Conformal cooling channels embedded in an injection molding die [Campbell et al. \(2013\)](#).

Different operating principles, production characteristics, and compatible material types are adopted for each AM process family. These characteristics affect the cost, quality, and sometimes color and scale of the parts that can be produced, and therefore have a significant impact on design decisions. When AM is combined with other direct manufacturing processes (e.g. machining) and indirect manufacturing processes (e.g. molding or casting), it is particularly important to consider the characteristics of specific processes in the design process as discussed by [Bernard et al. \(2003\)](#).

1.2.3.2 Additive manufacturing of lightweight structures

With the development of mature AM technologies and advanced materials, wide range of materials including metals, polymers, fibre reinforced polymers and ceramics can now be processed by AM. As shown in [Figure 1-27](#), paper, wood, foam, rubber and cork can be used for sheet lamination AM process. Investment casting molds have been printed in sand as reviewed by [Sivarupan et al. \(2021\)](#), and some large components have been fabricated in clay and concrete as introduced by [Khoshnevis et al. \(2006\)](#). Bio-compatible materials including cells, proteins, synthetic hydrogels, biological hydrogels, and bioactive glasses have also been used for additive manufacturing as reviewed by [Bartolo et al. \(2012\)](#), which ultimately aims at printing of human tissues and organs. In addition, the role of AM in the production of lightweight structures has become more and more significant. Its unique layer-by-layer build mode makes it possible to produce structures with complex internal structures and external contours, thus providing unlimited possibilities for the production of multifunctional lightweight structures. Examples of using metal and composite materials to produce lightweight structures have been increasing in recent years, therefore this section will review

the use of AM to manufacture metal and composite lightweight structures as well as new design strategies for additive manufacturing of lightweight parts.

Additive manufacturing of lightweight metallic structures

In metal AM processes, heat source is generally necessary to melt the metal substrates. As described by [Martina et al. \(2015\)](#), based on heat source utilization, metal AM processes can be divided into three different categories, including laser beam, electron beam, and arc plasma as shown in [Figure 1-31](#). These AM processes can be potentially applied to various metal materials, such as steel, titanium and magnesium alloy for the fabrication of lightweight functional parts. For lightweight and also multifunctional applications, lattice structures have received much attention in the past two decades. AM processes largely promoted the design and production of such porous lattice structures and they have been widely used in many fields such as automotive, medical, aerospace and consumer industries.

Metal implants especially those used for spine, hip and knee replacement are very important to the health and life of human beings. The actual clinical application determines the performance requirements of the implant. For example, femoral implants require superior compressive and tensile strength, while dental implants require high fatigue life and wear resistance. In addition, it is expected that the implant can be used for the whole life without failure or revision surgery. One challenge is that the elastic modulus of most metal implants is much higher than that of the bone to be replaced, which results in severe stress shielding. For example, the elastic modulus of human bones varies from 0.02-40 GPa, while that of commercial pure titanium Co-Cr alloy is 190-210 GPa and 316L stainless steel is 210-253 GPa as stated by [Geetha et al. \(2009\)](#). A feasible means of reducing such difference is to adopt the lattice implants as the lattice structure is less dense and less stiff compared to the pure solid metals. Some examples of FDA-approved Ti-6Al-4V lattice implants are shown in [Figure 1-32](#), in which (a) was from EIT, Germany; (b) was from Renovis, USA; (c) was from 4WEB Medical, USA; (d) was from Joimax, Germany; (e) was from K2M, USA and (f) was from Solidscape, USA as summarized by [Zhang et al. \(2018b\)](#).

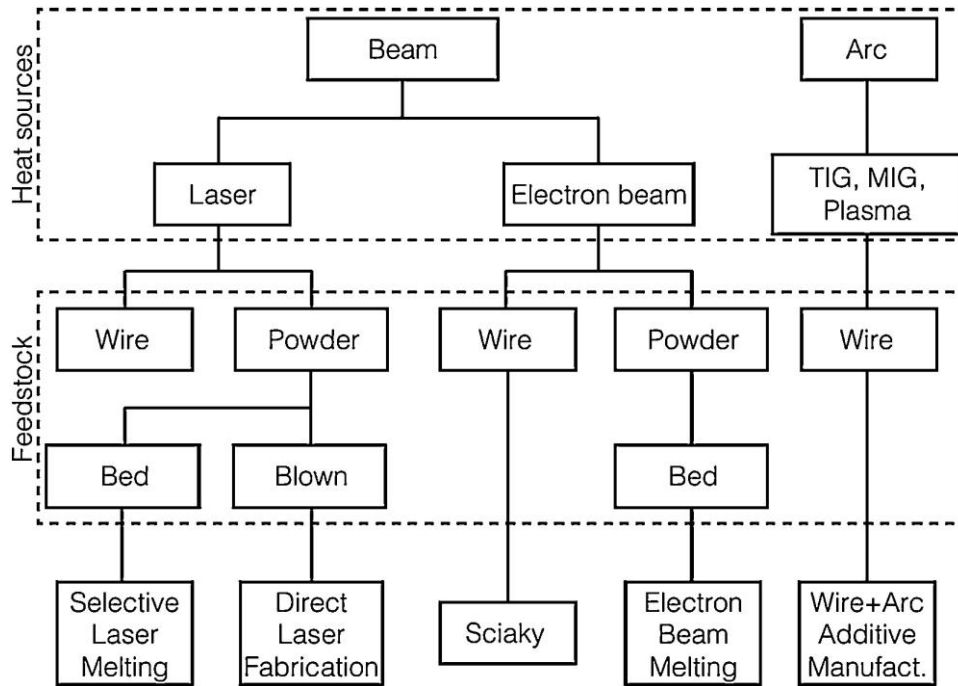


Figure 1-31. Classification of metal AM processes based on heat sources utilization [Martina et al. \(2015\)](#).

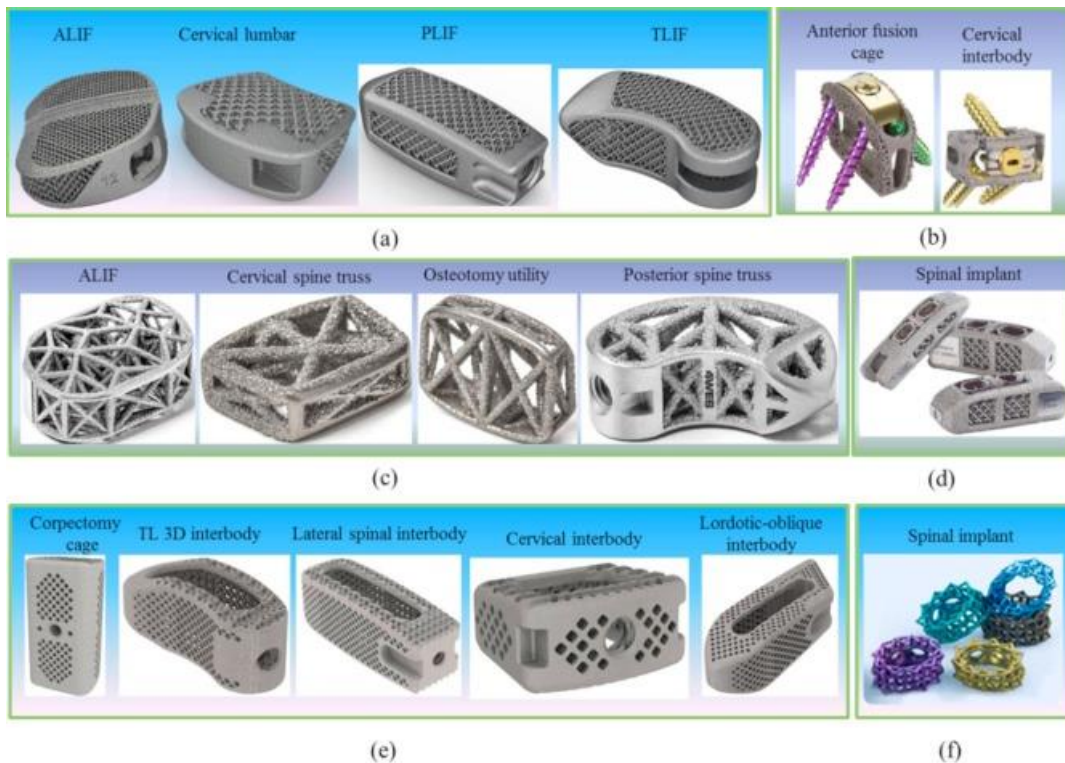


Figure 1-32. Examples of FDA-approved Ti-6Al-4V lattice implants [Zhang et al. \(2018b\)](#).

The above lattice implants not only reduce weight but also improve the compatibility of the human body and the implant, thus avoiding abrasion and damage to the human body. In

addition, metallic lattice structures also show excellent heat isolation, energy absorption, damping and vibration absorption properties, thus obtaining widespread use in many other engineering fields. For this purpose, many types of lattice structures have been produced by additive manufacturing using different AM processes and metal materials. Some popular metallic lattice structures produced by various AM technologies are summarized by [Zhang et al. \(2018b\)](#) as listed in [Table 1-1](#).

[Table 1-1](#). Metal lattice structures produced by AM processes summarized by [Zhang et al. \(2018b\)](#).

Lattice unit cell topology	Lattice structure	Material	AM process
Auxetic		Ti-6Al-4V	SEBM
BCC		Ti-6Al-4V	SLM
BCCZ		Al-12Si-Mg	SLM
Cross 1		Al-12Si-Mg	SLM
Cubic		Ti-6Al-4V	SEBM
		Ti-6Al-4V	SLM
		316L stainless steel	SLM
		Pure Titanium	SLM
		Al-12Si-Mg	SLM
Diamond		Ti-6Al-4V	SEBM
		Ti-6Al-4V	SLM
		Pure Ta	SLM
		Ti-6Al-4V	SEBM
Dode thin		Ti-6Al-4V	SEBM
		Co-29Cr-6Mo	SEBM
		Ni-21Cr-9Mo	SEBM
Dodecahedron		Ti-6Al-4V	SEBM
		Ti2448 (Ti-23.9Nb-3.9Zr- 8.2Sn-0.19O)	SEBM
		Ti-6Al-4V	SLM
FCC		Al-12Si-Mg	SLM
FCCZ		Ti-6Al-4V	SLM
		Al-12Si-Mg	SLM
FBC CZ		Ti-6Al-4V	SLM
		Al-12Si-Mg	SLM
FBC XYZ		Ti-6Al-4V	SLM
G7		Ti-6Al-4V	SEBM
Gyroid		Ti-6Al-4V	SLM
		316L stainless steel	SLM
Hatched		Ti-6Al-4V	SEBM
Hexagonal		Ti-6Al-4V	SEBM
		Ti-6Al-4V	SLM
		Pure Titanium	SLM
Honeycomb		Ti-6Al-4V	SEBM
Octahedron		Ti-6Al-4V	SEBM
Octet-truss		Ti-6Al-4V	SEBM
Tetrahedron		Ti-6Al-4V	SLM
Triangular		Ti-6Al-4V	SLM
Truncated cuboctahedron		Ti-6Al-4V	SLM
Rectangular		Ti-6Al-4V	SLM

Additive manufacturing of composites

Additive manufacturing of composites has been receiving more and more attention in the past two decades, with the rapid development of AM technologies including fused deposition modeling (FDM), laminated object manufacturing (LOM), stereolithography (SL), extrusion,

and selective laser sintering (SLS). With the aim of pursuing superior mechanical performance, various composite materials have been developed for composite-specific AM processes as summarized by [El Moumen et al. \(2019\)](#) in Table 1-2.

Table 1-2. Particle reinforced polymer composites manufactured by AM processes with enhanced property [El Moumen et al. \(2019\)](#).

Process	Material	Property enhancement
FDM	TiO ₂ /ABS	Improved tensile modulus and strength
	Carbon nanofibers/ABS	Improved physical properties
	Montmorillonite/ABS	Improved tensile modulus and strength, flexural modulus and strength, thermal stability and reduced thermal expansion coefficient
	Graphene/ABS	Improved thermal and electrical conductivities
SLA	Carbon nanofiber/Graphite/polystyrene	Improved electrical properties
	CNT/epoxy	Improved tensile strength and reduced of the elongation
	Graphene oxide/photopolymer	Improved tensile modulus and strength
	TiO ₂ /epoxy acrylate	Improved tensile modulus and strength, flexural strength and hardness
	BaTiO ₃ /PEGDA	Improved piezoelectric coefficient
	CNT/acrylic ester	Improved the coefficient of electromagnetic energy absorption
SLA	BST/epoxy	improved thermal conductivity
	Carbon black/nylon-12	Improved electrical conductivity
	TiO ₂ /nylon-12 and graphite/nylon-12	Improved tensile modulus and reduced the elongation
	Silica/Nylon-11	Improved tensile and compressive properties

As shown in [Figure 1-33](#), aiming at dealing with the AM process-induced anisotropy and support material removal, a snap-fit method was combined with the PolyJet technology for the fabrication of polymer lattice structures by [Liu et al. \(2020a\)](#) with simultaneously reduced printing materials and time. The lattice based on the minimum surface of the triple period was

produced by polymer additive manufacturing by [Maskery et al. \(2018\)](#), and was checked by combining experiments and calculation methods. In addition to polymer, printable carbon fiber reinforced plastics were also developed and used to fabricate various lightweight structures although printing of CFRP could be much more difficult than that of polymers without reinforcements. Various types of lattice structures were printed by [Plocher and Panesar \(2020\)](#) using short carbon fiber reinforced plastics, and their stiffness and energy absorption characteristics were systematically investigated by compression tests. A new epoxy-based ink was reported by [Compton and Lewis \(2014\)](#), which enables 3D printing of lightweight cellular composites with controlled alignment of multiscale, high-aspect ratio fiber reinforcement to create hierarchical structures as shown in [Figure 1-34\(a\)](#). For further improvement of mechanical performance of AM parts, continuous fiber reinforced plastics have been increasingly adopted to fabricate various components. As shown in [Figure 1-34\(b\)](#), continuous fiber reinforced thermosetting polymer composites were prepared by impregnation, printing, and curing stages for additive manufacturing and the effects of process parameters on mechanical properties were investigated by [Ming et al. \(2020\)](#). Impact damage resistance of 3D printed continuous fibre reinforced thermoplastic composites using fused deposition modelling was systematically investigated by [Caminero et al. \(2018\)](#), and demonstrated that impact resistance performance shown by 3D printed continuous carbon fiber composites are significantly superior than the common polymers, in some cases, even better than usual CFRP prepreg materials. To achieve the optimal structural efficiency of 3D printed parts, continuous curved carbon fibre composites were placed based on the loading condition and principal stress trajectories obtained in numerical results by [Zhang et al. \(2018a\)](#). As shown in [Figure 1-35](#), different from conventional layer-by-layer AM process, a free-hanging printing method for CFRP lattice structures was proposed by [Liu et al. \(2018\)](#) to realize the undercut and overhanging truss structure without any support although the accurate shape control in this process is difficult, and the obvious voids were presented in the cross sectional of the fiber crossed vertex due to the lack of printing pressure.

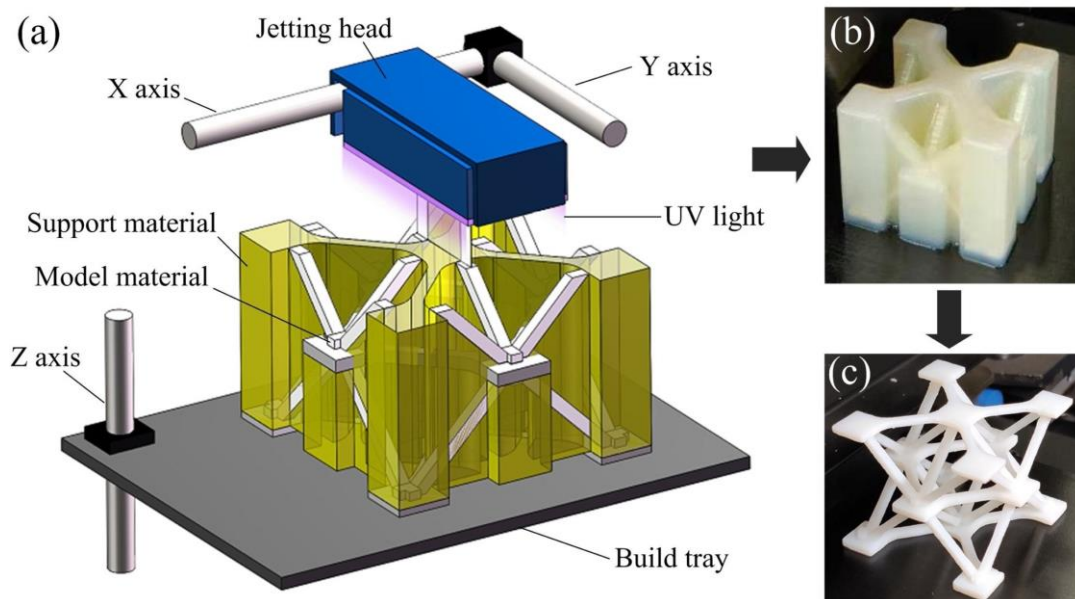


Figure 1-33. Fabrication of polymer lattice structures via the combination of snap-fit method with the PolyJet technology Liu et al. (2020a).

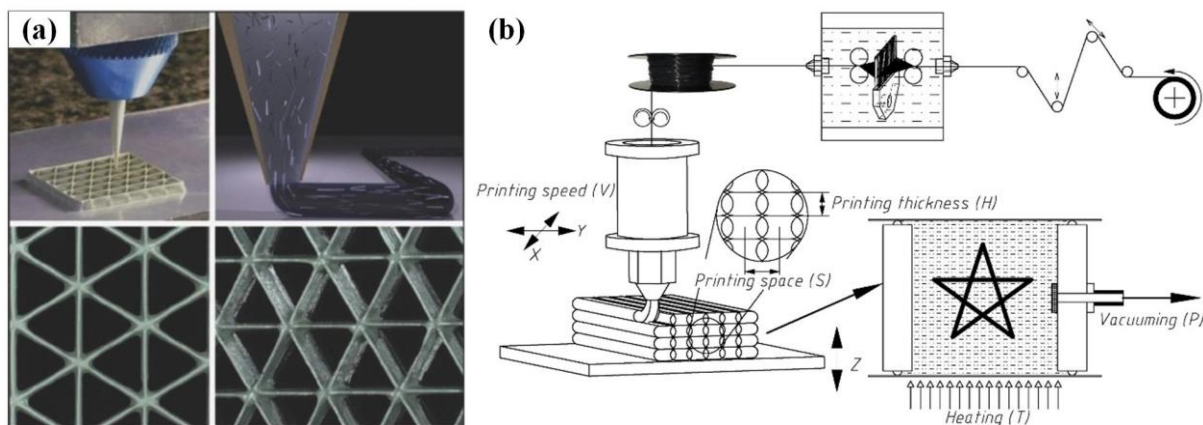


Figure 1-34. (a) Printing of lightweight cellular composites with controlled alignment of multiscale, high-aspect ratio fiber reinforcement Compton and Lewis (2014); (b) printing of continuous carbon fiber reinforced plastic Ming et al. (2020).

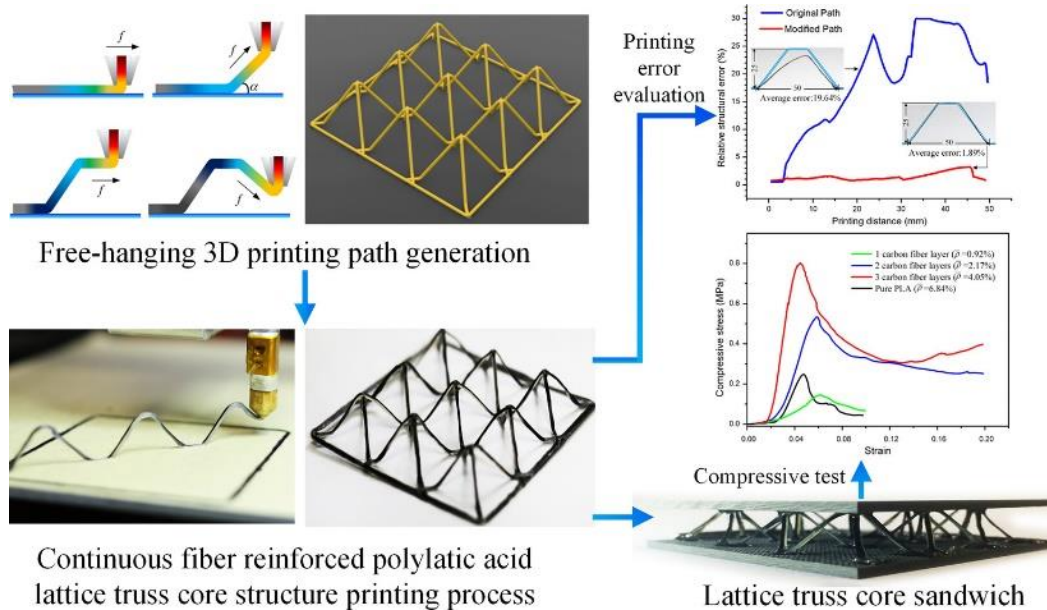


Figure 1-35. A free-hanging method for the printing of 3D lattice structure using continuous carbon fiber reinforced composites Liu et al. (2018).

New lightweight designs for additive manufacturing

Owing to the unique ability of AM to create structures with extremely complex shapes and topologies, the production of macro-structure topology optimized objects becomes much easier. Benefited from this, topology optimization (TO) has been integrated with additive manufacturing for the design and production of topologically optimized structures with improved structural and functional characteristics. Topology optimization is a numerical approach that finds where material should be allocated in a given domain to achieve a desired functionality (e.g. stiffness and strength) for a given set of loads and boundary conditions while optimizing for qualities such as minimal material usage/weight or uniform stress distribution. A typical topology optimization example was given in Figure 1-36, in which the purpose was to find the optimal material layout in the initial design zone subjected to a set of load and boundary conditions at the prescribed amount of material usage. It can be seen that the optimal design generally exhibits quite complex topology that is difficult to be produced by conventional processes, but it can be easily fabricated by additive manufacturing. Therefore, the synergy of topology optimization and additive manufacturing can provide much potential for the design and production of lightweight multifunctional parts. For this purpose, numerous topology optimization methods have been proposed, which can be mainly classified into the

density-based method proposed Bendsøe (1989) and Zhou and Rozvany (1991), the level-set approach proposed by Allaire et al. (2002) and Wang et al. (2003), the topological derivative method proposed by Sokolowski and Zochowski (2003), the phase field method proposed by Bourdin and Chambolle (2003), evolutionary approach proposed by Xie and Steven (1993) and moving morphable components (MMC) proposed by Guo et al. (2014). These approaches are all based on the foundation of the homogenization thought and numerical optimization methods proposed by Bendsøe and Kikuchi (1988).

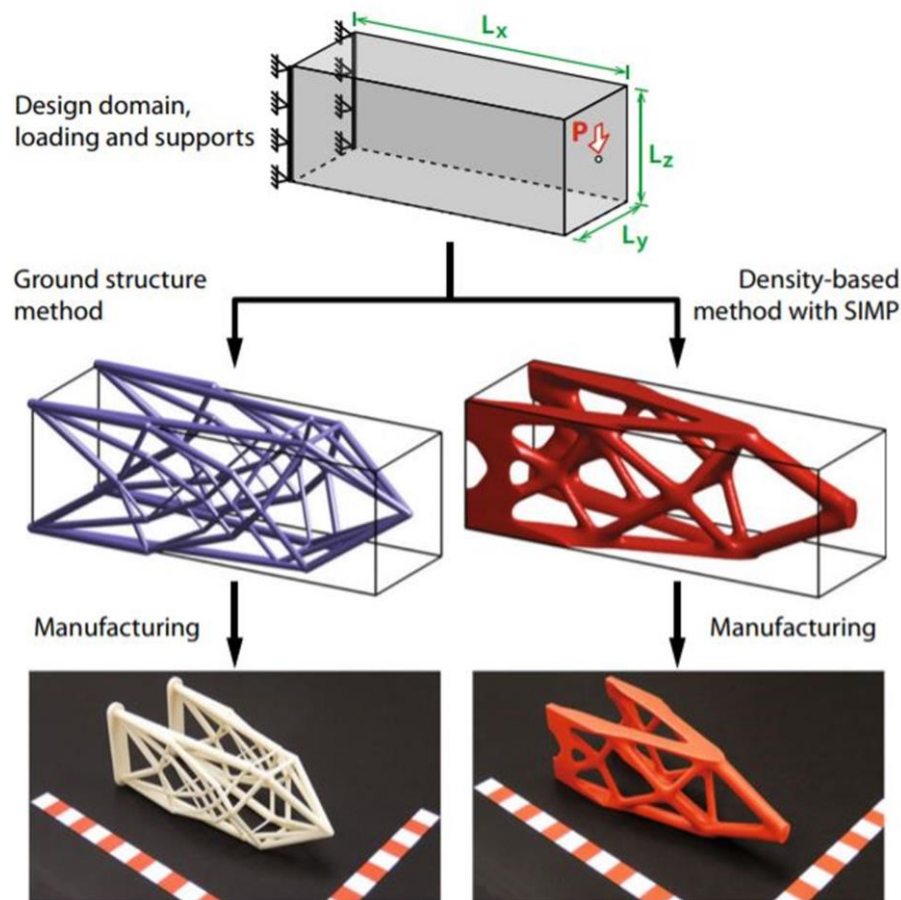
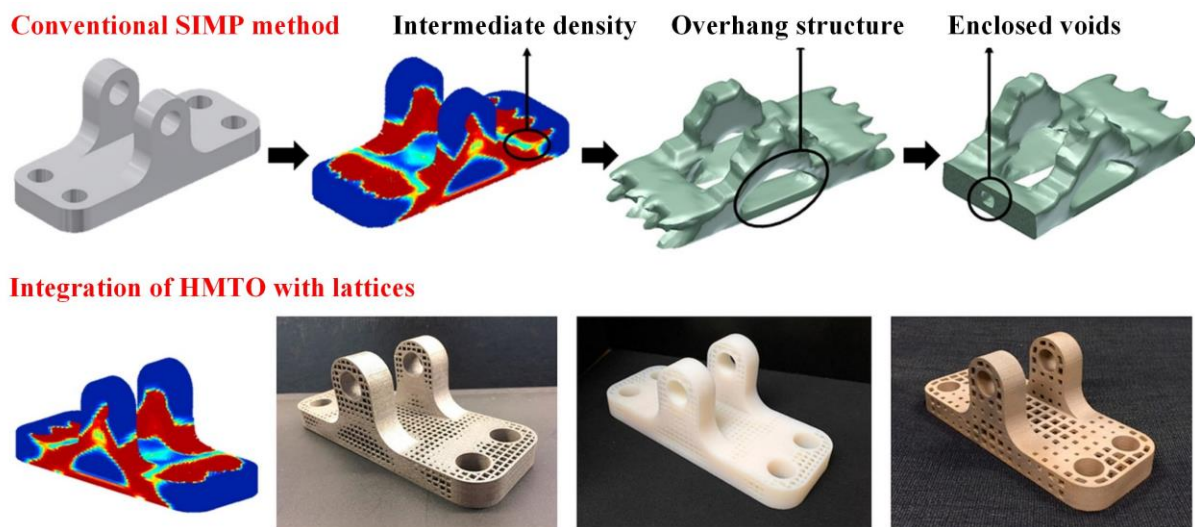


Figure 1-36. A typical topology optimization example.

The integration of topology optimization and additive manufacturing still faces many problems as introducing the AM constraints such as support structures/overhangs, minimum printable features, anisotropic material properties, heat-transfer, thermal strain/stress into topology optimization would result in complex constraints or boundary conditions, which makes it very difficult for the TO process to find the optimal solution efficiently and correctly. In addition, some AM constraints cannot be simply described by mathematical formulations as

relatively simple macro mechanic and geometric based calculations cannot handle multi-physical phenomena of AM. Therefore, how to consider above complex AM constraints in the TO process is still a challenge remains to be resolved. Nevertheless, some AM constraints can be well addressed by improving or modifying the existing TO methods. For instance, the lattice structure was integrated with the conventional density-based topology optimization method to achieve better manufacturability by [Cheng et al. \(2017\)](#). The flowchart of the above lattice-based topology optimization is shown in [Figure 1-37](#), in which the pillow bracket is used as an example and standard topology optimization is performed to minimize the compliance of the design while constraining the overall volume fraction to a target value. Obviously, several problems of the conventional Solid Isotropic Material with Penalization (SIMP) method need to be addressed. Firstly, one of the main problems is that a number of elements with intermediate densities are generated, which cannot be physically produced by AM as they do not have physical meaning. These elements with intermediate densities have to be converted to solid or void elements before they can be manufactured. Moreover, long overhang structures may be generated. To prevent these overhang structures from collapsing during AM build process, support structures have to be inserted under them. The use of support structures not only increases AM build time, cost, material and energy use, but also these support structures are difficult to remove without damaging the printed models. Another problem is that the enclosed voids may be generated. These enclosed voids will trap metal powders and support structures during metal powder bed AM process, or liquid resin and support structures during the plastic AM process. Apparently, the above problems lead to poor manufacturability of the topologically optimized structures by the conventional topology optimization method (SIMP). To overcome these issues, the homogenization-based topology optimization (HMTO) method has been proposed to be integrated with the lattice structures, in which the design elements are equivalent to porous lattice structures. The lattice structures are equivalent to the homogenous material of which mechanical properties are formulated as a function of its relative density. Then these mechanical properties are substituted into the stiffness matrix to calculate the objective function and the sensitivity of the objective function, and eventually the topology optimization problem is solved by the gradient-based optimization scheme. The obtained

optimal designs by the integration of HMTO with lattices can be seen in the bottom of [Figure 1-37](#). Compared with the conventional SIMP method, many advantages can be found. Firstly, the use of support structures can be largely reduced as the micro-lattices are composed of struts distributed in a tiny space so natural internal supports can be provided. Besides, the elements with intermediate densities can be easily converted to lattice structures of corresponding densities, so the elements with intermediate densities can be physically produced. Moreover, the original shape of the initial structure can be maintained so the enclosed voids will not be generated, which largely reduce the difficulty of post-processing. It can be seen that by the integration of the lattice structures with the HMTO method, the manufacturability of the optimal design can be highly improved. Owing to the above merits, such topology optimization methods have been extensively investigated in some literatures such as the integration of tetrahedral lattices with HMTO method for the design of hip implant as presented by [Wang et al. \(2018b\)](#).



[Figure 1-37](#). Comparison of conventional density based TO and HMTO integrated with lattice [Cheng et al. \(2017\)](#).

Owing to the tremendous potential from the integration of TO and AM, macro structure optimization is widely seen in the automotive and aerospace industries as the weight reduction can bring many benefits such as energy saving, higher fuel efficiency and longer usable life of the product. Some aerospace related applications have been summarized by [Thompson et al. \(2016a\)](#), and a typical example is given in [Figure 1-38](#), in which the nacelle hinge brackets are

optimized for Airbus A320 and A380. In addition, structural topology optimization has also been widely adopted to enrich functionalities of products such as those in biomedical devices as reviewed by Cucinotta et al. (2019) and consumer products as designed by Weeger et al. (2019) shown in Figure 1-39, and more.



Figure 1-38. Topologically optimized nacelle hinge brackets for Airbus A320 (left) and Airbus A380 (right) Thompson et al. (2016a).

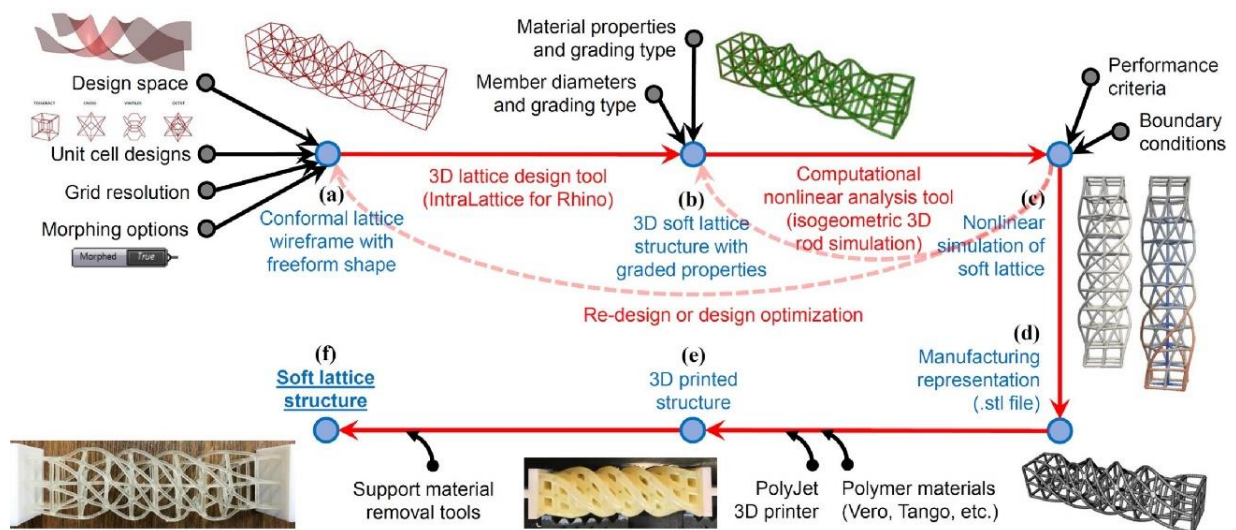


Figure 1-39. Digital design of soft lattices for multifunctional applications Weeger et al. (2019).

1.3 Motivation and research purpose

1.3.1 Key engineering issues to be resolved

1.3.1.1 Production efficiency and manufacturing cost

Low production efficiency is the first problem limiting commercial application of sandwich structures. The production of sandwich panels is complicated and involves multiple fabrication steps, making it very difficult to realize mass production. An extrusion and electrodischarge (EDM) method was employed by [Queheillalt et al. \(2008\)](#) to fabricate an A6061 aluminium alloy pyramidal lattice core. A CFRP pyramidal truss core was fabricated by compression moulding into a corrugated structure followed by laser cutting, as proposed by [Xiong et al. \(2012\)](#). A high-strength woven wire core was fabricated by [Kang \(2009\)](#), where Cr-Si spring steel wires were assembled into woven wire structures and then brazed together using brass brazing paste. As reported by [George et al. \(2014\)](#), an assembled carbon fibre lattice with inserted foams was stitched together using Kevlar fibres and then the whole structure was infused with an epoxy resin and cured to obtain a hybrid core. A snap-fit and vacuum brazing method has been developed by [Dong et al. \(2015\)](#) to fabricate three dimensional space filling octet-truss lattice structures from Ti-6Al-4V alloy sheets. This method involves the cutting, assembly and brazing. As introduced by [Liu et al. \(2020b\)](#) in [Figure 1-40](#), octet lattice structures were designed with CFRP hollow cylindrical struts, where water jet cutting, machining and mechanical assembly processes were adopted. As shown in [Figure 1-41](#), compression molding, cutting, assembly and adhesive bonding were involved in the manufacturing of a 3D double-arrow-head (DAH) auxetic structure designed by [Wang et al. \(2018a\)](#). As proposed by [Hu et al. \(2016\)](#), the lattice core is made up of orthogonal corrugated lattice trusses (CLTs) and manufactured by mould pressing, cutting, mechanical assembly and adhesive bonding as shown in [Figure 1-42](#). As shown in [Figure 1-43](#), a special mold is designed by [Mei et al. \(2017\)](#), CFRP prepregs were cut and then rolled into rods, and assembled into the designed mold followed by co-curing to obtain the final lattice structure. In addition, some other manufacturing processes for metallic lattice structures involve liquid-state processing including direct foaming and spray foaming, solid-state processing such as physical vapor

deposition (PVD) and electron beam-directed vapor deposition (EB-DVD) as discussed by Trifale et al. (2016) and Aly et al. (2016).

It is obvious that aforementioned manufacturing processes are labour-intensive and time-consuming, thus not suitable for mass production. In addition, special dies or tools are generally required in these manufacturing processes, which additionally increase the burden of investment. Considering the low manufacturing efficiency and high production cost, although these lightweight cellular structures may exhibit excellent mechanical properties, they can only be produced in small scales and their dimensions may also be restricted due to the limitation of the size of the dies or relevant production facilities. Therefore, for the mass production, an easy, rapid and continuous manufacturing process should be adopted to produce the inner macro structure, such as continuous bending, stamping and drawing.

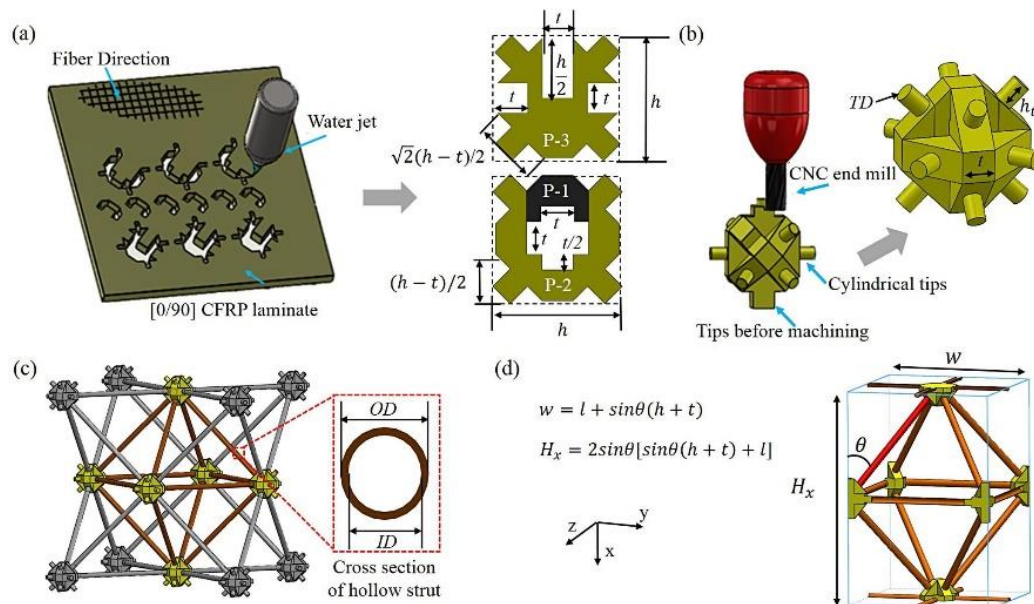


Figure 1-40. Octet lattice structures manufactured using CFRP hollow cylindrical struts Liu et al. (2020b).

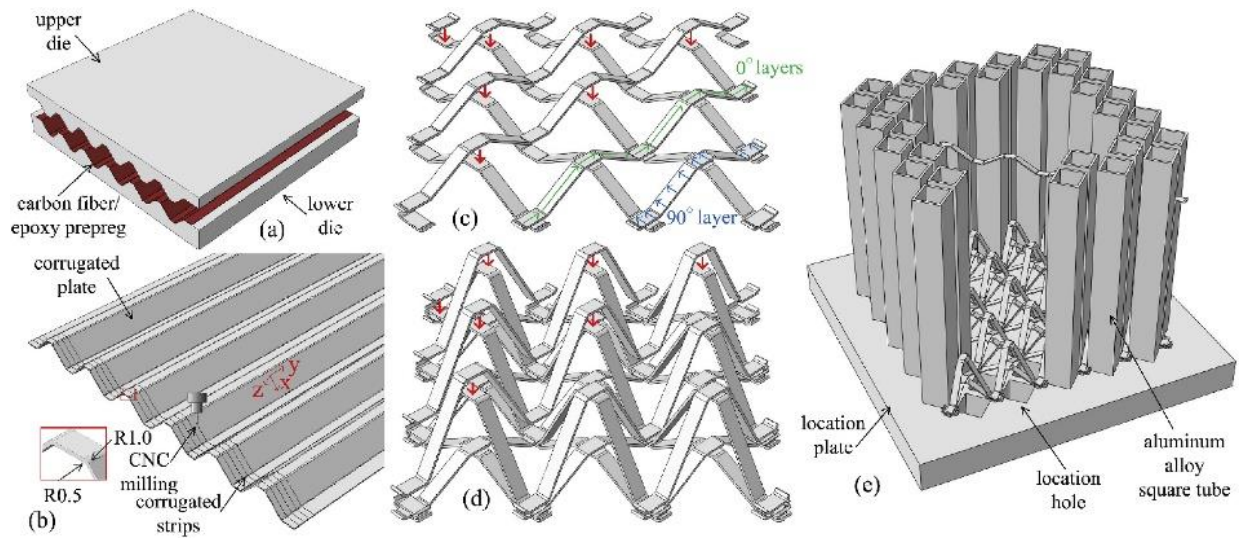


Figure 1-41. 3D double-arrow-head (DAH) auxetic structure fabricated using CFRP laminates Wang et al. (2018a).

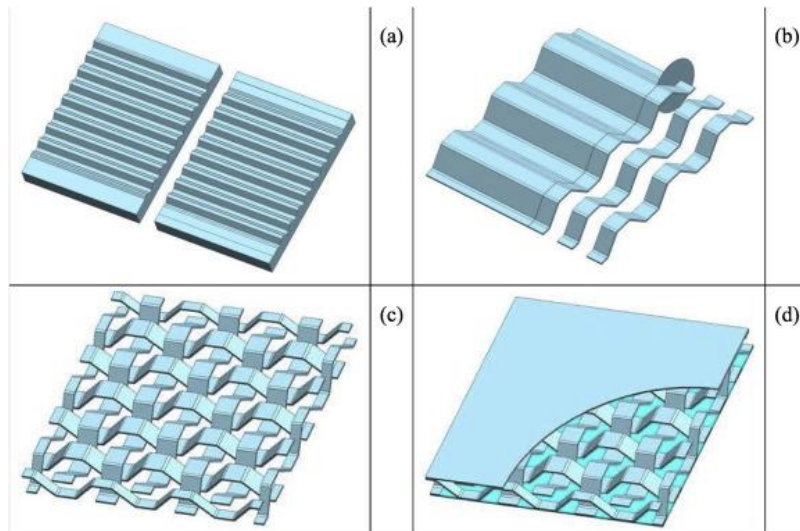


Figure 1-42. CFRP lattice core made up of orthogonal corrugated lattice trusses (CLTs) Hu et al. (2016).

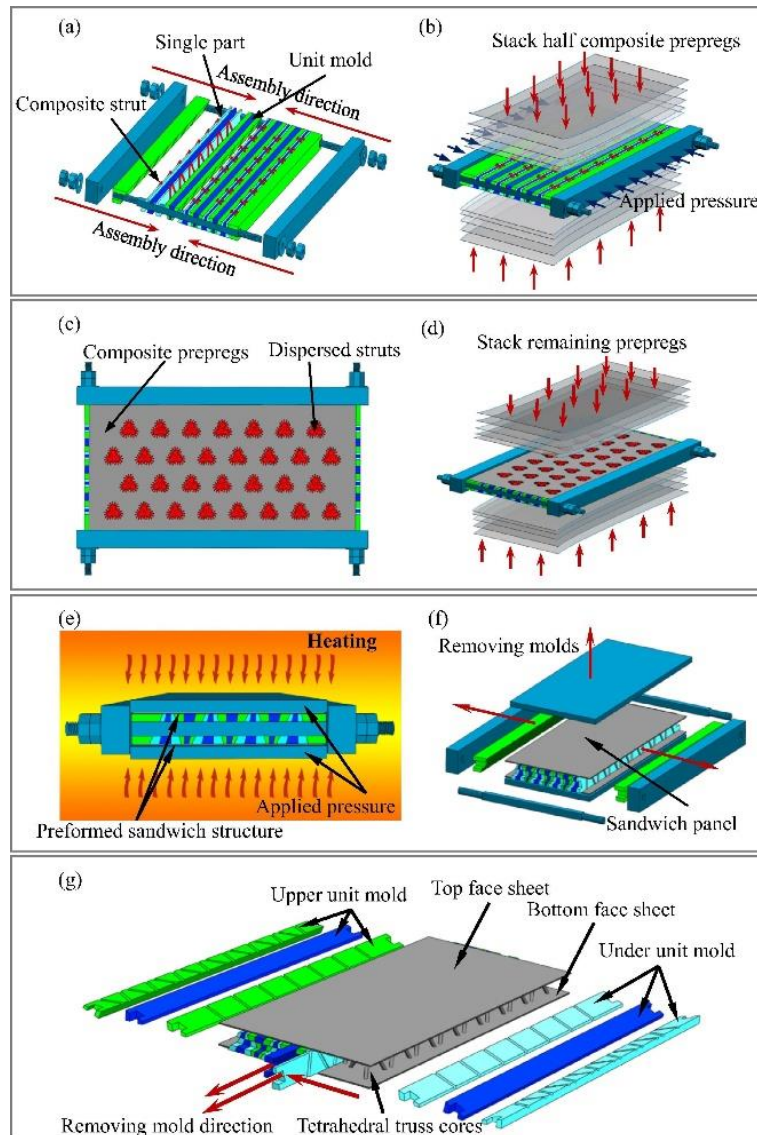


Figure 1-43. Fabrication process of all-CFRP tetrahedral truss core sandwich panel Mei et al. (2017).

1.3.1.2 Formability

The second problem is that most sandwich panels cannot be secondarily formed into three-dimensional shapes by conventional sheet forming methods such as stamping or drawing, limiting their applications to flat panel shapes. At present, sandwich sheets with relatively good formability are limited to those with a two-dimensional core, such as a polyethylene or aluminium foam core. As shown in Figure 1-44, the formability of sandwich sheets consisting of AA5052 skin and a two-dimensional polyethylene core was evaluated by Liu et al. (2013) and found to be better than that of monolithic AA5052 sheet. Three-dimensional sandwich

shells containing aluminium foam cores have been successfully produced by incremental sheet forming (ISF), as presented by Jackson et al. (2008). Gas pressure forming of sandwich sheets with an aluminium foam core was experimentally and numerically investigated by Nassar et al. (2012) and indicated that forming these sandwich panels to three-dimensional shapes while maintaining considerable core porosity was possible. Parsa and Ettehad (2010) examined the effects of sandwich geometries such as sandwich thickness and tool curvatures on the spring back behavior of PP core sandwich sheets with metal faces. Except for forming, shear cutting of sandwich sheets could also be a challenge, in which more complex mechanism arising during cutting compared to that of monolithic sheets. Groche et al. (2018) investigated the cutting mechanism through experimental and analytical approaches, while the factors influence the cutting surface quality of sandwich sheets during shear and counter shear cutting were systematically investigated by Liewald et al. (2013).

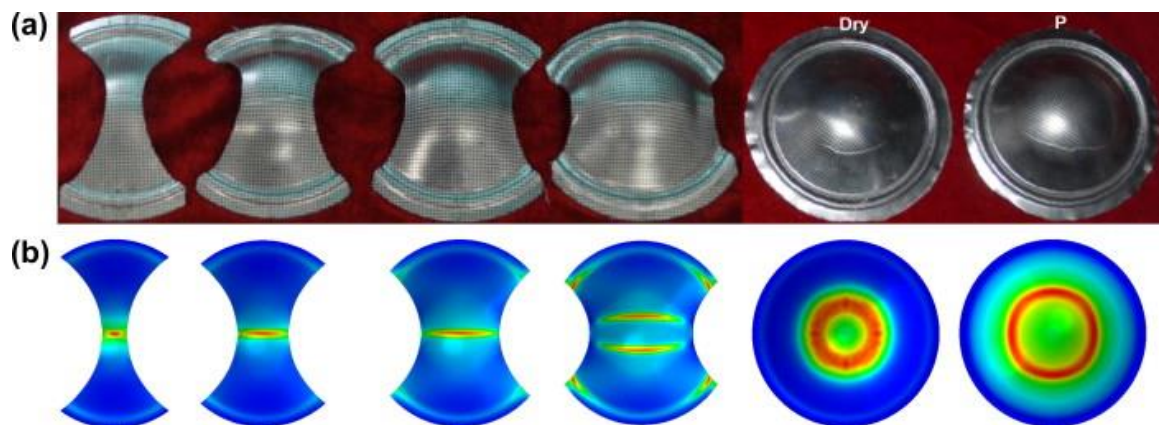
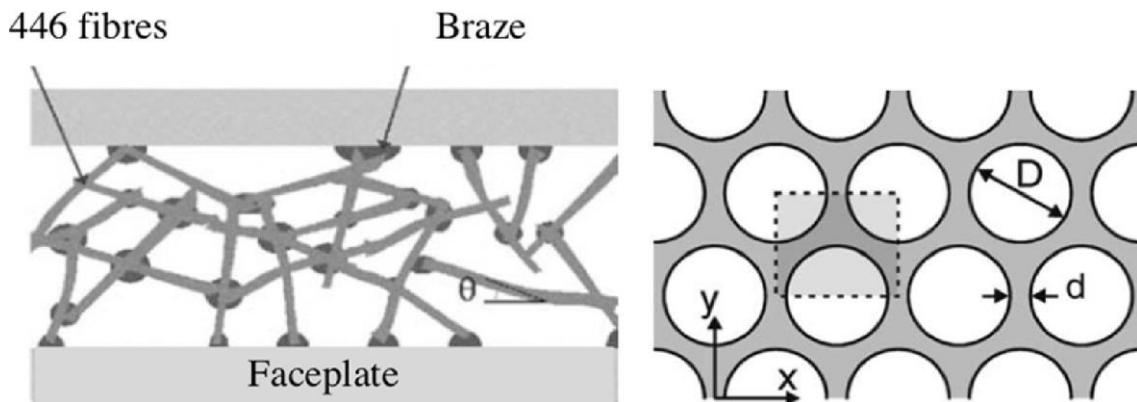


Figure 1-44. Forming of AA5052/PP/AA5052 sandwich sheets by Nakajima tests Liu et al. (2013).

However, secondary forming of sandwich sheets with a three-dimensional core remains a challenge and few relevant studies have been reported. Ahn (2015) and Dilthey et al. (2001) investigated the bendability of sandwich sheets containing a pyramidal truss core and a woven wire core, respectively, and found they can be bent to only a very limited curvature. Development of sandwich sheets that can be efficiently produced and secondarily formed into three-dimensional shapes is a key issue to expand the usage of sandwich sheets for ultra-lightweight structures. Seong et al. (2008) designed a dimple core which can be fabricated by

fast stamping and found its bendable curvature was improved compared to the pyramidal truss or woven wire structure. [Mohr \(2005\)](#) investigated the effects on forming behaviours of thin sandwich sheets and found that a good inner macrostructure for a bendable sandwich sheet is mainly characterized by its core shear strength. In this investigation, two types of metal cores including the fibrous core and perforated core, as shown in [Figure 1-45](#), were tested. The main failure mode of these thin metallic sandwich sheets is clarified to be core shear failure as shown in [Figure 1-46](#). The relations between the forming behavior and sandwich geometry and forming tool geometry were theoretically deduced for the design of formable metallic sandwich sheets. Following this principle, [Seong et al. \(2010\)](#) and [Besse and Mohr \(2012\)](#) designed the sheared dimple and bidirectional dome structures, respectively, and verified that sandwich sheets with these two types of cores can be successfully bent to a large curvature without failure. The fabrication process of the sheared dimple core is shown in [Figure 1-47](#), in which the piecewise sectional forming technology was adopted to continuously produce the inner core structure.



[Figure 1-45](#). Thin metallic sandwich sheet with fiber core (side view, left) and perforated core (top view, right) [Mohr \(2005\)](#).

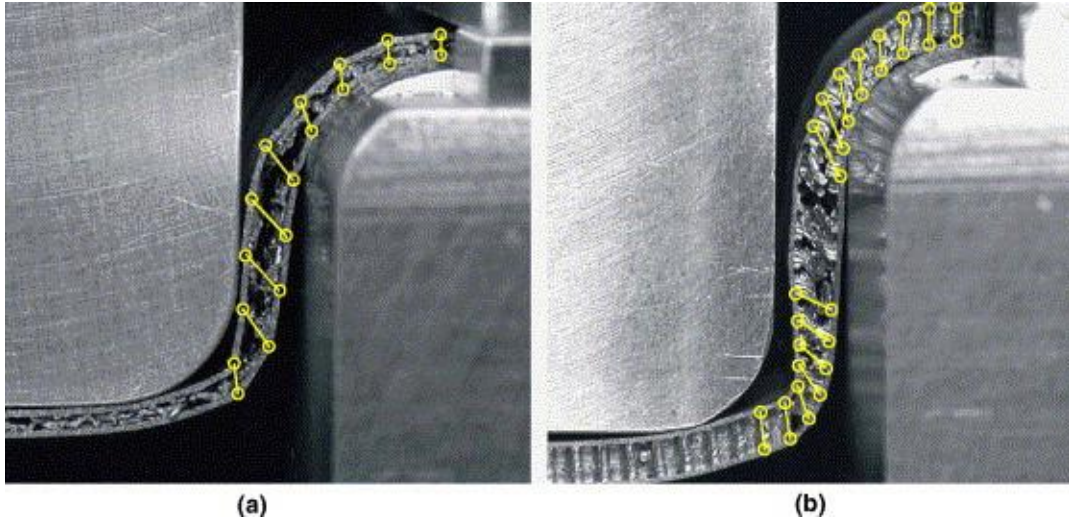


Figure 1-46. Shear failure of the sandwich cross section: (a) fiber core; (b) perforated core

Mohr (2005).

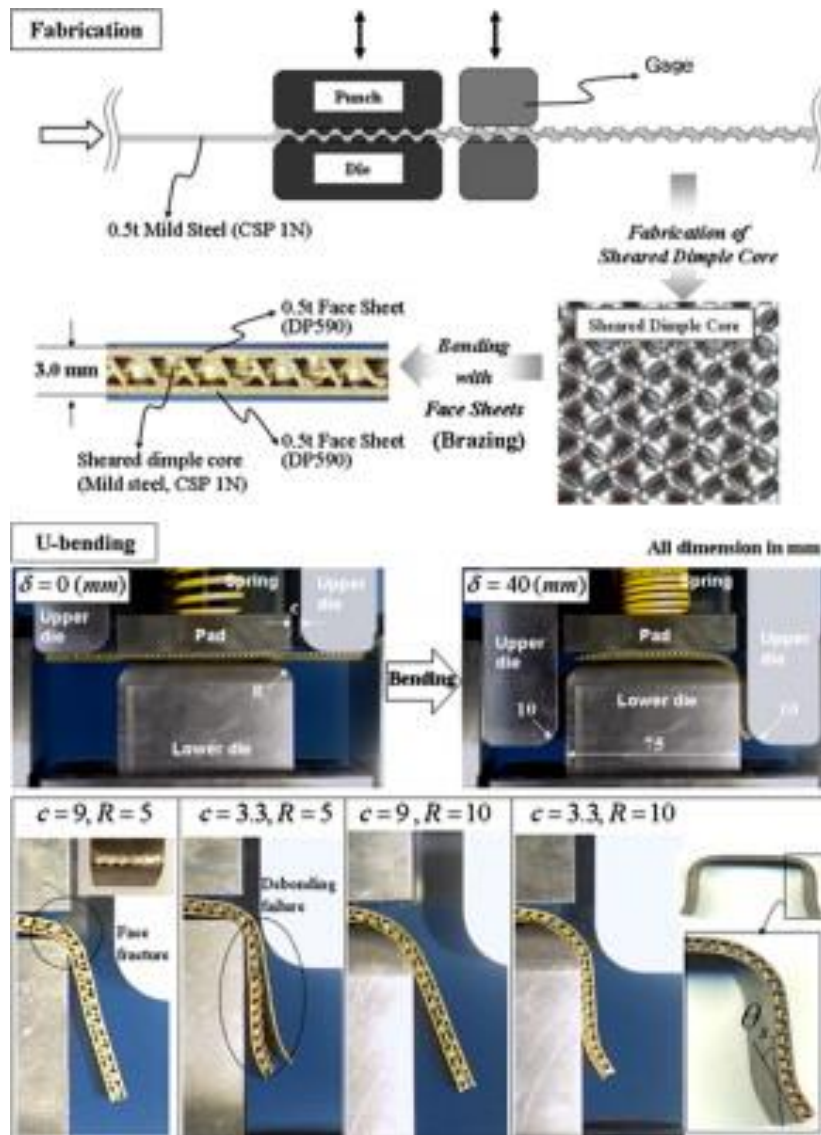


Figure 1-47. Fabrication process of sandwich sheets with a sheared dimple core by piecewise sectional forming technology and its secondary bending [Seong et al. \(2010\)](#).

The formability degrees of some sandwich sheets are summarized in [Figure 1-48](#), from which it is found that sandwich sheets with the 2D flat core can be formed to a certain degree without failure, but the flat core is not efficient in weight and stiffness as the thickness of flat core is generally small. For the full metallic sandwich sheets with a 3D core, their formability is quite limited and can only be bent to a small curvature. In addition, these sandwich sheets are made of full metallic materials, thus leading to limited specific strength and stiffness. From the above extensive review, it can be concluded that the formability of existing sandwich sheets is still limited and formable sandwich sheets with superior structural efficiency need to be

developed to expand the application ranges of current sandwich structures.

2D sandwich core
 Full metallic sandwich with 3D core

Not formable ○○○ Little ●○○ Mildly formable ●●○ Formable ●●●

Sandwich combination		Formability degree	Reference
Face sheet	Core		
Aluminum alloy	Aluminum foam	Little formable ●○○	Nassar et al. (2012)
Mild steel	Polypropylene	Formable ●●●	Jackson et al. (2008)
Aluminum alloy	Polypropylene	Formable ●●●	Jackson et al. (2008)
AA5052	Polypropylene	Formable ●●●	Liu et al. (2013)
A3105	Polypropylene	Little formable ●○○	Parsa and Etehad (2010)
Stainless steel	Ni-Cr fibers	Little formable ●○○	Mohr (2005)
Stainless steel	Perforated low-carbon steel	Mildly formable ●●○	Mohr (2005)
HSS (DP steel)	Mild steel, sheared dimple	Little formable ●○○	Seong et al. (2010)

Figure 1-48. Summary of formability degree of sandwich sheets investigated in the past.

1.3.1.3 Mechanical property and functionality

The purpose of the development of hybrid sandwich structures is to further improve the weight-specific mechanical properties or increase additional functionalities that cannot be achieved by the any of the single constituent alone. The methods to achieve this goal in the previous studies are mainly based on the change of material combinations or design of inner macro structures. As reviewed in **section 1.2**, a wide range of material combinations including metallic materials (aluminum, titanium, steel, etc.), polymers, fiber reinforced polymers (GFRP, CFRP, AFRP, etc.) have been used to fabricate hybrid structures to facilitate various engineering requirements of mechanical performance and functionality. In addition, another

feasible means to improve the mechanical performance and enrich the functionality of hybrid sandwich structures is to change the inner macro structure, as reviewed in the previous section, in which numerous core structures including but not limited to the honeycomb, pyramidal truss, woven wire, etc., have been designed and produced. The mechanical properties including specific compressive stiffness and strength of various typical inner sandwich macro structures were summarized by [Dong \(2020\)](#), in which the truss lattice structures show generally superior mechanical properties than foam structures. Nevertheless, these truss lattice structures may not be the optimal structures in terms of flexural stiffness and strength. In contrast to the conventional truss–lattices composed of beams or struts, novel plate–lattices composed of closed-cell sheets have been reported to exhibit superior mechanical properties and can potentially achieve isotropic elastic properties as reported by [Berger et al. \(2017\)](#). However, production of such plate–lattices composed of closed-cell sheets could be a big challenge by the conventional methods and it has to rely on new manufacturing technologies. Although the variable structural parameters of conventional manufacturing processes allow some control over pore shape and size, they remain limited to producing randomly organized structures. In addition, the incapability of manufacturing precise complex structures, the high manufacturing cost and the discrepancy in the properties of produced lattice structures also limit the applications of the above conventional fabrication methods.

The layer-by-layer fabrication paradigm of additive manufacturing (AM) enables the build of lattice materials with extremely intricate external geometries and high control of the internal architecture, overcoming the limitations of conventional fabrication methods. With the development of AM technology, selective laser melting (SLM) as reviewed by [Yap et al. \(2015\)](#), and electron beam melting (EBM) introduced by [Karlsson et al. \(2013\)](#) have been adopted to fabricate various types of lattice structures including body centred cubic unit cell (BCC) and face centered cubic unit cell with Z-struts (FCCZ) structures from various materials such as 316L stainless steel and Ti-6Al-4V titanium alloy. Owing to the capability of AM to produce complex geometries that were difficult or impossible to manufacture by the conventional casting, forming and cutting processes, a new class of lattice structures named functionally graded lattice structures have been developed, which provide further opportunities to improve

structural efficiency and realize a broader engineering application compared with uniform-density structures, especially in many energy absorption devices. Such functionally graded lattice structures have been successfully manufactured by AM processes, such as the laser engineering net shape (LENS) reviewed by [Mahmoud and Elbestawi \(2017\)](#) and SLM processes.

The advanced AM technology is now capable of producing lattice structures with widely variable dimensions, various topologies and desired space distributions, which enables the flexible design of lightweight lattice structures with multifunctional properties as reported by [Zheng et al. \(2014\)](#). The synergy of AM and lattices largely promotes the applications of multifunctional lightweight structures in many areas such as in thermal systems, energy absorption structures, consumer products, medical devices and soft robotics as reviewed by [Thompson et al. \(2016a\)](#). Therefore, from the viewpoint of improving the mechanical properties and functionality of sandwich sheets, lattice structures could be potentially good candidates for core structures. If sandwich sheets with lattice core structures can be bendable, they can be expected to replace conventional heavy monolithic sheets in various engineering applications, which is answer to the high demand for lightweight functional materials.

1.3.2 Research objectives

The design and fabrication of lightweight hybrid structures with optimal mechanical performance, production efficiency and improved functionality has always been driven by the pursuit of further reduction of energy consumption and greenhouse gas emissions. However, the above discussed technical issues associated with the design and production processes, such as the low manufacturing efficiency and high production cost, the limited formability and restricted mechanical performance and functionality, severely hindered the widespread use of such lightweight multifunctional hybrid structures. This doctoral thesis aims to overcome these engineering challenges by proposing more effective design strategies and efficient production processes. The research objectives of this dissertation mainly include:

- (i) Suitable material combinations of metal face/composite core sandwich structure

should provide enhanced mechanical property without losing formability compared to the monolithic constituent. The inner macro structure of sandwich sheet should be three-dimensional rather than flat two-dimensional for better weight-specific structural efficiency.

- (ii) The three-dimensional inner macro structure is expected to be fabricated by conventional sheet forming process such rapid stamping with high productivity. The shape of the three-dimensional core should be properly selected and optimized so as to have sufficient failure (e.g. core shear failure and face buckling) resistance during secondary forming process.
- (iii) The influence factors such as the sandwich geometry, forming tool geometry, core shapes and material properties of constituents on the formability and mechanical properties of sandwich sheets are expected to be clarified for instructing the design of formable sandwich sheets.
- (iv) The topology of inner macro structure of sandwich sheets should be optimized by suitable topology optimization strategies for the pursuit of superior structural efficiency and better formability. The manufacturability of the topologically optimized core structures should be ensured so as to be produced by additive manufacturing.
- (v) The structural unit cells with potential multifunctional characteristics should be introduced into the inner macro structure to enhance the multifunctional characteristics and applicability of the sandwich sheets without losing its mechanical property and formability as well as productivity.

Metal-based composite sheets, in which low-density three-dimensional CFRP macrostructure is sandwiched and bonded to thin but stiff metallic face sheets such as titanium alloys, aluminum alloys and steels, are proposed in this thesis to facilitate the above requirements of mechanical properties, formability and productivity. The sandwich sheets composed of metal face and CFRP core are suitable for mass production if the inner CFRP core can be efficiently fabricated by sheet forming process such as stamping. In addition, the combination of thin but stiff metal face sheets and a 3D CFRP core can be expected to provide

much higher stiffness and strength than any of the single constituent when standing alone. If such metal-based composite sheets could be secondarily stamped or bent into desired three-dimensional geometry without failure of inner macrostructure, such metal-based composite sheets could be used to replace heavy sheet metals in various applications such as framework parts of automobiles and airplanes, which answers for the strong demand for the reduction of energy consumption and emissions of vehicles.

Firstly, for the rapid fabrication of core macrostructure by conventional sheet metal forming methods such as stamping, the core macrostructure should have a continuous cross-sectional shape, relatively smooth profile and uniform thickness. The continuous cross-sectional shape of the macro core structure can avoid causing cracking of the basis sheet material during fabrication process, making it possible to produce by stamping of CFRP. The carbon fiber reinforced thermoplastic (CFRTP) will be adopted as the inner macrostructure with a smooth shape can be expected to be produced by warm stamping due to the improved formability of the CFRTP sheet at elevated temperatures. However, owing to the limited out-of-plane shear strength of CFRTP, the inner macrostructure shape will be optimized so as to yield a stable shear response to suppress the potential core shear failure during secondary forming. Furthermore, suitable structural parameters will be decided to ensure the gap between attachment points is sufficiently small to prevent face buckling.

The successful secondary forming of sandwich sheets depends on many factors, such as the material properties of sandwich constituents, the sandwich geometries, forming tool geometries, core shapes, forming processes, forming temperatures etc., the relation between formability and these influence factors will be clarified by experimental tests and theoretical analyses for the instruction of effective design and efficient fabrication process. In addition, the topology of inner macro core structure will be optimized so as to enable superior stiffness and formability of sandwich sheets while maintaining good manufacturability of the core structure.

The feasibility of effective design and efficient fabrication of hybrid metal face/CFRP core composite sheets with superior mechanical property, formability as well as productivity is demonstrated by a series of investigations presented in this thesis. To be specific, the suitable

inner core structure with superior mechanical property was designed and efficiently produced by warm stamping of CFRTP sheet. The effects of material properties of face sheets and core, sandwich geometries, forming tool geometries, core shapes, forming processes and forming temperatures on formability of sandwich sheets were systematically investigated by experiments and theoretical analyses. The homogenization-based topology optimization (HMTO) method was firstly integrated with the tetrahedral truss-based lattice structure to optimize the stiffness and later the elastically isotropic plate-based lattices with superior structural efficiency was further proposed to integrate with HMTO to improve the design efficiency, manufacturability, structural isotropy and computational efficiency. The stiffness and formability of sandwich sheets were simultaneously optimized by integrating the density-based topology optimization method with the multi-stage genetic algorithm.

1.4 Proposed solutions in this thesis

1.4.1 Proposal of formable metal face /CFRP core hybrid sandwich sheet

The idea of the formable metal face/CFRP core hybrid sandwich sheet originates from the studies conducted in Yanagimoto Lab in 2010 and 2012, as shown in [Figure 1-49](#). In the investigation conducted by [Yanagimoto et al. \(2010\)](#), significant enhancement of the bending formability of type-420J2 stainless steel sheets (brittle layer) was observed when they are layered by type-304 stainless steel sheets (ductile layer) and composed into a multilayer metallic sheet. The mechanism of the enhancement of the formability is due to the delay of the initiation of necking of type-420J2 stainless steel contributed by the surrounded ductile SUS304 sheets. Following this research, a new sheet forming process for solidified CFRP, in which a CFRP sheet is sandwiched by ductile dummy metallic sheets during cold and warm stamping, was proposed by [Yanagimoto and Ikeuchi \(2012\)](#). The dummy metallic sheets act as protective materials as well as media for heating the CFRP sheet. Similar to the mechanism of formability enhancement of brittle layer in multilayer metallic sheets, necking initiation in brittle CFRP layer is suppressed owing to the surrounded ductile metallic sheets, and thus the sound forming of CFRP sheet is achieved. Inspired by this investigation, the metal face/CFRP core hybrid sandwich sheet is proposed, in which the brittle 3D CFRP core layer is sandwiched between ductile metallic face sheets. Based on the formability enhancement mechanism in the previous two studies, the formability of the brittle 3D CFRP layer can be expected to be enhanced by the sandwiched ductile metallic face sheets and thus good forming of the hybrid sandwich sheets can be expected. Different from the conventional full metallic sandwich sheets with a 3D core or the sandwich sheet with a 2D flat core, the metal face/3D CFRP core sandwich sheet with potentially improved structural efficiency, productivity and formability is firstly proposed in this thesis. If such metal face/3D CFRP core sandwich sheets could be secondarily stamped or bent into desired three-dimensional shape without failure, such hybrid composite sheets could be used to replace heavy monolithic sheet metals in numerous applications such as framework parts of flying cars, automobiles and airplanes, which answers for the strong demand for the reduction of energy consumption and carbon emissions.

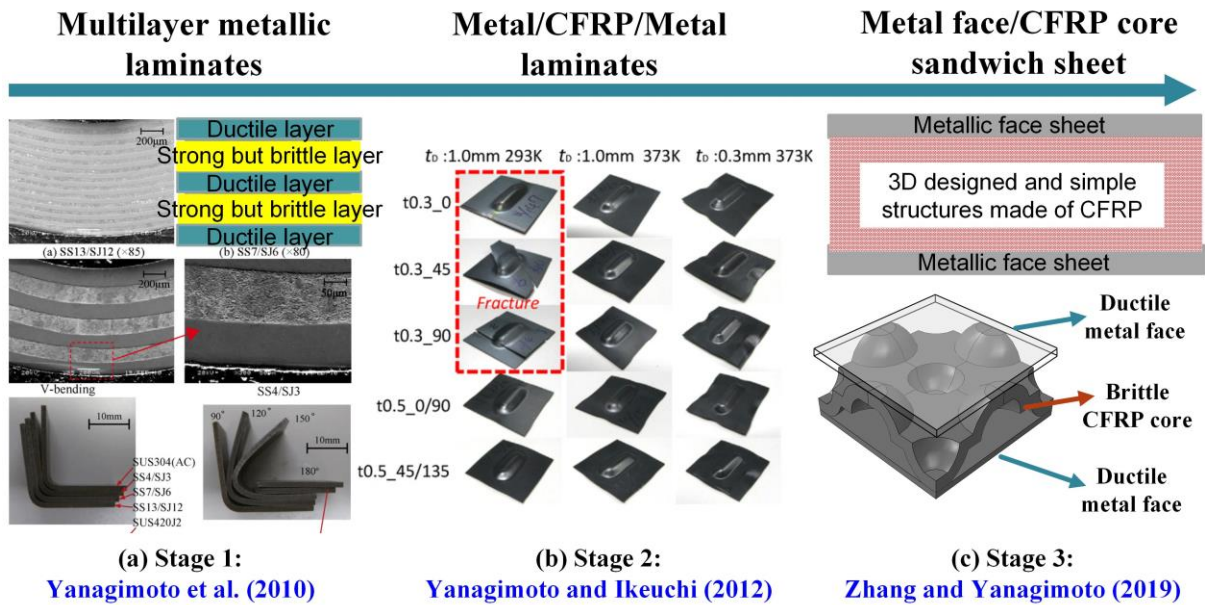


Figure 1-49. The research route from multilayer metallic sheets to metal face/CFRP core hybrid sandwich sheet.

1.4.2 Shape design for the improvement of mechanical property and formability of metal face/CFRP core sandwich sheet

The shape of the inner CFRP core structure should be properly designed as it is highly related to the productivity, mechanical property and formability of sandwich sheets. A feasible means of improving the manufacturing efficiency and formability of such metal-based composite sheets is to fabricate the inner macrostructure by warm stamping of CFRTP. Due to the improved formability of the CFRTP sheet at elevated temperatures, the inner macrostructure with a smooth shape is possible to be produced by warm stamping of CFRTP. For this purpose, the core macrostructure should have a continuous cross-sectional shape, relatively smooth profile and uniform thickness. In addition, owing to the limited out-of-plane shear strength of CFRTP, the inner macrostructure should yield a stable shear response to suppress the potential core shear failure. Furthermore, suitable structural parameters should be designed to ensure the gap between attachment points is sufficiently small to prevent face buckling. Previous investigations on the forming characteristics of sandwich sheets with various inner macrostructures have revealed that failure modes such as core-face sheet delamination, face buckling and core shear failure are highly related to material properties of

sandwich constituents, the sandwich geometries, forming tool geometries, core shapes, forming processes, forming temperatures, etc. Therefore, it is essential to clarify the relation between formability and these influence factors by systematical experimental tests and theoretical analyses for effective design and efficient fabrication process. The flowchart of the shape optimization, fabrication and property evaluation of sandwich sheets is shown in Figure 1-50, in which the inner core structure is firstly optimized by comprehensively considering the mechanical property, manufacturability and failure hindrance, followed by continuous manufacturing process of sandwich sheets and finally the mechanical property and formability are evaluated. Through this design and fabrication chain, the formable metal face/CFRP core sandwich sheet with superior mechanical property and high productivity is expected to be developed.

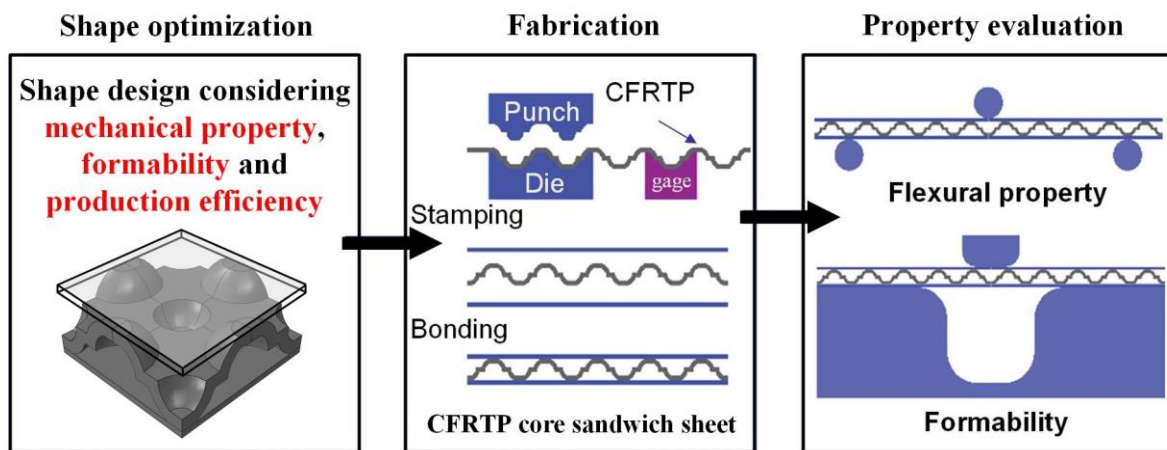


Figure 1-50. Flowchart of shape optimization, fabrication and property evaluation of sandwich sheets.

1.4.3 Synergy of topology optimization and additive manufacturing for the design and fabrication of formable sandwich sheets with superior mechanical property

Although conventional manufacturing processes allow some control over shape and size of the inner core structure, they remain limited to producing a certain type of specially designed structures and thus the mechanical property, formability and functionality of inner core structures may still be restricted. In addition, the incapability of manufacturing precise complex structures, the high manufacturing cost and the discrepancy in the properties of produced

structures also limit the applications of the conventional fabrication methods. The layer-by-layer fabrication paradigm of AM enables the build of lattice materials with extremely intricate external geometries and high control of the internal architecture, overcoming the limitations of conventional fabrication methods. The topology optimization enables the optimal material layout of the core structure at a given set of load and boundary conditions, and thus it can be relied on to optimize the core structure for the pursuit of higher structural efficiency and better formability. The synergy of topology optimization and additive manufacturing could be a perfect tool for the design and production of sandwich sheets with improved mechanical performance, formability and functionality. Therefore, the topology optimization is used to design optimal core structures with superior stiffness and formability following the development map shown in [Figure 1-51](#).

In stage 1, for the purpose of improving weight-specific mechanical performance, a new structure called a microlattice dome is proposed, in which microlattices replace the solid part of the dome structure owing to its advantages over solid materials. These advantages include lower density due to its networked frame, which supports more air than a solid material and less brittleness, as the struts or pairs of struts can flex separately, allowing it to bend or compress in ways that solid materials cannot. Therefore, it is reasonable to expect that the microlattice dome structure has higher weight-specific stiffness and energy absorption capability than a conventional solid dome. Furthermore, the embedding volume created by the microlattices allows the infill of other functional components such as thermal insulation and acoustic absorption materials. In this stage, a homogenization-based topology optimization method was integrated with the lattice structure to optimize the spatial distribution of microlattices to maximize the compression and bending stiffnesses as well as energy absorption of the microlattice dome.

In contrast to the conventional truss–lattices composed of beams or struts, novel plate–lattices composed of closed-cell sheets have been reported to exhibit superior mechanical properties and can potentially achieve isotropic elastic properties. If such elastically isotropic plate–lattices with superior mechanical properties are integrated with the HMTO method, the structural efficiency and isotropy can be expected to be further enhanced. Therefore, in stage

2, the HMTO method is integrated with elastically isotropic plate-lattices to further improve the manufacturability, structural efficiency, structural isotropy and computational efficiency.

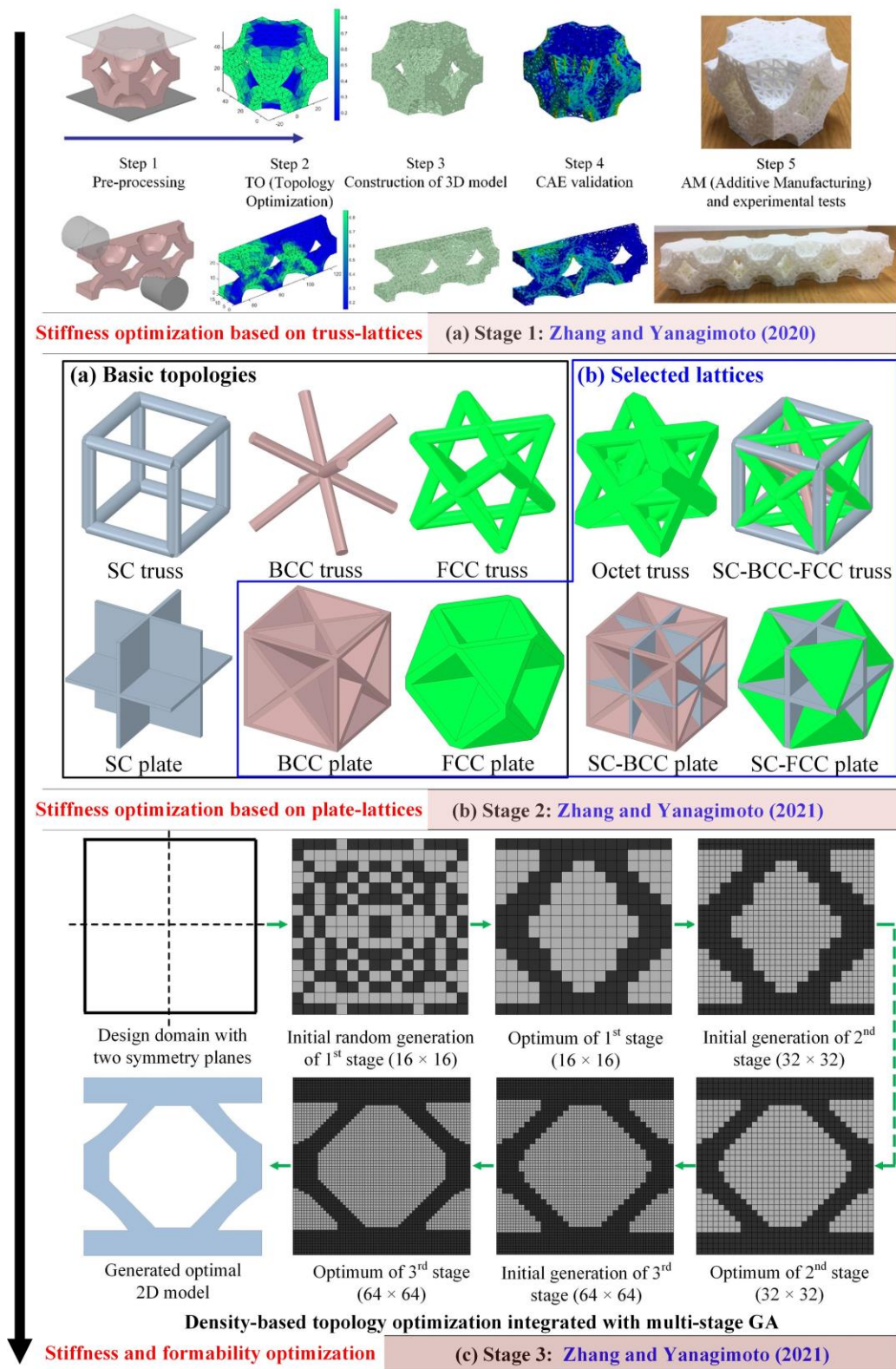


Figure 1-51. Development map of topology optimization for the design and fabrication of

formable sandwich sheets with superior mechanical property.

In the first two stages, only the stiffness is optimized while the formability is not considered. Inspired by the conventional density-based topology optimization concept, an intelligent topology optimization approach is proposed to design the sandwich sheets that can not only withstand potential failure modes but also have the optimal bending stiffness in stage 3. In the proposed approach, the density-based topology optimization is integrated with the multi-stage genetic algorithm (GA) to optimize the repeatable unit cell of the core structure of sandwich sheets. Two optimization schemes are adopted, in which one optimizes the formability and the other one optimizes the bending stiffness while fulfilling potential failure constraints. Through the synergy of topology optimization and additive manufacturing, the sandwich sheets with superior mechanical performance and formability can be expected to be effectively designed and efficiently produced.

1.5 Research framework

Totally six chapters are included in this dissertation, which starts with a brief introduction to lightweight hybrid structures, followed by the introduction of the state-of-the-art design methodology and fabrication process for hybrid structures. The key technical challenges for the development of lightweight hybrid structures are discussed, followed by the proposal of effective design strategy and efficient manufacturing process to solve these engineering issues. The latest design methods and fabrication technologies available in the literatures for lightweight hybrid structures are reviewed in each following chapter before the introduction of design method, fabrication process, results and discussion.

Focusing on the design and fabrication of lightweight metal face /CFRP core hybrid structures, this dissertation can be divided into two major research subjects as shown in the research framework in [Figure 1-52](#). The first subject is based on shape design strategies and conventional production methods to effectively design and efficiently fabricate lightweight metal face/CFRP core hybrid structures with excellent mechanical properties and good formability, in which **Chapter 2** and **3** are included. The synergy of intelligent topology optimization approaches and advanced additive manufacturing technologies is fully used to achieve optimal design and production of metal face/CFRP core sandwich sheets with improved mechanical performance and formability, which is investigated in **Chapter 4** and **5**. The specific research content of each chapter will be introduced one by one as follows.

In **Chapter 2**, the shape of the inner CFRP core structure is firstly determined based on empirical selection and structural parameter design as it is highly related to the productivity, mechanical property and formability of sandwich sheets. The shape of the inner core structure is optimized comprehensively considering its productivity, mechanical property and formability. To achieve the rapid fabrication of the inner macrostructure by warm stamping of CFRTP, the core macrostructure with a continuous cross-sectional shape, relatively smooth profile and uniform thickness is designed. In addition, to yield a stable shear response to suppress the potential core shear failure, a dome-like core structure is finally determined. Furthermore, structural parameters are further optimized to achieve superior structural

efficiency and to prevent face buckling. The rapid fabrication of the inner CFRP core is achieved by a continuous piecewise sectional forming technology. The mechanical property of produced sandwich sheets is evaluated by the three-point bending test while the formability is systematically investigated by L-bending and draw-bending tests under cold and warm forming conditions.

The influence factors on forming characteristics of sandwich sheets are systematically studied in **Chapter 3**. Previous investigations on the forming characteristics of sandwich sheets with various inner macrostructures have revealed that failure modes such as core-face sheet delamination, face buckling and core shear failure are highly related to material properties of sandwich constituents, the sandwich geometries, forming tool geometries, core shapes, forming processes, forming temperatures, etc. Therefore, the relation between formability and these influence factors is clarified by systematical experimental tests and theoretical analyses for effective design and efficient fabrication process. In addition, the functional lattice structures are embraced in the core structure for the improvement of potential functionality of sandwich sheets. The effects of lattice core topologies and relative densities on the mechanical property and forming behavior are also extensively investigated.

In **Chapter 4**, for the further improvement of structural efficiency of sandwich sheets, the topology of the inner core structure is optimized by novel topology optimization strategies. To improve the weight-specific stiffness and energy absorption capability of the conventional dome commonly used as the core of sandwich sheets, a new concept of filling the solid part of the dome with stretch-dominated microlattices is proposed. The optimal density distribution of microlattices is obtained by integrating the homogenization-based topology optimization (HMTO) method with the tetrahedral lattice structure. Then 3D models are constructed from topology optimization results for CAE validation and AM, and the additively manufactured prototypes are experimentally tested under compression and three-point bending. Moreover, to further improve the manufacturability, computational efficiency, structural efficiency and isotropy, the plate-based lattice structures with superior mechanical properties and excellent elastic isotropy are integrated with the HMTO method to optimize two typical structures subjected to three-point bending and compression.

A novel topology optimization strategy that can optimize the bending stiffness while maintaining good formability is proposed in **Chapter 5**, in which the density-based topology optimization is integrated with the multi-stage genetic algorithm (GA) to optimize the repeatable unit cell of the core structure of sandwich sheets. Two optimization schemes are adopted, in which one optimizes the formability and the other one optimizes the bending stiffness while fulfilling potential failure constraints. The failure constraints on core shear failure and face buckling are theoretically deduced to mathematically formulate the topology optimization problem, which is solved by the adaptive multi-stage GA to increase the possibility of generating physically meaningful and additively manufacturable topologies. Then, the optimal topologies are converted to 3D models that are additively manufacturable, after which the prototypes are additively manufactured using carbon fibre reinforced nylon. Finally, the produced sandwich sheets are subjected to three-point bending tests to validate the bending stiffness and energy absorption abilities, while the L-bending and draw-bending tests are employed to check the formability.

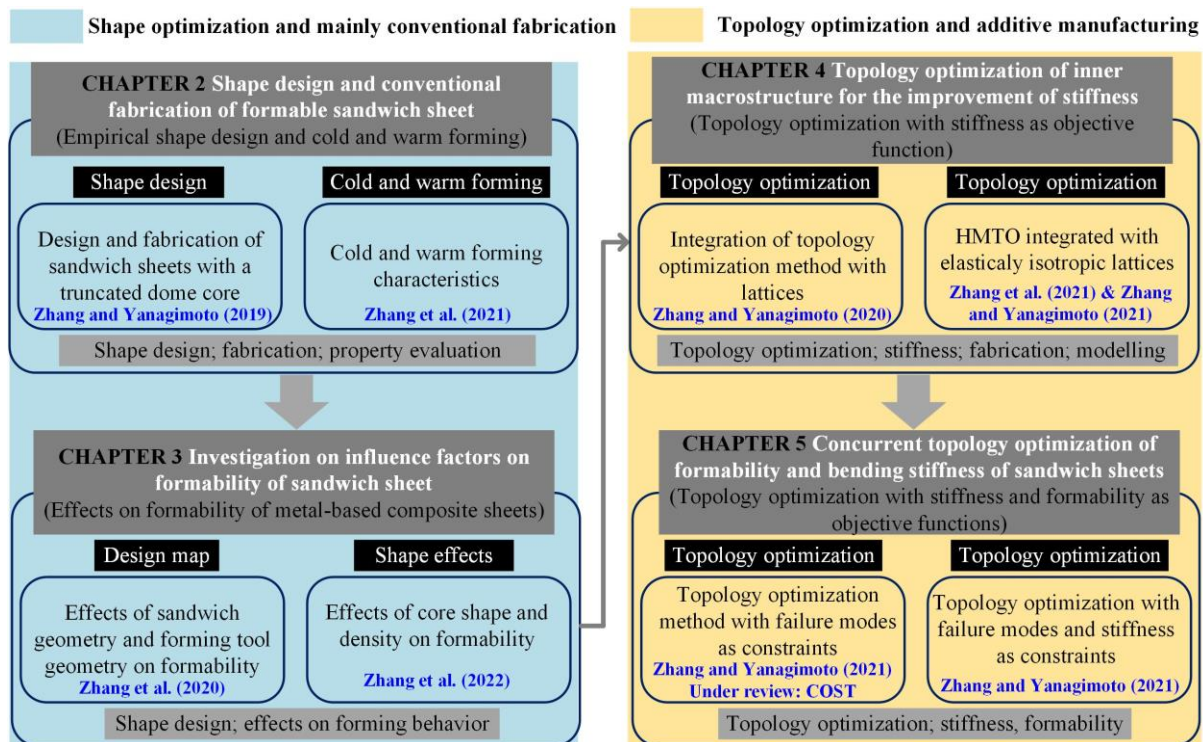


Figure 1-52. Research framework of this dissertation.

1.6 References

- Ahn, D.-G., 2015. Research trends of metallic sandwich plates with single layer periodically repeated metallic inner structures (PRMIS)-focused on design, manufacturing and formability. *International Journal of Precision Engineering and Manufacturing-Green Technology* 2, 377-391.
- Ahuja, B., Schaub, A., Karg, M., Schmidt, R., Merklein, M., Schmidt, M., 2015. high power laser beam melting of Ti-6Al-4V on formed sheet metal to achieve hybrid structures, *Laser 3D Manufacturing II*. International Society for Optics and Photonics, p. 93530X.
- Allaire, G., Jouve, F., Toader, A.-M., 2002. A level-set method for shape optimization. *Comptes Rendus Mathematique* 334, 1125-1130.
- Aly, S., Arif, A., Al-Athel, K., Mostaghimi, J., Zubair, S., 2016. Performance of open pore metal foam heat sinks fabricated with thermally sprayed interface. *Applied Thermal Engineering* 105, 411-424.
- Bartolo, P., Kruth, J.-P., Silva, J., Levy, G., Malshe, A., Rajurkar, K., Mitsuishi, M., Ciurana, J., Leu, M., 2012. Biomedical production of implants by additive electro-chemical and physical processes. *CIRP annals* 61, 635-655.
- Beaman, J.J., Barlow, J.W., Bourell, D.L., Crawford, R.H., Marcus, H.L., McAlea, K.P., 1997. *Solid freeform fabrication: a new direction in manufacturing*. Kluwer Academic Publishers, Norwell, MA 2061, 25-49.
- Bendsøe, M.P., 1989. Optimal shape design as a material distribution problem. *Structural optimization* 1, 193-202.
- Bendsøe, M.P., Kikuchi, N., 1988. Generating optimal topologies in structural design using a homogenization method. *Computer methods in applied mechanics and engineering* 71, 197-224.
- Berger, J., Wadley, H., McMeeking, R., 2017. Mechanical metamaterials at the theoretical limit of isotropic elastic stiffness. *Nature* 543, 533-537.
- Bernard, A., Delplace, J.C., Perry, N., Gabriel, S., 2003. Integration of CAD and rapid manufacturing for sand casting optimisation. *Rapid Prototyping Journal*.
- Bernd-Arno, B., Sven, H., Nenad, G., Moritz, M.-C., Tim, W., André, N., 2017. Forming and joining of carbon-fiber-reinforced thermoplastics and sheet metal in one step. *Procedia Engineering* 183, 227-232.
- Besse, C.C., Mohr, D., 2012. Plasticity of formable all-metal sandwich sheets: Virtual experiments and constitutive modeling. *International Journal of Solids and Structures* 49, 2863-2880.
- Bitzer, T., 1997. *Honeycomb technology: materials, design, manufacturing, applications and testing*. Springer Science & Business Media.
- Bourdin, B., Chambolle, A., 2003. Design-dependent loads in topology optimization. *ESAIM: Control, Optimisation and Calculus of Variations* 9, 19-48.
- Bruschi, S., Cao, J., Merklein, M., Yanagimoto, J., 2021. Forming of metal-based composite parts. *CIRP Annals* 70, 567-588.
- Camirero, M., Chacón, J., García-Moreno, I., Rodríguez, G., 2018. Impact damage resistance of 3D printed continuous fibre reinforced thermoplastic composites using fused deposition

modelling. *Composites Part B: Engineering* 148, 93-103.

Campbell, R.I., Jee, H., Kim, Y.S., 2013. Adding product value through additive manufacturing, DS 75-4: Proceedings of the 19th International Conference on Engineering Design (ICED13), Design for Harmonies, Vol. 4: Product, Service and Systems Design, Seoul, Korea, 19-22.08. 2013.

Cheng, L., Zhang, P., Biyikli, E., Bai, J., Robbins, J., To, A., 2017. Efficient design optimization of variable-density cellular structures for additive manufacturing: theory and experimental validation. *Rapid Prototyping Journal*.

Chernikov, D., Erisov, Y., Petrov, I., Alexandrov, S., Lang, L., 2019. Research of different processes for forming fiber metal laminates. *International Journal of Automotive Technology* 20, 89-93.

Chua, C.K., Leong, K.F., Lim, C.S., 2010. *Rapid prototyping: principles and applications (with companion CD-ROM)*. World Scientific Publishing Company.

Compton, B.G., Lewis, J.A., 2014. 3D-printing of lightweight cellular composites. *Advanced materials* 26, 5930-5935.

Cucinotta, F., Guglielmino, E., Longo, G., Risitano, G., Santonocito, D., Sfravara, F., 2019. Topology optimization additive manufacturing-oriented for a biomedical application, *Advances on Mechanics, Design Engineering and Manufacturing II*. Springer, pp. 184-193.

Dehghani, F., Salimi, M., 2016. Analytical and experimental analysis of the formability of copper-stainless-steel 304L clad metal sheets in deep drawing. *The International Journal of Advanced Manufacturing Technology* 82, 163-177.

Del Pero, F., Delogu, M., Pierini, M., 2017. The effect of lightweighting in automotive LCA perspective: Estimation of mass-induced fuel consumption reduction for gasoline turbocharged vehicles. *Journal of Cleaner Production* 154, 566-577.

Dilthey, U., Ghandehari, A., Kopp, R., Hohmeier, P., Beiss, P., Iglesias Figueredo, E., El-Magd, E., Kranz, A., 2001. Development of porous steel structures for steam turbines. *Advanced engineering materials* 3, 111-119.

Ding, Z., Wang, H., Luo, J., Li, N., 2021. A review on forming technologies of fibre metal laminates. *International Journal of Lightweight Materials and Manufacture* 4, 110-126.

Dong, L., 2020. Mechanical responses of snap-fit Ti-6Al-4V warren-truss lattice structures. *International Journal of Mechanical Sciences* 173, 105460.

Dong, L., Deshpande, V., Wadley, H., 2015. Mechanical response of Ti-6Al-4V octet-truss lattice structures. *International Journal of Solids and Structures* 60, 107-124.

El Moumen, A., Tarfaoui, M., Lafdi, K., 2019. Additive manufacturing of polymer composites: Processing and modeling approaches. *Composites Part B: Engineering* 171, 166-182.

Fan, H., Meng, F., Yang, W., 2006. Mechanical behaviors and bending effects of carbon fiber reinforced lattice materials. *Archive of Applied Mechanics* 75, 635-647.

Geetha, M., Singh, A.K., Asokamani, R., Gogia, A.K., 2009. Ti based biomaterials, the ultimate choice for orthopaedic implants—a review. *Progress in materials science* 54, 397-425.

George, T., Deshpande, V.S., Sharp, K., Wadley, H.N., 2014. Hybrid core carbon fiber composite sandwich panels: Fabrication and mechanical response. *Composite structures* 108, 696-710.

- George, T., Deshpande, V.S., Wadley, H.N., 2013. Mechanical response of carbon fiber composite sandwich panels with pyramidal truss cores. *Composites Part A: Applied Science and Manufacturing* 47, 31-40.
- Gonzalez-Canche, N., Flores-Johnson, E., Carrillo, J., 2017. Mechanical characterization of fiber metal laminate based on aramid fiber reinforced polypropylene. *Composite structures* 172, 259-266.
- Groche, P., Übelacker, D., Stein, P., Steinbach, F., Tekkaya, A.E., 2018. Experimental and analytical investigation of the force requirements in shear cutting of metal-polymer-metal composites. *International Journal of Material Forming* 11, 213-224.
- Guo, X., Zhang, W., Zhong, W., 2014. Doing topology optimization explicitly and geometrically—a new moving morphable components based framework. *Journal of Applied Mechanics* 81.
- Hu, Y., Li, W., An, X., Fan, H., 2016. Fabrication and mechanical behaviors of corrugated lattice truss composite sandwich panels. *Composites Science and Technology* 125, 114-122.
- ISHIO, M., 1989. Manufacturing Process and Bonding Mechanism of Clad Metals by Cold Roll Welding. *Tetsu-to-Hagane* 75, 716-722.
- Jackson, K., Allwood, J., Landert, M., 2008. Incremental forming of sandwich panels. *Journal of Materials Processing Technology* 204, 290-303.
- Kai, M., Taya, S., Tomaru, H., 2013. Influence of Material Properties on Pet-Hair of Laminated Steel in The Forming Process of DI Can. *TETSU TO HAGANE-JOURNAL OF THE IRON AND STEEL INSTITUTE OF JAPAN* 99, 20-25.
- Kang, B.-S., Kang, G.-J., Moon, B.-Y., 2003. Hole and lead plug effect on fiber reinforced elastomeric isolator for seismic isolation. *Journal of materials processing technology* 140, 592-597.
- Kang, K.-J., 2009. A wire-woven cellular metal of ultrahigh strength. *Acta Materialia* 57, 1865-1874.
- Karlsson, J., Snis, A., Engqvist, H., Lausmaa, J., 2013. Characterization and comparison of materials produced by Electron Beam Melting (EBM) of two different Ti–6Al–4V powder fractions. *Journal of materials processing technology* 213, 2109-2118.
- Keating, S., Oxman, N., 2013. Compound fabrication: A multi-functional robotic platform for digital design and fabrication. *Robotics and Computer-Integrated Manufacturing* 29, 439-448.
- Khoshnevis, B., Hwang, D., Yao, K.-T., Yeh, Z., 2006. Mega-scale fabrication by contour crafting. *International Journal of Industrial and Systems Engineering* 1, 301-320.
- Kim, J.-K., Yu, T.-X., 1997. Forming and failure behaviour of coated, laminated and sandwiched sheet metals: a review. *Journal of Materials Processing Technology* 63, 33-42.
- Kooistra, G.W., Wadley, H.N., 2007. Lattice truss structures from expanded metal sheet. *Materials & design* 28, 507-514.
- Lee, J., Bae, D., Chung, W., Kim, K., Lee, J., Cho, Y., 2007. Effects of annealing on the mechanical and interface properties of stainless steel/aluminum/copper clad-metal sheets. *Journal of Materials Processing Technology* 187, 546-549.
- Liewald, M., Bolay, C., Thullner, S., 2013. Shear cutting and counter shear cutting of sandwich materials. *Journal of Manufacturing Processes* 15, 364-373.
- Liewald, M., Hofmann, D., 2017. Investigations on Delamination Behavior of Sandwich

Sheets. *Procedia Engineering* 183, 71-76.

Liu, J., Liu, W., Xue, W., 2013. Forming limit diagram prediction of AA5052/polyethylene/AA5052 sandwich sheets. *Materials & Design* 46, 112-120.

Liu, S., Li, Y., Li, N., 2018. A novel free-hanging 3D printing method for continuous carbon fiber reinforced thermoplastic lattice truss core structures. *Materials & Design* 137, 235-244.

Liu, W., Song, H., Huang, C., 2020a. Maximizing mechanical properties and minimizing support material of PolyJet fabricated 3D lattice structures. *Additive Manufacturing* 35, 101257.

Liu, X., Alizadeh, V., Hansen, C.J., 2020b. The compressive response of octet lattice structures with carbon fiber composite hollow struts. *Composite Structures* 239, 111999.

Mahmoud, D., Elbestawi, M.A., 2017. Lattice structures and functionally graded materials applications in additive manufacturing of orthopedic implants: a review. *Journal of Manufacturing and Materials Processing* 1, 13.

Maier, V., Hausöl, T., Schmidt, C.W., Böhm, W., Nguyen, H., Merklein, M., Höppel, H.W., Göken, M., 2012. Tailored heat treated accumulative roll bonded aluminum blanks: microstructure and mechanical behavior. *Metallurgical and Materials Transactions A* 43, 3097-3107.

Martina, F., Colegrove, P.A., Williams, S.W., Meyer, J., 2015. Microstructure of interpass rolled wire+ arc additive manufacturing Ti-6Al-4V components. *Metallurgical and Materials Transactions A* 46, 6103-6118.

Maskery, I., Sturm, L., Aremu, A., Panesar, A., Williams, C., Tuck, C., Wildman, R.D., Ashcroft, I., Hague, R.J., 2018. Insights into the mechanical properties of several triply periodic minimal surface lattice structures made by polymer additive manufacturing. *Polymer* 152, 62-71.

Mei, J., Liu, J., Liu, J., 2017. A novel fabrication method and mechanical behavior of all-composite tetrahedral truss core sandwich panel. *Composites Part A: Applied Science and Manufacturing* 102, 28-39.

Ming, Y., Zhang, S., Han, W., Wang, B., Duan, Y., Xiao, H., 2020. Investigation on process parameters of 3D printed continuous carbon fiber-reinforced thermosetting epoxy composites. *Additive Manufacturing* 33, 101184.

Mohr, D., 2005. On the role of shear strength in sandwich sheet forming. *International Journal of Solids and Structures* 42, 1491-1512.

Mueller, B., 2012. Additive manufacturing technologies—Rapid prototyping to direct digital manufacturing. *Assembly Automation*.

Nassar, H., Albakri, M., Pan, H., Khraisheh, M., 2012. On the gas pressure forming of aluminium foam sandwich panels: Experiments and numerical simulations. *CIRP annals* 61, 243-246.

Parsa, M., Ettihad, M., 2010. Experimental and finite element study on the spring back of double curved aluminum/polypropylene/aluminum sandwich sheet. *Materials & Design* 31, 4174-4183.

Plocher, J., Panesar, A., 2020. Effect of density and unit cell size grading on the stiffness and energy absorption of short fibre-reinforced functionally graded lattice structures. *Additive Manufacturing* 33, 101171.

- Queheillalt, D.T., Murty, Y., Wadley, H.N., 2008. Mechanical properties of an extruded pyramidal lattice truss sandwich structure. *Scripta Materialia* 58, 76-79.
- Rubino, V., Deshpande, V., Fleck, N., 2009. The dynamic response of clamped rectangular Y-frame and corrugated core sandwich plates. *European Journal of Mechanics-A/Solids* 28, 14-24.
- Russell, B., Deshpande, V., Wadley, H., 2008. Quasistatic deformation and failure modes of composite square honeycombs. *Journal of mechanics of materials and structures* 3, 1315-1340.
- Russo, A., Zuccarello, B., 2007. Experimental and numerical evaluation of the mechanical behaviour of GFRP sandwich panels. *Composite Structures* 81, 575-586.
- Saadatfard, A., Gerdooei, M., Jalali Aghchai, A., 2020. Drawing potential of fiber metal laminates in hydromechanical forming: A numerical and experimental study. *Journal of Sandwich Structures & Materials* 22, 1386-1403.
- Saito, Y., 1998. Ultra-fine grained bulk aluminum produced by accumulative roll-bonding (ARB) process. *Scripta mater.* 39, 1221-1227.
- Seong, D.-Y., Jung, C.G., Yang, D.-Y., Ahn, D.G., 2008. Bending behavior of simply supported metallic sandwich plates with dimpled cores. *International Journal of Modern Physics B* 22, 6179-6184.
- Seong, D., Jung, C.G., Yang, D.-Y., Kim, J., Chung, W., Lee, M., 2010. Bendable metallic sandwich plates with a sheared dimple core. *Scripta materialia* 63, 81-84.
- Sexton, A., Cantwell, W., Kalyanasundaram, S., 2012. Stretch forming studies on a fibre metal laminate based on a self-reinforcing polypropylene composite. *Composite Structures* 94, 431-437.
- Shellabear, M., Nyrhilä, O., 2004. DMLS-Development history and state of the art. *Laser Assisted Netshape engineering* 4, proceedings of the 4th LANE, 21-24.
- Sinmazçelik, T., Avcu, E., Bora, M.Ö., Çoban, O., 2011. A review: Fibre metal laminates, background, bonding types and applied test methods. *Materials & Design* 32, 3671-3685.
- Sivarupan, T., Balasubramani, N., Saxena, P., Nagarajan, D., El Mansori, M., Salonitis, K., Jolly, M., Dargusch, M.S., 2021. A review on the progress and challenges of binder jet 3D printing of sand moulds for advanced casting. *Additive Manufacturing*, 101889.
- Sokolowski, J., Zochowski, A., 2003. Optimality conditions for simultaneous topology and shape optimization. *SIAM journal on control and optimization* 42, 1198-1221.
- Suryakumar, S., Karunakaran, K., Bernard, A., Chandrasekhar, U., Raghavender, N., Sharma, D., 2011. Weld bead modeling and process optimization in hybrid layered manufacturing. *Computer-Aided Design* 43, 331-344.
- Sypeck, D.J., Wadley, H.N., 2002. Cellular metal truss core sandwich structures. *Advanced Engineering Materials* 4, 759-764.
- Tagarielli, V., Deshpande, V., Fleck, N., 2008. The high strain rate response of PVC foams and end-grain balsa wood. *Composites Part B: Engineering* 39, 83-91.
- Thompson, M.K., Moroni, G., Vaneker, T., Fadel, G., Campbell, R.I., Gibson, I., Bernard, A., Schulz, J., Graf, P., Ahuja, B., 2016a. Design for Additive Manufacturing: Trends, opportunities, considerations, and constraints. *CIRP annals* 65, 737-760.
- Thompson, M.K., Stolfi, A., Mischkot, M., 2016b. Process chain modeling and selection in

an additive manufacturing context. *CIRP Journal of Manufacturing Science and Technology* 12, 25-34.

Trifale, N., Nauman, E., Yazawa, K., 2016. Thermal and mechanical modeling of metal foams for thermal interface application. *Journal of Heat Transfer* 138.

Troch-Nagels, G., Winand, R., Weymeersch, A., Renard, L., 1992. Electron conducting organic coating of mild steel by electropolymerization. *Journal of applied electrochemistry* 22, 756-764.

Tseng, H.-C., Hung, J.-C., Hung, C., Lee, M.-F., 2011. Experimental and numerical analysis of titanium/aluminum clad metal sheets in sheet hydroforming. *The International Journal of Advanced Manufacturing Technology* 54, 93-111.

VDI-Guideline, N., 2009. 3404: Additive fabrication-Rapid technologies (rapid prototyping)-fundamentals, terms and definitions, quality parameter, supply agreements. Berlin: Beuth Verlag.

Wadley, H.N., 2006. Multifunctional periodic cellular metals. *Philosophical Transactions of the Royal Society A: Mathematical, Physical and Engineering Sciences* 364, 31-68.

Wang, M.Y., Wang, X., Guo, D., 2003. A level set method for structural topology optimization. *Computer methods in applied mechanics and engineering* 192, 227-246.

Wang, X.-T., Wang, B., Wen, Z.-H., Ma, L., 2018a. Fabrication and mechanical properties of CFRP composite three-dimensional double-arrow-head auxetic structures. *Composites Science and Technology* 164, 92-102.

Wang, Y., Arabnejad, S., Tanzer, M., Pasini, D., 2018b. Hip implant design with three-dimensional porous architecture of optimized graded density. *Journal of Mechanical Design* 140, 111406.

Weeger, O., Boddeti, N., Yeung, S.-K., Kaijima, S., Dunn, M.L., 2019. Digital design and nonlinear simulation for additive manufacturing of soft lattice structures. *Additive Manufacturing* 25, 39-49.

Williams, S.W., Martina, F., Addison, A.C., Ding, J., Pardal, G., Colegrove, P., 2016. Wire+ arc additive manufacturing. *Materials Science and Technology* 32, 641-647.

Wohlers, T., Gornet, T., 2014. History of additive manufacturing. *Wohlers report* 24, 118.

Xie, Y.M., Steven, G.P., 1993. A simple evolutionary procedure for structural optimization. *Computers & structures* 49, 885-896.

Xiong, J., Ma, L., Vaziri, A., Yang, J., Wu, L., 2012. Mechanical behavior of carbon fiber composite lattice core sandwich panels fabricated by laser cutting. *Acta Materialia* 60, 5322-5334.

Xiong, J., Ma, L., Wu, L., Wang, B., Vaziri, A., 2010. Fabrication and crushing behavior of low density carbon fiber composite pyramidal truss structures. *Composite Structures* 92, 2695-2702.

Yahiro, A., Masui, T., Yoshida, T., Doi, D., 1991. Development of nonferrous clad plate and sheet by warm rolling with different temperature of materials. *ISIJ international* 31, 647-654.

Yanagimoto, J., Ikeuchi, K., 2012. Sheet forming process of carbon fiber reinforced plastics for lightweight parts. *CIRP annals* 61, 247-250.

Yanagimoto, J., Oya, T., Kawanishi, S., Tiesler, N., Koseki, T., 2010. Enhancement of bending formability of brittle sheet metal in multilayer metallic sheets. *CIRP annals* 59, 287-

290.

Yap, C.Y., Chua, C.K., Dong, Z.L., Liu, Z.H., Zhang, D.Q., Loh, L.E., Sing, S.L., 2015. Review of selective laser melting: Materials and applications. *Applied physics reviews* 2, 041101.

Zhang, H., Yang, D., Sheng, Y., 2018a. Performance-driven 3D printing of continuous curved carbon fibre reinforced polymer composites: A preliminary numerical study. *Composites Part B: Engineering* 151, 256-264.

Zhang, X., Leary, M., Tang, H., Song, T., Qian, M., 2018b. Selective electron beam manufactured Ti-6Al-4V lattice structures for orthopedic implant applications: current status and outstanding challenges. *Current Opinion in Solid State and Materials Science* 22, 75-99.

Zheng, X., Lee, H., Weisgraber, T.H., Shusteff, M., DeOtte, J., Duoss, E.B., Kuntz, J.D., Biener, M.M., Ge, Q., Jackson, J.A., 2014. Ultralight, ultrastiff mechanical metamaterials. *Science* 344, 1373-1377.

Zhou, M., Rozvany, G., 1991. The COC algorithm, Part II: Topological, geometrical and generalized shape optimization. *Computer methods in applied mechanics and engineering* 89, 309-336.

Chapter 2 Shape design and conventional fabrication of formable sandwich sheet

Sandwich structures have had remarkable success in engineering applications, but their applications are mostly limited to flat panel types because of their poor formability. To expand the range of applications of sandwich structures, new metal face/CFRP core sandwich sheets are proposed, where a CFRP core structure is designed to increase formability and structural performance. This chapter first introduces the design methods followed by the fabrication processes and finally reports the flexural properties and formability of the proposed sandwich sheets.

Comprehensively considering the mechanical property, manufacturability and failure resistance ability, a truncated dome core made of carbon fiber reinforced thermoplastics (CFRTP) was determined to be the inner macrostructure of sandwich sheets. The proposed truncated dome core structure was composed of a periodic array of domes which were introduced into an initially flat CFRTP sheet through warm stamping. The numerical investigation shows that the optimal relative density of the truncated dome core is 0.22 in terms of comprehensive consideration of bending stiffness, shear modulus and face buckling degree. The optimal forming conditions of CFRTP sheet were investigated prior to the continuous fabrication process of long CFRTP core by piecewise sectional forming technology. The flexural properties were tested by three-point bending, and formability of sandwich sheets was evaluated experimentally by cold and warm L-bending and draw-bending tests. The results indicate that the sandwich sheets composed of metallic face sheets and CFRTP core have better formability when cold formed, while the sandwich sheets composed of CFRTP face sheets and CFRTP cores have superior formability when warm formed. The development of formable metal face/CFRP core sandwich sheets is expected to expand the application range of sandwich structures and promote the use of lightweight parts in engineering fields.

2.1 Research background and literature review

The demand for the development of lightweight components without sacrificing structural performance has been increasing to decrease greenhouse gas emissions and energy consumption. Advanced high-strength steels are commonly used to produce lightweight components for automobiles because of their higher specific strength than conventional steels. However, advanced high-strength steels cannot meet the lightweight requirement when applied to stiffness-critical parts owing to their same stiffness as that of conventional steels. Sandwich sheets composed of stiff face sheets and a three-dimensional porous core can provide lightweight alternatives to conventional monolithic metallic components owing to their superior specific stiffness and strength. Sandwich panels consisting of CFRP face sheets and aluminum or Nomex honeycomb cores have realized commercial production and been widely used in aerospace applications, as reviewed by [Vasiliev et al. \(2012\)](#). The combination of GFRP face sheets with a closed-cell foam or open-cell foam core is a typical option in civil and marine structures, as summarized by [Birman and Kardomateas \(2018\)](#). It has been reported by [Möhring et al. \(2015\)](#) that a weight by 40% of laser cutting and high-speed milling machines can be reduced by replacing the aluminum designs with sandwich panels containing tubular and grid-shaped core structures.

Low production efficiency is the first problem limiting commercial application of sandwich structures. The production of sandwich panels is complicated and involves multiple fabrication steps, making it very difficult to realize mass production. An extrusion and electro discharge (EDM) method was employed to fabricate an A6061 aluminum alloy pyramidal lattice core as proposed by [Queheillalt et al. \(2008\)](#). A CFRP pyramidal truss core was fabricated by compression molding into a corrugated structure followed by laser cutting as described by [Xiong et al. \(2012\)](#). A high-strength woven wire core was fabricated by [\(Kang, 2009\)](#), where Cr-Si spring steel wires were assembled into woven wire structures and then brazed together using brass brazing paste. As reported by [George et al. \(2014\)](#), an assembled carbon fiber lattice with inserted foams was stitched together using Kevlar fibers and then the whole structure was infused with an epoxy resin and cured to obtain a hybrid core. It is obvious

that these manufacturing processes are labor-intensive and time-consuming, thus not suitable for mass production. The second problem is that most sandwich panels cannot be secondarily formed into three-dimensional shapes by conventional sheet forming methods such as stamping or drawing, limiting their applications to flat panel shapes. At present, sandwich sheets with relatively good formability are limited to those with a two-dimensional core, such as a polyethylene or aluminum foam core. The formability of sandwich sheets consisting of AA5052 skin and a two-dimensional polyethylene core was evaluated by [Liu et al. \(2013\)](#) and found to be better than that of monolithic AA5052 sheet. Three-dimensional sandwich shells containing aluminum foam cores have been successfully produced by incremental sheet forming (ISF) proposed by [Jackson et al. \(2008\)](#). Gas pressure forming of sandwich sheets with an aluminum foam core was experimentally and numerically investigated by [Nassar et al. \(2012\)](#) and indicated that forming these sandwich panels to three-dimensional shapes while maintaining considerable core porosity was possible. However, secondary forming of sandwich sheets with a three-dimensional core remains a challenge and few relevant studies have been reported. The bendability of sandwich sheets containing a pyramidal truss core and a woven wire core were investigated by [Ahn \(2015\)](#) and [Dilthey et al. \(2001\)](#), respectively, and found they can be bent to only a very limited curvature.

Development of sandwich sheets that can be efficiently produced and secondarily formed into three-dimensional shapes is a key issue to expand the usage of sandwich sheets for ultra-lightweight structures. A dimple core which can be fabricated by fast stamping was designed by [Seong et al. \(2008\)](#) and its bendable curvature was improved compared to the pyramidal truss or woven wire structure. The effects on forming behaviors of thin sandwich sheets were investigated by [Mohr \(2005\)](#) and found that a good inner macrostructure for a bendable sandwich sheet is mainly characterized by its core shear strength. Following this principle, the sheared dimple and bidirectional dome structures were designed by [Seong et al. \(2010\)](#) and [Besse and Mohr \(2012\)](#), respectively, and verified that sandwich sheets with these two types of cores can be successfully bent to a large curvature without failure. However, these sandwich sheets are made of full metallic materials, thus leading to limited specific strength and stiffness. To improve these properties, a metal-based sandwich sheet, in which thin metallic face sheets

such as aluminum alloy (A2017P) or stainless steel (SUS304) were used to sandwich and bond with a three-dimensional CFRTP core, is proposed here. The inner core structure will firstly be designed to satisfy the requirement of high productivity, excellent mechanical performance and good formability. As the inner macrostructure is made of CFRTP, of which ductility can be expected to be improved at elevated temperatures, warm forming could be promising to suppress failure modes commonly encountered during cold forming. Since warm forming behaviors of such sandwich sheet have never been reported, warm forming characteristics of such metal-based sandwich sheets will be investigated by a series of forming tests. To demonstrate the feasibility of effective design and efficient production of lightweight sandwich sheets with superior mechanical property, high productivity and good formability, it is essential to investigate the mechanical property and formability of such metal face/CFRP core sandwich sheets through a complete design-fabrication-evaluation chain.

2.2 Basic knowledge about failure characteristics of sandwich sheets

2.2.1 Failure modes of sandwich structure

The formability of sandwich sheet is highly related to several kinds of potential failure modes. In addition to commonly observed sheet metal forming limits such as sheet fracture and wrinkling, several sandwich-specific failure modes are likely to restrict the formability of sandwich sheets. Following listed failure modes are main failure modes requiring special attention in sandwich sheet forming.

1. core-face sheet delamination

For most sandwich structures, face sheet is commonly glued or welded on to core material. The effective bonding strength is typically lower than yield strength of base materials. In some forming processes, tremendous shear stresses need to be transmitted between face sheet and core and thus, the core-face sheet bonding interfaces break before the base material reaches its yield strength. [Figure 2-1\(a\)](#) illustrates the core-face sheet delamination.

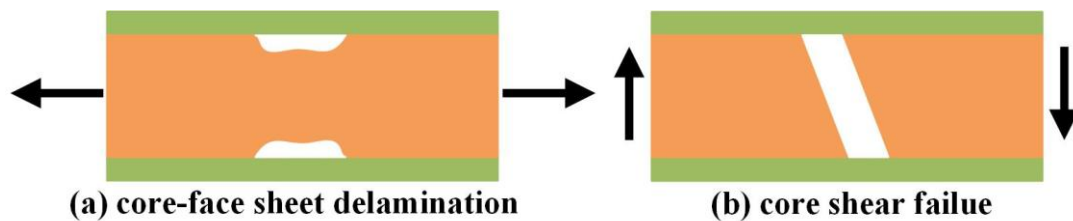


[Figure 2-1](#). (a) Delamination; (b) Core shear failure

2. core shear failure

High transverse shear load induced in forming processes may cause core shear failure. In addition to shear, compressive stresses along thickness-direction accumulated as the sheet curvature is changed. The imposed compressive stresses increase the shear resistance of the core-face sheet bonding interface, but they may weaken the shear strength of the core material. Therefore, sufficient core shear strength is required to prevent core shear failure. [Figure 2-1\(b\)](#) shows the core shear failure caused by excessive transverse shear load.

3. face sheet fracture

Face sheet fracture typically occur where strong core materials and small bending radius are adopted. The strains of the outer skins of the sandwich structure and the strains of the

homogenous plate of the same thickness are in one order of magnitude. A suitable bending radius should be selected to avoid face fracture. Face fracture is illustrated by Figure 2-2(a).

4. face sheet buckling

Face sheet needs sufficient support from core material to prevent local buckling and large out-of-plane deflection. The maximum compressive stress should be smaller than its buckling strength to prevent face buckling. Figure 2-2(b) shows the face sheet indentation.

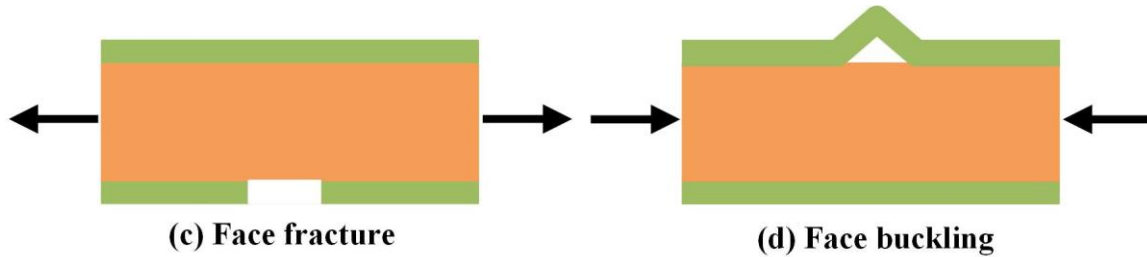


Figure 2-2. (a) Face fracture; (b) Face buckling

2.2.2 Failure constraints

As illustrated in Figure 2-3, failure modes such as core shear failure, face buckling, face fracture and delamination limit the formability of sandwich sheets. Core shear failure is generally caused by insufficient core shear strength, especially for a low-density hollow core. To suppress core shear failure, sufficient core shear strength should be ensured, that is, the core shear strength should be greater than the required core shear strength as expressed by:

$$\tau_c > \tau_{re} \quad (2-1)$$

where τ_c and τ_{re} are core shear strength and the required core shear strength, respectively.

Consider the bending model presented in Figure 2-4. Supposing that the sandwich sheet undergoes stable bending and unbending deformation without consideration of friction effect between forming tool and the specimen. The subscripts ‘ u ’ and ‘ l ’ represent the quantities associated with the upper and lower face sheets while superscripts ‘ b ’ and ‘ ub ’ denote those involved in bending and unbending, respectively. During bending, the upper face sheet of initial length S_0 is stretched to S_u^b and the lower face sheet is compressed to S_l^b . During bending, the kinematical constraint is:

$$\frac{S_u^b}{S_l^b} = 1 + \varepsilon^* \quad (2-2)$$

where ε^* is defined by:

$$\varepsilon^* = (2h_c + 2t_f) / (2R + t_f) \quad (2-3)$$

in which R is the predefined bending radius, and h_c and t_f are geometrical parameters of sandwich sheets as illustrated in [Figure 2-4](#).

Similarly, when the sandwich sheet undergoes unbending, S_u^b and S_l^b are respectively changed to S_u^{ub} and S_l^{ub} , and the following kinematical constraint should be satisfied:

$$\frac{S_u^b}{S_l^b} \frac{S_l^{ub}}{S_u^{ub}} = 1 + \varepsilon^* \quad (2-4)$$

Assuming that the length of the mid-plane remains unchanged during bending:

$$\frac{S_u^b + S_l^b}{2} = S_0 \quad (2-5)$$

and

$$S_l^{ub} = S_u^{ub} = S_0 \quad (2-6)$$

So from [Eqs. \(2-2\)](#) and [\(2-5\)](#), the following equations can be deduced:

$$\frac{S_u^b}{S_0} = 1 + \frac{\varepsilon^*}{2 + \varepsilon^*} \quad (2-7)$$

and

$$\frac{S_l^b}{S_0} = 1 - \frac{\varepsilon^*}{2 + \varepsilon^*} \quad (2-8)$$

If the logarithmic strains are adopted, the tensile strain in the upper face sheet is

$$\varepsilon_u^b = \ln\left(1 + \frac{\varepsilon^*}{2 + \varepsilon^*}\right) \geq 0 \quad (2-9)$$

and the compressive strain in the bottom face sheet is

$$\varepsilon_l^b = \ln\left(1 - \frac{\varepsilon^*}{2 + \varepsilon^*}\right) \leq 0 \quad (2-10)$$

Since the face sheets can be considered to be membranes, at a constant loading speed of α , the internal dissipation rate ψ in the face sheet is:

$$\psi = 2t_f \alpha \left\{ \int_0^{2|\varepsilon_u^b|} \sigma d\varepsilon + \int_0^{2|\varepsilon_l^b|} \sigma d\varepsilon \right\} \quad (2-11)$$

Assuming that face sheets have a yield strength and hardening modulus of σ_f and E_T , the ψ becomes:

$$\psi = 4t_f \alpha \sigma_f \left\{ (\varepsilon_u^b - \varepsilon_l^b) + \frac{E_T}{\sigma_f} [(\varepsilon_u^b)^2 + (\varepsilon_l^b)^2] \right\} \quad (2-12)$$

The rate of external work W_{ex} can be calculated by multiplying the punch force P and punch velocity α :

$$W_{ex} = P\alpha \quad (2-13)$$

Since Eq. (2-12) should be equal to Eq. (2-13), reaction force P of punch is determined as:

$$P = 4t_f \sigma_f \left\{ (\varepsilon_u^b - \varepsilon_l^b) + \frac{E_T}{\sigma_f} [(\varepsilon_u^b)^2 + (\varepsilon_l^b)^2] \right\} \quad (2-14)$$

With punch force, the maximum average core shear stress is calculated as

$$\tau_{re} = P / (2h_c) = 2t_f / h_c \left\{ \sigma_f (\varepsilon_u^b - \varepsilon_l^b) + E_T [(\varepsilon_u^b)^2 + (\varepsilon_l^b)^2] \right\} \quad (2-15)$$

Then the critical value of core shear strength required for bendable sandwich sheets is approximately expressed by Eq. (2-15).

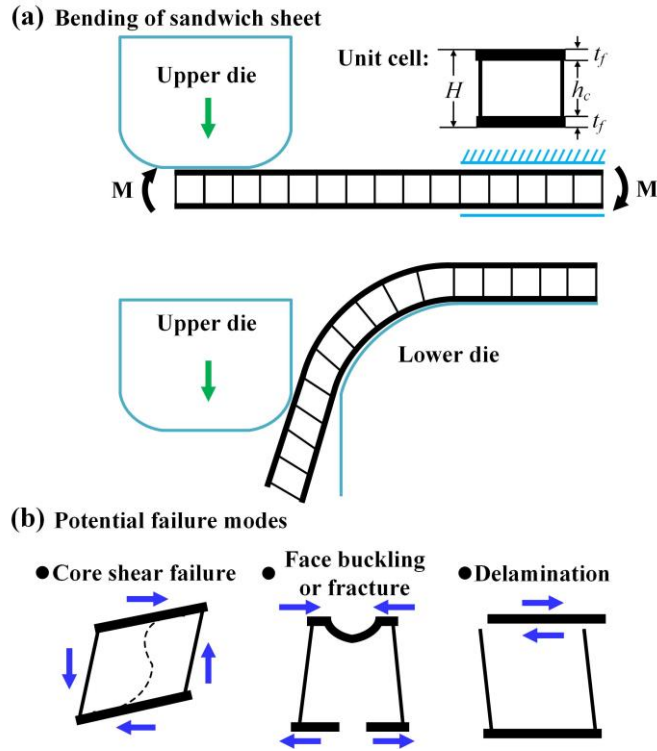


Figure 2-3. Illustration of potential failure modes of sandwich sheets during bending.

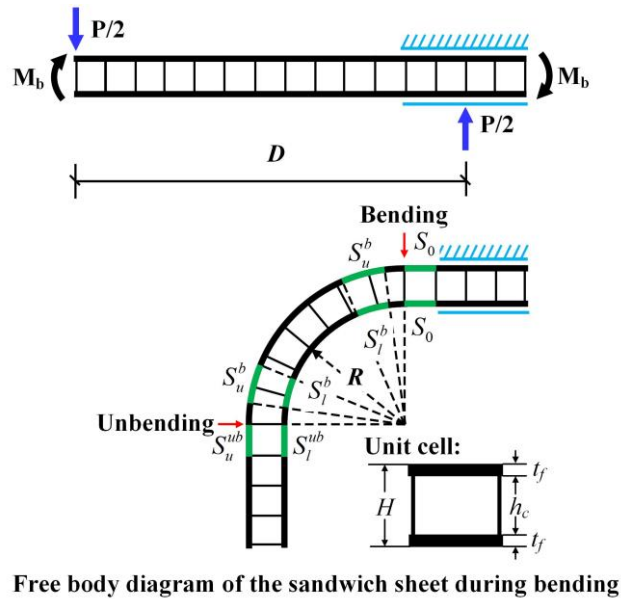


Figure 2-4. Free body diagram of sandwich sheets during bending.

2.3 Structures and materials

2.3.1 Selection of core structure

The development of sandwich sheets that can be formed into three-dimensional shapes using conventional sheet metal forming methods could be the key to expanding the range of applications of sandwich structures. One of the candidates of the core is the bidirectionally corrugated core designed by Yanagimoto et al. (2016). A metallic sandwich plate with a pyramidal truss core or woven wire core can be bent with a small curvature and applied to products with a shallow drawing depth, while the forming depth of a dimple core sandwich sheet is larger than that of one with a pyramidal truss core or woven wire core. Sandwich sheets with a sheared dimple core or bidirectional dome core can be bent without failure. The fabrication process of a sandwich sheet with a pyramidal truss core involves cutting, die punching, crimping and brazing, while sandwich sheets with dimple cores and sheared dimple cores are fabricated by sectional forming and brazing. A sandwich sheet with a woven wire core is produced by wire forming, weaving and brazing. The fabrication of a sandwich sheet with a bidirectional dome core requires sectional forming, joining of dome layers then bonding with the face sheet. The aforementioned sandwich structures are characterized on a two-dimensional plane with the relative bendable radius and relative density as the axes as summarized in Figure 2-5. Here, R is the bendable radius, H is the thickness of sandwich sheet, h is the core height and t is the thickness of core material. The degree of fabrication complexity is in terms of the number of fabrication steps and production efficiency.

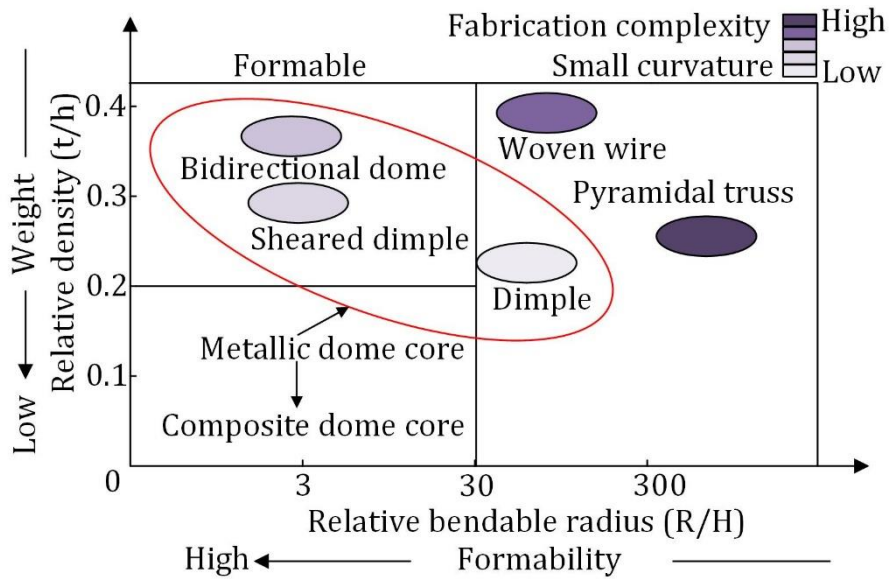
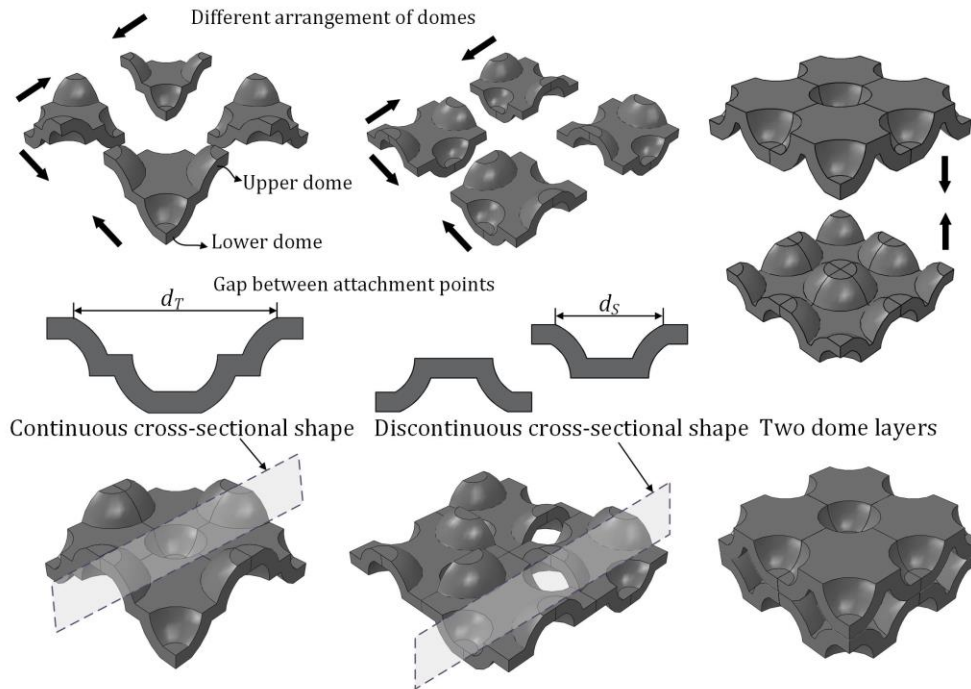


Figure 2-5. Metallic core sandwich sheets characterized in two-dimensional plane with ‘relative bendable radius’ and ‘relative density’ axes.

From Figure 2-5, several important findings can be deduced: (1) formable metallic cores with a relative density below 0.2 remain to be explored; (2) sandwich sheets with a domelike core such as those with a sheared dimple core and bidirectional dome core exhibit good formability; (3) the fabrication complexity of the domelike core is relatively low. The use of composites with high specific strength and stiffness, particularly CFRP (carbon fibre reinforced plastic), to produce inner core structures will contribute to superior structural performance, thereby meeting the demand for formable cores with low relative densities. Therefore, replacing metallic dome cores with CFRP dome cores can markedly expand the range of applications of sandwich sheets and improve the structural performance of components. However, no studies on the development of formable CFRP core sandwich sheets have been conducted. A sheared dimple core is extremely difficult to fabricate using CFRP owing to its discontinuous cross-sectional shape. A bidirectional dome core requires additional joining of dome layers, thus making it difficult to manufacture. Here, we propose a truncated dome core where the upper and lower domes are repeatedly and alternately arranged, which is conceptually similar to an egg-box structure. In contrast to the egg-box structure, the contact areas between core and face sheets are expanded to flat round faces, thus decreasing the gap between attachment points, reducing the risk of delamination and face buckling in the forming

process. Moreover, the truncated dome core can be simply produced by the press forming of CFRTP, thus reducing the fabrication complexity. This chapter describes design methods and fabrication processes for a truncated dome core made of CFRTP and presents the results of flexural properties and formability tests.

Inspired by the sheared dimple core and bidirectional dome core, a truncated dome core has been proposed as shown in [Figure 2-6](#), where the section of the hemispherical shell yields a stable shear response for the cores. In contrast to the sheared dimple core, a continuous cross-sectional shape is achieved by changing the arrangement of the domes for the truncated dome core, which makes it possible to produce by stamping of CFRTP. Moreover, the truncated dome core comprising of single dome layer can be simply fabricated without additional joining compared with the bidirectional dome core, greatly reducing the fabrication complexity. However, since the out-of-plane shear strength of CFRTP is generally lower than that of metallic materials, the truncated dome core made of CFRTP has a relatively lower resistance of shear fracture, which may cause core shear failure. Moreover, the dome arrangement of the truncated dome core increases the gap between attachment points compared with the sheared dimple core and bidirectional dome core, as shown in [Figure 2-6](#), where d_T is greater than d_S , resulting in a higher risk of face buckling.

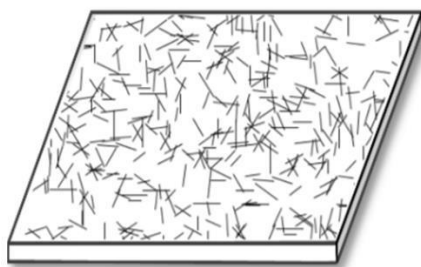


(a) Truncated dome core (b) Sheared dimple core (c) Bidirectional dome core

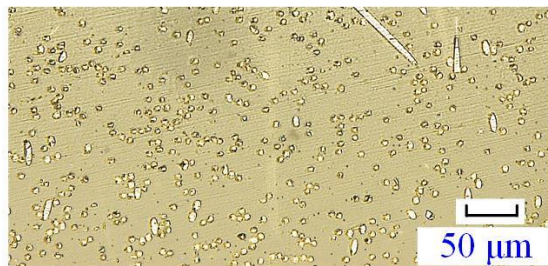
Figure 2-6. Geometrical characteristics of dome-like structures.

2.3.2 Materials

PA6 composite sheet with carbon fiber volume fraction of 14% is used to fabricate proposed dome core structure. The thickness of CFRTP sheet is 1mm. Short carbon fiber is randomly dispersed in polyamide 6 resin matrix as shown in Figure 2-7, thus isotropic mechanical properties is displayed. The CF-PA6 is supplied by Toray Plastics Precision Co.,Ltd. The 0.3-mm-thick stainless steel (SUS304), 0.5-mm-thick aluminium alloy (A2017P) and 1-mm-thick CFRTP were used as face sheets. The mechanical properties of SUS304, A2017P and CFRTP are shown in Table 2-1.



(a) Illustration of CFRTP



(b) Cross-sections of CFRTP

Figure 2-7. Short carbon fiber reinforced thermoplastic.

Table 2-1. Mechanical properties of A2017P, SUS304 and CFRTP.

	Young's modulus (GPa)	Poisson's ratio	Yield strength (MPa)	Tensile strength (MPa)	Linear hardening modulus (GPa)
A2017P	70	0.33	250	390	1.5
SUS304	200	0.29	215	560	2.3
CFRTP	13.5	0.35	135	196	2.1

2.4 Determination of optimal structural parameters

2.4.1 Evaluation of core shear strength

As shown in Figure 2-8, the truncated hemispherical dome core is composed of repeated alternately arranged truncated hemispherical dome. The radius of contact area between face sheet and core is denoted as R_0 , radiuses of lower and upper dome are denoted as R_1 and R_2 , respectively. Thicknesses of face sheet and core material are t_f and t_c , respectively. The relative density describes the ratio of the overall mass density of the core structure to the density of the basis sheet material. Assuming that the basis sheet material is incompressible, the relative density of the core structure is given by

$$\rho = \frac{t_c}{h_c} = \frac{t_c}{2\sqrt{R^2 - R_0^2} + t_c} \quad (2-16)$$

The core shear strength is approximately predicted by assuming that the area of the shear fracture is composed of two quarter-rings for repeated unit cell as shown in Figure 2-8 (b).

Thus, the core shear strength can be expressed by following equation:

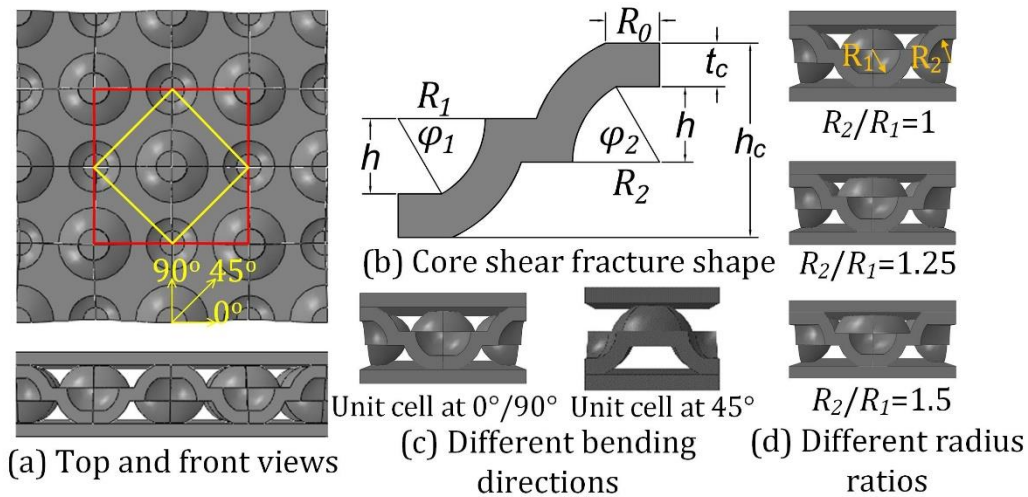


Figure 2-8. Schematics of truncated dome core and repeated unit cell

$$\tau_c = \tau_T \cdot t_c \left[R_0 + \sqrt{R_2^2 - (R_1^2 - R_0^2)} + R_1\varphi_1 + R_2\varphi_2 \right] / h_c / (R_1 + R_2 + 2t_c) \quad (2-17)$$

$$\varphi_1 = \arccos(R_0 / R_1) \quad (2-18a)$$

$$\varphi_2 = \arccos \left[\sqrt{R_2^2 - (R_1^2 - R_0^2)} / R_2 \right] \quad (2-18b)$$

$$h_c = 2\sqrt{R_1^2 - R_0^2} + t_c \quad (2-18c)$$

Where τ_T is the shear strength of core material, h_c is the core height.

For different face sheet materials, combining Eq. (2-15)-(2-18c), the effect of bending radius and dome radius on the ratio of τ_c to τ_{re} is shown in Figure 2-9. Here, R_0 was set to 1.24 mm and R_l equals R_2 . Two bending radii 20 mm and 30 mm were chosen. Figure 2-9 shows that only when the bending radius is 30 mm and the dome radius is 2 mm can the constraint that τ_c is greater than τ_{re} be satisfied for all three types of face sheets. Thus, the structural parameters were set as shown in Table 2-2 to prevent core shear failure under constraint of Eq. (2-1).

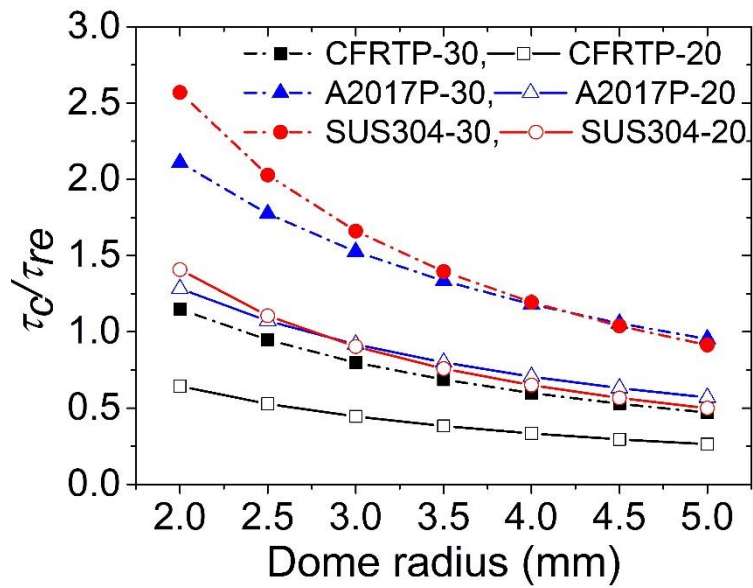


Figure 2-9. The effects of the bending radius and the dome radius on the ratio of τ_c to τ_{re} .

Table 2-2 Structural parameters in design

Required core shear strength		Core shear strength	
R (mm)	30	R_0 (mm)	1.24
h_c (mm)	4.5	R_l (mm)	2
t_f (mm)	0.3/0.5/1	R_2 (mm)	2
A2017P- τ_{re} (MPa)	12.4	t_c (mm)	1

SUS304- τ_{re} (MPa)	19.1	τ_T (MPa)	113.2
CFRTP- τ_{re} (MPa)	22.8	τ_c (MPa)	26.1

2.4.2 Evaluation of bending stiffness by CAE

To find optimal structure parameters with the highest bending stiffness, pure bending analysis of sandwich sheet with different core structural parameters are conducted. Since core structure is composed of repeated unit cell, the analysis of repeated unit cell can be more efficient and accurate. Therefore, to evaluate bending stiffness more efficiently and accurately, periodic boundary conditions (PBCs) are adopted to conduct pure bending analysis. The periodic boundary conditions for pure bending are deduced as presented in the [Appendix A](#), in which the details codes of the MPC user subroutine for the implementation has also been included in the [Appendix B](#).

As shown in [Figure 2-8](#) (d), bending stiffness of unit cells with different radius ratios between R_1 and R_2 are evaluated. To investigate radius ratio effect on bending stiffness, three different ratios 1, 1.25, and 1.5 are chosen, namely, R_1 is set as 2 mm while R_2 is set as 2 mm, 2.5 mm and 3 mm respectively. Besides, bending directions can be different as shown in [Figure 2-8](#) (c). Bending direction effect on bending stiffness is investigated when bending in orientation of $0^\circ/90^\circ$ and 45° to the dome core's principal axes. When bending at 0° and 90° , the same unit cell can be picked, therefore, bending at 0° and 90° have the same bending behavior. The unit cell picked for bending at 0° and 90° is shown in the red block in [Figure 2-8](#) (c), while the unit cell in the yellow block is for bending analysis in orientation of 45° .

The specific bending moment-curvature curves at different radius ratios and different bending directions are shown in [Figure 2-10](#). With increase of radius ratio, specific bending moment displays a decrease trend. Anisotropic bending behavior is presented as specific bending moment at 45° is larger than that of $0^\circ/90^\circ$. Bending stiffness are calculated for models at different radius ratios and different bending directions as shown in [Table 2-3](#). Highest specific bending stiffness appears when radius ratio is 1 and bending at 45° .

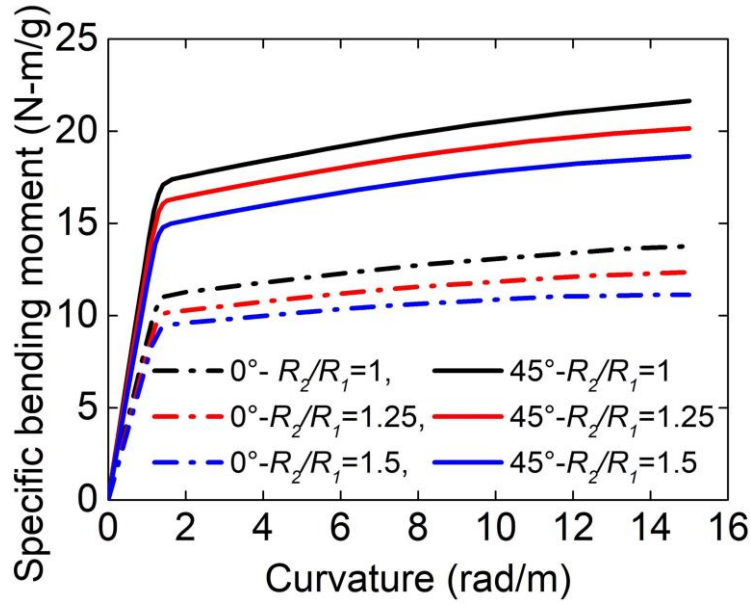


Figure 2-10. Bending moment-curvature curves at different radius ratios and different bending directions.

Table 2-3. Bending stiffness at different radius ratios and bending directions.

Model	0°-1	0°-1.25	0°-1.5	45°-1	45°-1.25	45°-1.5
Stiffness(N-m ² /g)	8.64	7.91	7.44	13.46	12.65	11.68

2.4.3 Evaluation of face buckling degree and shear modulus

Structural characteristics such as the degree of face buckling and shear modulus with respect to the relative density were evaluated by CAE. On the basis of the comprehensive evaluation of the degree of face buckling and shear modulus, the optimal relative density was determined. Here, R_0 was fixed as 1 mm to maintain the same contact area between the core and the face sheet. Six different relative densities, ranging from 0.15 to 0.325, were selected and the corresponding dome radii calculated using Eq. (2-16) are shown in Table 2-4. To evaluate the degree of face buckling, periodic boundary conditions for pure bending given in the Appendix A were applied to the repeated unit cell, as shown in Figure 2-11, to represent a full model.

Table 2-4. Relative densities and corresponding dome radii.

Relative density	0.15	0.185	0.22	0.255	0.29	0.325
------------------	------	-------	------	-------	------	-------

Dome radius R (mm)	3	2.4	2	1.77	1.58	1.44
----------------------	---	-----	---	------	------	------

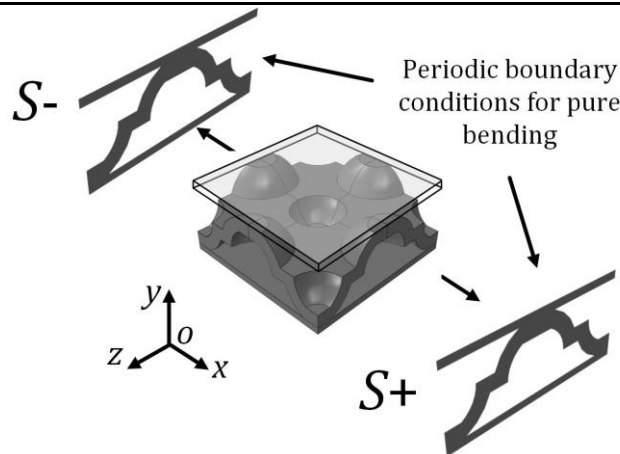


Figure 2-11. Illustration of the implementation of periodic boundary conditions for pure bending.

The shear modulus of sandwich sheets with different relative densities was examined by pure shear analysis. The repeated unit cell used in the pure shear analysis was the same as that in the pure bending analysis, the boundary conditions for the pure shear analysis are illustrated in Figure 2-12. The displacements of the node on the left boundary surface in the yoz plane were the same as those of the corresponding node with the same y and z coordinates on the right boundary plane to maintain the periodicity of the structure in the x direction. A uniform displacement u_X in the x direction was applied to all the nodes on the top boundary surface in the xoz plane, while it was set to zero for the bottom boundary plane. The displacement in the y direction was set to zero for both the top and bottom boundary planes.

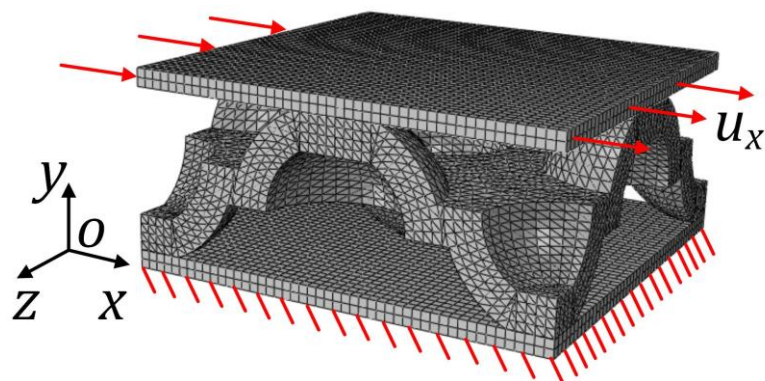


Figure 2-12. Illustration of boundary conditions for the pure shear analysis.

The specific shear modulus G_{xy} was determined from the slope of the computed linear relationship between the shear force F_X and the shear displacement u_X in the x direction as:

$$G_{xy} = \frac{1}{m} \left(\frac{dF_L}{du_L} \right) \frac{h_c}{D^2} \quad (2-19)$$

where D is the side length of the unit cell.

The pure bending and shear analyses were conducted using ABAQUS standard codes. Reduced integration eight-node (C3D8R) and linear four-node tetrahedron (C3D4) elements were used to mesh the A2017P face sheet and CFRTP core, respectively. A tie contact model was used to bond the CFRTP core with the A2017P face sheet, namely, the slip at the CFRTP/metal interface was assumed to be zero. The thicknesses of the face sheet and core material were set to 0.5 mm and 1 mm, respectively.

For a bending curvature of 0.002 rad/mm, the pure bending deformation contours of sandwich sheets with different relative densities are shown in [Figure 2-13 \(a\)](#). The shape of the face sheet in the yz plane after buckling is plotted in the form of y and z coordinates in [Figure 2-13 \(c\)](#), which indicates that the face buckling height (h_b) increases as the relative density decreases. The degree of face buckling is defined as the ratio of the face buckling height (h_b) to the gap between attachment points (d_p) along the z direction, as shown in [Figure 2-13 \(b\)](#). The degree of face buckling for different relative densities is shown in [Figure 2-13 \(c\)](#), where the degree of face buckling decreases with increasing relative density.

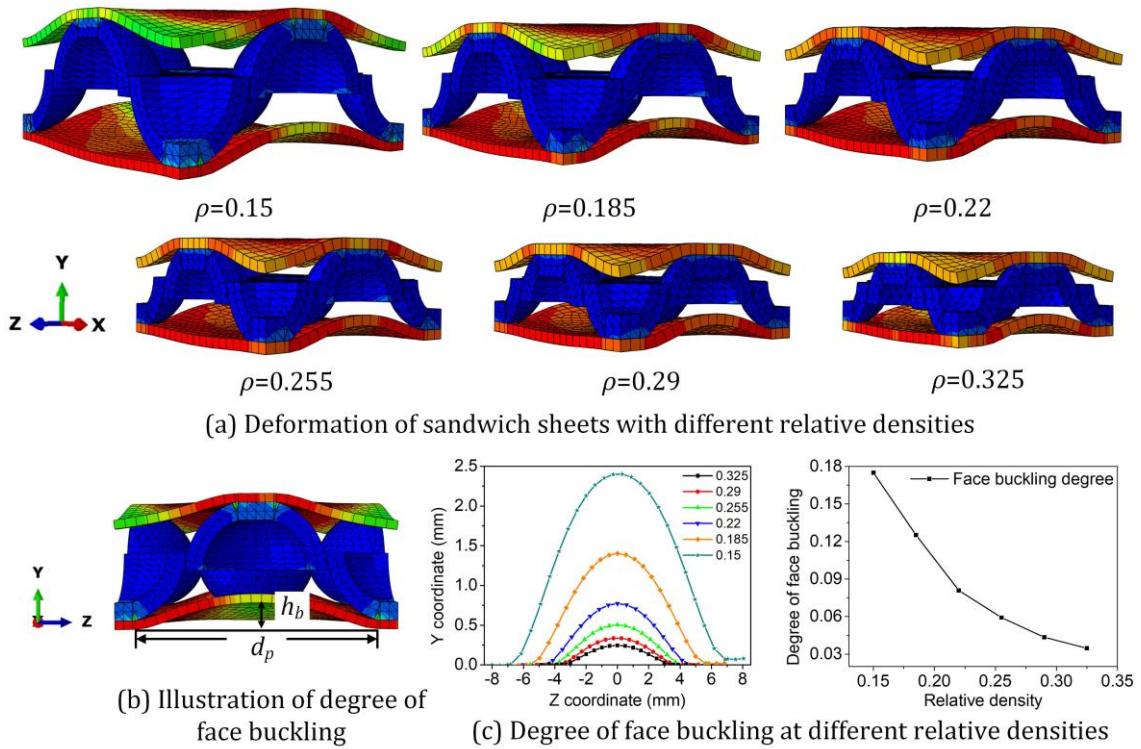


Figure 2-13. Pure bending deformation and face buckling of sandwich sheets with different relative densities.

The calculated specific shear moduli and bending stiffness of sandwich sheets with different relative densities are shown in Figure 2-14, which indicates that the specific shear modulus increases while the bending stiffness decreases with the relative density. The comprehensive evaluation of the degree of face buckling and specific shear modulus illustrates that a higher relative density contributes to a lower degree of face buckling and a higher specific shear modulus but causes a lower specific bending stiffness. Recall that face buckling decreases the bending moment when the relative density is lower than 0.22, as shown in Figure 2-14 (a), the optimal relative density is considered to be 0.22 on the basis of the comprehensive trade-off between the degree of face buckling, specific bending stiffness and shear modulus. Thus, the corresponding dome radius is 2 mm and the structural parameters are listed in Table 2-5.

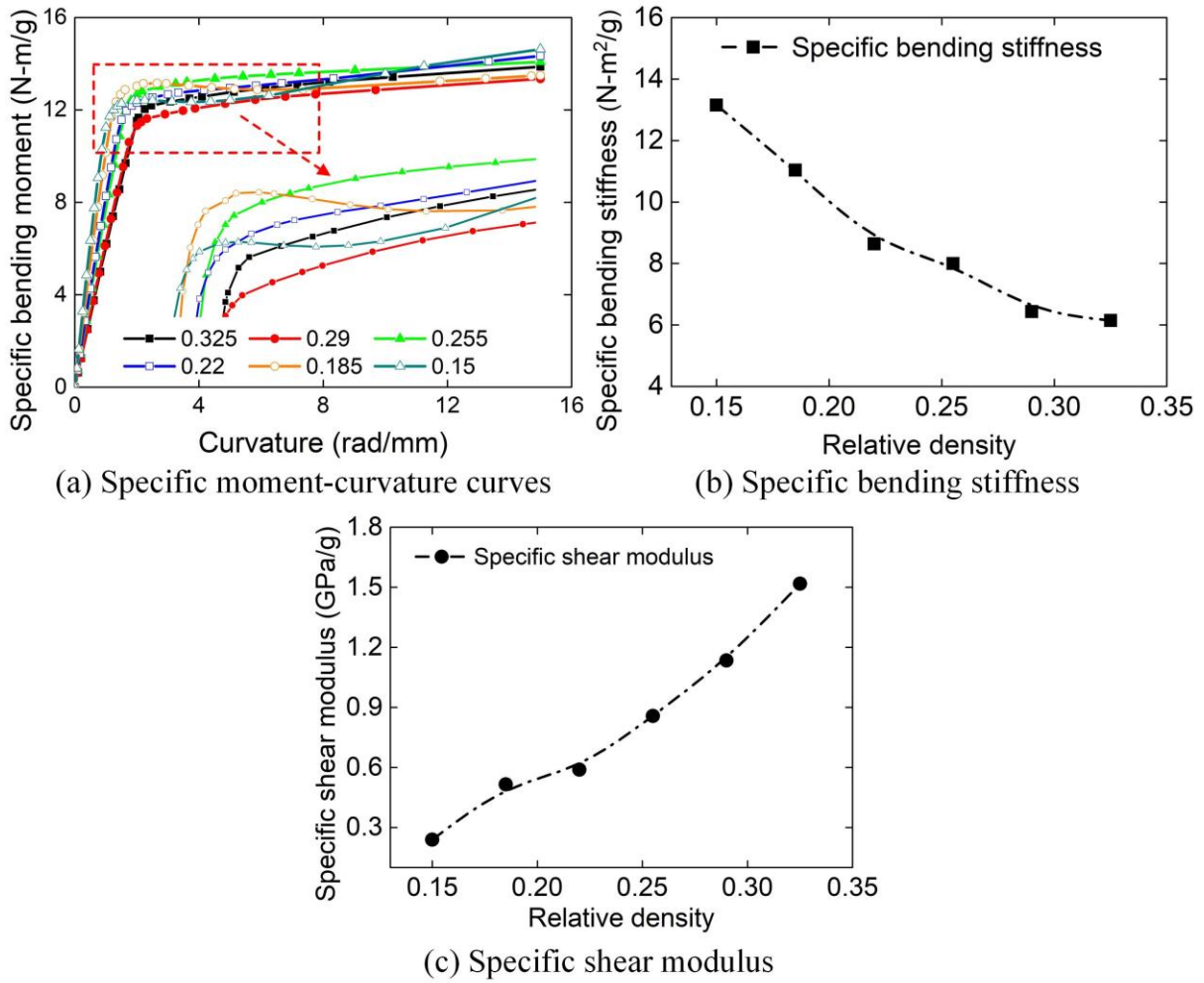


Figure 2-14. Specific shear modulus and bending stiffness with the relative density.

Table 2-5. Optimal structural parameters in design.

Structural Parameter	R	R_0	t_c	h	h_c
Value (mm)	2	1	1	1.75	4.5

2.4.4 Comparison of mechanical properties of various types of core structures

The specific bending stiffness and shear modulus of sandwich sheets with different core types such as the conventional flat core, sheared dimple core, bidirectional dome core, bidirectionally corrugated core and truncated dome core were investigated and the results are shown in Figure 2-15. For consistency with the designed structural parameters of the truncated dome core, the dome inner and outer radii for each core type were set to 2 mm and 3 mm, respectively.

The specific bending stiffness and shear modulus of the sandwich sheet with the truncated dome core are greater than those of the sandwich sheets with the flat core, sheared dimple core and bidirectionally corrugated core. The specific bending stiffness and shear modulus of the sandwich sheet with the truncated dome core are 5 and 2 times larger than those of the sandwich sheet with the flat core, respectively, which proves the structural superiority of the sandwich sheet with the truncated dome core. Although the sandwich sheet with the bidirectional dome core possesses the highest specific bending stiffness and shear modulus, its fabrication involves an additional process to join the two dome layers, thus making it extremely difficult to manufacture. From the comprehensive perspectives of specific bending stiffness, shear modulus and fabrication feasibility, the sandwich sheet with the truncated dome core may be the best option.

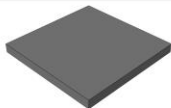
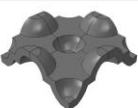
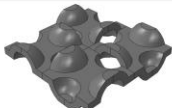
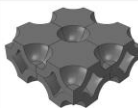


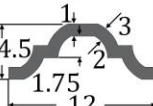
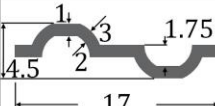


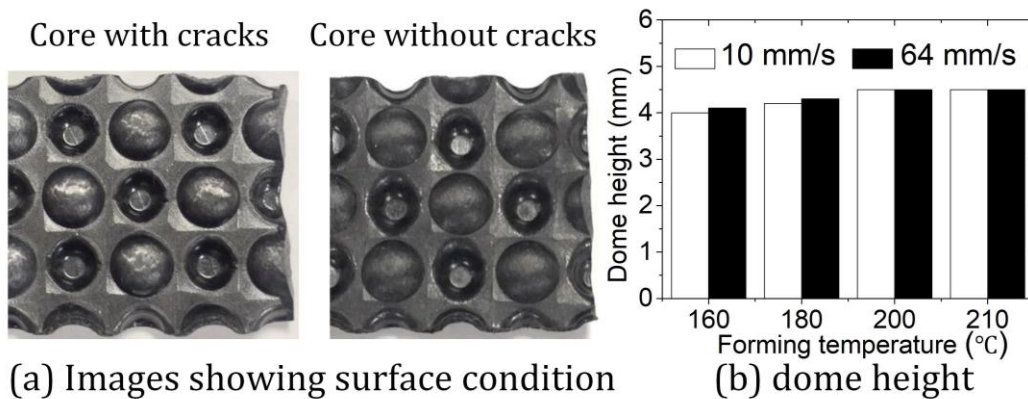
	Flat core	Truncated dome core	Sheared dimple core	Bidirectional dome core	Bidirectionally corrugated core
Core type					
Structural parameter (mm)					
Specific bending stiffness (N-m ² /g)	1.702	8.644	4.111	11.081	6.167
Specific shear modulus (GPa/g)	0.295	0.589	0.246	0.900	0.536

Figure 2-15. Comparison of mechanical properties of sandwich sheets with different types of core structures.

2.5 Production of sandwich sheets

2.5.1 Optimal forming conditions of CFRTP

The designed truncated dome core was fabricated by press forming of CFRTP sheet using a servo press machine (H1F110, Komatsu, Japan). It has been reported by [Rao et al. \(2011\)](#) that short fiber reinforced composites can be successfully formed within a forming window ranging from recrystallization temperature to melting point. Here, the optimal forming window was found by incrementally increasing forming temperature. At each forming temperature, two press forming speeds, 10 mm/s and 64 mm/s, were utilized. After each stamping, the core height was measured and the surface condition was examined. The experimental conditions and results are shown in [Figure 2-16](#). The dome height increases with forming temperature owing to improved formability of CFRTP. When forming temperature exceeds 210°C, CFRTP is partially melted and adheres to the dies, thus, the dome core structure cannot be maintained. Therefore, suitable forming temperature range is from 200°C to 210°C. However, surface cracks cannot be avoided using single-stroke stamping.



[Figure 2-16](#). Surface condition observation and dome height measurements.

To eliminate surface cracks, multi stroke stamping reported by [Osakada et al. \(2011\)](#) to improve formability of metal sheets, was adopted. After each trial, the number of cracked domes was recorded. The experimental conditions and results are shown in [Table 2-6](#). The number of cracked domes decreases when a lower forming speed and longer holding time are employed in the first stroke. Surface cracks are eliminated as shown in [Figure 2-16 \(a\)](#). The

optimal forming conditions when surface cracks are entirely eliminated are chosen as the forming parameters to fabricate the core structure.

Table 2-6. Multi stroke press forming conditions and results.

Total stroke (mm)	Stroke 1-2 (mm)	Speed 1-2 (mm/s)	Holding time 1-2 (s)	Number of cracks out of 15
3.5	2.3-1.2	64-64	5-10	9
3.5	2.3-1.2	32-64	5-10	6
3.5	2.3-1.2	10-64	5-10	5
3.5	2.3-1.2	64-64	10-10	5
3.5	2.3-1.2	32-64	10-10	2
3.5	2.3-1.2	10-64	10-10	0

2.5.2. Piecewise sectional forming and bonding

Piecewise sectional forming was employed to fabricate truncated dome cores with the desired dimensions. A gage with the same shape as the forming part was used to control the position of specimen in each forming step as shown in Figure 2-17. The effective forming area was 24 mm × 24 mm. The dimensions of fabricated truncated dome core were 24 mm (width) × 144/240 mm (length) × 4.5 mm (height).

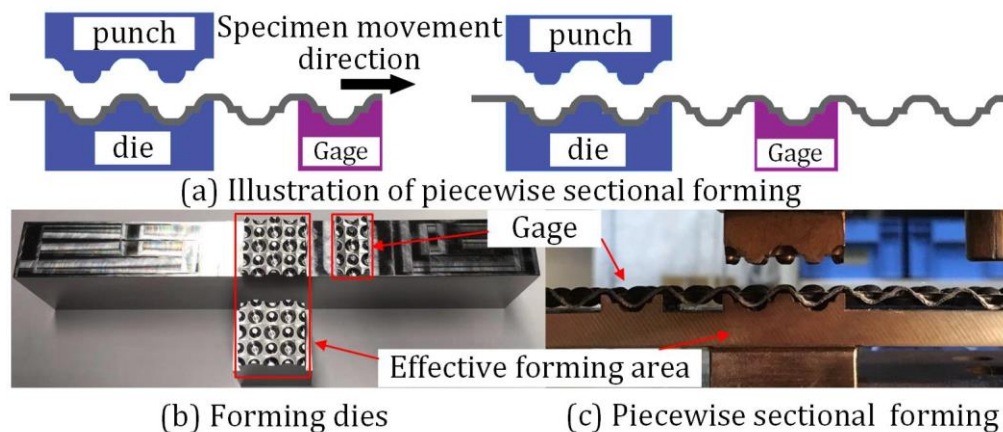


Figure 2-17. Forming dies and piecewise sectional forming process.

Three types of face sheets, SUS304, A2017P and CFRTP, were bonded with CFRTP core employing the one-component epoxy adhesive IW2190 (3M, USA) with maximum bonding temperature of 120°C, pressure of 0.3 MPa, and holding time of 1 h. Bonding was performed in an autoclave with a heating rate of 4°C/min and a cooling rate of 5°C/min, and pressure was

applied when temperature was above 100°C.

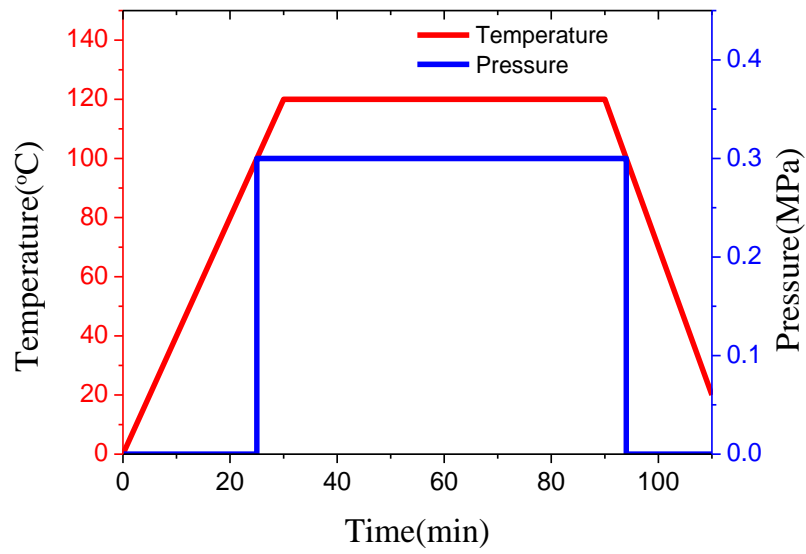


Figure 2-18. Bonding conditions in autoclave.

2.6 Property evaluation

2.6.1 Evaluation of bending stiffness by three-point bending test

Produced sandwich sheets were subjected to three-point bending to test the flexural properties. Dimensions of specimen subjected to three-point bending were 24 mm (width) × 144 mm (length) × 5.5 mm (A2017P)/5.1 mm (CFRTP)/6.5 mm (CFRTP) (height). Three-point bending test was conducted by using material testing machine (SERVOPULSER, SHIMADZU, JAPAN) as shown in [Figure 2-19](#). The load capacity of servopulser material testing machine was 20 kN. Both the radius of upper and lower rollers were 10 mm and span length was 100 mm as shown in [Figure 2-20](#). Cross head speed 3 mm/min was utilized.



[Figure 2-19](#). Servopulser material testing machine.

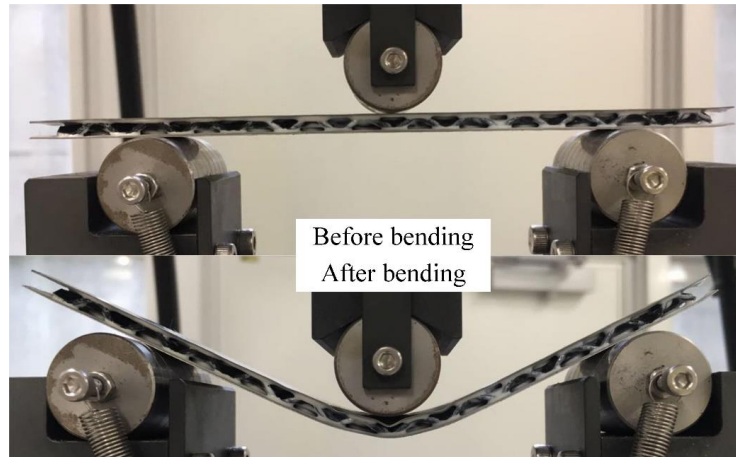


Figure 2-20. Three-point bending test configuration.

The obtained bending load–displacement curves are shown in Figure 2-21. The bending load was divided by the mass of each structure to calculate specific bending load. The masses of A2017P, SUS304 and CFRTP skin sandwich sheets are 13.83 g, 20.35 g and 12.65 g, respectively. The specific flexural stiffnesses of A2017P, SUS304 and CFRTP skin sandwich sheets are 17.06 N/(g·mm), 13.66 N/(g·mm) and 5.38 N/(g·mm), respectively. The maximum loads of A2017P, SUS304 and CFRTP skin sandwich sheets are 53.72 N/g, 30.86 N/g and 43.56 N/g, respectively. The specific energy absorption of A2017P, SUS304 and CFRTP skin sandwich sheets are 0.637 J/g, 0.352 J/g and 0.212 J/g, respectively. For A2017P skin, bending load curve shows a decreasing trend after displacement exceeds 6 mm owing to face buckling. Since face fracture and core fracture occur when bending displacement reaches 9 mm, bending load abruptly drops to 0 for CFRTP skin sandwich sheet. For SUS304 face sheet, a sudden decrease in load caused by core fracture appears at around 14 mm. A2017P and SUS304 skin sandwich sheets have higher specific flexural stiffness and a larger displacement to failure than the CFRTP skin sandwich sheet, whereas load tolerance of the CFRTP skin sandwich sheet is higher than that of the SUS304 skin sandwich sheet.

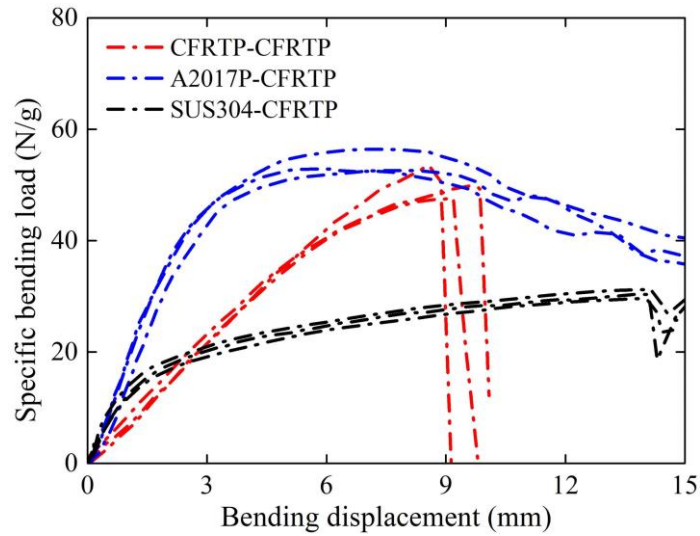


Figure 2-21. Bending load-displacement curves.

Table 2-7. Flexural properties of sandwich sheets.

Property	CFRTP– CFRTP	A2017P– CFRTP	SUS304– CFRTP
Specific three-point bending stiffness (N/(g·mm))	8.66±0.13	16.55±0.26	15.45±0.17
Specific peak load (N/g)	50.40±1.37	53.92±1.04	30.55±0.43
Specific energy absorption (J/g)	0.292±0.008	0.625±0.008	0.375±0.011
Weight (g)	12.65	13.83	20.35

2.6.2 Formability test

2.6.2.1 Forming tools

To evaluate the formability, produced sandwich sheet was subjected to L-bending and hat bending. The same pair of forming tools were used for L-bending and hat bending as shown in Figure 2-22. Half of the punch and die was used to conduct L-bending as shown in Figure 2-22 (b).



Figure 2-22. Forming tools for draw-bending and L-bending tests.

Radii of punch and die were 20 and 30 mm, respectively. Three-point bending test indicated that core fracture and face sheet fracture limits the formability of CFRTP skin sandwich sheet at room temperature. In this study, it is desirable to suppress core fracture and face sheet fracture by warm forming. Since the maximum temperature the adhesive can resist without losing much bonding strength was around 150°C, maximum forming temperature was set as 150°C.

To heat the forming tools, the punch and die were fixed in the die holder. Die holders were heated by cartridge heater, temperature of punch and die were recorded and controlled by temperature controller. Configuration of forming apparatus was shown in Figure 2-23. The forming tests were conducted with the following procedures. Firstly, the forming tools were heated to forming temperature. Then, specimen was put onto forming tool and warmed for several seconds followed by forming. After that, punch and die were held and cooled down to room temperature. Finally, punch and die were opened and product was removed.

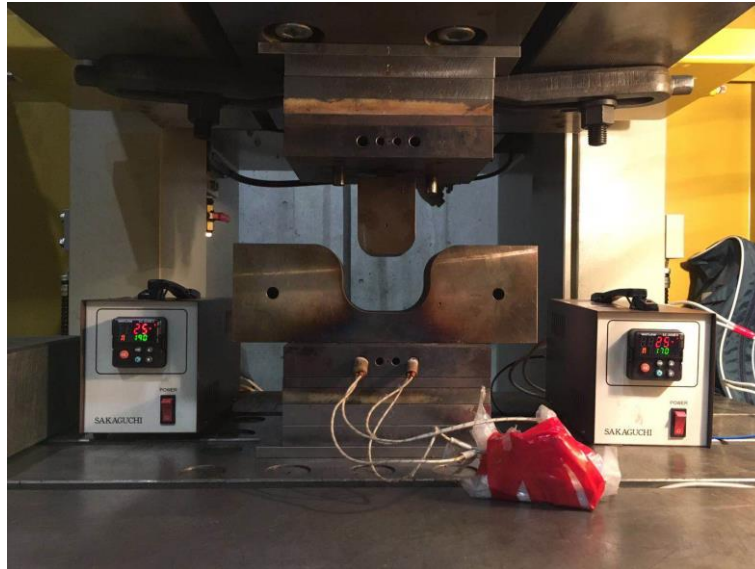


Figure 2-23. Configuration of warm forming apparatus.

2.6.2.2 L-bending test results

Dimensions of specimens subjected to L-bending were 24 mm (width) \times 144 mm (length) \times 5.5 mm (A2017P)/6.5 mm (CFRTP) (height). Load rate was 1 mm/s. Clearance was set as 8mm and 15mm. Forming temperatures were set as 150°C.

For A2017P skin sandwich sheet, when clearance was 8mm, bending process and formed part were shown in Figure 2-24 and Figure 2-25, respectively. Delamination was found during bending process. When clearance increased to 15mm, delamination was suppressed during bending process as shown in Figure 2-26, A2017P skin sandwich sheet was successfully formed without any failure including face buckling, face fracture, core shear failure and delamination as shown in Figure 2-27.

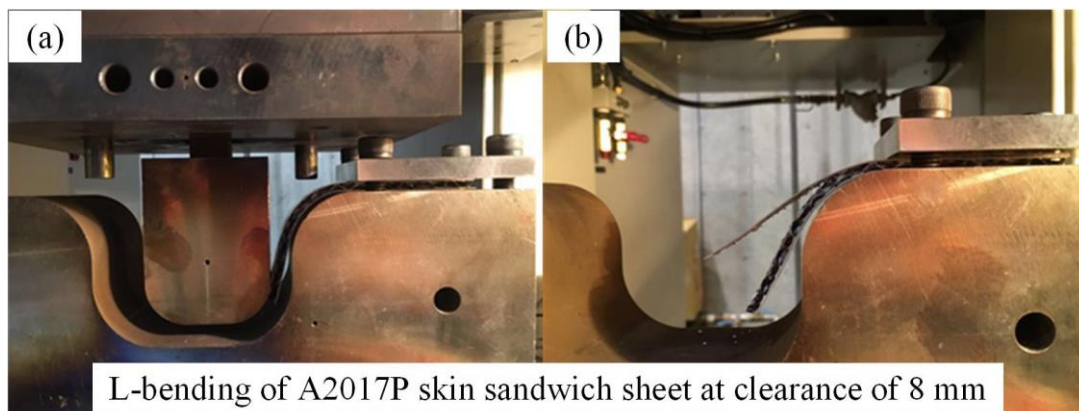


Figure 2-24. L-bending test of sandwich sheets with A2017P faces at clearance of 8 mm.



Figure 2-25. Deformed sandwich sheets with A2017P faces at clearance of 8 mm.

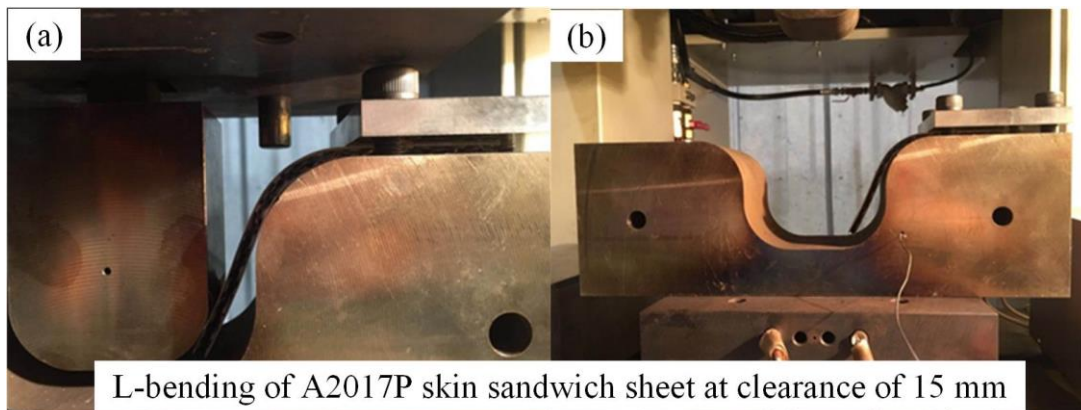


Figure 2-26. L-bending test of sandwich sheets with A2017P faces at clearance of 15 mm.



Figure 2-27. Deformed sandwich sheets with A2017P faces at clearance of 15 mm.

For CFRTP skin sandwich sheet, when clearance was 8 mm, the bending process and formed part were shown in Figure 2-28 and Figure 2-29, respectively. No failure occurred during bending process. When clearance increased to 15mm, the bending process and formed part were shown as Figure 2-30 and Figure 2-31, CFRTP skin sandwich sheet was successfully formed without any failure. The CFRTP skin sandwich sheet displayed good bendability when

subjected to different clearances.

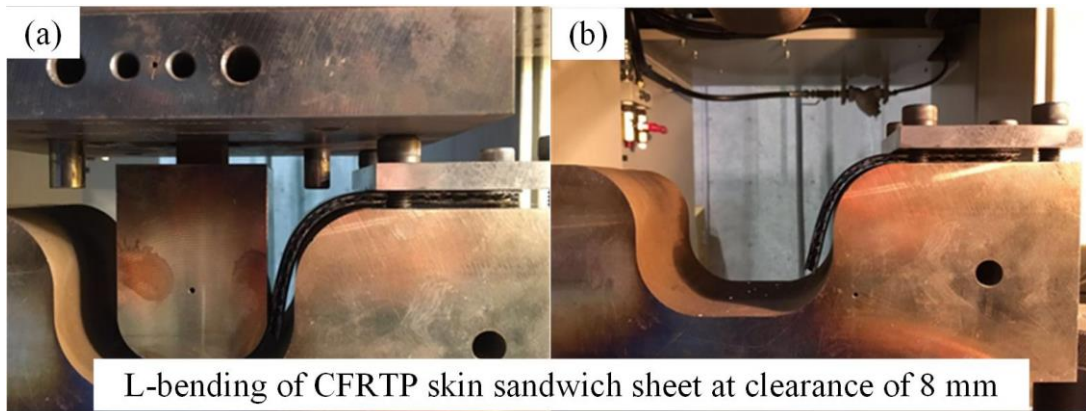


Figure 2-28. L-bending test of sandwich sheets with CFRTP faces at clearance of 8 mm.



Figure 2-29. Deformed sandwich sheets with CFRTP faces at clearance of 8 mm.

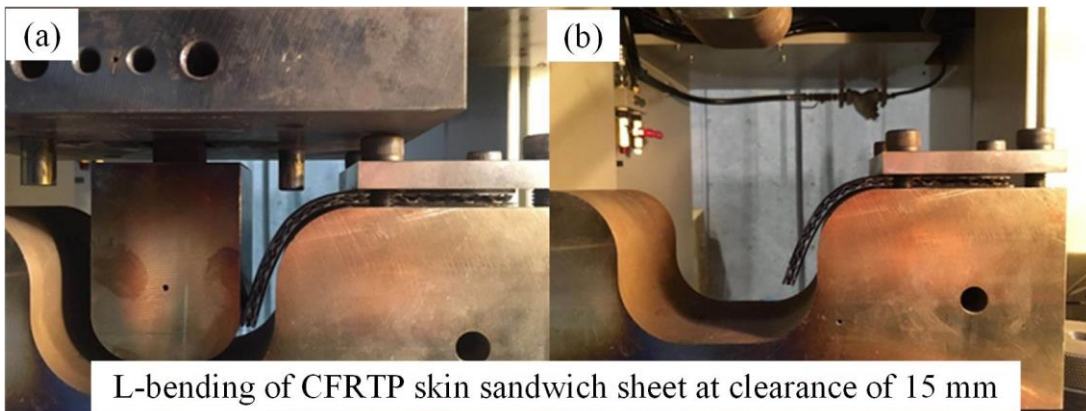


Figure 2-30. L-bending test of sandwich sheets with CFRTP faces at clearance of 15 mm.



Figure 2-31. Deformed sandwich sheets with CFRTTP faces at clearance of 15 mm.

From the above L-bending experiment, it was found that delamination was the failure mode in the bending process of A2017P skin sandwich sheet. The delamination was mainly due to the shear deformation of the sandwich panel, which was more severe when the clearance was smaller, that was why the delamination was caused in the case of smaller clearance. Delamination was suppressed when clearance was increased and good bendability of A2017P sandwich sheet was displayed. For CFRTTP skin sandwich sheet, no failure occurred in L-bending process, good bendability of CFRTTP was shown in warm forming process.

Since delamination limits the formability at 150°C, the SUS304 skin sandwich sheet was formed at 25°C. The L-bending was conducted at only clearance of 15 mm to save time. The experimental configuration and formed part are shown in Figure 2-32. The face buckling occurs in bending region during the forming process.

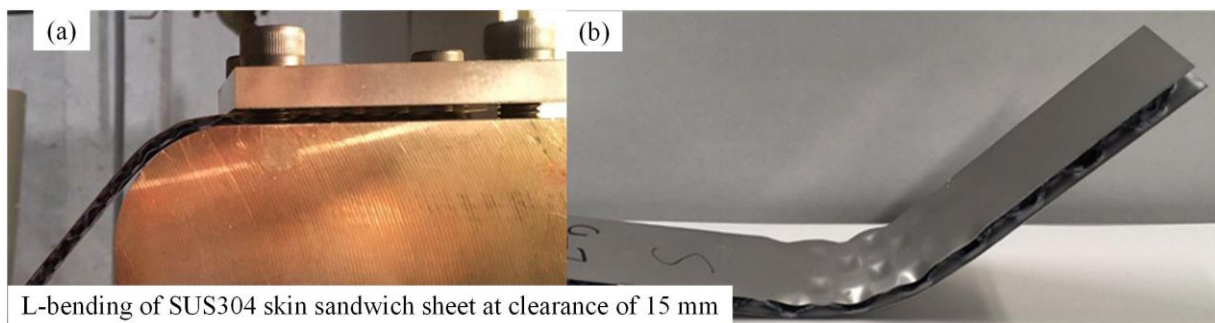


Figure 2-32. L-bending of sandwich sheet with SUS304 faces at clearance of 15 mm.

2.6.2.3 Draw-bending test results

Formability of fabricated sandwich sheets was examined by draw-bending test. Experimental configuration and formed parts are shown in Figure 2-33. Radii of the punch and die were 20 mm and 30 mm, respectively. Punch velocity was 1 mm/s. Dimension of specimen subjected to draw-bending was 24mm(width) × 240 mm (length)×5.5 mm (A2017P-T3)/6.5

mm (CFRTP) (height). Clearance between forming tools was 15 mm. To clarify forming temperature effect on formability of produced sandwich sheet, three temperatures 25°C, 100°C and 150°C were utilized. During the forming process, the forming depth was gradually increased by gradually increasing the stroke until the sample failed. The maximum forming depth where the failure initiated was recorded. Failure modes of sandwich sheets were investigated under different forming temperatures.

Figure 2-33 shows secondarily formed (with draw-bending) sandwich sheets with a CFRTP core given a forming temperature of 25 °C. Face buckling of A2017P–CFRTP and SUS304–CFRTP is observed as the face sheets cannot receive sufficient support from the core structure when drawing depth is greater than 25 and 35 mm, respectively. For CFRTP–CFRTP, face sheet and core fractures occur when drawing depth is higher than 14 mm owing to limited ductility at room temperature.

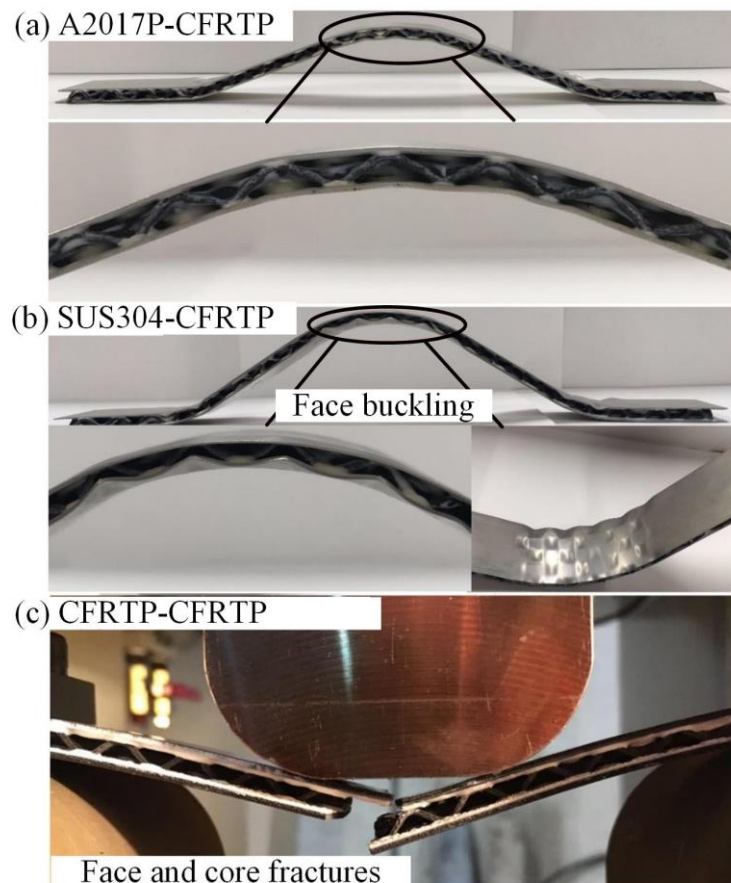


Figure 2-33. Secondarily formed sandwich sheets with a CFRTP core formed at 25 °C: (a) A2017P–CFRTP; (b) SUS304–CFRTP; (c) CFRTP–CFRTP.

The secondarily formed sandwich sheets given a forming temperature of 100 °C are shown in Figure 2-34. For A2017P–CFRTP, core shear failure is caused when forming depth reaches 14 mm owing to insufficient shear strength of CFRTP. Face buckling, initiated when forming depth reaches 16 mm, limits the formability of SUS304–CFRTP. For CFRTP–CFRTP, the forming depth is increased to 47 mm before face sheet and core fractures initiate, indicating that the raised forming temperature highly improves the formability of CFRTP–CFRTP.

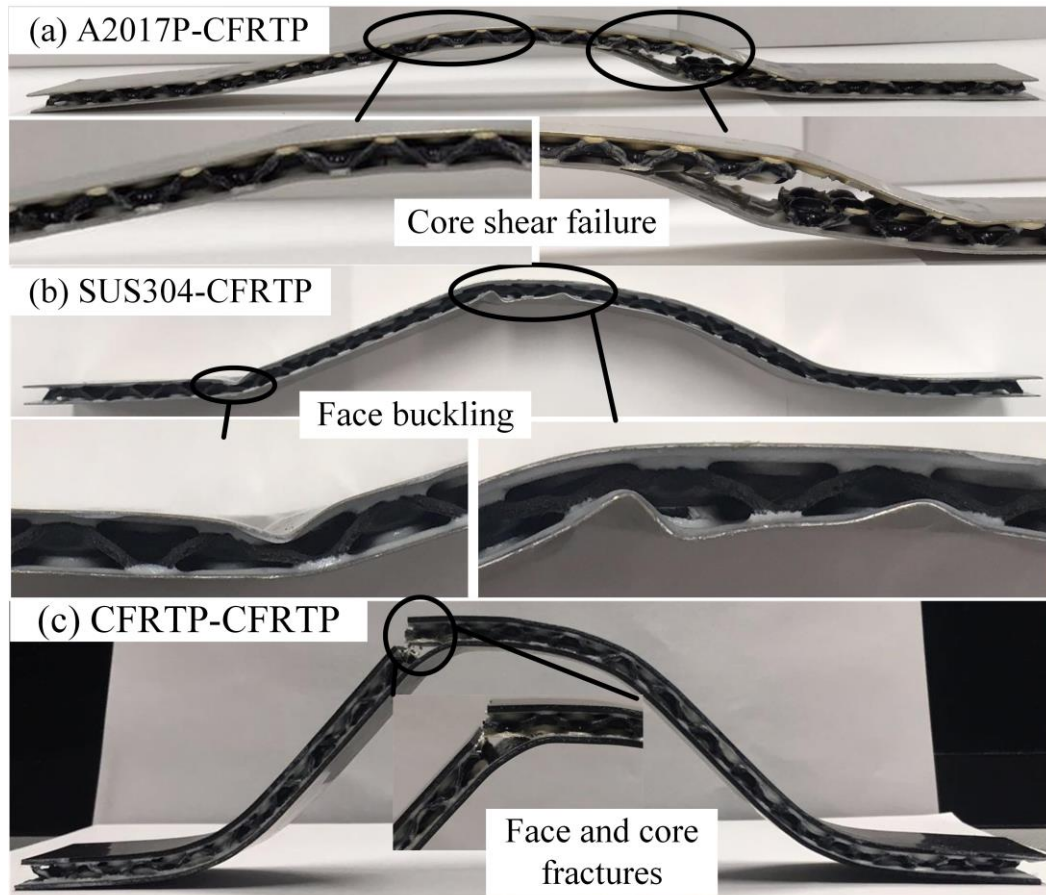


Figure 2-34. Secondary formed sandwich sheets with a CFRTP core formed at 100 °C: (a) A2017P–CFRTP; (b) SUS304–CFRTP; (c) CFRTP–CFRTP.

Figure 2-35 shows the secondarily formed sandwich sheets with a CFRTP core given a forming temperature of 150 °C. For A2017P–CFRTP and SUS304–CFRTP, delamination, occurring after the drawing depth is higher than 14 and 18 mm, respectively, is the main failure mode. The delamination of A2017P–CFRTP and SUS304–CFRTP owes to the highly deteriorated bonding strength at 150 °C. Although the bonding strength is significantly weakened at 150 °C, the delamination is not a problem for CFRTP–CFRTP as the yield strength

of CFRTP is also highly deteriorated at the elevated temperature so that it is lower than the interface strength. Therefore, fracture of the interface is suppressed owing to yielding of CFRTP. CFRTP–CFRTP is successfully formed without failures to drawing depth of 55 mm.

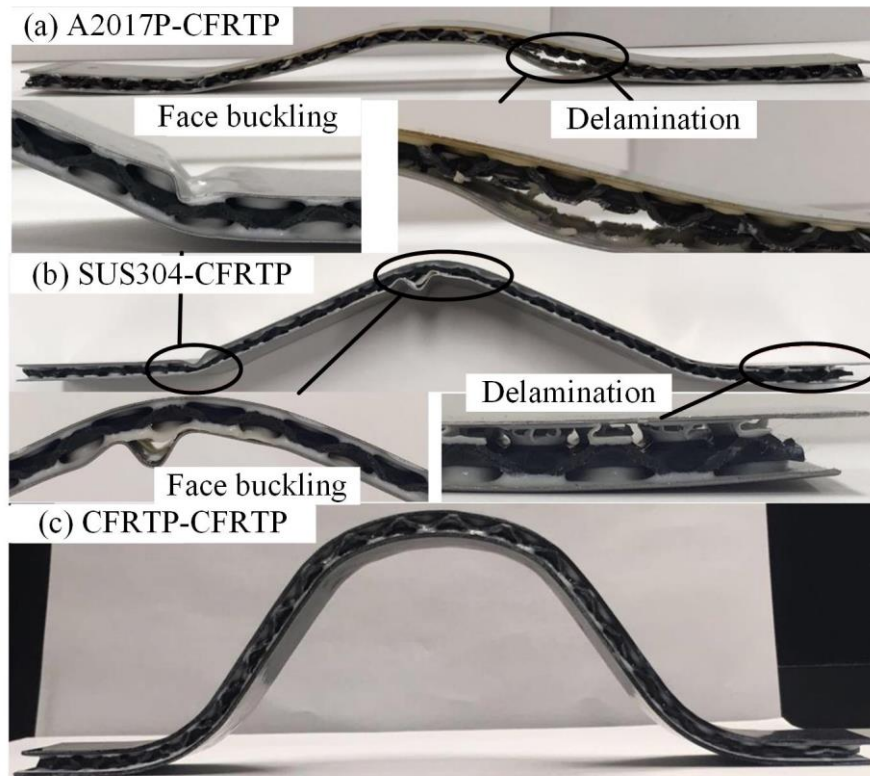


Figure 2-35. Secondary formed sandwich sheets with a CFRTP core formed at 150 °C: (a) A2017P–CFRTP; (b) SUS304–CFRTP; (c) CFRTP–CFRTP.

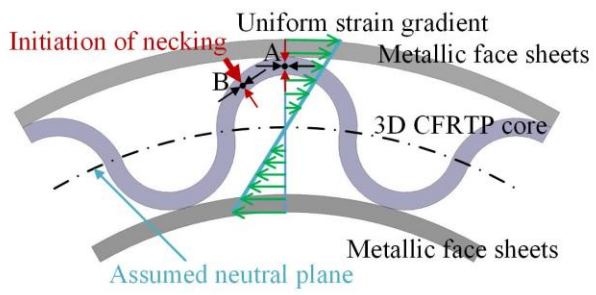
From the above draw-bending results of sandwich sheets at different forming temperatures, several concise conclusions can be deduced: (1) When formed at 25 °C, face fracture limits formability of CFRTP–CFRTP, while face buckling is the main failure mode for A2017P–CFRTP and SUS304–CFRTP; (2) Increased forming temperature improves formability of CFRTP–CFRTP, while delamination occurs for A2017P–CFRTP and SUS304–CFRTP.

To further explain the failure behaviours in cold and warm forming conditions, the following explanation models are provided in Figure 2-36. As stated above, the tendency is that the sandwich sheets composed of metallic face sheets and CFRTP core have better formability when cold formed, while the sandwich sheets composed of CFRTP face sheets and CFRTP cores have superior formability when warm formed. It has been revealed by Yanagimoto and

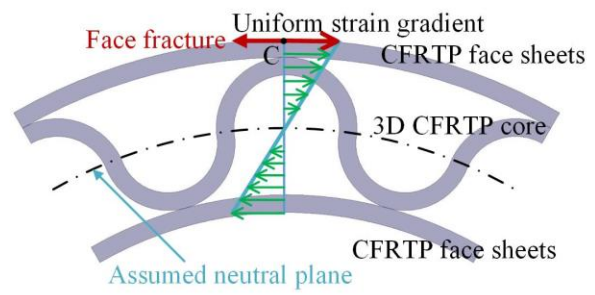
Ikeuchi (2012) that for thin sandwich sheets, the strain gradient is uniformly distributed in the thickness direction during bending, as highlighted by the blue green arrow in Figure 2-36. For sandwich sheets composed of metallic face sheets and the CFRTP core, as shown in Figure 2-36(a), initiation of necking of the CFRTP core at point B tends to generate a compensation strain increment at adjacent point A to maintain the hoop strain constant. However, such a redundant strain increment will be suppressed due to the uniformly distributed strain gradient in the thickness direction, thus decelerating the fracture of the CFRTP core. In contrast, for the CFRTP face sheets as shown in Figure 2-36(b), the brittle CFRTP face sheets will experience fracture first as the maximum strain gradient is generated at point C in the outer face sheets. Therefore, the sandwich sheets with ductile metallic face sheets tend to exhibit better formability than those with brittle CFRTP face sheets when cold formed.

Elevated forming temperatures decrease the stiffness and strength of CFRTP and adhesive, which changes the deformation behaviour of the CFRTP core and interface, leading to different forming characteristics of sandwich sheets. As shown in Figure 2-36(c), for the sandwich sheet composed of metallic face sheets and the CFRTP core, shear stress greater than the interface strength (reduced by elevated temperature) is generated to maintain the uniformity of the strain gradient at point D, resulting in delamination. As shown in Figure 2-36(d), the shear stress generated to ensure the uniformity of the strain gradient in the thickness direction is lower than the interface strength when CFRTP having similar strength is used as face sheets, thus effectively suppressing delamination. Meanwhile, compared with Figure 2-36(b), since the ductility of CFRTP is greatly improved at higher temperatures, even the maximum strain gradient in the outer face sheets does not cause face fracture. The above analyses are consistent with the experimental results and demonstrate again that the formability of the proposed metal-based sandwich sheets can be improved by adjusting material combinations and forming temperatures.

Cold forming

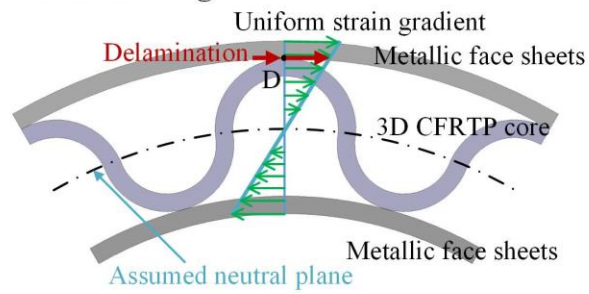


(a) Metallic face sheets-CFRTP core

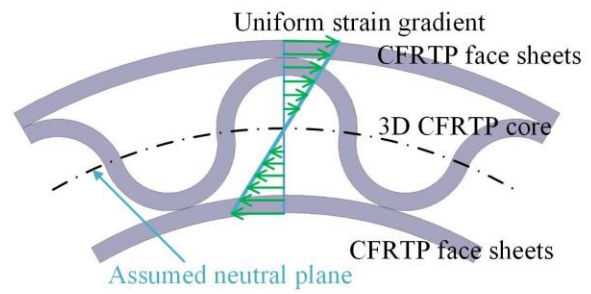


(b) CFRTP face sheets-CFRTP core

Warm forming



(c) Metallic face sheets-CFRTP core



(d) CFRTP face sheets-CFRTP core

Figure 2-36. Explanation models of failure behaviors of sandwich sheets during cold and warm forming.

2.7 Summary

The formable metal face/CFRP core sandwich sheet has been designed and fabricated, where a truncated dome was designed comprehensively considering productivity, mechanical property and formability. The structural parameters were optimized to improve bending stiffness, shear modulus and failure resistance. Sandwich sheets having a three-dimensional CFRTP core were successfully fabricated, and their mechanical properties and cold and warm forming characteristics were evaluated. Compared with conventional sandwich sheets, fabricated metal face/CFRP core sandwich sheet achieves higher specific bending stiffness, higher production efficiency and better formability. The development of formable metal face/CFRP core sandwich sheets is expected to expand the application range of sandwich structures and promote the use of lightweight parts in engineering fields. More detailed conclusions can be drawn as follows.

- (i) Rapid continuous manufacturing of a three-dimensional core structure can be achieved by warm stamping an initially flat CFRP sheet at a forming temperature of 200°C, demonstrating the feasibility of mass production of metal face/CFRP core sandwich sheets.
- (ii) The specific bending stiffness and shear modulus of the sandwich sheet with the truncated dome core are 5 and 2 times larger than those of the sandwich sheet with the conventional flat core, respectively, which proves the structural superiority of the sandwich sheet with the truncated dome core.
- (iii) Forming tests indicate that the failure mode and maximum drawing depth of sandwich sheets are closely related to forming temperature, and good formability can be achieved by adjusting forming temperature.
- (iv) The sandwich sheets composed of metallic face sheets and CFRTP core have better formability when cold formed, while the sandwich sheets composed of CFRTP face sheets and CFRTP cores have superior formability when warm formed.
- (v) Sandwich sheets composed of metallic face sheets and CFRTP core can be subjected to shallow drawing without failure under ambient temperature, while the

sandwich sheets composed of CFRTP face sheet and CFRTP core can be well formed at a forming temperature of 150°C.

- (vi) The investigations in this chapter demonstrate feasibility of rapid production and of secondary forming by conventional forming methods, which is expected to expand the commercial application of sandwich structures.

It should be pointed out that the bending stiffness of deformed sandwich sheets is very important in the practical applications although it was not evaluated in this study. As the bending stiffness after deformation could be affected by many factors such as potential defects and residual stresses caused during deformation, the optimization of bending stiffness after bending could be very difficult. Nevertheless, higher bending stiffness of the intact sandwich sheets generally gives higher bending stiffness of deformed sandwich sheets if they can be bent without failure.

2.8 References

- Ahn, D.-G., 2015. Research trends of metallic sandwich plates with single layer periodically repeated metallic inner structures (PRMIS)-focused on design, manufacturing and formability. *International Journal of Precision Engineering and Manufacturing-Green Technology* 2, 377-391.
- Besse, C.C., Mohr, D., 2012. Plasticity of formable all-metal sandwich sheets: Virtual experiments and constitutive modeling. *International Journal of Solids and Structures* 49, 2863-2880.
- Birman, V., Kardomateas, G.A., 2018. Review of current trends in research and applications of sandwich structures. *Composites Part B: Engineering* 142, 221-240.
- Dilthey, U., Ghandehari, A., Kopp, R., Hohmeier, P., Beiss, P., Iglesias Figueredo, E., El-Magd, E., Kranz, A., 2001. Development of porous steel structures for steam turbines. *Advanced engineering materials* 3, 111-119.
- George, T., Deshpande, V.S., Sharp, K., Wadley, H.N., 2014. Hybrid core carbon fiber composite sandwich panels: Fabrication and mechanical response. *Composite structures* 108, 696-710.
- Jackson, K., Allwood, J., Landert, M., 2008. Incremental forming of sandwich panels. *Journal of Materials Processing Technology* 204, 290-303.
- Kang, K.-J., 2009. A wire-woven cellular metal of ultrahigh strength. *Acta Materialia* 57, 1865-1874.
- Liu, J., Liu, W., Xue, W., 2013. Forming limit diagram prediction of AA5052/polyethylene/AA5052 sandwich sheets. *Materials & Design* 46, 112-120.
- Mohr, D., 2005. On the role of shear strength in sandwich sheet forming. *International Journal of Solids and Structures* 42, 1491-1512.
- Möhring, H.-C., Brecher, C., Abele, E., Fleischer, J., Bleicher, F., 2015. Materials in machine tool structures. *CIRP Annals* 64, 725-748.
- Nassar, H., Albakri, M., Pan, H., Khraisheh, M., 2012. On the gas pressure forming of aluminium foam sandwich panels: Experiments and numerical simulations. *CIRP annals* 61, 243-246.
- Osakada, K., Mori, K., Altan, T., Groche, P., 2011. Mechanical servo press technology for metal forming. *CIRP annals* 60, 651-672.
- Queheillalt, D.T., Murty, Y., Wadley, H.N., 2008. Mechanical properties of an extruded pyramidal lattice truss sandwich structure. *Scripta Materialia* 58, 76-79.
- Rao, S., Jayaraman, K., Bhattacharyya, D., 2011. Short fibre reinforced cores and their sandwich panels: Processing and evaluation. *Composites Part A: Applied Science and Manufacturing* 42, 1236-1246.
- Seong, D.-Y., Jung, C.G., Yang, D.-Y., Ahn, D.G., 2008. Bending behavior of simply supported metallic sandwich plates with dimpled cores. *International Journal of Modern Physics B* 22, 6179-6184.
- Seong, D., Jung, C.G., Yang, D.-Y., Kim, J., Chung, W., Lee, M., 2010. Bendable metallic sandwich plates with a sheared dimple core. *Scripta materialia* 63, 81-84.
- Vasiliev, V.V., Barynin, V.A., Razin, A.F., 2012. Anisogrid composite lattice structures—

Development and aerospace applications. *Composite structures* 94, 1117-1127.

Xiong, J., Ma, L., Vaziri, A., Yang, J., Wu, L., 2012. Mechanical behavior of carbon fiber composite lattice core sandwich panels fabricated by laser cutting. *Acta Materialia* 60, 5322-5334.

Yanagimoto, J., Ikeuchi, K., 2012. Sheet forming process of carbon fiber reinforced plastics for lightweight parts. *CIRP annals* 61, 247-250.

Yanagimoto, J., Wake, Y., Zeise, P., Mao, H., Shikazono, N., 2016. Design and optimization of stamping process of ultra-thin stainless sheet into bidirectionally corrugated shape for finless high-efficiency heat exchanger. *CIRP Annals* 65, 289-292.

Chapter 3 Investigation on influence factors on forming behaviors of sandwich sheet

Previous investigations on the forming characteristics of sandwich sheets with various inner macrostructures have revealed that failure modes such as core-face sheet delamination, face buckling and core shear failure are highly related to material properties of sandwich constituents, the sandwich geometries, forming tool geometries, core shapes, forming processes, forming temperatures, etc. Therefore, the relation between formability and these influence factors is clarified by systematically experimental tests and theoretical analyses for effective design and efficient fabrication process. In addition, the functional lattice structures are embraced in the core structure for the improvement of mechanical performance and potential functionality of sandwich sheets. The effects of lattice core topologies and relative densities on the mechanical property and forming behavior are extensively investigated.

Firstly, for the sandwich sheets with a truncated dome core designed in the previous chapter, theoretical analyses were conducted to determine the conditions required for successfully forming these sandwich sheets into curved shapes. Experimental results of formability tests agree well with the theoretical predictions, which demonstrates the validity of the theoretical models. Sandwich sheets with both A2017P and SUS304 face sheets of a thickness of 0.5 mm can be bent without any failure at a bending radius of 60 mm.

To further improve structural performance, bendability and potential functionality of metal-based sandwich sheets, the 3D lattice cores were sandwiched between thin metallic face sheets. The bending properties of sandwich sheets with 3D printed CFRP lattice cores originating from basic topologies of spherical shell, tetrahedral truss and tetrahedral plate were systematically investigated. The effects of core topologies, core relative densities, core heights, face sheet thicknesses on structural properties were clarified. The common failure modes during bending of sandwich sheets, such as face buckling and shear failure of core, were deeply investigated by theoretical models and experimental tests. At a prescribed radius of 60 mm, the sandwich sheets with the bilayered dome, octet truss and plate lattice cores of relative density

of 50%, height of 6 mm and face sheet thickness of 0.5 mm are bendable. The feasibility of design and production of bendable sandwich sheets with 3D lattice cores is demonstrated based on the theoretical and experimental validations. The designed bendable sandwich sheets can be adopted to replace conventional heavy monolithic metal sheets in various engineering applications, which is anticipated to fulfill the high demand for lightweight functional materials.

3.1 Effects of forming tool geometries and sandwich geometries on formability

Previous investigations on the forming characteristics of sandwich sheets with various inner macrostructures have revealed that failure modes such as core-face sheet delamination, face buckling and core shear failure are highly related to inner core macrostructure, face sheet thickness, bending radius, and material properties of face sheet and core. Therefore, the rational design of inner core macrostructure and appropriate selection of the face sheet and core materials are expected to effectively suppress the potential core shear failure and face buckling of metal face/CFRP sandwich sheets, which relies on the theoretical analysis of the failure mode to obtain a process window for a formable sandwich sheet. In this section, for the development of bendable metal-based composite sheets with a truncated dome core made of CFRTP, the design map for predicting core shear failure and face buckling is built based on newly proposed theoretical models, in which the dependence of failure modes such as core shear failure and face buckling on sandwich geometry, forming tool geometry and face sheet properties is clarified.

3.1.1 Research background and literature review

Conventional curved sandwich structures are typically manufactured by forming the face sheet and core separately into three-dimensional shapes followed by joining them together, where numerous fabrication procedures and forming tools are required, resulting in low production efficiency and a high manufacturing investment. Metal-based composite sheets, in which three-dimensional CFRP macrostructure is sandwiched and bonded to thin metallic face sheets such as titanium alloys, aluminum alloys and steels, are suitable for high-speed mass productions. If such metal-based composite sheets could be stamped or bent into desired three-dimensional geometry without failure of inner macrostructure, varied metal-based composite sheets could be used to replace heavy sheet metals in various applications such as framework parts of automobiles and airplanes.

However, there are two challenges in the development of such formable metal-based composite sheets. One is the low efficiency to fabricate the inner macrostructure with complex

shape using CFRP. Conventional inner macrostructures such as the pyramidal truss, kagome lattice and honeycomb cores are mostly produced using CFRTS (carbon fibre reinforced thermosetting resin), where production process involves autoclave co-curing, mechanical slotting reported by [Russell et al. \(2008\)](#), hot-press molding proposed by [Xiong et al. \(2010\)](#) and mechanical “snap-fit” described by [George et al. \(2013\)](#), resulting in low production efficiency and a high manufacturing cost. The other challenge is the limited formability of such metal-based composite sheets because the inner macrostructure made of CFRTS is brittle and impossible to be formed in the cold and warm conditions.

A feasible means of improving the manufacturing efficiency and formability of such metal-based composite sheets is to fabricate the inner macrostructure by warm stamping of CFRTP. Due to the improved formability of the CFRTP sheet at elevated temperatures, the inner macrostructure with a smooth shape is possible to be produced by warm stamping of CFRTP. However, owing to the limited out-of-plane shear strength of CFRTP, the inner macrostructure should yield a stable shear response to suppress the potential core shear failure. Inspired by the sheared dimple core proposed by [Seong et al. \(2010b\)](#) and bidirectional dome core designed by [Besse and Mohr \(2012\)](#), a truncated dome core has been proposed by [Zhang and Yanagimoto \(2019\)](#) in the previous chapter, where the section of the hemispherical shell yields a stable shear response for the cores. In contrast to the sheared dimple core, a continuous cross-sectional shape is achieved by changing the arrangement of the domes for the truncated dome core, which makes it possible to produce by stamping of CFRTP. Moreover, the truncated dome core comprising of single dome layer can be simply fabricated without additional joining compared with the bidirectional dome core, greatly reducing the fabrication complexity. However, since the out-of-plane shear strength of CFRTP is generally lower than that of metallic materials, the truncated dome core made of CFRTP has a relatively lower resistance of shear fracture, which may cause core shear failure. Moreover, the dome arrangement of the truncated dome core increases the gap between attachment points compared with the sheared dimple core and bidirectional dome core, resulting in a higher risk of face buckling. Previous investigations on the forming characteristics of sandwich sheets including but not limited to those conducted by [Fam and Sharaf \(2010\)](#), have revealed that failure modes such as core-face

sheet delamination, face buckling and core shear failure are highly related to inner core macrostructure, face sheet thickness, bending radius, and material properties of face sheet and core. Therefore, the rational design of inner core macrostructure and appropriate selection of the face sheet and core materials are expected to effectively suppress the potential core shear failure and face buckling of sandwich sheets with a truncated dome core made of CFRTP, which relies on the theoretical analysis of the failure mode to obtain a process window for a formable sandwich sheet.

In this section, for the development of bendable metal-based composite sheets with a truncated dome core made of CFRTP, the design map for predicting core shear failure and face buckling is built based on newly proposed theoretical models, in which the dependence of failure modes such as core shear failure and face buckling on sandwich geometry, forming tool geometry and face sheet properties is clarified. The content includes the following parts: (i) the theoretical analysis of failure modes is conducted and the process window for bendable sandwich sheets is obtained and (ii) the formability of sandwich sheets are examined experimentally.

3.1.2 material and structure

The CFRTP used to fabricate the core structure was a short carbon fibre reinforced polyamide 6 composite sheet with a carbon fibre volume fraction of 14%. Since short carbon fibres are randomly dispersed in the polyamide 6 matrix, the CFRTP displays an isotropic mechanical property. CFRTP sheets with a thickness of 1 mm were supplied by Toray Plastics Precision Co., Ltd. For the face sheet, aluminum alloy (A2017P) and stainless steel (SUS304) were adopted. The mechanical properties of A2017P, SUS304 and the CFRTP are shown in [Table 3-1](#).

[Table 3-1](#). Mechanical properties of A2017P, SUS304 and the CFRTP.

	Young's modulus (GPa)	Poisson's ratio	Yield strength (Mpa)	Tensile strength (Mpa)	Linear hardening modulus (GPa)
SUS304	200	0.29	215	560	2.3
A2017P	70	0.33	250	390	1.5

CFRTP	13.5	0.35	135	196	2.1
-------	------	------	-----	-----	-----

The same core type as investigated in **chapter 2**, namely the truncated dome core, was adopted in this section. The top and front views of the sandwich sheet with a truncated dome core is shown in **Figure 3-1(a)**, where the core structure is composed of repeated alternately arranged truncated domes. The repeated unit cell of the sandwich sheet and the structural parameters of the dome structure are shown in **Figure 3-1(b)** and **Figure 3-1(c)**, where t_c is the thickness of the core material, h is the dome depth, h_c is the core height, R is the dome inner radius and R_0 is the radius of the contact area between the core and the face sheet.

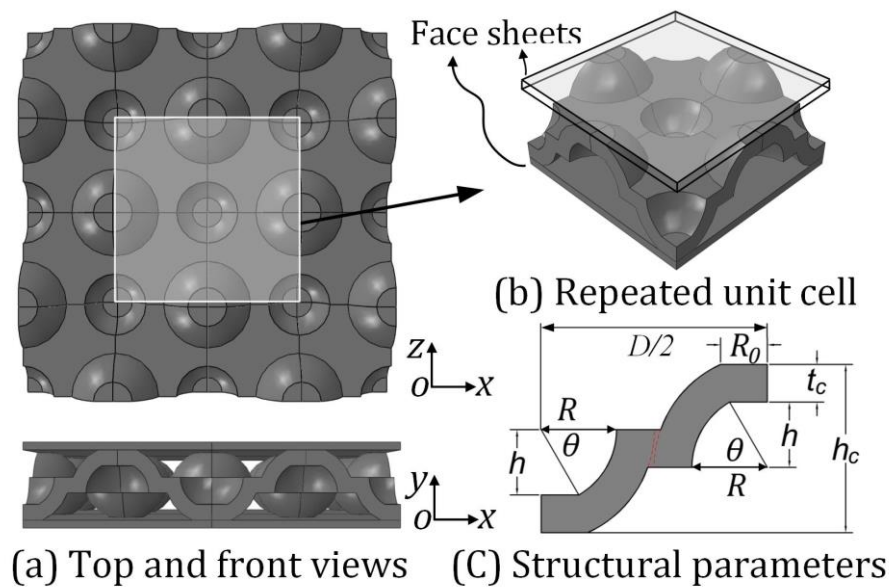


Figure 3-1. Illustration of the sandwich sheet with the truncated dome core.

Recall that in **chapter 2**, the optimal relative density is considered to be 0.22 on the basis of the comprehensive trade-off between the degree of face buckling, specific bending stiffness and shear modulus. Thus, the corresponding dome radius is 2 mm and the structural parameters are listed in **Table 3-2**.

Table 3-2. Structural parameters in design.

Structural Parameter	R	R_0	t_c	h	h_c
Value (mm)	2	1	1	1.75	4.5

3.1.3 Theoretical analysis of failure modes

3.1.3.1 Core shear failure

To suppress the core shear failure, the following constraint should be satisfied:

$$\tau_c > \tau_{re} \quad (3-1)$$

where τ_c is the core shear strength and τ_{re} is the required core shear strength.

The required core shear strength for a bendable sandwich sheet has been deduced in **chapter 2** and is expressed as

$$\tau_{re} = 2t_f / h_c \left[\sigma_y (\varepsilon_t - \varepsilon_b) + E_T (\varepsilon_t^2 + \varepsilon_b^2) \right] \quad (3-2)$$

$$\varepsilon_t = \ln \left[1 + \varepsilon^* / (2 + \varepsilon^*) \right] \quad (3-3a)$$

$$\varepsilon_b = \ln \left[1 - \varepsilon^* / (2 + \varepsilon^*) \right] \quad (3-3b)$$

$$\varepsilon^* = (2h_c + 2t_f) / (2R_F + t_f) = \frac{2 + 2t_f / h_c}{2R_F / h_c + t_f / h_c} \quad (3-3c)$$

where h_c is the core height, t_f is the face sheet thickness, R_F is the bending radius, σ_y is the yield strength of the face sheet and E_T is the linear hardening modulus of the face sheet.

The core shear strength of the sandwich sheet with the truncated dome core was approximately predicted by assuming that the area of core shear fracture is composed of two half-rings for the repeated unit cell as shown in **Figure 3-2**. Thus, the core shear strength can be expressed as

$$\tau_c = \tau_T \times t_c \left[2R_0 + 2R\theta \right] / (h_c * (2R + 2t_c)) \quad (3-4)$$

$$\theta = \arccos(R_0 / R) \quad (3-5)$$

where τ_T is the shear strength of the core material.

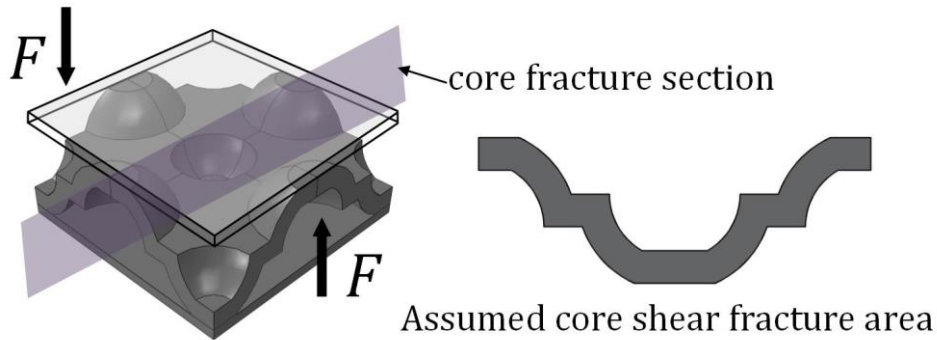


Figure 3-2. Shear failure mode of the truncated dome core.

3.1.3.2 Face buckling

Face buckling is generally caused by the large gap between attachment points, in which case the face sheets cannot receive sufficient supports. Therefore, the gap between attachment points should be limited to be lower than the critical value to avoid the face buckling. The face buckling mode of the sandwich sheet with the truncated dome core is illustrated in Figure 3-3, where the face sheet is subjected to compressive stress (σ_c) in the longitudinal direction (x direction). Since the face sheet is composed of the repeated unit cell in unsupported region, the repeated unit cell was analyzed as shown in Figure 3-3(b). The longitudinal compressive stress can be decomposed into the biaxial compressive stress (σ_a and σ_b) and in-plane shear stress (τ_{ab}). Through the stress transformation, biaxial compressive stress σ_a , σ_b and in-plane shear stress τ_{ab} can be obtained as

$$\sigma_a = \sigma_c \sin^2(\pi/4) \quad (3-6)$$

$$\sigma_b = \sigma_c \cos^2(\pi/4) \quad (3-7)$$

$$\tau_{ab} = \sigma_c \sin(\pi/4)\cos(\pi/4) \quad (3-8)$$

Following the free body diagram in Figure 2-4, the tensile and compressive forces generated in the upper and lower face sheets should satisfy the force equilibrium during bending:

$$F_u^b + F_l^b = 0 \quad (3-9)$$

where

$$\frac{F_u^b}{t_f} = \frac{\sigma_f + E_T \varepsilon_u^b}{\exp \varepsilon_u^b} \geq 0 \quad (3-10)$$

$$\frac{F_l^b}{t_f} = \frac{-\sigma_f + E_T \varepsilon_l^b}{\exp \varepsilon_l^b} \leq 0 \quad (3-11)$$

From Eqs. (2-2) and (3-9)–(3-11), the maximum value of the compression strain generated in the lower face sheet is:

$$\varepsilon_c^{\max} = \frac{1}{2 + \varepsilon^*} \left[\frac{\sigma_f}{E_f} \varepsilon^* - \ln(1 + \varepsilon^*) \right] \quad (3-12)$$

in which ε^* is expressed by Eq. (3-3c).

Therefore, the maximum compressive stress σ_c^{\max} can be calculated from the maximum compressive strain as

$$\sigma_c^{\max} = |\varepsilon_c^{\min}| E \quad (3-13)$$

here, E is the elastic modulus of the face sheet and ε_c^{\min} is the minimum strain of the face sheet.

Since the four ends of the repeated unit cell of the face sheet are fixed by being joined to the core structure, the repeated unit cell of the face sheet can be regarded as a simply supported plate. Thus, the inelastic buckling strength of the repeated unit cell of the face sheet under biaxial compression, σ_{cr} , can be expressed as given by Jones (2006)

$$\sigma_{cr} = \frac{k_{cc} \pi^2 E t_f^2}{12(1 - \nu^2) d^2} \quad (3-14)$$

where k_{cc} is a biaxial compressive buckling coefficient related to the load ratio of σ_a to σ_b and the aspect ratio of the plate. For a given load ratio of 1 and an aspect ratio of 1, k_{cc} was set to 2. ν is the poisson's ratio of the face sheet and d is the designed gap between attachment points as shown in Figure 3-3(b).

The inelastic buckling strength of the simply supported plate under shear stress mode, τ_{cr} , can be expressed as deduced by Galambos (1998)

$$\tau_{cr} = \frac{k_s \pi^2 E t_f^2}{12(1 - \nu^2) d^2} \quad (3-15)$$

where k_s is a nondimensional shear buckling coefficient. For simply supported edges, k_s equals 9.34.

In the special case that the repeated unit cell of the face sheet has equal side lengths, the criterion of face buckling for the combined loading of biaxial compressive stress and shear stress is expressed by Seong et al. (2010a)

$$\left(\frac{\sigma_a}{\sigma_{cr}}\right) + \left(\frac{\tau_{ab}}{\tau_{cr}}\right)^2 \leq 1 \quad (3-16)$$

Combining Eqs. (3-6)–(3-16), the following constraint of face buckling can be deduced:

$$d \leq \sqrt{\frac{-A + \sqrt{A^2 + 4B^2}}{2B^2}} = d_{cr} \quad (3-17)$$

where

$$A = \frac{12(1-\nu^2)\sin^2(\pi/4)|\varepsilon_c^{\min}|}{k_{cc}\pi^2 t_f^2} \quad (3-18a)$$

$$B = \frac{12(1-\nu^2)\sin(\pi/4)\cos(\pi/4)|\varepsilon_c^{\min}|}{k_s\pi^2 t_f^2} \quad (3-18b)$$

d_{cr} is the critical gap between attachment points, and the designed gap d should be smaller than the critical gap d_{cr} to suppress the face buckling.

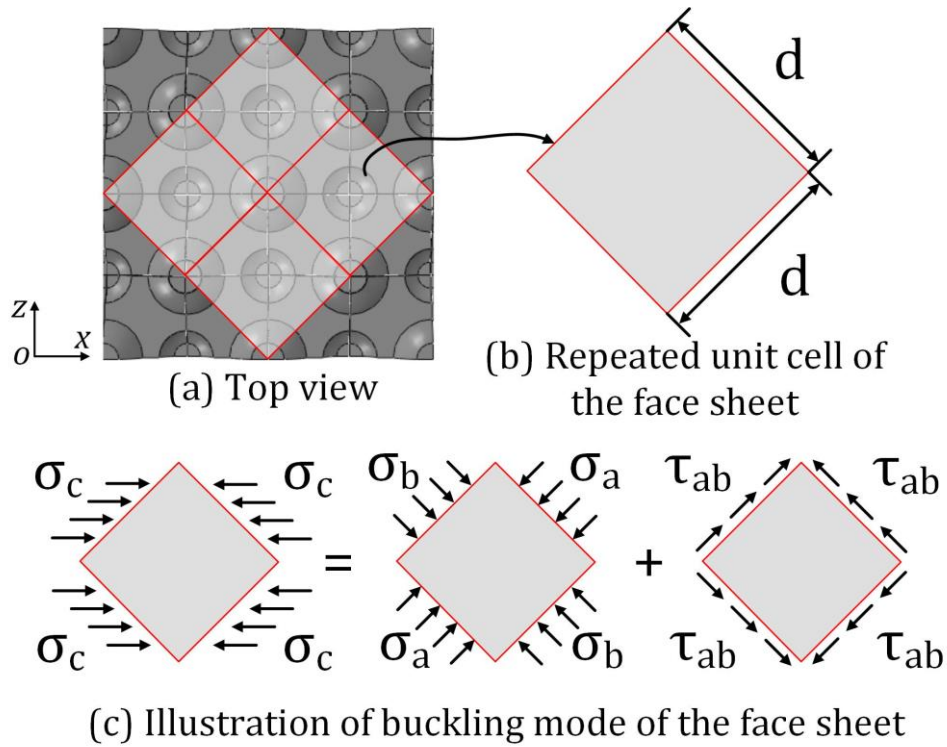


Figure 3-3. Illustration of the face buckling mode of the sandwich sheet with the truncated dome core.

3.1.4 Design map for bendable sandwich sheets

Above theoretical analyses indicate that the required core shear strength (τ_{re}) and the critical gap between attachment points (d_{cr}) are closely related to the ratio of the face sheet thickness to the core height (t_f/h_c), the ratio of the bending radius to the core height (R_F/h_c) and the ratio of the linear hardening modulus to the yield strength (E_T/σ_y), where t_f/h_c represents the sandwich geometry, R_F/h_c describes the forming tool geometry and E_T/σ_y represents the face sheet properties. Namely, face buckling and core shear failure are dominated by the sandwich geometry, forming tool geometry and the face sheet properties. To theoretically clarify the effects of these factors on the formability of sandwich sheets with a truncated dome core, the design map was developed to illustrate the dependence of the failure modes on the sandwich geometry, forming tool geometry and face sheet properties.

Here, A2017P and SUS304 were chosen as the face sheet materials. For each type of face sheet, for the given core height of 4.5 mm and the designed gap between attachment points of 6 mm, the ratio of the required core shear strength to the core shear strength (τ_{re}/τ_c) and the ratio of the critical gap between attachment points to the designed gap (d_{cr}/d) were calculated for different face sheet thicknesses and bending radii. R_{re} is the relative bending radius which was defined as the ratio of the bending radius to the core height (R_F/h_c). Six relative bending radii ranging from 4 to 13, corresponding to the bending radii ranging from 18 mm to 60 mm, were selected to build the design map.

For the A2017P face sheet, thicknesses of 0.5 mm, 0.75 mm and 1 mm were selected and the design map is shown in [Figure 3-4](#), while for the SUS304 face sheet, thicknesses of 0.3 mm, 0.4 mm and 0.5 mm were selected and the design map is shown in [Figure 3-5](#). The x -axis and y -axis of the design map represent the d_{cr}/d and τ_{re}/τ_c , respectively. The value of 1 or lower of d_{cr}/d indicates that the face buckling is caused, and the value of 1 or higher of τ_{re}/τ_c means that the core shear failure initiates. Thus, for both the A2017P and SUS304 face sheets, the design map is divided into four regions, where each region represents the corresponding failure mode and the gray region is the process window for the bendable sandwich sheet. From the design map, it is found that the increasing face sheet thickness causes the core shear failure and the

increasing bending radius eliminates the core shear failure and face buckling. In addition, the design map indicates that sandwich sheets with both A2017P and SUS304 face sheets of a thickness of 0.5 mm can be bent without any failure at a bending radius of 60 mm.

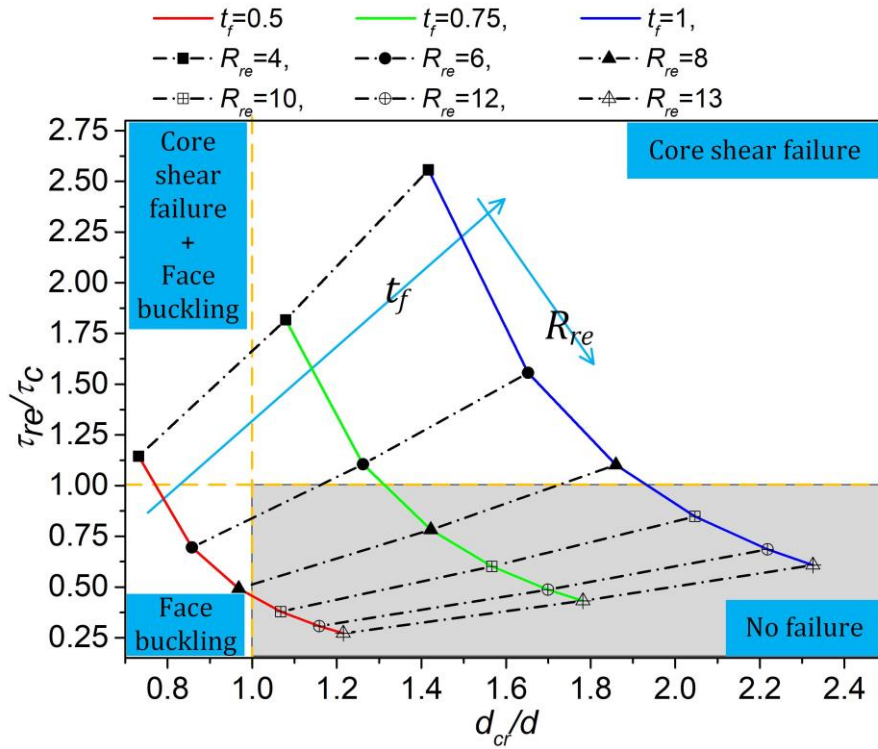


Figure 3-4. Design map for the sandwich sheet with the A2017P face sheet.

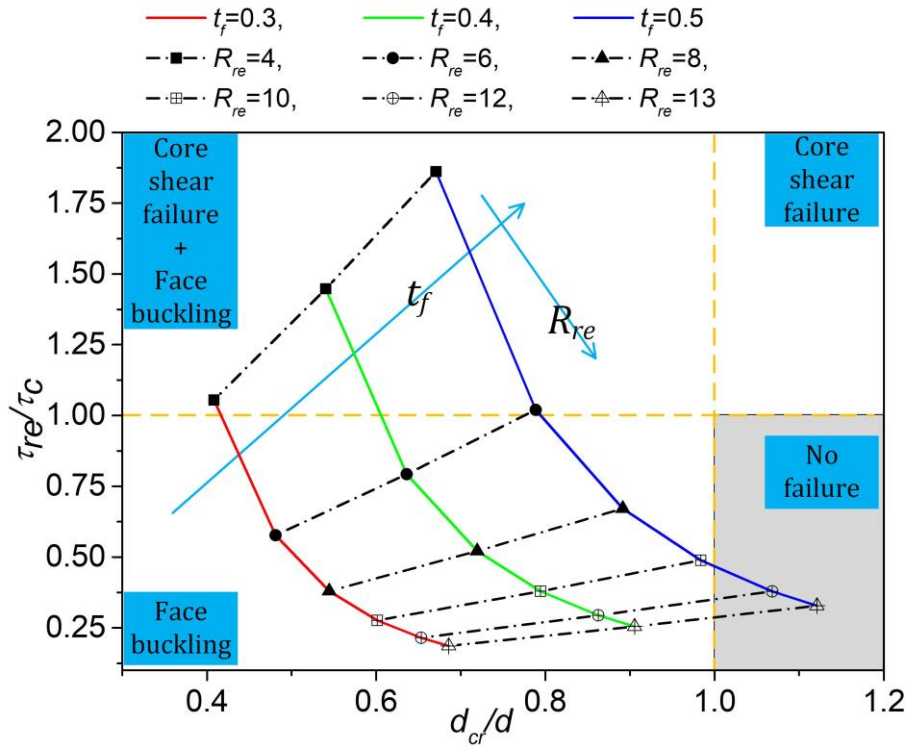


Figure 3-5. Design map for the sandwich sheet with the SUS304 face sheet.

3.1.5 Experimental validation

3.1.5.1 Fabrication of specimens

The truncated dome core with the desired dimensions of 24 mm (width) \times 144/240 mm (length) \times 4.5 mm (height) was fabricated by the piecewise sectional forming of a CFRTP sheet with an initial thickness of 1 mm. The optimal forming conditions of CFRTP have been investigated in **chapter 2**. The piecewise sectional forming process and fabricated specimen are shown in **Figure 3-6**. The effective forming area of the upper and lower dies was 24 mm \times 24 mm and a gage with the same shape as the forming part was used to control the position of the specimen in each forming step.

A2017P and SUS304 face sheets with different thicknesses were bonded to the CFRTP core using the one-component epoxy resin adhesive IW2190 (3M, USA) in an autoclave with a maximum bonding temperature of 120 °C, a pressure of 0.3 MPa, and a holding time of 1 h. The face sheet surface was polished by 80 grit sandpaper followed by washing in acetone. The adhesive was cured in an autoclave with a heating rate of 4 °C/min and a cooling rate of

5 °C/min. A pressure of 0.3 MPa was applied when the temperature was higher than 100 °C.

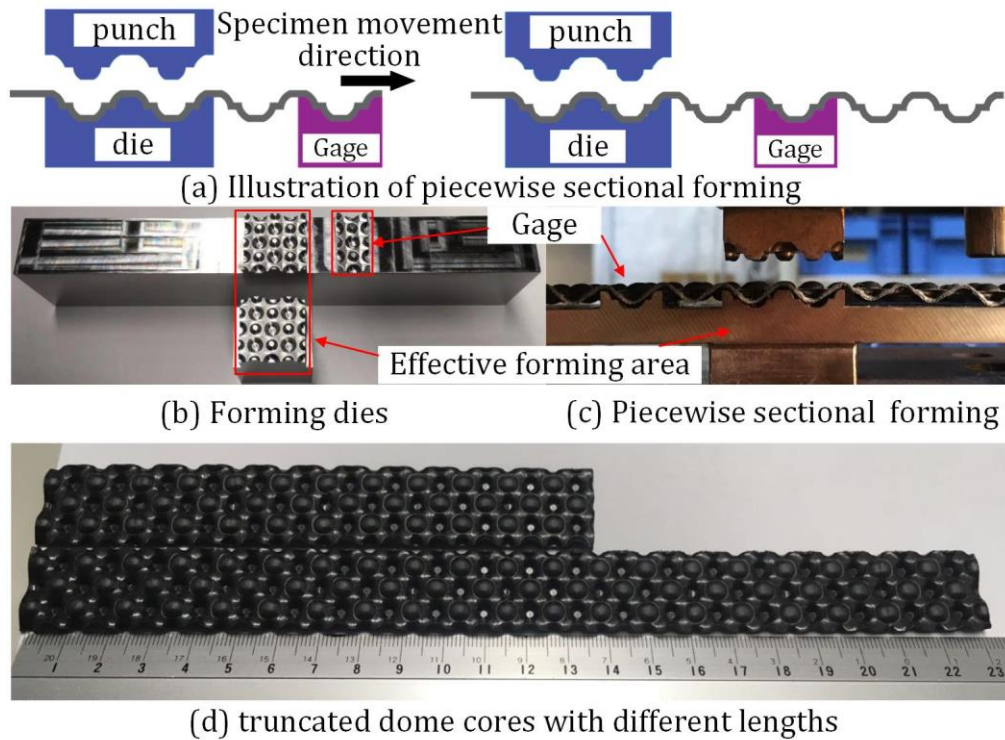


Figure 3-6. Piecewise sectional forming process and produced core structures.

3.1.5.2 Experimental setup for L-bending test

The failure mode of sandwich sheets with the A2017P and SUS304 face sheets of different thicknesses was examined by L-bending tests with bending radii of 30 mm and 60 mm. The experimental configuration of L-bending test was shown in Figure 3-7. The thickness of the A2017P face sheet was set to 0.5 mm and 1 mm, and the thickness of the SUS304 face sheet was set to 0.3 mm and 0.5 mm. When the bending radius was 30 mm, the radius of the upper punch was 20 mm and the length of the specimen was 144 mm, while the radius of the upper punch was 40 mm and the length of the specimen was 240 mm for the bending radius of 60 mm. The clearance between the punch and the die was set to 15 mm for both bending radii and the punch velocity was set to 1 mm/s.



Figure 3-7. Experimental configuration of the L-bending test.

3.1.5.3 Experimental results

The experimental results of sandwich sheets with the A2017P face sheet are shown in Figure 3-8. For the bending radius of 30 mm, as shown in Figure 3-8(a), when the face sheet thickness is 0.5 mm, face buckling occurs in the bending zone, while the core shear failure is observed when the face sheet thickness is 1 mm. The forming characteristics of sandwich sheets for the bending radius of 60 mm are shown in Figure 3-8(b). When the face sheet thickness is 0.5 mm, the sandwich sheet is well formed without any failure, while the core shear failure is caused when the face sheet thickness is 1 mm.

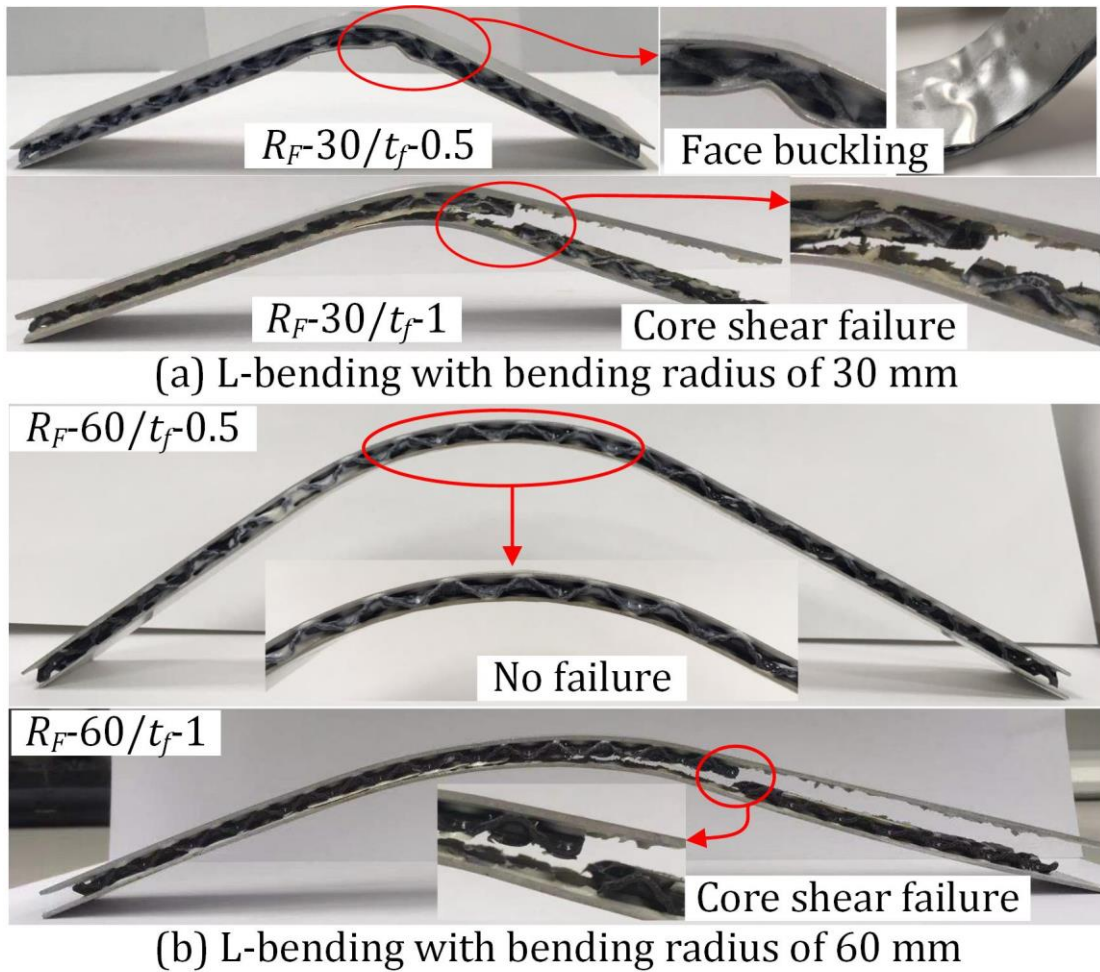


Figure 3-8. L-bending tests of sandwich sheets with A2017P face sheets: (a) bending radius of 30 mm; (b) bending radius of 60 mm.

The failure modes of sandwich sheets with SUS304 face sheets are shown in Figure 3-9. For the bending radius of 30 mm, as shown in Figure 3-9(a), the face buckling is observed in the bending zone when the face sheet thicknesses are 0.3 mm and 0.5 mm. The deformed sandwich sheets for the bending radius of 60 mm are shown in Figure 3-9(b). When the face sheet thickness is 0.3 mm, the face buckling of the sandwich sheet is caused, while the sandwich sheet with the face sheet thickness of 0.5 mm is successfully formed without any failure.

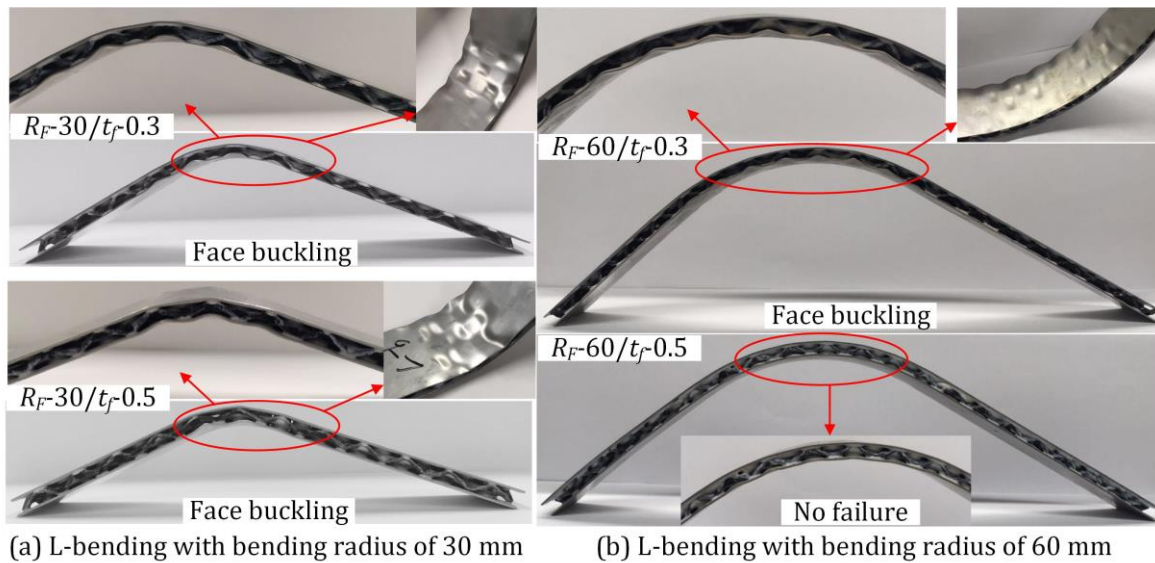


Figure 3-9. L-bending tests of sandwich sheets with SUS304 face sheets: (a) bending radius of 30 mm; (b) bending radius of 60 mm.

A comparison between the experimental results and the theoretical predictions from the design map is shown in Table 3-3. For sandwich sheets with both the A2017P and SUS304 face sheets, the experimental results are almost in agreement with the theoretical predictions from the design map. However, there is one inconsistency between the experimental results and the theoretical predictions. For the sandwich sheet with the A2017P face sheet, although the design map indicates no failure for the bending radius of 60 mm and the face sheet thickness of 1 mm, the core shear failure occurs in the L-bending test, which indicates that the core shear strength is overestimated in the theoretical calculations. In fact, the required core shear strength should be larger than the core shear strength under the above forming conditions. Since the core shear strength is overestimated in the theoretical calculations, the required core shear strength is smaller than the core shear strength in the design map, resulting in the incorrect prediction that core shear failure does not occur. One possible reason why the core shear strength is overestimated in the theoretical calculations is that the actual area in which the core shear fracture occurs is smaller than the assumed area. The other one might be that the thinning effect of the CFRTP sheet in the piecewise sectional forming process is neglected. The overestimation of the shear fracture area and thickness of the core material results in the overestimated theoretical value of the core shear strength.

Table 3-3. Comparison of failure modes between theoretical predictions and experimental results.

	$R_F-30/t_f-0.5$	R_F-30/t_f-1	$R_F-60/t_f-0.5$	R_F-60/t_f-1
A2017P-Theory	Face buckling	Core shear failure	No failure	No failure
A2017P-Exp	Face buckling	Core shear failure	No failure	Core shear failure
	$R_F-30/t_f-0.3$	$R_F-30/t_f-0.5$	$R_F-60/t_f-0.3$	$R_F-60/t_f-0.5$
SUS304-Theory	Face buckling	Face buckling	Face buckling	No failure
SUS304-Exp	Face buckling	Face buckling	Face buckling	No failure

3.1.6 Conclusion of section 3.1

The formability of metal-based composite sheets with a truncated dome core made of CFRTP was investigated theoretically and experimentally, and bendable sandwich sheets were successfully developed. Theoretical models were developed to predict failure modes including face buckling and core shear failure in the bending process, and suitable sandwich geometry and forming tool geometry were determined to bend sandwich sheets into curved shapes without any failure. It was shown in the design map that the rise of face sheet thickness caused core shear failure and increasing the bending radius contributed to the elimination of core shear failure and face buckling. The failure modes of sandwich sheets under different forming conditions showed good agreement with the theoretical predictions. Sandwich sheets with both A2017P and SUS304 face sheets can be successfully bent without any failure when the face sheet thickness is 0.5 mm and the bending radius is 60 mm. The investigations on the failure modes provide insights into the formability of sandwich sheets with a CFRTP core and contribute to the development of formable sandwich sheets, which is expected to expand the range of applications and improve the structural performance of sandwich structures.

3.2 Effects of core topology on formability

To further improve structural performance, bendability and functionality of metal-based sandwich sheets, the 3D lattice cores were sandwiched between thin metallic face sheets in this study. The bending properties of sandwich sheets with 3D printed CFRP lattice cores originating from basic topologies of spherical shell, tetrahedral truss and tetrahedral plate were systematically investigated. The effects of core topologies, core relative densities, core heights, face sheet thicknesses on structural properties were clarified. The common failure modes during bending of sandwich sheets, such as buckling of face sheet and shear failure of core, were deeply investigated by theoretical models and experimental tests. At a prescribed radius of 60 mm, the sandwich sheets with the bilayered dome, octet truss and plate lattice cores of relative density of 50%, height of 6 mm and face sheet thickness of 0.5 mm are bendable. This study demonstrates the feasibility of design and production of bendable sandwich sheets with 3D lattice cores based on the theoretical and experimental validations. The designed bendable sandwich sheets can be adopted to replace conventional heavy monolithic metal sheets in various engineering applications, which is expected to fulfill the high demand for the lightweight functional materials.

3.2.1 Research background and literature review

In the last few decades, impressive mechanical properties and potential various functionalities of sandwich plates have drawn much attention especially from the scientists and designers in the field of lightweight engineering, and relevant research and development have been mirrored in many aspects such as their structural designs, fabrication processes and mechanical tests. However, most sandwich plates can only be used as flat panels as it is almost impossible to form them into curved shapes. Nowadays, the production process of three-dimensional sandwich structures is still complicated. The typical method is to deform the two face sheets and the inner core structure into certain curvatures and then bond them together. Apparently, many production processes and forming apparatus are necessary in the above method, and thus not suitable for mass production.

If bendable sandwich sheets are successfully developed, the conventional flat sandwich panels can thus be bent into 3D curved shapes and highly broaden their application ranges. For this reason, [Bruschi et al. \(2021\)](#) made extensive review on recent progresses and challenges about the forming of metal-based sandwich sheets. Extensive forming tests of aluminum/polymer/aluminum sheets were carried out to build the forming limit diagram (FLD) which was capable of predicting experimental results as presented by [Kim et al. \(2003\)](#). [Weiss et al. \(2007\)](#) studied how forming temperatures influence deformation behaviors of aluminum/polypropylene/aluminum laminates for the establishment of FLD at different temperatures. [Logesh and Raja \(2017\)](#) found the formability of AA8011/PP/AA1100 sandwich sheets is sufficient to be formed into automotive body panels and bonnets. Solid and mesh steel inlays were found to improve the formability of steel/polymer/steel sheets during bending as reported by [Sokolova et al. \(2011\)](#). Compared with that of the monolithic aluminum sheet, superior formability of aluminum/polyethylene/aluminum sandwich sheet was reported by [Liu et al. \(2013\)](#). Incremental sheet forming (ISF) technique was firstly adopted to deform metal/polymer/metal sandwich panels by [Jackson et al. \(2008\)](#) and revealed that the sandwich panel can be deformed without core indentation. [Harhash and Palkowski \(2021\)](#) found that sandwich sheets show earlier failure when shaped by the incremental forming compared to the monolithic metal sheets. Aluminum foam sandwich panels were successfully deformed to large curvature by gas pressure while maintaining low core density as demonstrated by [Nassar et al. \(2012\)](#). However, when a 3D hollow core is adopted as the inner structure, it could be much more difficult to well shape sandwich sheets as complicated failure modes can be easily encountered due to the insufficient shear resistance and oversized gap possessed by the low-density cellular core. Shear failure of porous cores has been demonstrated to be the dominant forming problem for thin metallic sandwich sheets as presented by [Mohr \(2005\)](#). [Cai et al. \(2018\)](#) adopted multi-point forming technique and found wrinkling and dimpling of face sheet and fracture of egg-box-like cores during forming process. Face buckling constraint during bending of a bi-directionally corrugated structure has been theoretically deduced by [Seong et al. \(2010a\)](#). Metallic sandwich sheets with dome-like cores have been reported to effectively prevent buckling and shear failure during bending by [Seong et al. \(2010b\)](#), inspired by which

a CFRP dome core has been designed and effects of forming temperatures on its formability have also been clarified using cold and warm forming tests conducted by [Zhang et al. \(2021\)](#).

However, the aforementioned studies are mainly based on 2D flat or 3D dome-like cores, and thus mechanical properties, functionality and formability may still be limited. As shown in [Figure 3-10](#), with inspirations from some typical biological structures such as the grass leaf stem and hornbill beak, hybrid CFRP face/metal honeycomb core and CFRP face/metal foam core sandwich panels have been developed. The unique combinations of stiff outer layer and low-density inner layer are capable of providing exceptionally high specific strength and stiffness, and thus receiving huge success in various engineering structures. Recently, inspired by these biological features, many types of lattice structures such as the strut-based and plate-based lattices have been designed by [Berger et al. \(2017\)](#). The advanced additive manufacturing (AM) technology is now capable of producing lattice structures with widely variable dimensions, various topologies and desired space distributions, which enables the flexible design of lightweight lattice structures with multifunctional properties as reported by [Zheng et al. \(2014\)](#). The synergy of AM and lattices largely promotes the applications of multifunctional lightweight structures in many areas such as in thermal systems, energy absorption structures, consumer products, medical devices and soft robotics as reviewed by [Thompson et al. \(2016\)](#). Therefore, from the viewpoint of improving the mechanical properties and functionality of sandwich sheets, lattice structures could be potentially good candidates for core structures. If sandwich sheets with lattice core structures can be bendable, they can be expected to replace conventional heavy monolithic sheets in various engineering applications, which is answer to the high demand for lightweight functional materials. However, the bendability of sandwich sheets with lattice core structures may be limited as the buckling or fracture of thin lattice struts can be easily caused subjected to large bending deformation. For the design and production of sandwich sheets with superior mechanical performance and better bendability, it is essential to systematically investigate the effects of core topologies on bending properties.

In this section, the mechanical properties and bendability of sandwich sheets with 3D printed CFRP lattice cores originating from basic topologies of spherical shell, tetrahedral truss and tetrahedral plate were systematically investigated. The effects of core topologies, core

relative densities, core heights, face sheet thicknesses on bending properties were studied. The failure behaviors during bending of sandwich sheets, such as buckling of face sheet and shear failure of core, were deeply investigated by theoretical predictions and experimental validations.

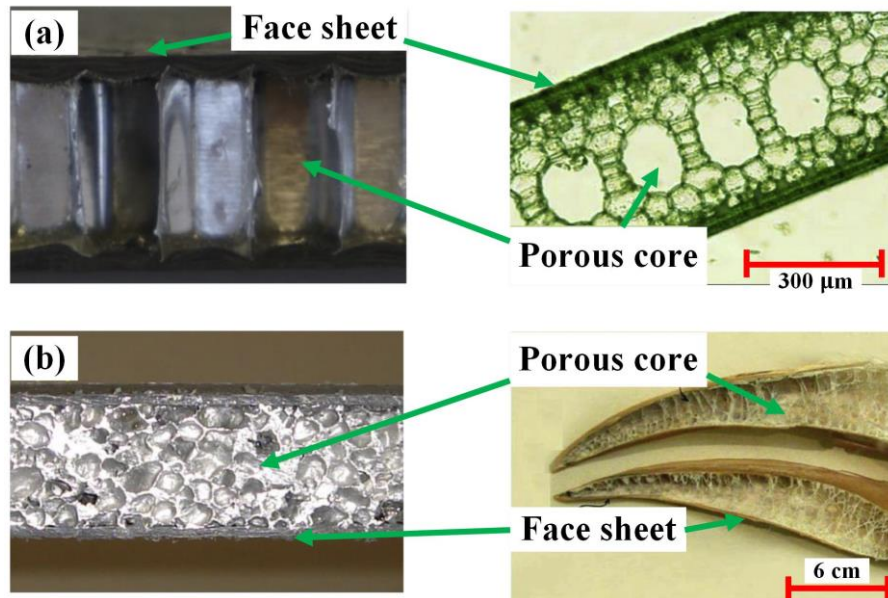


Figure 3-10. Sandwich designs inspired by biological structures: (a) CFRP face/metal honeycomb core sandwich panel and grass leaf stem; (b) CFRP face/metal foam core sandwich plate and hornbill beak.

3.2.2 Selection of core structures

In this section, the mechanical properties and bendability of sandwich sheets with 3D printed CFRP lattice cores originating from basic topologies of spherical shell, tetrahedral truss and tetrahedral plate were systematically investigated. The effects of core topologies, core relative densities, core heights, face sheet thicknesses on bending properties were studied. The failure behaviors during bending of sandwich sheets, such as buckling of face sheet and shear failure of core, were deeply investigated by theoretical predictions and experimental validations.

As shown in [Figure 3-11](#), three types of lattice structures originating from basic topologies of spherical shell, tetrahedral truss and tetrahedral plate were selected, in which the bilayered dome consists of two layers of domes formed by periodic hemispherical shells, while the octet

truss and plate lattices are respectively composed of periodically arranged beam-based tetrahedral trusses and closed-cell tetrahedral plates. The structural parameters of basic lattices are shown in Figure 3-12, the lattice constant and lattice thickness are denoted as L_e and t , respectively. For the lattice structure, its relative density ρ is determined by the lattice thickness. To obtain the relationship between them, the lattice thickness was changed at small intervals and relative densities of generated lattices were calculated by CAD programs. The computed results are given in Figure 3-13, from which the relative density as a function of lattice thickness can be obtained by polynomial fittings. With the relation between lattice relative density and lattice thickness, the lattice structure at an arbitrary relative density can be easily constructed.

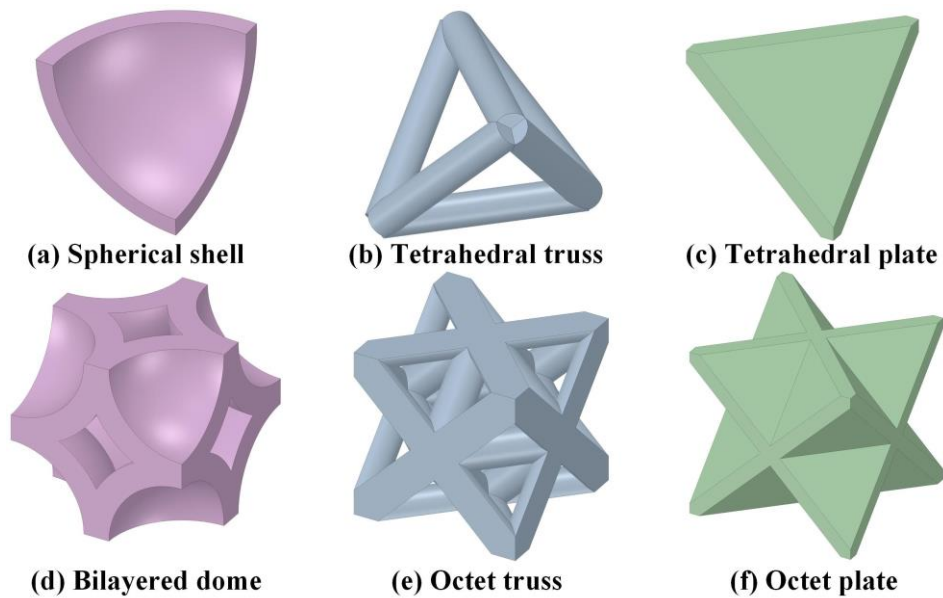


Figure 3-11. Representative lattice structures originating from basic topologies of shell, strut and plate: (a) spherical shell; (b) tetrahedral truss; (c) tetrahedral plate; (d) bilayered dome composed of spherical shell; (e) octet truss composed of tetrahedral truss; (f) octet plate composed of tetrahedral plate.

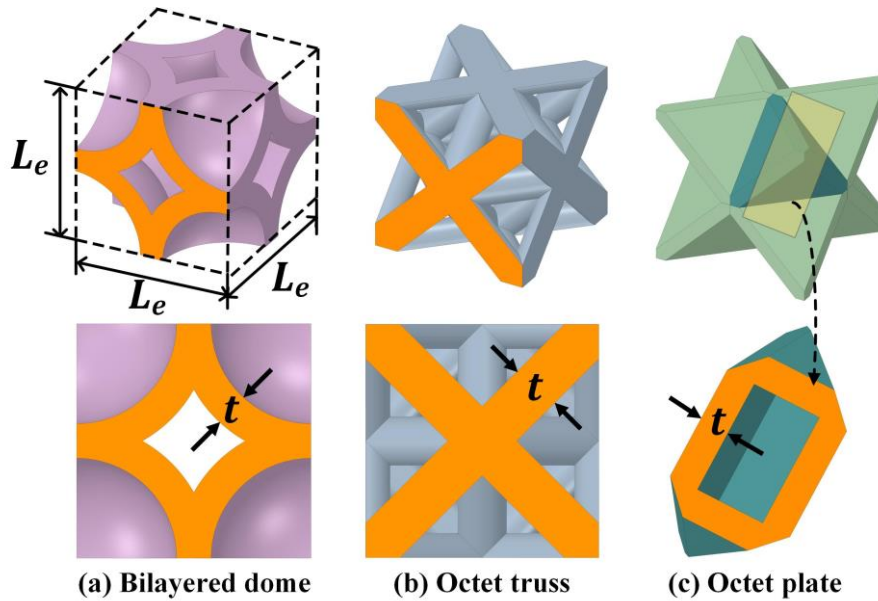


Figure 3-12. Lattice constant L_e and lattice thickness t of representative lattice structures: (a) bilayered dome structure; (b) octet truss structure; (c) octet plate structure.

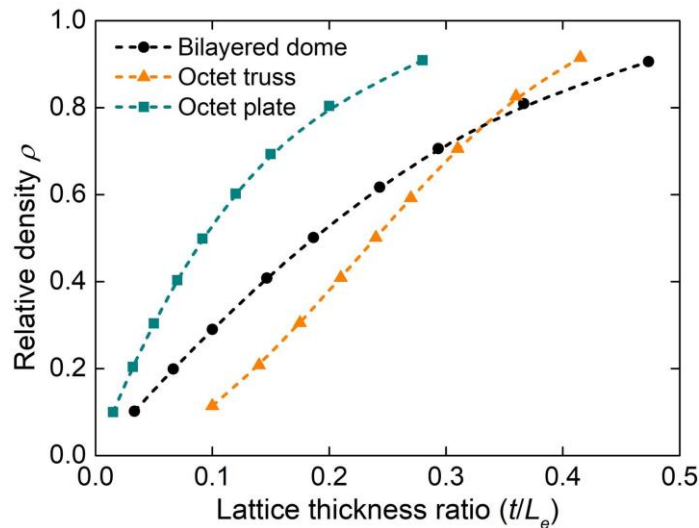


Figure 3-13. Lattice relative density corresponds to lattice thickness ratio.

3.2.3 Evaluation of flexural rigidity and shear strength of unit lattice by FEM

A significant advantage of sandwich sheets is that they have higher weight-specific stiffness than monolithic sheets, but simultaneously, an obvious disadvantage is their poor bendability. To systematically investigate the bending properties, the above two characteristics, that is, the bending stiffness and bendability were mainly concerned here.

As shown in Figure 3-14(a), periodic boundary conditions were adopted for the efficient

evaluation of flexural rigidity. Detailed explanations about the implementation of periodic boundary conditions were discussed in the [Appendix A](#) and [Appendix B](#).

Since the bendability of sandwich sheets is mainly determined by shear resistance, the macroscopic shear strength of lattice structures was evaluated by shear simulation with the boundary conditions illustrated in [Figure 3-14\(c\)](#), in which the detailed descriptions of the boundary conditions were discussed in [chapter 2](#). With the shear stress–strain curve, based on the definition given by [Mohr \(2005\)](#), the intersection of the linear extrapolations of the elastic and elasto-plastic parts was determined to be the macroscopic shear strength as indicated in [Figure 3-14\(d\)](#). The macroscopic shear strength was then compared with the critical value of shear strength to evaluate the initiation of the core shear failure.

The FEM analyses were implemented by static-general algorithm in commercial software ABAQUS, in which face sheet and core were meshed using C3D8R and C3D4 type elements, respectively. To ensure that the results were mesh-independent, a mesh sensitivity analysis was performed. The interaction property between core and face sheet was modelled by a tie contact.

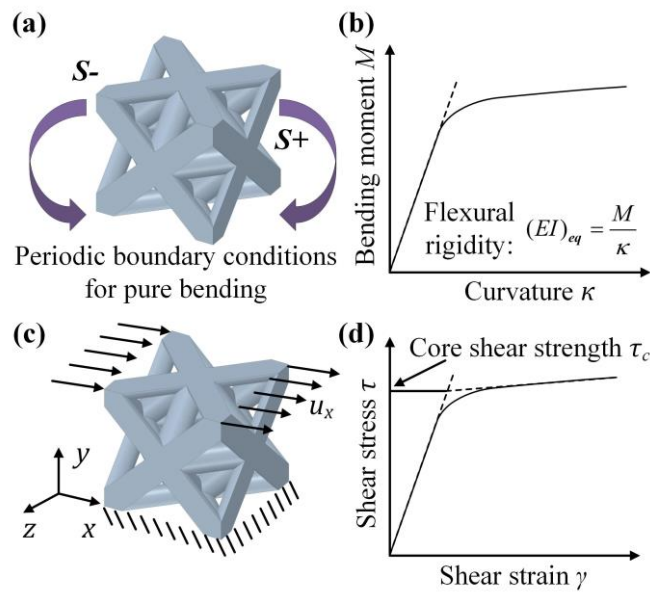


[Figure 3-14](#). Boundary conditions for FEM analyses and determination of flexural rigidity and macroscopic shear strength: (a) pure bending analysis; (b) determination of flexural rigidity from bending moment–curvature curve; (c) shear analysis; (d) determination of shear strength from shear stress–strain curve.

3.2.4 Theoretical prediction of failure modes

For bendable sandwich sheets with the required core shear strength of τ_{re} , the macroscopic core shear strength τ_c that is obtained from FEM analysis in the previous section should be ensured to be sufficient. The required core shear strength of τ_{re} has been deduced in **chapter 2** by Eq. (2-15). So by comparing the macroscopic core shear strength τ_c as obtained by FEM in **section 3.2.2** with the required core shear strength of τ_{re} , the initiation of core shear failure can be judged.

For sandwich sheets with the bilayered dome, octet truss and octet plate cores, the face buckling mode can be illustrated in Figure 3-15. Consider the unsupported region of the face sheet as shown in Figure 3-15(b). Note that the actual unsupported region for the bilayered dome is a circle, which is approximated as an inscribed quadrilateral of this circle so that it is consistent with those of the octet truss and plate lattices, and thus facilitating unified face buckling judgment. As the face buckling mode in Figure 3-15 is similar to that of the sandwich sheets with the truncated dome core in **section 3.1.2.2**, following Eqs. (3-6) to (3-16), the critical value of the gap between attachment point d_{cr} can be determined by Eq. (3-17). Then the designed gap d should be smaller than the critical gap d_{cr} to suppress the face buckling.

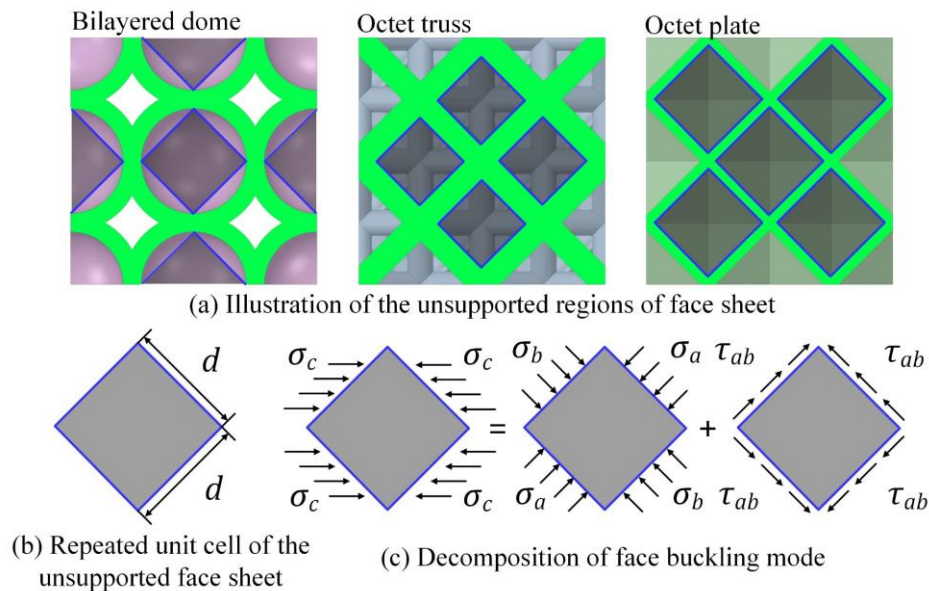


Figure 3-15. Face buckling modes of sandwich sheets with bilayered dome, octet truss and octet plate cores: (a) unsupported regions of face sheet bonded to the bilayered dome, octet

truss and octet plate cores indicated by the grey section; (b) repeated unit cell of unsupported face sheet; (c) face buckling mode decomposed into biaxial compression and shear modes.

3.2.5 Production of specimen and experimental tests

3.2.5.1 Materials

Carbon fiber reinforced nylon (Onyx) was selected to produce the core structures while the face sheet was stainless steel SUS304, of which material properties are shown in Table 3-4. The onyx was selected as it has high strength, toughness, and chemical resistance when printed for the fused deposition modeling (FDM) type 3D printer *MarkTwo* (*Markforged*, USA), which enables the fabrication of complex structures with good quality.

Table 3-4. Mechanical properties of SUS304 and Onyx.

	Young's modulus (GPa)	Poisson's ratio	Yield strength (MPa)	Linear hardening modulus (GPa)
SUS304	200	0.29	215	2.3
Onyx	1.4	0.3	36	2.1

Based on the theoretical analyses in previous sections, it is clear that the failure modes are mainly affected by the core height h_c , face sheet thickness t_f and bending radius R . Here, to experimentally clarify the effects of above parameters on failure modes, core heights of 6 and 8 mm and face sheet thicknesses of 0.3 and 0.5 mm were selected for the fabrication of sandwich sheets.

3.2.5.2 Fabrication of the sandwich sheet

The bilayered dome, octet truss and octet plate core structures with heights of 6 and 8 mm and relative densities of 40% and 50% were fabricated by additive manufacturing. The process parameters for additive manufacturing are listed in Table 3-5. To check the structural accuracy of printed core structures, a 3D measurement system controller (Keyence VR-5000, Japan) was used to measure the lattice thickness. Face sheets were adhesively bonded to the core structures using the one-component epoxy resin IW2460 (3M, USA), which was cured in an autoclave at a temperature of 120°C for 75 minutes. Here, the face sheet of thickness 0.3 mm was bonded with the core structure of relative density 40%, while the face sheet of thickness 0.5 mm was

bonded with the core structure of relative density 50%. Therefore, there are totally 12 types of sandwich sheets composed of three core topologies, two face sheet thicknesses (two core densities) and two core heights.

Table 3-5. Process parameters for additive manufacturing of carbon fibre reinforced nylon.

Description	Value
Material	Carbon fibre reinforced nylon
Nozzle temperature (°C)	275
Bed temperature (°C)	Room temperature
Fill pattern	Solid
Fill density (%)	100
Wall layers	2
Layer thickness (mm)	0.1

3.2.5.3 Three-point bending and L-bending tests

The flexural properties such as bending stiffness and energy absorption capability were evaluated by the three-point bending test using a 50-kN hydraulic servo press (Fujidempa, Japan). Radii of the upper and lower rollers were both 5 mm and the span length was 50 mm. The cross-head speed was 3 mm/min and the total stroke was set to 10 mm. For L-bending test, the radii of the upper and lower dies were 40 and 60 mm, respectively. The clearance between the punch and the die was set to 15 mm and the forming velocity was set to 1 mm/s. The specimen was fixed by setting a clearance of 2 mm between the sample and the blank holder during bending. The lengths of samples for three-point bending and L-bending tests are 96 mm and 192 mm, respectively. The widths of sandwich sheets with core height of 6 and 8 mm were respectively 18 and 24 mm as three unit cells were arranged along the width direction. The configuration of the three-point bending and L-bending tests can be seen in [Figure 3-16](#).

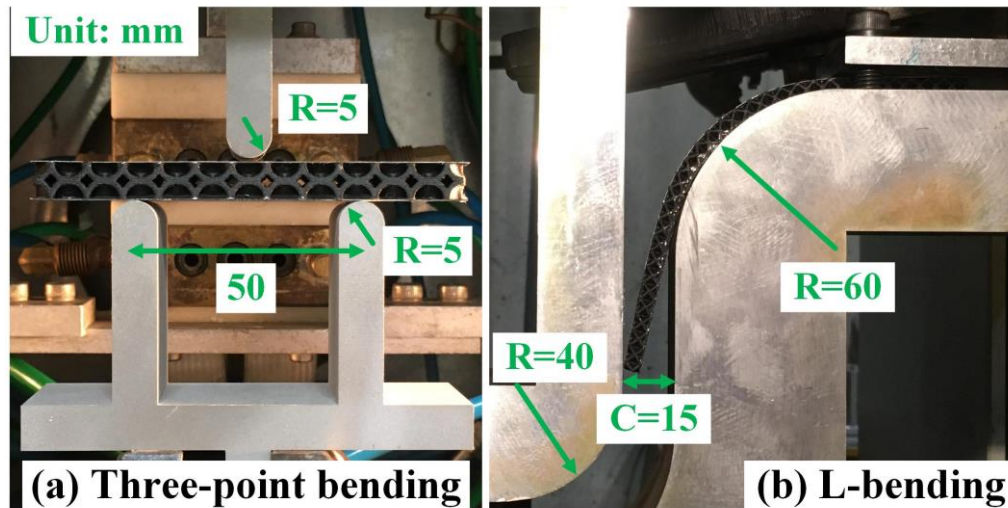


Figure 3-16. Experimental configuration of three-point bending and L-bending tests: (a) three-point bending test; (b) L-bending test.

3.2.6 Results and discussion

3.2.6.1 Produced sandwich sheets

Printed bilayered dome, octet truss and octet plate core structures with relative densities of 40% and 50% and heights of 6 and 8 mm are shown in Figure 3-17. Since the face sheet of thickness 0.3 mm was bonded to core structures of relative density 40% while 0.5 mm face sheet was combined with core structures of relative density 50%, totally 12 types of sandwich sheets were fabricated as shown in Figure 3-18. The lattice cores were observed as shown in Figure 3-19. The measured lattice thicknesses of the printed models were compared with those of the 3D models built by CAD programs to check the structural accuracy of the samples as presented in Figure 3-20. The core structures with larger relative densities and core heights tend to have greater lattice thicknesses, which is consistent with the truth. However, the lattice thicknesses of printed samples are generally slightly larger than those of the 3D models, which may owing to the additional wall layers added during printing process and this will lead to a certain error of measurement.

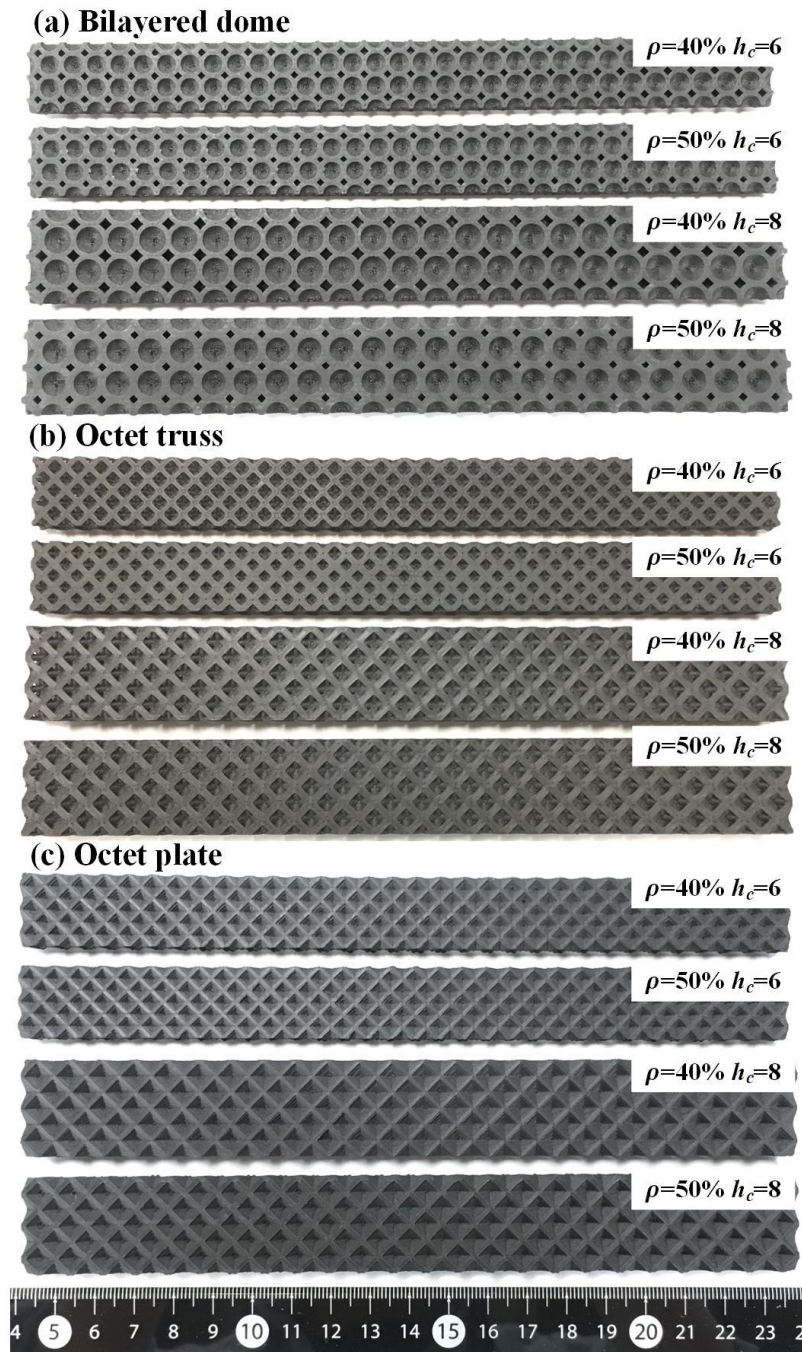


Figure 3-17. Produced bilayered dome, octet truss and octet plate core structures with relative densities of 40% and 50% and core heights of 6 and 8 mm: (a) bilayered dome; (b) octet truss; (c) octet plate.

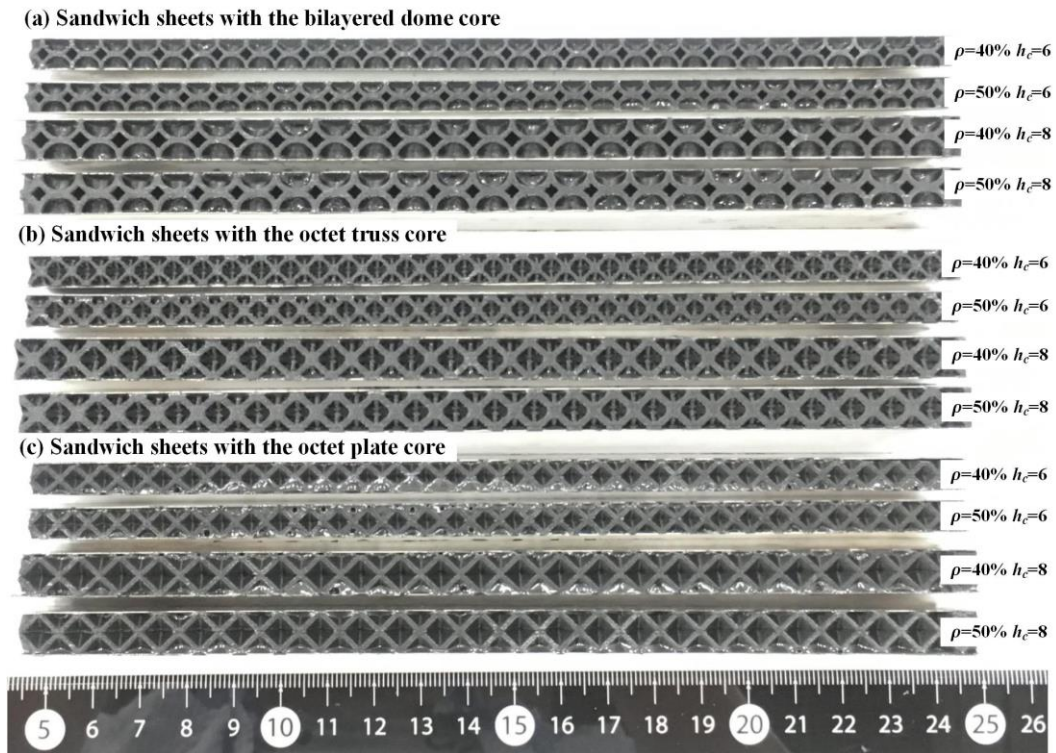


Figure 3-18. Sandwich sheets with bilayered dome, octet truss and octet plate core structures of relative densities of 40% and 50% and core heights of 6 and 8 mm: (a) sandwich sheets with bilayered dome core; (b) sandwich sheets with octet truss core; (c) sandwich sheets with octet plate core.

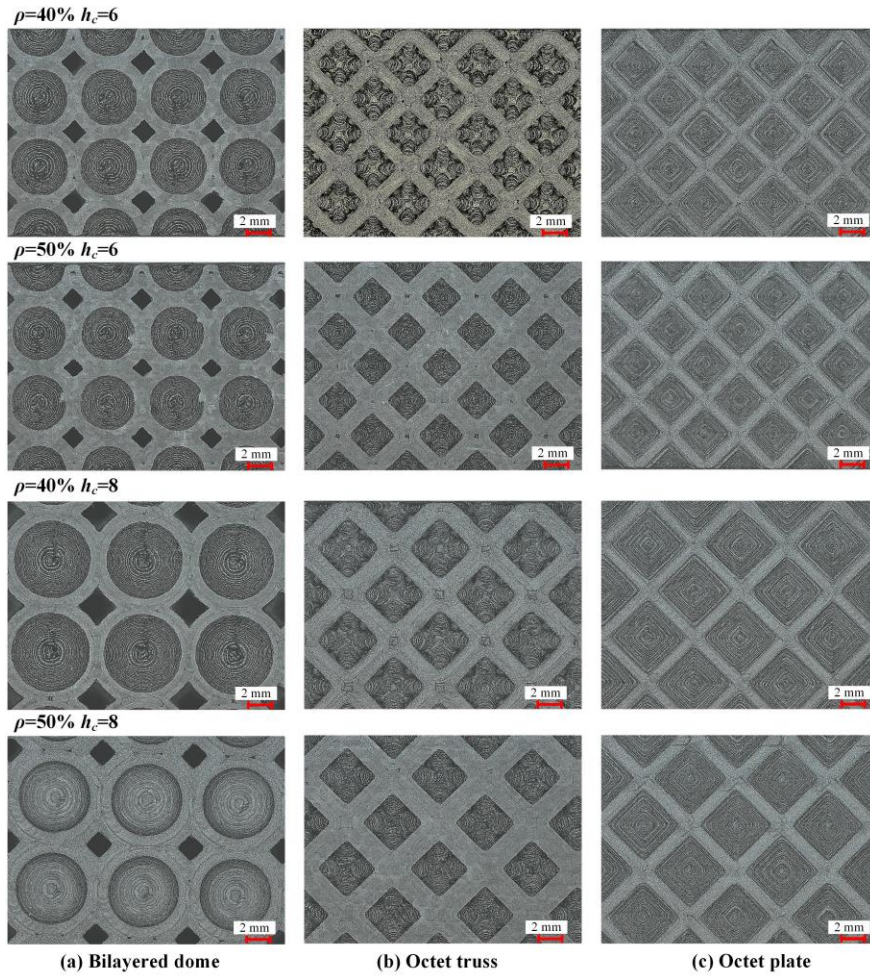


Figure 3-19. Lattice structures observed at a magnification 12 ×: (a) bilayered dome; (b) octet truss; (c) octet plate.

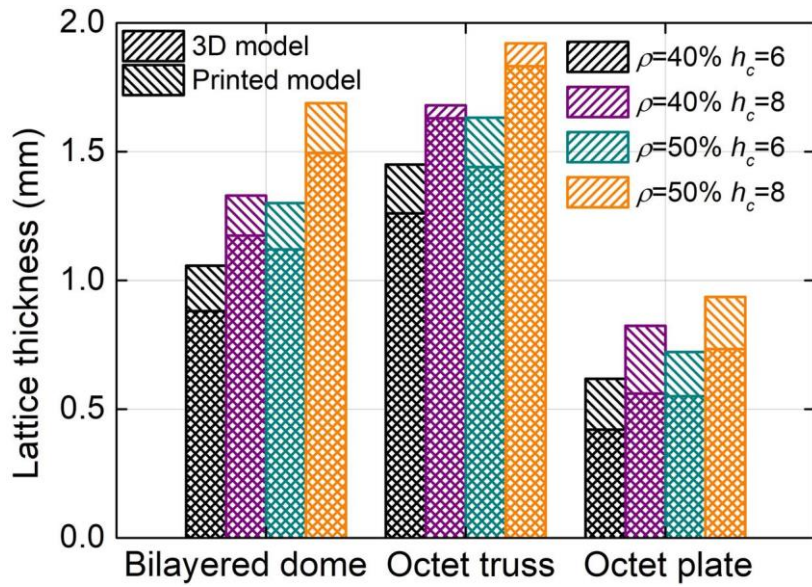


Figure 3-20. Comparison of lattice thicknesses of printed models and 3D models built by

CAD programs.

3.2.6.2 Mechanical properties

The specific bending moment–curvature curves of bilayered dome, octet truss and plate lattice structures are shown in [Figure 3-21](#), in which the elastic range is zoomed in to highlight the difference. The specific flexural rigidity was calculated as shown in [Figure 3-22](#). For the same core density and height, the octet plate exhibits highest flexural rigidity and the octet truss displays superior flexural rigidity than the bilayered dome. The specific bending moment–curvature curves for sandwich sheets with bilayered dome, octet truss and octet plate cores are shown in [Figure 3-23](#), from which the calculated specific flexural rigidity is presented in [Figure 3-24](#). It is found that sandwich sheets with the bilayered dome, octet truss and octet plate cores have very similar specific flexural rigidity, which indicates that the flexural rigidity is mainly contributed by face sheet while the core topologies have little effect. This is reasonable, especially when the face sheet stiffness is much higher than the core material and thus the flexural rigidity is mainly attributed to the face sheets distributed in outer layer. For the same core density and height, sandwich sheets of face sheet thickness 0.5 mm generally have a higher specific flexural rigidity than those of face sheet thickness 0.3 mm. The specific flexural rigidity of the sandwich sheets and cores is compared in [Figure 3-25](#), in which it is clearly shown that the specific flexural rigidity of cores is much improved by sandwiching them between face sheets. For 0.3 mm face sheet, the specific flexural rigidity of the sandwich sheets is around 75-200 times higher than that of the core structures, while it is up to 100-250 times for 0.5 mm face sheet. This is verified by the stress distribution contours of the core structures and sandwich sheets in [Figure 3-26](#), in which the normal stress of the sandwich sheets is much higher than that of the core structures at the same bending curvature of 0.2 rad/m.

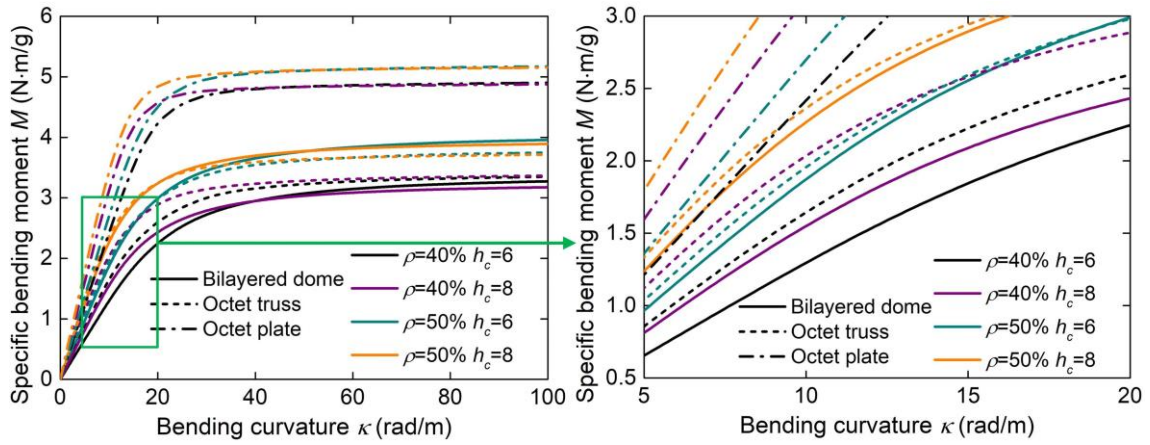


Figure 3-21. Specific bending moment–curvature curves of bilayered dome, octet truss and octet plate structures.

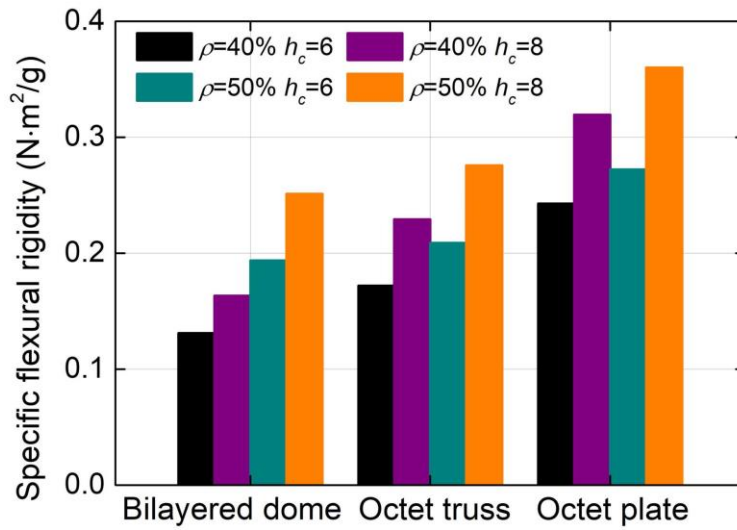


Figure 3-22. Specific flexural rigidity of bilayered dome, octet truss and octet plate structures.

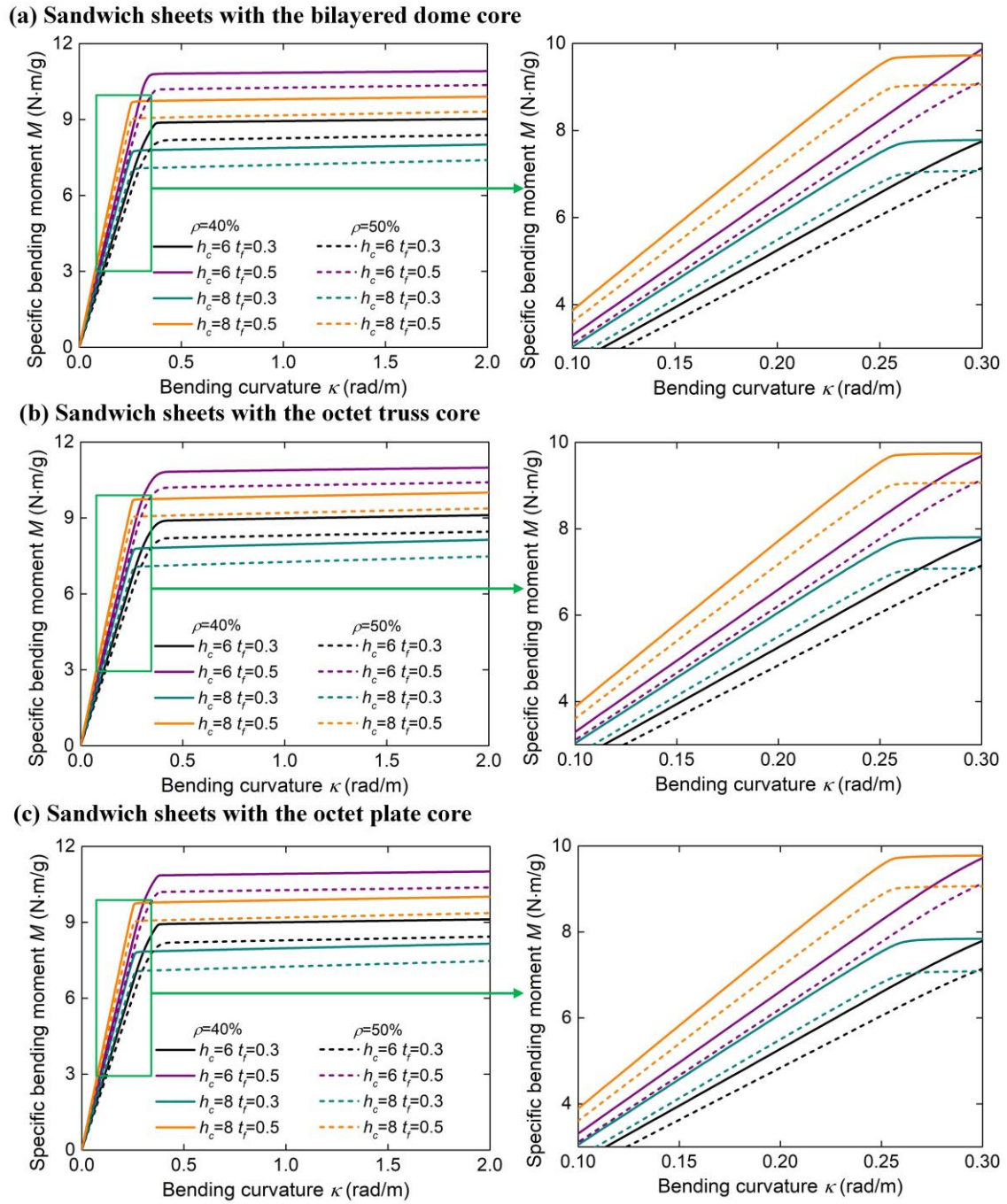


Figure 3-23. Specific bending moment–curvature curves: (a) sandwich sheets with bilayered dome core; (b) sandwich sheets with octet truss core; (c) sandwich sheets with octet plate core.

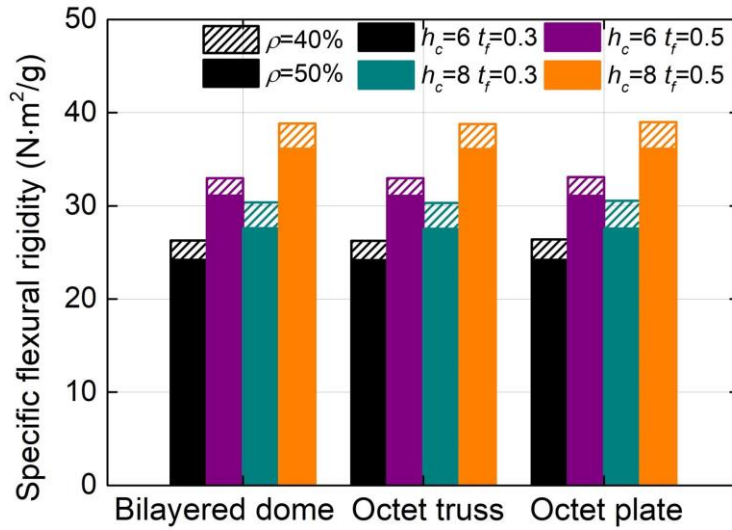


Figure 3-24. Specific flexural rigidity of sandwich sheets with bilayered dome, octet truss and octet plate cores.

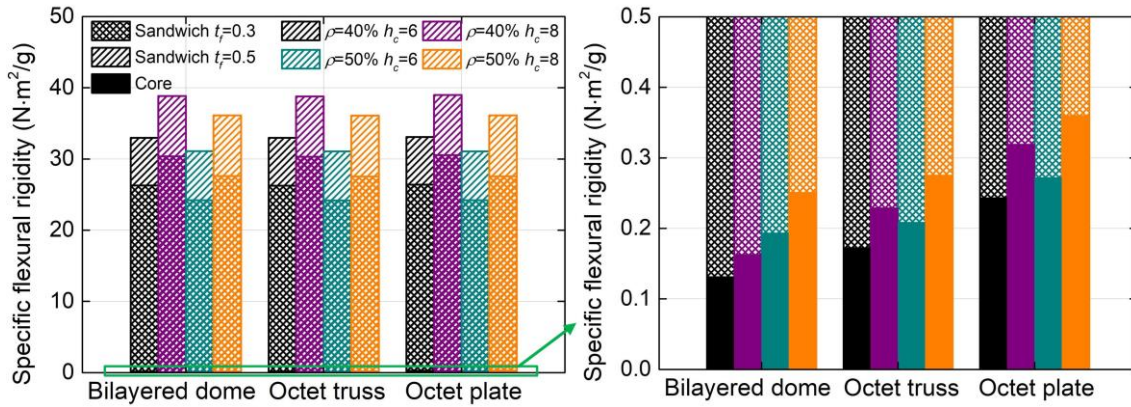


Figure 3-25. Comparison of specific flexural rigidity between sandwich sheets and cores.

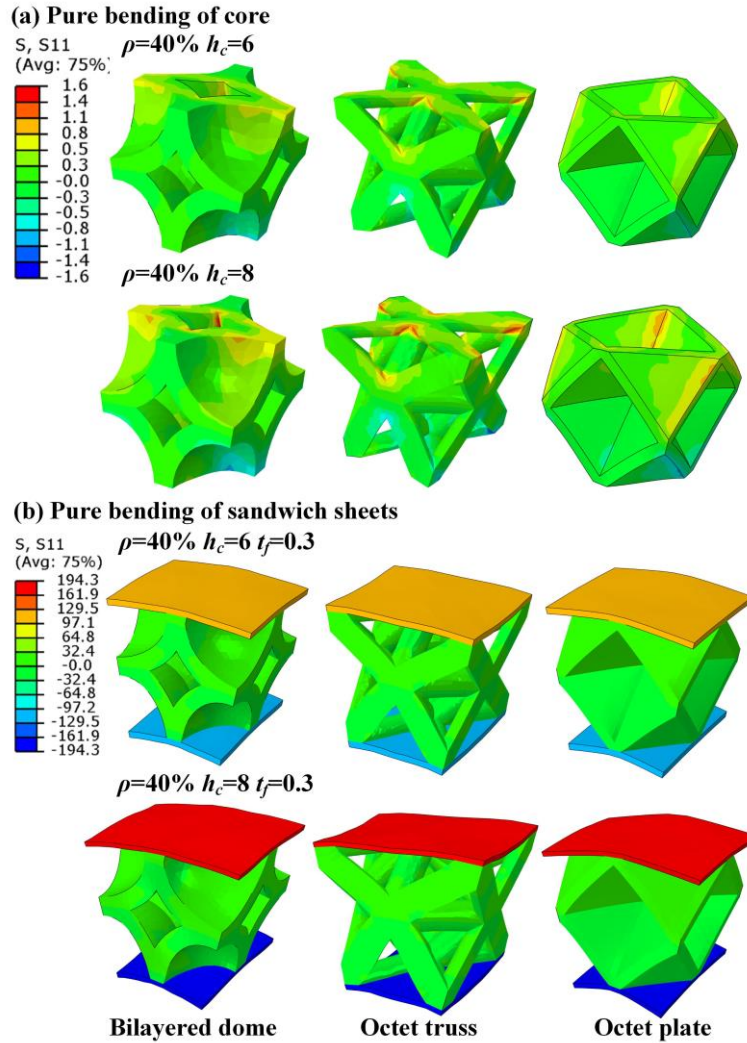


Figure 3-26. Stress distribution contours of the core structures and sandwich sheets: (a) core structures; (b) sandwich sheets.

During three-point bending test, dominant failure modes were captured as shown in Figure 3-27. Core indentation in the center is generally observed for sandwich sheets with the bilayered dome core, which is due to the relatively larger gap between attachment points that may not provide sufficient support to the face sheet. Owing to insufficient shear strength of octet truss, core fracture is the dominant failure mode. Two typical failure behaviors were observed for the octet plate core. Core fracture is the main failure mode at relative density of 40% while the face buckling becomes the dominant failure for relative density of 50%. Core fracture is due to the insufficient core shear strength at a lower density while face buckling is owing to the fact that the gap between attachment points is too large.

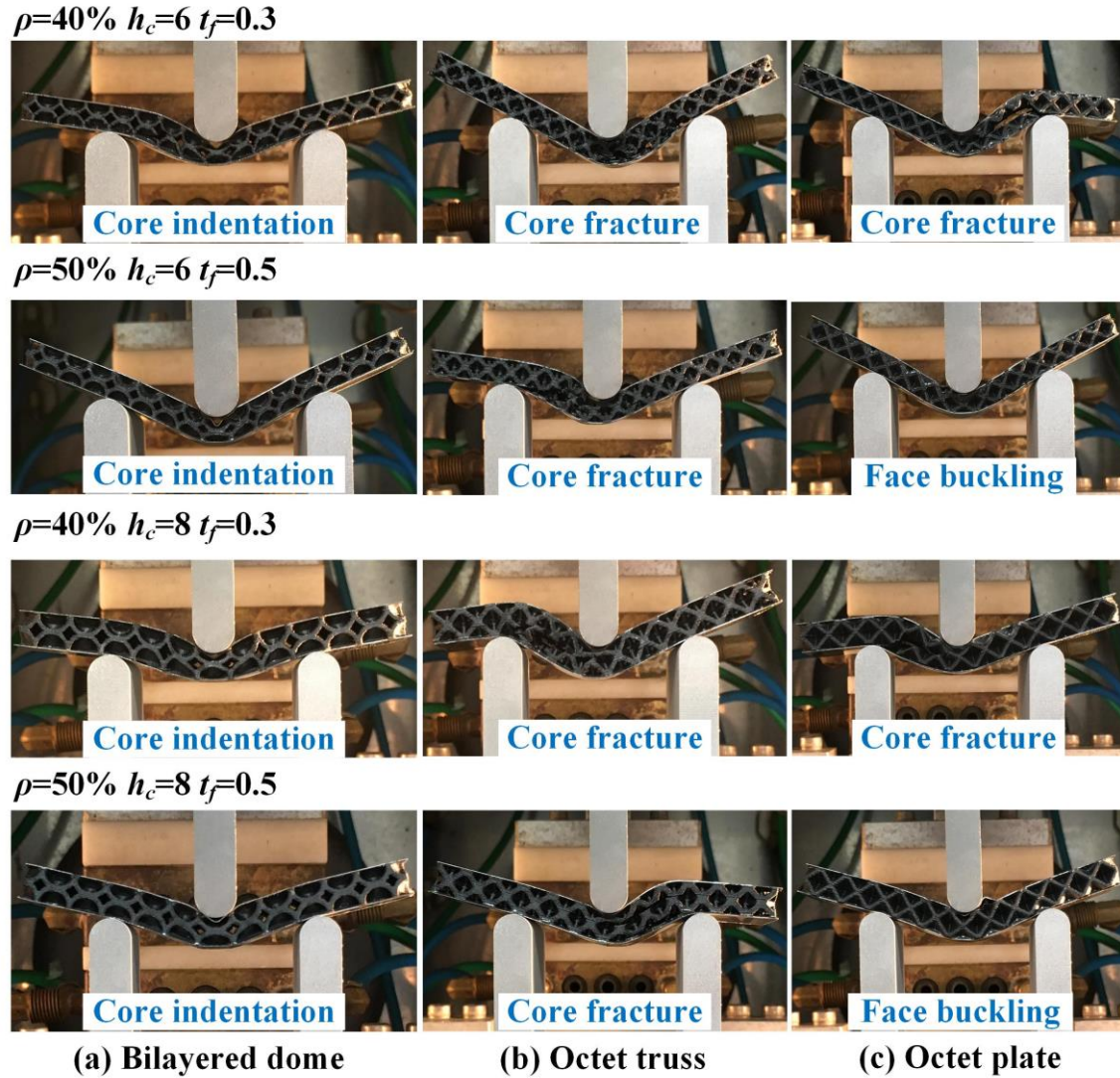


Figure 3-27. Dominant failure modes during three-point bending process.

The experimental curves are shown in Figure 3-28, in which the load within the elastic range is zoomed in to highlight the difference. From the load versus displacement curves, the stiffness and absorbed energy were obtained and presented in Figure 3-29. Sandwich sheets with the octet plate core have best mechanical performance, while those with the bilayered dome core are slightly better than those with the octet truss core. Under the four combinations listed in Figure 3-29, the bending stiffness of octet plate core sandwich sheets are respectively 82.08%, 68.33%, 42.01% and 48.13% over those with the octet truss core, while the absorbed energy are improved by 205.93%, 66.25%, 34.40% and 106.61%, respectively. Compared with bilayered dome core, the bending stiffness of the octet plate core sandwich sheets are respectively improved by 62.58%, 33.68%, 36.53% and 15.08%, while the absorbed energies

are enhanced by 39.48%, 29.17%, 9.02% and 8.11%, respectively. Recall that sandwich sheets with above three core topologies display very close flexural rigidity as found in FEM. However, the specific three-point bending stiffness are found to have certain difference. This is reasonable as the three-point bending stiffness not only depends on the flexural rigidity but also is related to the out-of-plane shear rigidity deduced by [Deshpande and Fleck \(2001\)](#):

$$K = \left\{ \frac{l^3}{48(EI)_{eq}} + \frac{l}{4(AG)_{eq}} \right\}^{-1} \quad (3-19)$$

Eq. (3-19) indicates that the three-point bending stiffness K is determined by both the flexural rigidity $(EI)_{eq}$ and out-of-plane shear rigidity $(AG)_{eq}$. Especially when the span length l is small, the contribution of $(AG)_{eq}$ to three-point bending stiffness cannot be ignored. This explains why the flexural rigidity and three-point bending stiffness show certain different trends.

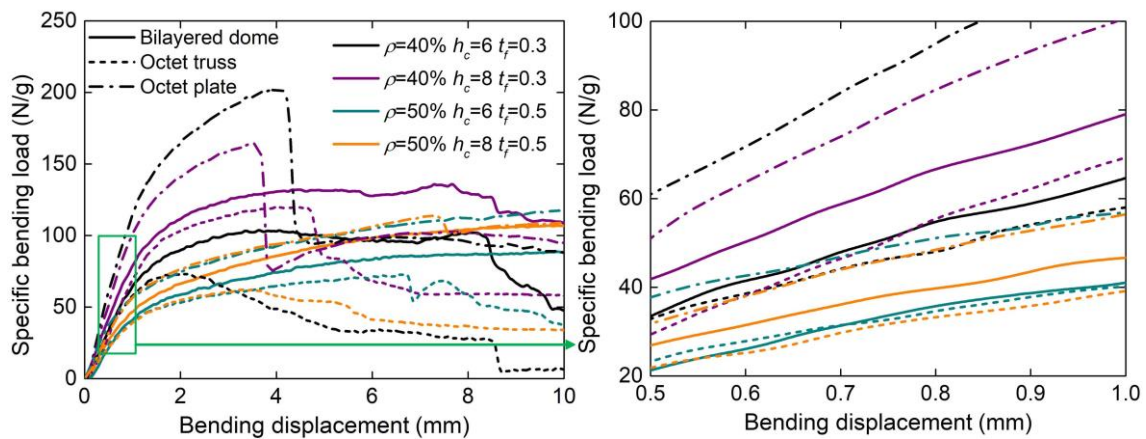


Figure 3-28. Results of three-point bending tests.

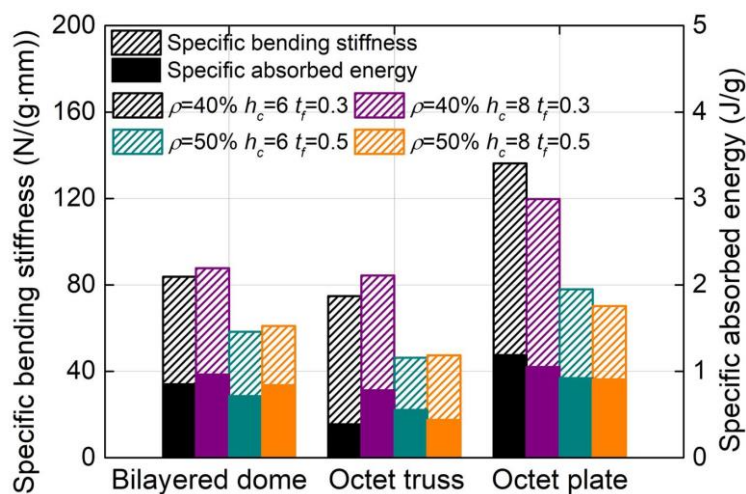


Figure 3-29. Stiffness and absorbed energy from three-point bending tests.

3.2.6.3 Bendability

The shear stress–strain curves of bilayered dome, octet truss and plate lattice structures at relative densities from 10% to 90% are given in Figure 3-30, from which the macroscopic shear strengths were obtained using the approach described in section 3.2.2. The macroscopic core shear strengths of bilayered dome, octet truss and octet plate of relative densities from 10% to 60% are shown in Figure 3-30(d). It can be seen that the shear strengths are proportional to the relative density, and the octet plate generally has the highest shear strength while the octet truss and bilayered dome have very close shear strengths. This indicates that, from the viewpoint of shear failure, the octet plate is more suitable to be used as the core structure as it has higher shear resistance.

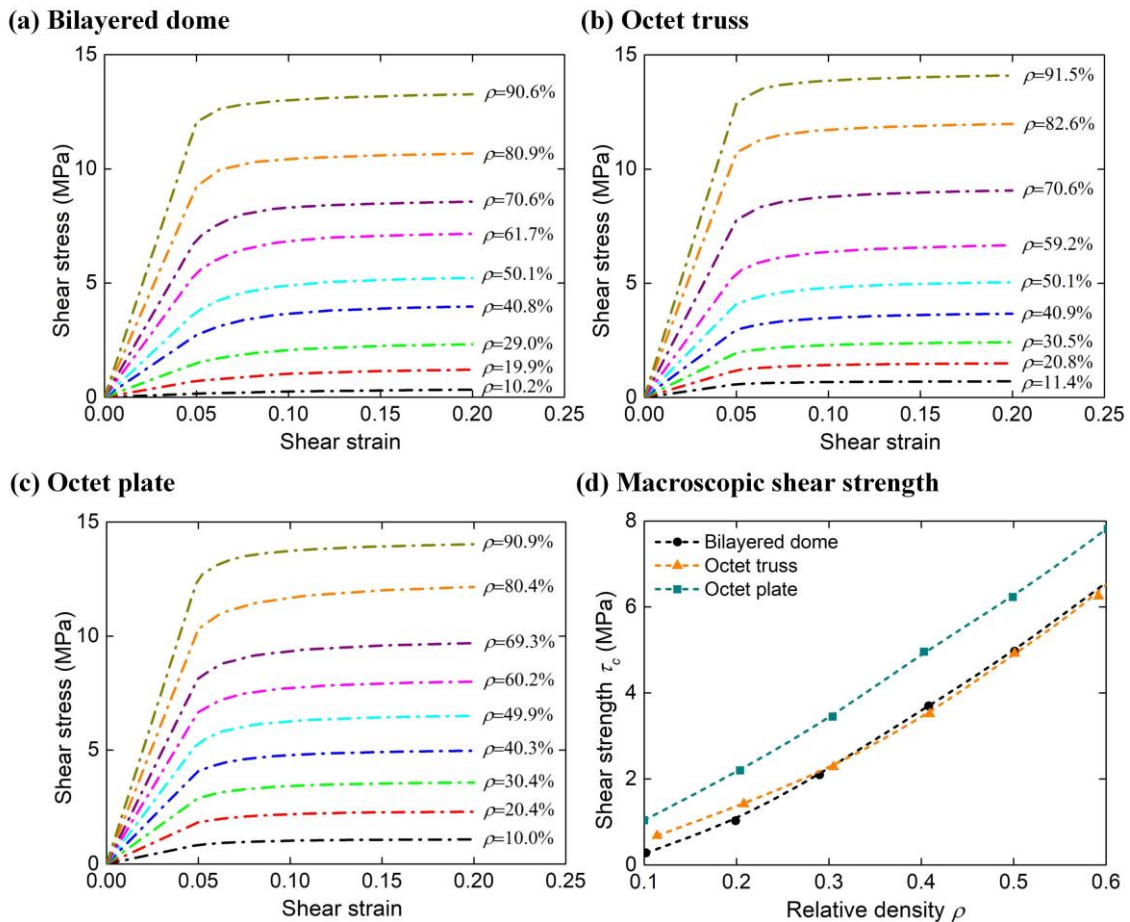


Figure 3-30. Shear stress–strain curves of bilayered dome, octet truss and plate lattice structures at various relative densities: (a) bilayered dome; (b) octet truss; (c) octet plate; (d)

macroscopic shear strength.

With above core shear strengths (τ_c) and required core shear strengths (τ_{re}) that were theoretically calculated by Eq. (2-15), the shear strength ratio (τ_c/τ_{re}) was used as the indicator to evaluate whether the core shear failure will be triggered or not. If this ratio is higher than 1, namely the core shear strength is above the required, then the core shear failure is suppressed and vice versa. Note that, with the consideration of the clearance between punch and die, the actual bending radius (defined as $R+C-H$) was adopted for the computation of the required core shear strength. R is the lower die radius, C is the clearance between forming tools and H is thickness of sandwich sheets. As shown in Figure 3-31, the shear strength ratios were calculated for bending radii of 30 and 60 mm, 0.3 and 0.5 mm face sheet thicknesses, 6 and 8 mm core heights and core relative densities from 10% to 90%, in which the red dashed line was used to delimit the critical line of core shear failure. With Figure 3-31, it is convenient to judge whether the core shear failure will be caused or not at given bending conditions. For example, Figure 3-31(c) can be referred to if we would like to know whether the core shear failure will occur for 40% core relative density, 6 mm core height and 0.3 mm face sheet thickness at a bending radius of 60mm, in which it is clearly shown that core shear failure will not happen as all the points under above conditions are above the red dashed line.

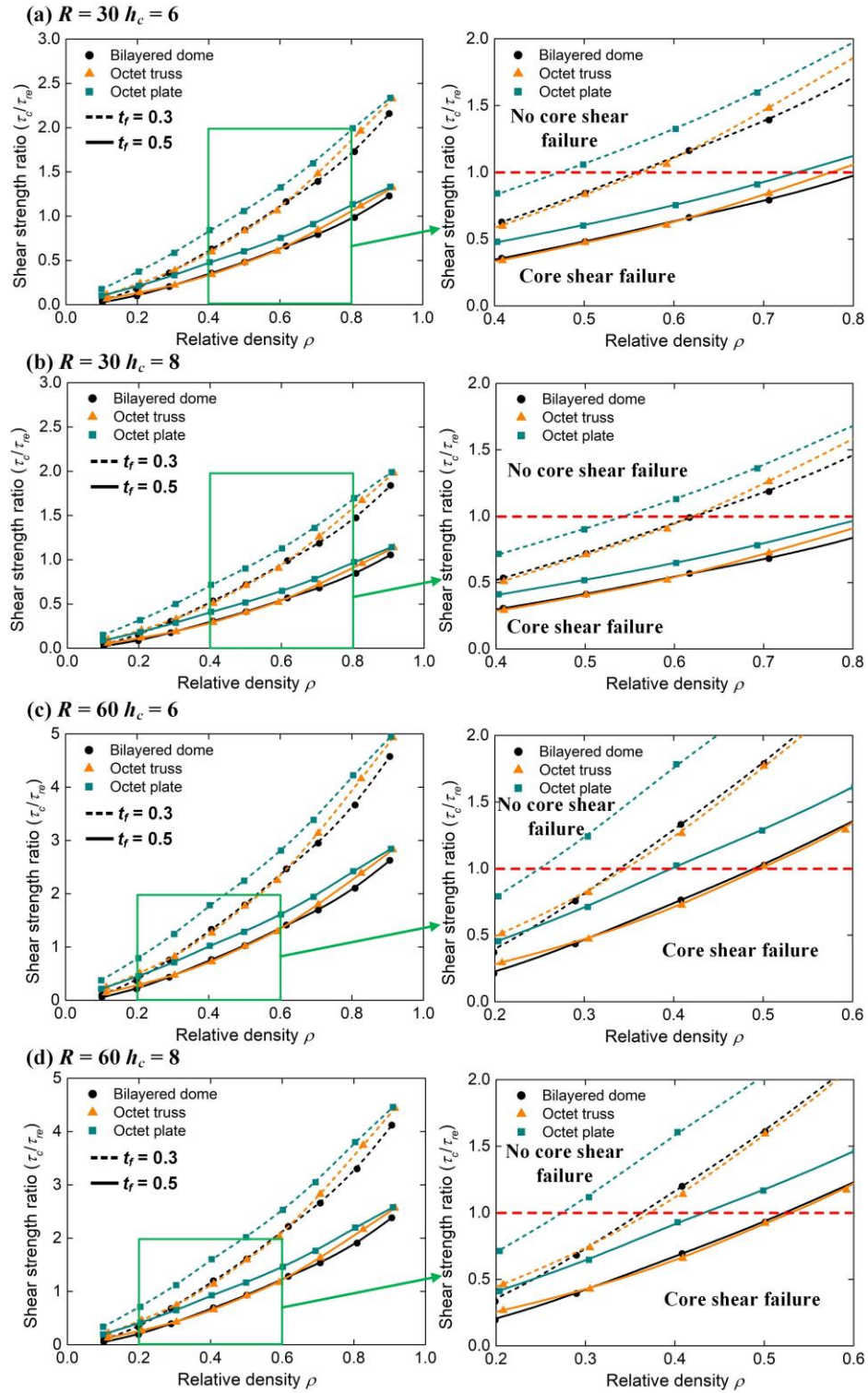


Figure 3-31. Shear strength ratios (τ_c/τ_{re}) calculated for 30 and 60 mm bending radii, 0.3 and 0.5 mm face sheet thicknesses, 6 and 8 mm core heights and 10% to 90% core relative densities for the judgement of core shear failure.

For the prediction of face buckling, the gap ratios (d/d_{cr}) was adopted as the indicator,

which were calculated as shown in Figure 3-32, in which the red dashed line is the critical line of face buckling. Similarly, the face buckling can be easily judged by referring to this map. For instance, Figure 3-32(c) indicates that the face buckling will occur at 40% core relative density, 6 mm core height, 0.3 mm face sheet thickness when the bending radius is 60 mm as all the gap ratios corresponding to above conditions are above the red dashed line.

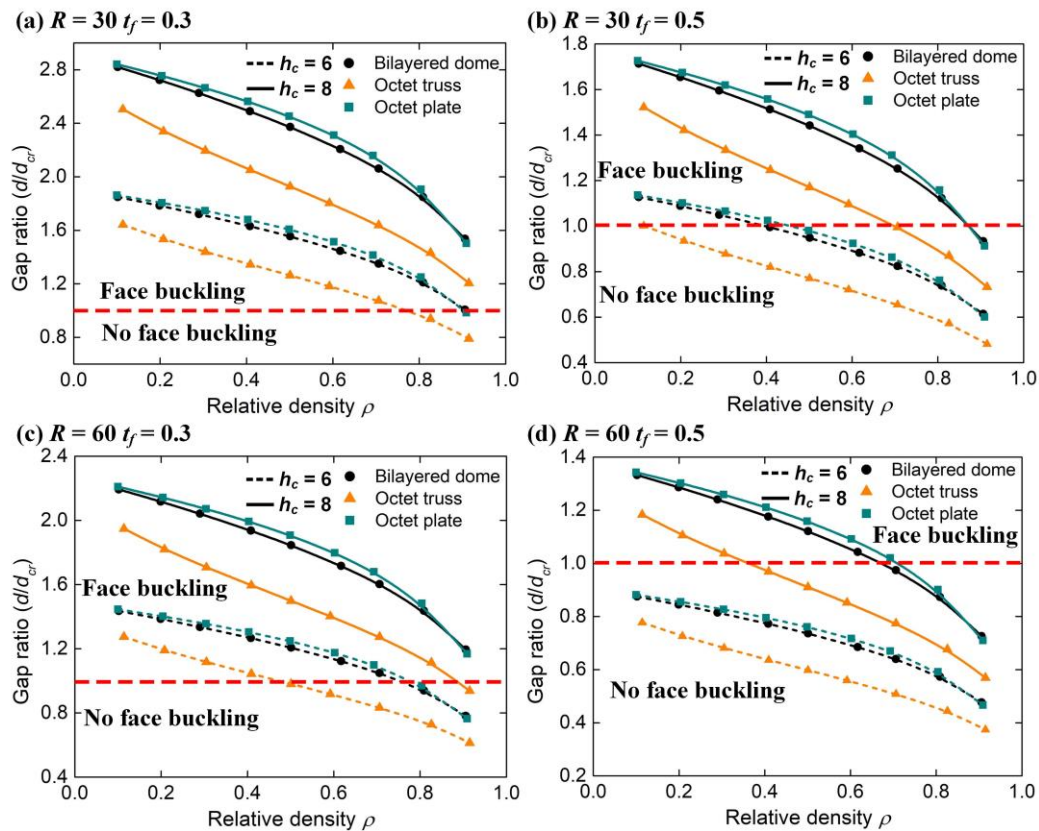
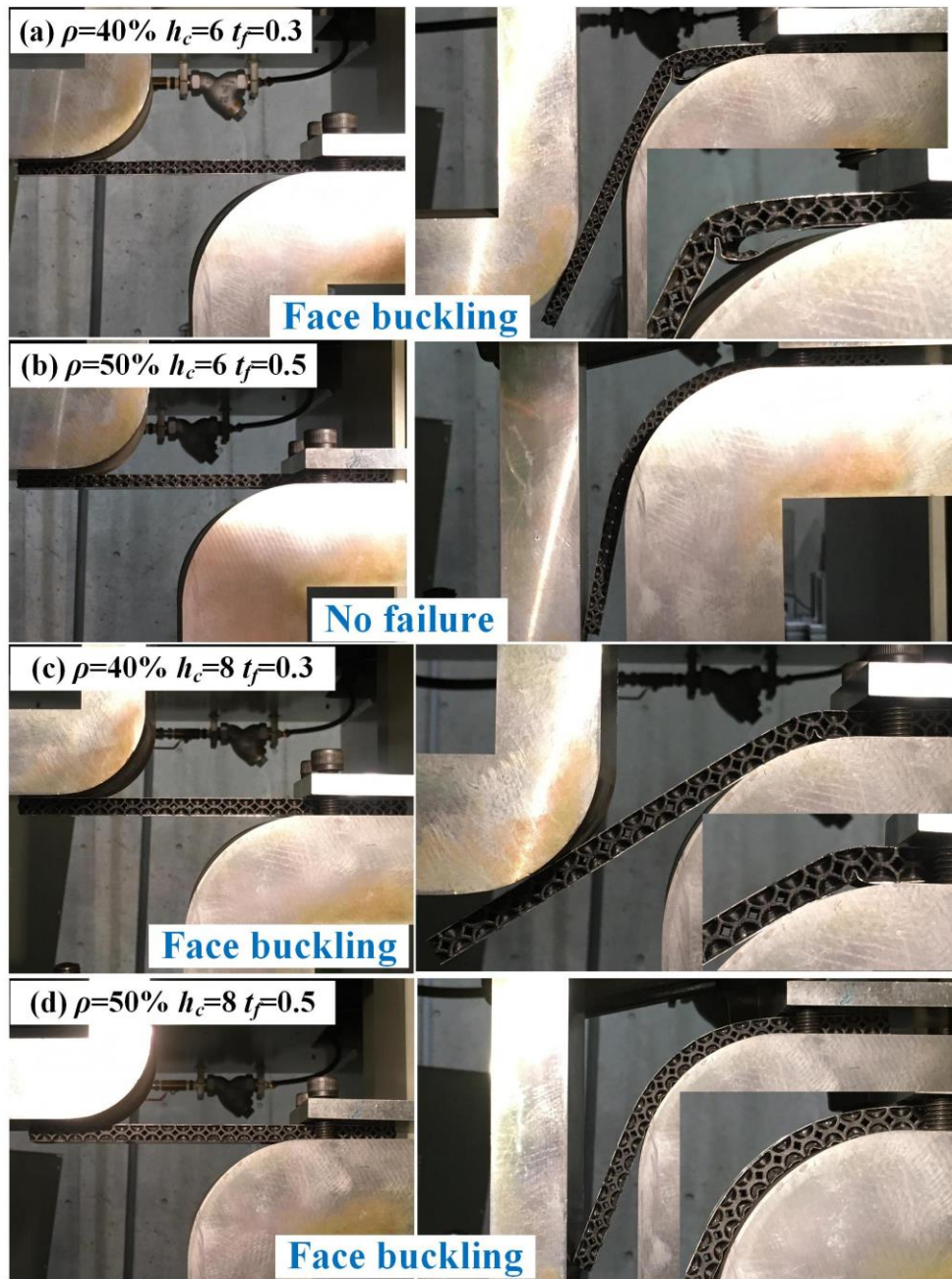


Figure 3-32. Gap ratios (d/d_{cr}) calculated for 30 and 60 mm bending radii, 0.3 and 0.5 mm face sheet thicknesses, 6 and 8 mm core heights and 10% to 90% core relative densities for the evaluation of face buckling.

To experimentally validate the theoretical models, the L-bending tests were conducted at a 60 mm bending radius. Tested specimens have 40% and 50% core relative densities, 6 and 8 mm core heights and 0.3 and 0.5 mm face sheet thicknesses. Figure 3-33 and Figure 3-34 show the L-bending processes and deformed sandwich sheets having bilayered dome cores. For easier expression, condition (a), (b), (c) and (d) were respectively used to represent the forming situations (a), (b), (c) and (d) shown in the figures. It is found that face buckling is the main failure mode in conditions (a), (c) and (d), while the sandwich sheet can be well bent without

failure in condition (b).



Bending of sandwich sheets with the bilayered dome core

Figure 3-33. Deformation of specimens having the bilayered dome core.

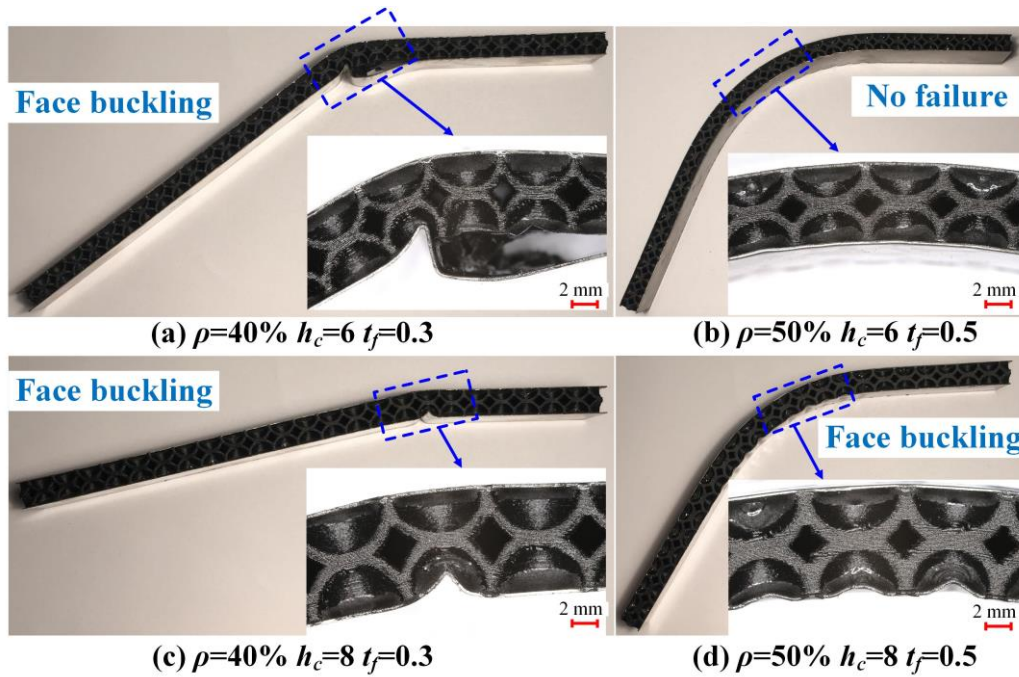


Figure 3-34. Deformed specimens having the bilayered dome core after L-bending.

The L-bending processes of specimens having the octet truss core and the deformed sandwich sheets are shown in Figure 3-35 and Figure 3-36, respectively. It is indicated that face buckling is caused under condition (a) while core shear failure under conditions (c) and (d). The sandwich sheet with the octet truss core can be well bent without any failure in condition (b).

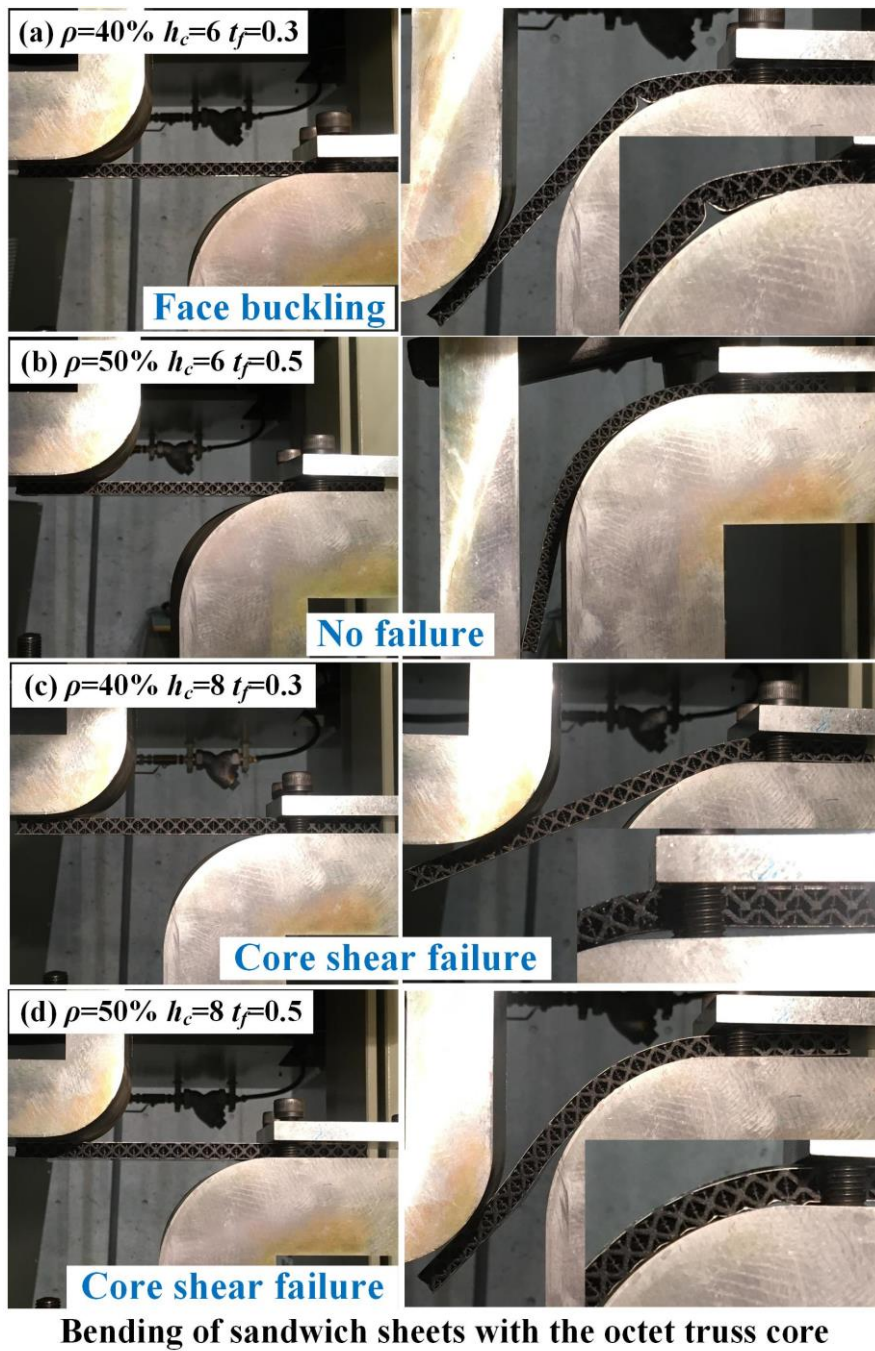


Figure 3-35. Deformation of specimens having the octet truss core during L-bending.

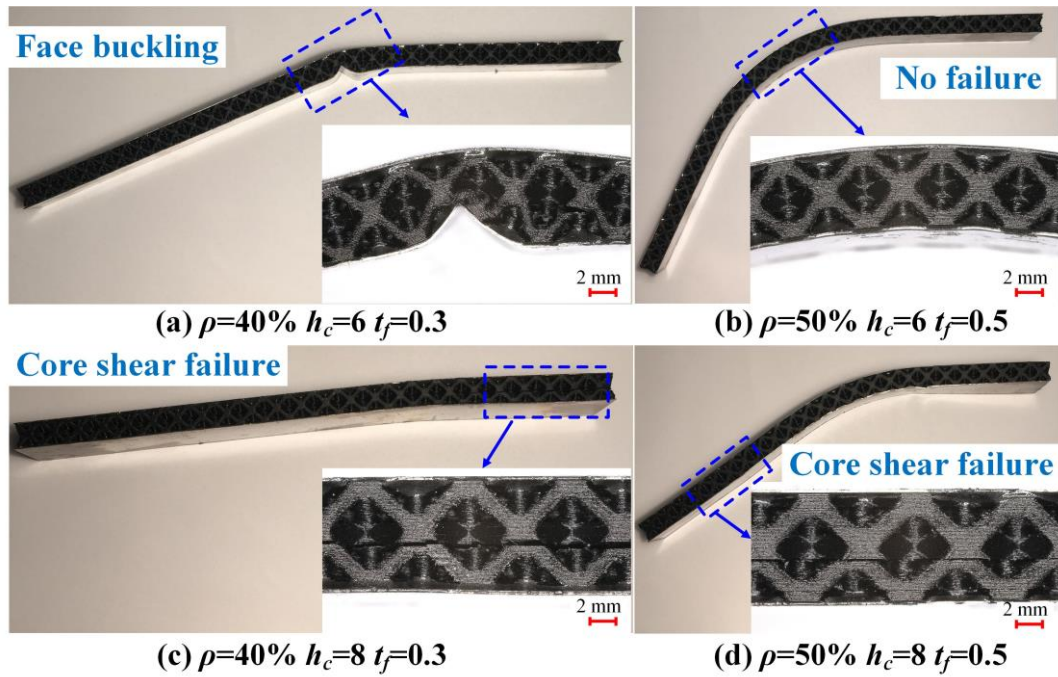


Figure 3-36. Deformed specimens having the octet truss core after L-bending.

Figure 3-37 and Figure 3-38 show the L-bending processes of specimens having the octet plate core and the deformed sandwich sheets after L-bending, respectively. Face buckling occurred in conditions (a), (c) and (d), and the specimen with the octet plate core can be well bent without failure in condition (b).



Bending of sandwich sheets with the octet plate core

Figure 3-37. Deformation of specimens having the octet plate core during L-bending.

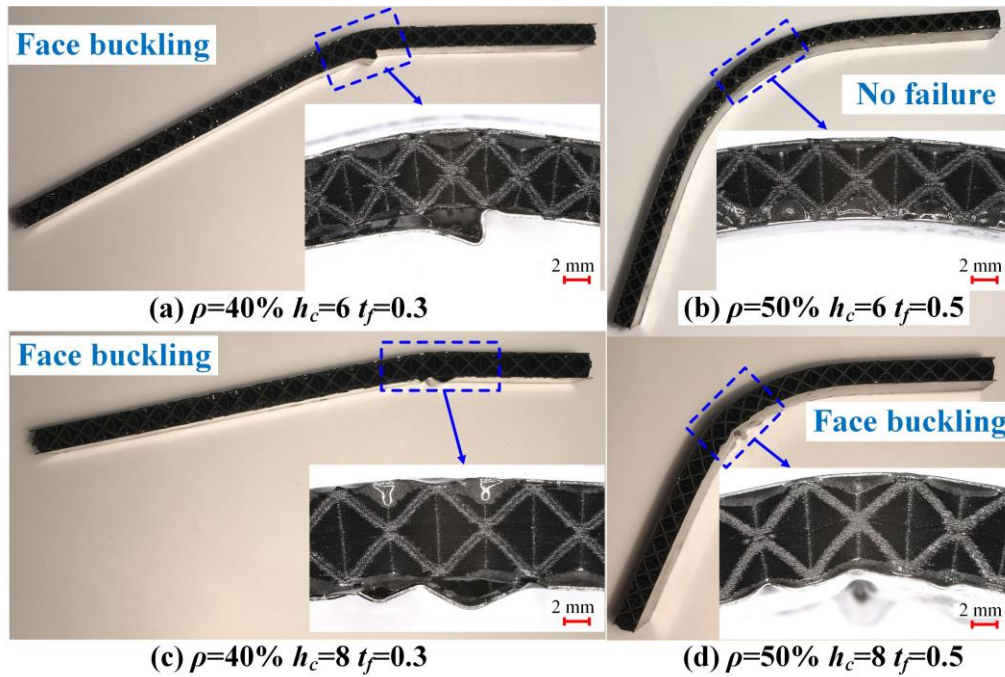


Figure 3-38. Deformed specimens having the octet plate core after L-bending.

The theoretically predicted failure modes and experimental results are summarized in Figure 3-39, in which the theoretical predictions agree well with the experimental results, except for the situation highlighted by the blue texts. In this case, the core shear failure rather than the face buckling is caused, which is owing to the deteriorated shear strength between layers induced in the printing process. The theoretical models can well predict the failure modes of sandwich sheets with 3D hollow cores during bending and thus they can be used to determine the design map for bendable sandwich sheets.

Sandwich core topology	$h_c=6$		$h_c=8$	
	$\rho=40\%$ $t_f=0.3$	$\rho=50\%$ $t_f=0.5$	$\rho=40\%$ $t_f=0.3$	$\rho=50\%$ $t_f=0.5$
Bilayered dome Theory	Face buckling	No failure	Face buckling	Face buckling
Bilayered dome Experiment	Face buckling	No failure	Face buckling	Face buckling
Octet truss Theory	Face buckling	No failure	Face buckling	Core shear failure
Octet truss Experiment	Face buckling	No failure	Core shear failure	Core shear failure
Octet plate Theory	Face buckling	No failure	Face buckling	Face buckling
Octet plate Experiment	Face buckling	No failure	Face buckling	Face buckling

Figure 3-39. Summarized failure modes in theoretical predictions and experimental tests.

3.2.7 Conclusion of section 3.2

The effects of core topologies, core heights, core relative densities and face sheet thicknesses on mechanical properties and bendability of sandwich sheets with 3D printed CFRP lattice cores originating from basic topologies of spherical shell, tetrahedral truss and tetrahedral plate were systematically investigated. Octet plate has the highest specific flexural rigidity and the specific flexural rigidity of the octet truss is higher than that of the bilayered dome. The specific flexural rigidity of sandwich sheets is up to 75-250 times higher than that of the core. Sandwich sheets with the octet plate core have best mechanical performance, while those with the bilayered dome core are slightly better than those with the octet truss core. The shear strength of the octet plate is highest while octet truss and bilayered dome have very similar shear strengths, indicating that the octet plate is more suitable to be the core structures in terms of its higher shear resistance. The failure modes during bending can be well predicted by proposed theoretical models. When the face sheet thickness is 0.5 mm, the sandwich sheets with bilayered dome, octet truss and octet plate cores of relative density of 50%, height of 6 mm are well bendable subjected to a bending radius of 60 mm. This study demonstrates the feasibility of design and production of bendable sandwich sheets with 3D lattice cores based on the theoretical and experimental validations. The bendable sandwich sheets produced in this

study can be used to replace conventional heavy monolithic sheets in various engineering applications, which is expected to satisfy the high demand for the lightweight functional materials.

3.3 Summary

The effects of material properties of sandwich constituents, the sandwich geometries, forming tool geometries, core shapes, etc. on forming behaviors of sandwich sheets were investigated by systematically experimental tests and theoretical analyses for the effective design and efficient fabrication process. For the improvement of mechanical performance and potential functionality of sandwich sheets, the functional lattice structures were introduced into the core structure. The effects of lattice core topologies and relative densities on the mechanical property and forming behavior were also extensively investigated.

In **section 3.1**, for the sandwich sheets with a truncated dome core proposed in **chapter 2**, theoretical analyses were conducted to determine the conditions required for successfully forming them into curved shapes. The design maps for bendable metal face/CFRP core sandwich sheets with the truncated dome core were developed based on the theoretical predictions of core shear failure and face buckling. By referring to the design maps, bendable sandwich sheets could be effectively and efficiently designed and thus could be very valuable for designer and manufacturer. Experimental results of formability tests agree well with the theoretical predictions, which demonstrates the validity of the theoretical models. Sandwich sheets with both A2017P and SUS304 face sheets of a thickness of 0.5 mm can be bent without any failure at a bending radius of 60 mm.

The bending properties of sandwich sheets with 3D printed CFRP lattice cores originating from basic topologies of spherical shell, tetrahedral truss and tetrahedral plate were systematically investigated in **section 3.2**. The effects of core topologies, core relative densities, core heights, face sheet thicknesses on structural properties were clarified. The common failure modes during bending of sandwich sheets, such as face buckling and shear failure of core, were deeply investigated by theoretical models and experimental tests. At a prescribed radius of 60 mm, the sandwich sheets with the bilayered dome, octet truss and plate lattice cores of relative density of 50%, height of 6 mm and face sheet thickness of 0.5 mm are bendable. The feasibility of design and production of bendable sandwich sheets with 3D lattice cores is demonstrated based on the theoretical and experimental validations. The designed bendable sandwich sheets

can be adopted to replace conventional heavy monolithic metal sheets in various engineering applications, which is anticipated to fulfill the high demand for lightweight functional materials.

3.4 References

- Ahn, D.-G., 2015. Research trends of metallic sandwich plates with single layer periodically repeated metallic inner structures (PRMIS)-focused on design, manufacturing and formability. *International Journal of Precision Engineering and Manufacturing-Green Technology* 2, 377-391.
- Berger, J., Wadley, H., McMeeking, R., 2017. Mechanical metamaterials at the theoretical limit of isotropic elastic stiffness. *Nature* 543, 533-537.
- Besse, C.C., Mohr, D., 2012. Plasticity of formable all-metal sandwich sheets: Virtual experiments and constitutive modeling. *International Journal of Solids and Structures* 49, 2863-2880.
- Bruschi, S., Cao, J., Merklein, M., Yanagimoto, J., 2021. Forming of metal-based composite parts. *CIRP Annals* 70, 567-588.
- Cai, Z.-Y., Zhang, X., Liang, X.-B., 2018. Multi-point forming of sandwich panels with egg-box-like cores and failure behaviors in forming process: analytical models, numerical and experimental investigations. *Materials & Design* 160, 1029-1041.
- Deshpande, V.S., Fleck, N., 2001. Collapse of truss core sandwich beams in 3-point bending. *International Journal of Solids and Structures* 38, 6275-6305.
- Dilthey, U., Ghandehari, A., Kopp, R., Hohmeier, P., Beiss, P., Iglesias Figueredo, E., El-Magd, E., Kranz, A., 2001. Development of porous steel structures for steam turbines. *Advanced engineering materials* 3, 111-119.
- Fam, A., Sharaf, T., 2010. Flexural performance of sandwich panels comprising polyurethane core and GFRP skins and ribs of various configurations. *Composite Structures* 92, 2927-2935.
- Galambos, T.V., 1998. *Guide to stability design criteria for metal structures*. John Wiley & Sons.
- George, T., Deshpande, V.S., Wadley, H.N., 2013. Mechanical response of carbon fiber composite sandwich panels with pyramidal truss cores. *Composites Part A: Applied Science and Manufacturing* 47, 31-40.
- Harhash, M., Palkowski, H., 2021. Incremental sheet forming of steel/polymer/steel sandwich composites. *Journal of Materials Research and Technology* 13, 417-430.
- Jackson, K., Allwood, J., Landert, M., 2008. Incremental forming of sandwich panels. *Journal of Materials Processing Technology* 204, 290-303.
- Jones, R.M., 2006. *Buckling of bars, plates, and shells*. Bull Ridge Corporation.
- Kim, K., Kim, D., Choi, S., Chung, K., Shin, K., Barlat, F., Oh, K., Youn, J., 2003. Formability of AA5182/polypropylene/AA5182 sandwich sheets. *Journal of Materials Processing Technology* 139, 1-7.
- Liu, J., Liu, W., Xue, W., 2013. Forming limit diagram prediction of AA5052/polyethylene/AA5052 sandwich sheets. *Materials & Design* 46, 112-120.
- Logesh, K., Raja, V.B., 2017. Formability analysis for enhancing forming parameters in AA8011/PP/AA1100 sandwich materials. *The International Journal of Advanced Manufacturing Technology* 93, 113-120.
- Mohr, D., 2005. On the role of shear strength in sandwich sheet forming. *International*

- Journal of Solids and Structures 42, 1491-1512.
- Nassar, H., Albakri, M., Pan, H., Khraisheh, M., 2012. On the gas pressure forming of aluminium foam sandwich panels: Experiments and numerical simulations. *CIRP annals* 61, 243-246.
- Russell, B., Deshpande, V., Wadley, H., 2008. Quasistatic deformation and failure modes of composite square honeycombs. *Journal of mechanics of materials and structures* 3, 1315-1340.
- Seong, D.-Y., Jung, C.G., Yang, D.-Y., Ahn, D.G., 2008. Bending behavior of simply supported metallic sandwich plates with dimpled cores. *International Journal of Modern Physics B* 22, 6179-6184.
- Seong, D., Jung, C., Yang, D.-Y., Moon, K., Ahn, D., 2010a. Quasi-isotropic bending responses of metallic sandwich plates with bi-directionally corrugated cores. *Materials & Design* 31, 2804-2812.
- Seong, D., Jung, C.G., Yang, D.-Y., Kim, J., Chung, W., Lee, M., 2010b. Bendable metallic sandwich plates with a sheared dimple core. *Scripta materialia* 63, 81-84.
- Sokolova, O.A., Carradò, A., Palkowski, H., 2011. Metal–polymer–metal sandwiches with local metal reinforcements: A study on formability by deep drawing and bending. *Composite Structures* 94, 1-7.
- Thompson, M.K., Moroni, G., Vaneker, T., Fadel, G., Campbell, R.I., Gibson, I., Bernard, A., Schulz, J., Graf, P., Ahuja, B., 2016. Design for Additive Manufacturing: Trends, opportunities, considerations, and constraints. *CIRP annals* 65, 737-760.
- Weiss, M., Dingle, M., Rolfe, B., Hodgson, P., 2007. The influence of temperature on the forming behavior of metal/polymer laminates in sheet metal forming.
- Xiong, J., Ma, L., Wu, L., Wang, B., Vaziri, A., 2010. Fabrication and crushing behavior of low density carbon fiber composite pyramidal truss structures. *Composite Structures* 92, 2695-2702.
- Zhang, J., Taylor, T., Yanagimoto, J., 2021. Mechanical properties and cold and warm forming characteristics of sandwich sheets with a three-dimensional CFRTP core. *Composite Structures* 269, 114048.
- Zhang, J., Yanagimoto, J., 2019. Design and fabrication of formable CFRTP core sandwich sheets. *CIRP Annals* 68, 281-284.
- Zheng, X., Lee, H., Weisgraber, T.H., Shusteff, M., DeOtte, J., Duoss, E.B., Kuntz, J.D., Biener, M.M., Ge, Q., Jackson, J.A., 2014. Ultralight, ultrastiff mechanical metamaterials. *Science* 344, 1373-1377.

Chapter 4 Design and fabrication of inner macrostructure with enhanced stiffness via topology optimization and additive manufacturing

Although conventional manufacturing processes allow some control over shape and size of the inner core structure, they remain limited to producing a certain type of specially designed structures and thus the mechanical property, formability and functionality of inner core structures may still be restricted. In addition, the incapability of manufacturing precise complex structures, the high manufacturing cost and the discrepancy in the properties of produced structures also limit the applications of the conventional fabrication methods. The layer-by-layer fabrication paradigm of AM enables the build of lattice materials with extremely intricate external geometries and high control of the internal architecture, overcoming the limitations of conventional fabrication methods. The topology optimization enables the optimal material layout of the core structure at a given set of load and boundary conditions, and thus it can be relied on to optimize the core structure for the pursuit of higher structural efficiency and better formability. The synergy of topology optimization and additive manufacturing could be a perfect tool for the design and production of sandwich sheets with improved mechanical performance, formability and functionality. Therefore, the topology optimization is used to design optimal core structures with superior stiffness and formability in this chapter.

In **section 4.1**, to improve the weight-specific stiffness and energy absorption capability of the conventional dome commonly used as the core of sandwich sheets, a new concept of filling the solid part of the dome with stretch-dominated microlattices is proposed. The optimal density distribution of microlattices is obtained by integrating the homogenization-based topology optimization method with the lattice structure. The compressive and bending stiffnesses of the optimized variable-density microlattice domes are demonstrated to be 41.8% and 33.7% higher than those of the conventional solid domes, while the energy absorption of the microlattice dome during compression and three-point bending is increased by 297.5% and 85%, respectively. Investigation of the cell size effect on the mechanical properties of the

microlattice dome reveals that a larger cell size contributes more to the weight-specific stiffness and energy absorption capability at a given overall volume fraction constraint.

To further improve the design manufacturability, structural efficiency, structural isotropy and computational efficiency, the HMTO method was proposed to integrate with plate-lattices exhibiting superior mechanical properties and excellent elastic isotropy, as presented in **section 4.2**. The validity of the proposed method was demonstrated by comparing the optimized models with conventional models composed of truss-lattices and solid materials. Results show that the proposed method highly improves stiffness and energy absorption capability. For the rectangular beam, the stiffness values of the optimized SC-FCC model are 103.5%, 127.2% and 24.9% higher than those of the solid, unoptimized octet and SC-FCC models, while the absorbed energies are 19.2% and 44.7% higher than those of the solid and unoptimized octet models, respectively. For the pyramidal structure, the optimized SC-FCC model exhibits 6.5%, 117.5% and 28.3% higher stiffness than the solid, unoptimized octet and SC-FCC models, respectively, while the absorbed energy is respectively improved by 53.3%, 120.7% and 26.0%. Both examples show highly improved stiffness and energy absorption capability of optimized models obtained by the proposed method.

4.1 Topology optimization of microlattice dome with enhanced stiffness

The synergy of additive manufacturing (AM) with topology optimization has become a useful method for developing ultralight, ultrastiff structures with high energy absorption capability. To improve the weight-specific stiffness and energy absorption capability of the conventional dome commonly used as the core of sandwich sheets, a new concept of filling the solid part of the dome with stretch-dominated microlattices is proposed. The optimal density distribution of microlattices is obtained by integrating the homogenization-based topology optimization method with the lattice structure. The compressive and bending stiffnesses of the optimized variable-density microlattice domes are demonstrated to be 41.8% and 33.7% higher than those of the conventional solid domes, while the energy absorption of the microlattice dome during compression and three-point bending is increased by 297.5% and 85%, respectively. Investigation of the cell size effect on the mechanical properties of the microlattice dome reveals that a larger cell size contributes more to the weight-specific stiffness and energy absorption capability at a given overall volume fraction constraint. The topology optimization and construction methods described in this paper are universal and can be used for the further development of ultralight, ultrastiff structures with arbitrary macro shapes with microlattices as constituent units.

4.1.1 Research background and literature review

Cellular materials such as lattice and open cell foam structures have been developed, inspired by biological structures, such as the stem of giant bird of paradise plant introduced by [Meyers et al. \(2013\)](#), porcupine quills designed by [Yang et al. \(2013\)](#), toucan beaks described by [Seki et al. \(2005\)](#) and feather rachis [Lingham-Soliar \(2014\)](#), which are all composed of a dense outer layer and a low-density hollow internal structure, thus exhibiting a high stiffness-to-weight ratio. Owing to their distinctive properties, lattice structures have been used in numerous applications and been specially designed to realize materials with functions of energy absorption, weight saving, heat transfer and thermal insulation for use in bio-medical implants [Dumas et al. \(2017\)](#) and electrochemical devices [Zhu et al. \(2015\)](#). In addition to the

sheet metal technique, conventional manufacturing processes for metallic lattice structures involve liquid-state processing including direct foaming and spray foaming, solid-state processing such as physical vapor deposition (PVD) and electron beam-directed vapor deposition (EB-DVD) as reviewed by [Atwater et al. \(2018\)](#). Several conventional fabrication methods for composite lattice structures such as hot press molding, interlocking and textile techniques have been developed to improve structural efficiency. Although the variable structural parameters of such manufacturing processes allow some control over pore shape and size, they remain limited to producing randomly organized structures. In addition, the incapability of manufacturing precise complex structures, the high manufacturing cost and the discrepancy in the properties of produced lattice structures also limit the applications of the above conventional fabrication methods. The layer-by-layer fabrication paradigm of AM enables the build of lattice materials with extremely intricate external geometries and high control of the internal architecture, overcoming the limitations of conventional fabrication methods. With the development of AM technology, selective laser melting (SLM) as reviewed by [Yap et al. \(2015\)](#) and electron beam melting (EBM) as introduced by [Karlsson et al. \(2013\)](#) have been adopted to fabricate various types of lattice structures including body centered cubic unit cell (BCC) and face centered cubic unit cell with Z-struts (FCCZ) structures from various materials such as 316L stainless steel and Ti-6Al-4V titanium alloy.

Owing to the capability of AM to produce complex geometries that were difficult or impossible to manufacture by the conventional casting, forming and cutting processes, a new class of lattice structures named functionally graded lattice structures have been developed, which provide further opportunities to improve structural efficiency and realize a broader engineering application compared with uniform-density structures, especially in many energy absorption devices. Such functionally graded lattice structures have been successfully manufactured by AM processes, such as the laser engineering net shape (LENS) reviewed by [Mahmoud and Elbestawi \(2017\)](#) and SLM processes. Although the mechanical characteristics of lattice structures with different design strategies such as lattice structures with continuous and abrupt density variation, as described by [Panesar et al. \(2018\)](#) and [Maskery et al. \(2016\)](#) have been experimentally and numerically investigated, and structures with relatively high

energy absorption, stiffness or strength have been explored, such design strategies are limited to a narrow range of choices and the development of products that have high quality, satisfy tolerances and are economic to produce relies on smarter design strategies.

Some designs now have high specific stiffness or strength with minimum material wastage, mainly through the synergy of AM with topology optimization, which is a structural optimization technique that iteratively improves the material layout in a given design space, under a given set of loads and boundary conditions as reviewed by [Zegard and Paulino \(2016\)](#). The hexahedral lattice has been integrated with topology optimization to enhance the stiffness and strength of a pillow bracket as introduced by [Cheng et al. \(2017\)](#). The density distribution of a hip implant made of the lattice with a tetrahedron-based cell has been optimized to reduce the risk of periprosthetic fracture and the probability of revision surgery as proposed by [Wang et al. \(2018\)](#). Moreover, embracing the lattice structure in design has other merits such as enabling the fabrication of a topology optimization result with intermediate densities, reducing part distortions, as their inherent networked frame minimizes residual stresses as discussed by [Panesar et al. \(2018\)](#), reducing the need for support through the inclusion of self-supporting unit cells as pointed out by [Hussein et al. \(2013\)](#), and improved design robustness. Therefore, from the viewpoints of structural efficiency and manufacturing aspects of AM, adopting the lattice structure in design can be advantageous.

Integrating lattices with topology optimization creates the potential for the further development of ultralight, ultrastiff structures for AM, which can be used to design cores with high weight-specific mechanical performance for sandwich sheets. Some commonly used core structures of sandwich sheets are characterized on a two-dimensional plane with the relative density and relative modulus as the axes, as summarized in [Figure 4-1](#), in which the weight-specific stiffness of dome structures is much lower than that of other cellular structures such as lattices, honeycombs and foams. For the purpose of improving weight-specific mechanical performance, a new structure called a microlattice dome is proposed in this study, in which microlattices replace the solid part of the dome structure owing to its advantages over solid materials. These advantages include lower density due to its networked frame, which supports more air than a solid material and less brittleness, as the struts or pairs of struts can flex

separately, allowing it to bend or compress in ways that solid materials cannot. Therefore, it is reasonable to expect that the microlattice dome structure has higher weight-specific stiffness and energy absorption capability than a conventional solid dome. Furthermore, the embedding volume created by the microlattices allows the infill of other functional components such as thermal insulation and acoustic absorption materials. In this study, a homogenization-based topology optimization method was integrated with the lattice structure to optimize the spatial distribution of microlattices to maximize the compression and bending stiffnesses as well as energy absorption of the microlattice dome. Then 3D models were constructed from topology optimization results for CAE validation and AM. Finally, the additively manufactured prototypes were experimentally tested to measure their stiffnesses and energy absorption under compression and three-point bending.

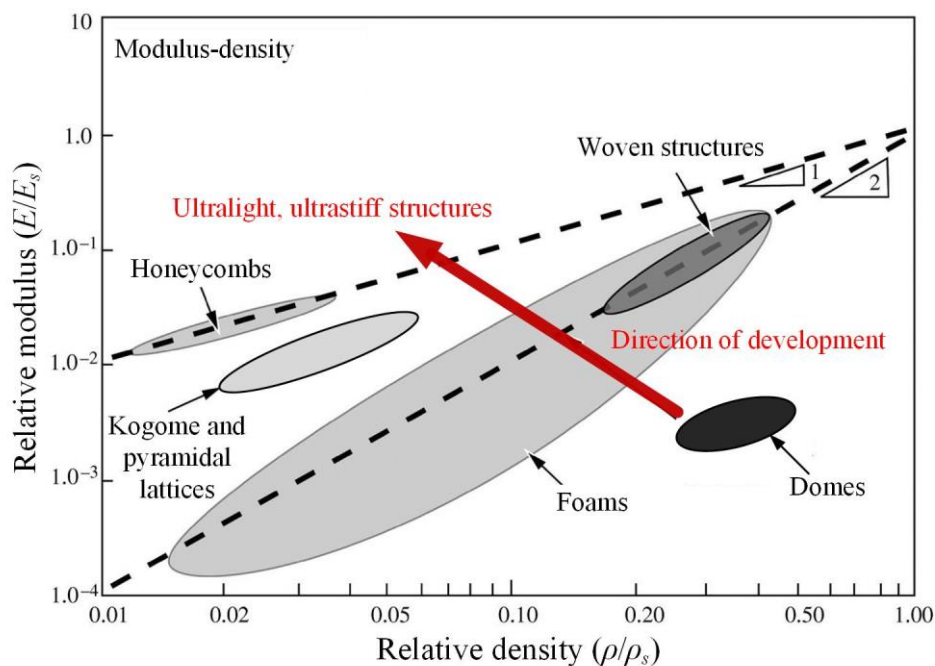


Figure 4-1. Commonly used core structures of sandwich sheets characterized by relative density, relative modulus and failure resistance, adapted from Ashby (2006).

4.1.2 Introduction to the microlattice dome structure

Based on basic unit cell topologies, the lattice structures are commonly categorized as being either strut-based, such as BCC, FCC, octet-truss and diamond, or triply periodic minimal

surfaces (TPMS), including the Schoen gyroid, Schwartz diamond and Neovius. Since strut-based topologies can be generated more simply from topology optimization results, a strut-based lattice was chosen in this study. The mechanical responses of 3D strut-based topologies, are generally characterized as being either compliant bending-dominated or stiff stretch-dominated based on the Maxwell stability criterion described by the following equation:

$$M=b-3n+6 \tag{4-1}$$

where b and n are the numbers of struts and joints, respectively.

If $M<0$, the number of struts is not sufficient to equilibrate external forces without equilibrating moments induced at the joints, causing a bending-dominated mechanical response of the struts. If $M>0$, external loads can be equilibrated by axial tension and compression stresses carried by struts, making struts stretch-dominated. Owing to these phenomena, an underlying principle can be concluded: stretch-dominated structures tend to be stiffer and stronger than bending-dominated structures. Therefore, the selection of a stretch-dominated lattice to replace the solid part of the dome structure can contribute more than a bending-dominated lattice to its structural stiffness. Examples of some idealized cell shapes are shown in Figure 4-2, where cells that satisfy the Maxwell criterion are labeled ‘Stretch-D’, while ‘Bending-D’ represents the bending-dominated topology. It can be seen that tetrahedron and octahedron in combination fill the space to form a stiff framework, thus, the simplest tetrahedral lattice is selected as the basic cell topology to replace the solid part of the dome structure.

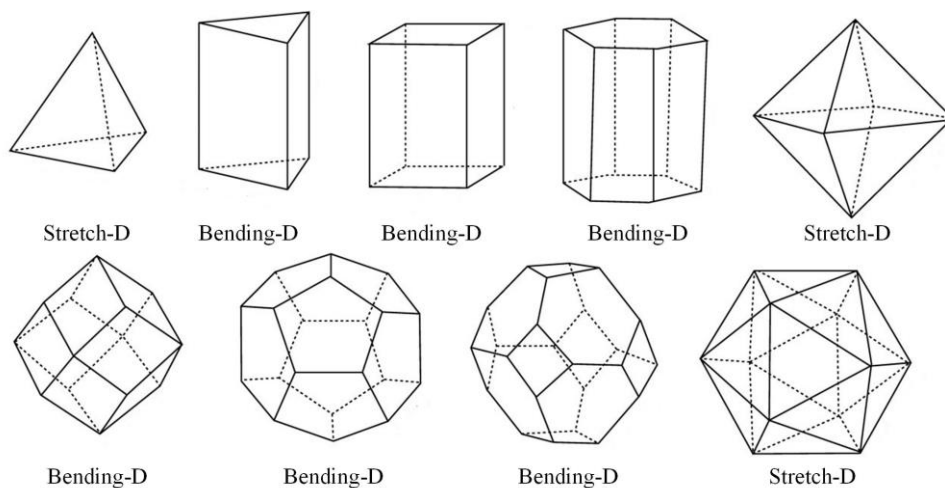


Figure 4-2. Polyhedral cells categorized as the stretch-dominated or bending-dominated following the Maxwell stability criterion.

Different from the cellular topology of honeycombs, foams and lattices, the cross-repeat arrangement of quarter-hemispherical shells constitutes the basic topology of the dome structure as shown in [Figure 4-3\(a\)](#). For the dome structure, although a higher relative density is caused compared with honeycombs, foams and lattices, the section of its hemispherical shell yields a stable shear response, which contributes to the suppression of core shear failure. In addition, the ring shaped contact area between face sheet and core reduces the risk of face buckling which is one of the main failure modes for honeycombs and lattices. As described by [Besse and Mohr \(2012\)](#), the bidirectional dome structure is composed of a periodic array of domes that are introduced into an initial flat sheet through stamping. The basic cell topology of the bidirectional dome is shown in [Figure 4-3\(a\)](#), where the bilayer assembly is symmetric with respect to the central xy plane. Furthermore, each layer is symmetric with respect to the xz and yz planes. The front view and structural parameters of the bidirectional dome are shown in [Figure 4-3\(b\)](#), where t is the initial thickness of the sheet used to produce a single dome layer and d is the dome depth. R_1 and R_2 are the inner and outer dome radii, respectively. The height h and width (length) w satisfy the following constraints:

$$h=2(t+d) \quad (4-2)$$

$$w=2R_2 \quad (4-3)$$

On the basis of the proposed design concept that the stretch-bending dominated tetrahedral lattice can replace the solid part of the bidirectional dome to improve its weight-specific mechanical performance, the combination of the tetrahedral lattice and the bidirectional dome is used as illustrated in [Figure 4-4](#), where the tetrahedral microlattices fill the solid part of the bidirectional dome. It can be seen that the solid dome has become a porous microlattice dome, which reduces the weight and simultaneously allows the embedding volume to be used for functional components. Through such a combination, the lighter microlattice dome is expected to have better weight-specific mechanical performance than the conventional solid dome. The optimal density distribution of the microlattices that maximizes the structural stiffness and energy absorption is found by integrating topology optimization with the lattice structure as discussed in the following sections.

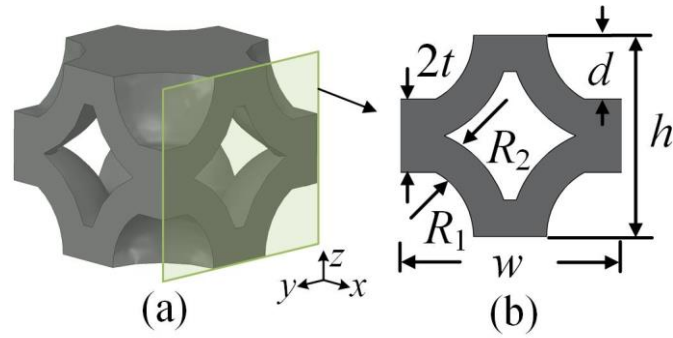


Figure 4-3. Basic cell topology of the bidirectional dome and its structural parameters.

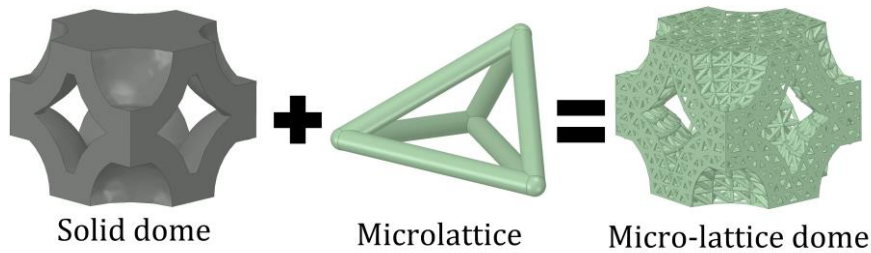


Figure 4-4. Illustration of the microlattice dome.

4.1.3 Design flowchart

In this study, a microlattice dome structure with an optimal density distribution was designed through the steps shown in Figure 4-5. Each step is described in detail below.

Step 1: Preprocessing. A 3D macro dome structure was built before it was meshed with tetrahedral elements and the position information of each element and its nodes was stored, which was used for topology optimization and structural construction. Since tetrahedral elements can be used to mesh a macro geometry of any complex shape, the tetrahedral lattice can be integrated with topology optimization to design structures with arbitrary geometric shapes, which is another significant advantage over the topology optimization method integrated with the hexahedral lattice proposed by Cheng et al. (2017).

Step 2: Topology optimization. At given boundary conditions and volume fraction constraints, the optimal density distribution of the microlattices was obtained through topology optimization. Details of the topology optimization method will be discussed in section 3.

Step 3: Construction of the microlattice dome. After obtaining the cell density distribution, a concise method for linking the structural parameters of the lattice structure with its relative

density was used to construct microlattice dome structures for CAE validation and AM.

Step 4: CAE validation. The constructed model was used for CAE simulation, and the optimal structure was verified by comparing the stress distribution with the density distribution obtained from topology optimization. In addition, the mechanical properties under compression and three-point bending were numerically obtained and compared with the results of experimental tests.

Step 5: AM and experimental tests. In accordance with the constructed 3D models, a prototype of the optimal design was fabricated using 3D printing and its stiffness and energy absorption were measured by conducting compression and three-point bending tests.

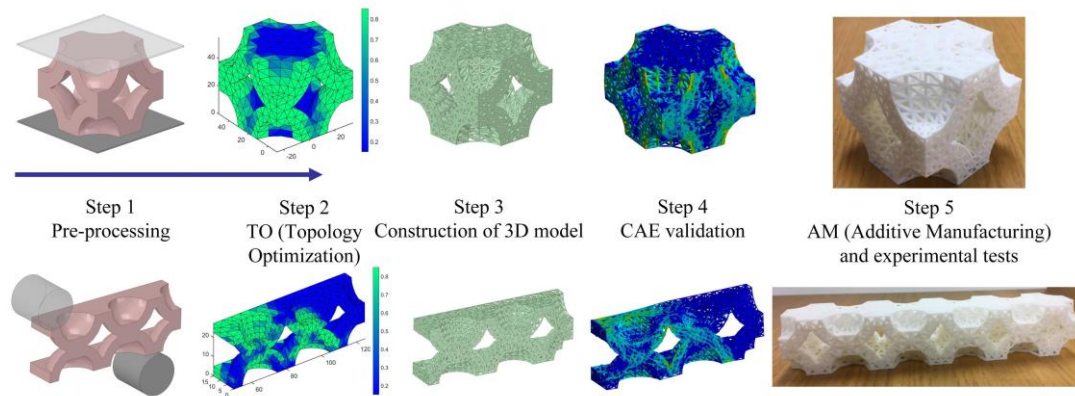


Figure 4-5. Design flowchart.

4.1.4 Topology optimization

4.1.4.1 Mathematical formulation of topology optimization problem

Generally, an optimization problem consists of three parts: objective functions, design variables and constraints. The density-based topology optimization is to update the design variables, such as the relative density of elements, at given constraints, such as boundary conditions and volume fraction constraints, until the optimal solution of the objective function, such as the minimum value of the compliance, is found. Since the objective of this study is to maximize the stiffness of the microlattice dome structure, namely, minimize the compliance, the objective function in the optimization problem is selected as the compliance. The topology optimization problem is described by the following equations:

$$\min_{\rho_e} : c(\rho_e) = \mathbf{U}^T \mathbf{K} \mathbf{U} = \sum_{e=1}^N \mathbf{u}_e^T \mathbf{k}_e \mathbf{u}_e \quad (4-4)$$

$$\frac{V(\rho_e)}{V_0} = f \quad (4-5)$$

$$\mathbf{K} \mathbf{U} = \mathbf{F} \quad (4-6)$$

$$0 \leq \rho_{\min} \leq \rho_e \leq \rho_{\max} \leq 1 \quad (4-7)$$

where the compliance c is the objective function, and the element relative density ρ_e is the design variable. Here, \mathbf{k}_e and \mathbf{u}_e are the element displacement and stiffness, respectively. \mathbf{U} denotes any admissible displacement field and \mathbf{K} is the global stiffness matrix. N is the number of elements, and V and V_0 are the volumes of the solid material and all elements, respectively. \mathbf{F} and f are applied loads and the prescribed volume fraction, respectively. The upper and lower bounds of the relative density are denoted as ρ_{\max} and ρ_{\min} , respectively.

The procedures for calculating the compliance by FEA are as follows.

As described in **section 4.1.3**, the position information of each element and its nodes has been stored. Using the position information of the elements and nodes, such as coordinates, the strain-displacement matrix \mathbf{B} of the element can be derived, and then the element strain $\boldsymbol{\varepsilon}$ and stress $\boldsymbol{\sigma}$ can be calculated using the following equations:

$$\boldsymbol{\varepsilon} = \mathbf{B} \mathbf{u} \quad (4-8)$$

$$\boldsymbol{\sigma} = \mathbf{D} \boldsymbol{\varepsilon} \quad (4-9)$$

where \mathbf{D} is the constitutive matrix for an isotropic element given by

$$\mathbf{D} = \begin{bmatrix} \frac{E(1-\nu)}{(1+\nu)(1-2\nu)} & \frac{E\nu}{(1+\nu)(1-2\nu)} & \frac{E\nu}{(1+\nu)(1-2\nu)} & 0 & 0 & 0 \\ \frac{E\nu}{(1+\nu)(1-2\nu)} & \frac{E(1-\nu)}{(1+\nu)(1-2\nu)} & \frac{E\nu}{(1+\nu)(1-2\nu)} & 0 & 0 & 0 \\ \frac{E\nu}{(1+\nu)(1-2\nu)} & \frac{E\nu}{(1+\nu)(1-2\nu)} & \frac{E(1-\nu)}{(1+\nu)(1-2\nu)} & 0 & 0 & 0 \\ 0 & 0 & 0 & G & 0 & 0 \\ 0 & 0 & 0 & 0 & G & 0 \\ 0 & 0 & 0 & 0 & 0 & G \end{bmatrix} \quad (4-10)$$

After that, the element stiffness matrix can be obtained according to the principle of virtual work, as calculated using

$$\mathbf{k}_e = \iiint_V \mathbf{B}^T \mathbf{D} \mathbf{B} dx dy dz \quad (4-11)$$

Finally, the displacement matrix \mathbf{U} can be obtained from the equilibrium equation, and then the objective function compliance can be calculated using Eq. (4-4).

4.1.4.2 Updating scheme for design variables

The optimization algorithm used to update the design variables is the optimality criterion proposed by Bendsøe and Sigmund (1995), which is a classical approach to structural optimization problems and is used in the standard topology optimization methods, such as the SIMP method discussed by Bendsoe and Sigmund (2003). Following the optimality criteria, the design variable is updated according to the following formulas:

$$\rho_e^{new} = \begin{cases} \max(\rho_{\min}, \rho_e - m) & \text{if } \rho_e B_e^\eta \leq \max(\rho_{\min}, \rho_e - m), \\ \rho_e B_e^\eta & \text{if } \max(\rho_{\min}, \rho_e - m) < \rho_e B_e^\eta < \min(\rho_{\max}, \rho_e + m), \\ \min(\rho_{\max}, \rho_e + m) & \text{if } \min(\rho_{\max}, \rho_e + m) \leq \rho_e B_e^\eta, \end{cases} \quad (4-12)$$

where ρ_e is the density of the element in the current iteration step, and ρ_e^{new} is the updated density. Here, m is a positive move limit with a value set to 0.2 and η is a numerical damping coefficient with a value of 0.5 recommended by Sigmund (2001). B_e is found according to the optimality condition as

$$B_e = -\frac{1}{\lambda} \frac{\partial c / \partial \rho_e}{\partial V / \partial \rho_e} \quad (4-13)$$

where λ is a Lagrange multiplier that is determined by a root-finding algorithm such as the bisection method and the element sensitivity is given by

$$\frac{\partial c}{\partial \rho_e} = -\mathbf{U}^T \frac{\partial \mathbf{K}}{\partial \rho_e} \mathbf{U} = -\mathbf{U}^T \mathbf{B}^T \frac{\partial \mathbf{D}}{\partial \rho_e} \mathbf{B} \mathbf{U} \quad (4-14)$$

However, topology optimization approaches are likely to encounter some numerical difficulties such as checkerboard patterns, mesh dependence and local minima as discussed by Bendsoe and Sigmund (2003). To mitigate such issues and ensure the existence of solutions,

density filters are recommended by [Sigmund \(1997\)](#) for minimum compliance problem. A density filter function is defined as

$$\bar{\rho}_e = \frac{\sum_{j \in N_e} H_{ej} v_j \rho_j}{\sum_{j \in N_e} H_{ej} v_j} \quad (4-15)$$

where H_{ej} is the convolution operator and N_e is the neighborhood of an element e defined as

$$N_e = \{j: \text{dist}(e, j) \leq R\} \quad (4-16)$$

where the operator $\text{dist}(e, j)$ is the distance between the center of element e and the center of element j , and R is the filter radius, which is equal to or slightly larger than the element size.

The convolution operator is defined as a function of the distance between neighboring elements as

$$H_{ej} = R - \text{dist}(e, j) \quad (4-17)$$

The filtered density defines a modified density field, which is now incorporated in the topology optimization formulas and modifies the element sensitivity to

$$\left(\frac{\partial c}{\partial \rho_e} \right)_{new} = \frac{1}{\max(\delta, \rho_e) \sum_{j \in N_e} H_{ej}} \sum_{j \in N_e} H_{ej} \rho_j \frac{\partial c}{\partial \rho_j} \quad (4-18)$$

where $\delta (= 10^{-4})$ is a small number used to avoid division by zero.

4.1.4.3 Integrating topology optimization with microlattice structure

The basic concept of the optimization method used here is similar to the so-called homogenization-based method originally proposed by [Bendsøe and Kikuchi \(1988\)](#), where each element in the design domain is assumed to be a microlattice structure. Apparently, a fully resolved resolution of a large lattice domain with explicit modeling of its microstructural features can be very time-consuming, making it impractical for use in the optimization process. Therefore, the lattice structure is equivalent to that of a homogeneous solid material, and the equivalent mechanical properties corresponding to different relative densities are calculated by the asymptotic homogenization method introduced by [Arabnejad and Pasini \(2013\)](#). In the homogenization-based topology optimization method, the equivalent mechanical property of each element must be calculated at each iteration step, resulting in very low computational efficiency. To improve the computational efficiency of the optimization process, the equivalent

mechanical properties corresponding to different relative densities are precalculated, and then a polynomial fitting is performed to obtain the function between the equivalent property and relative density, which is directly used for FEA, thereby achieving high-efficiency calculation of the objective function. The tetrahedral lattice is selected not only because of its stretch-dominated mechanical behavior, but also it can fit the irregular shape of the dome structure well. However, the analyses of the equivalent mechanical property of lattice structures are mostly based on the hexahedral unit cells and the analysis of tetrahedral unit cells by elastomechanical equivalence remains a challenge as tetrahedral lattice unit cells are freer in shape and lack obvious orthogonality. Therefore, an approximate solution is that the tetrahedron is assembled to form a hexahedron, and then the equivalent elastic constants of the assembled hexahedron are obtained and considered to be the equivalent mean value of the equivalent elastic constants of the tetrahedron. Although such treatment may lead to certain behaviour deviation, it could be an alternative owing to its feasibility and simplicity. The relationship between the effective equivalent mechanical properties of such a hexahedral unit cell, as shown in [Figure 4-6](#), and its relative density have been calculated by [Wang et al. \(2018\)](#) and are shown by the following equations:

$$\begin{aligned}
 E &= E_s (0.8861\rho_e^2 + 0.0928\rho_e + 0.0127) \\
 G &= E_s (0.4517\rho_e^2 - 0.1043\rho_e + 0.0154) \\
 \nu &= \nu_s (0.5352\rho_e^3 - 0.4307\rho_e^2 + 0.3466\rho_e + 0.5526)
 \end{aligned}
 \tag{4-19}$$

where E_s and ν_s are the elastic modulus and Poisson's ratio of the solid material, respectively. E , G and ν are the equivalent elastic modulus, shear modulus and Poisson's ratio of the tetrahedral lattice, respectively.

The above equations are directly used to replace the elastic constants in [Eq. \(4-10\)](#) to calculate the element stiffness matrix and the objective function during the optimization process.

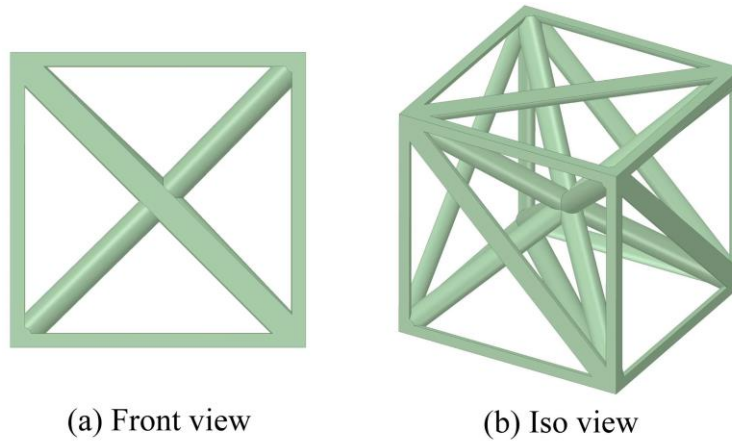


Figure 4-6. Hexahedral unit cell composed of tetrahedra.

4.1.4.4 Topology optimization models

In this study, the proposed topology optimization method is used to find the optimal distribution of the lattices that maximizes the compression and bending stiffnesses of the microlattice dome. The structural parameters of the models for compression and three-point bending are shown in Table 4-1, where the dimensions of the unit cell of the model for compression are twice those of the one for three-point bending. The numbers of unit cells for compression and three-point bending were set as 1 and 5, respectively, where only a 1/4 model was used for three-point bending to improve the efficiency of topology optimization, 3D construction and CAE validation.

Table 4-1. Structural parameters of models for topology optimization.

Structural parameters	Value (mm)	
	Compression model	Three-point bending model
R_1	20	10
R_2	30	15
t	10	5
d	17.5	8.75
h	55	27.5
w	60	30

The boundary conditions for the compression model are shown in Figure 4-7(a), where a vertical displacement was applied to its top surface and its bottom surface was fixed. For the three-point bending model, as shown in Figure 4-7(b), symmetrical boundary conditions were applied to the two symmetry planes of the 1/4 model, respectively, and a vertical displacement

was applied onto the middle of the upper surface.

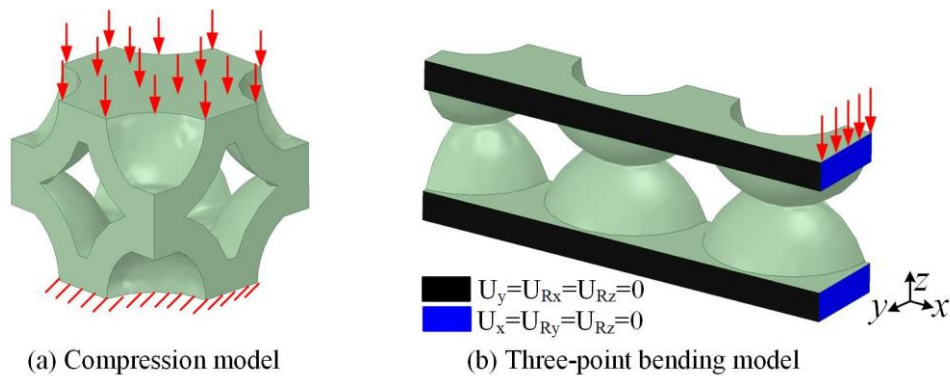


Figure 4-7. Boundary conditions for topology optimization models.

4.1.4.5 Topology optimization results

The upper and lower bounds of the element density were set to 0.15 and 0.85, respectively. The overall volume fraction constraint was set to 50%. To investigate the effect of the cell size on the mechanical properties of the microlattice dome, tetrahedral elements with two different sizes were used to mesh the macro dome structure. For the compression model, the mesh size was chosen to be 10 or 6 mm, while the mesh size was selected to be 5 mm or 3 mm for the three-point bending model. The optimal density distribution obtained by topology optimization for microlattice domes with different cell sizes are shown in Figure 4-8 and Figure 4-9, where the denser cells are represented in green and blue regions indicate cells with lower densities.

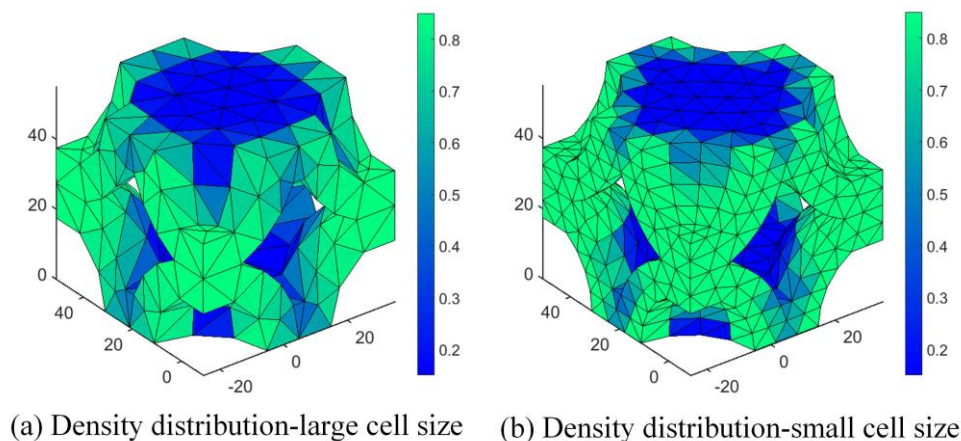


Figure 4-8. Optimal density distribution of lattices for compression models obtained from topology optimization.

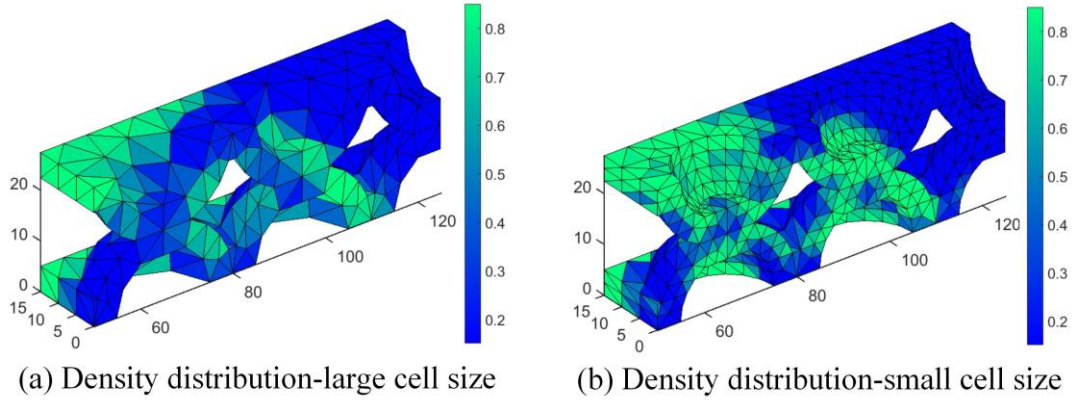


Figure 4-9. Optimal density distribution of lattices for three-point bending models obtained from topology optimization.

4.1.5 3D construction of microlattice dome

4.1.5.1 Construction method

After obtaining the element density distribution through topology optimization, the next step is to construct the 3D model for numerical and experimental verification. During the construction process, the corresponding tetrahedral lattice structure is generated according to the density of the elements, which requires the establishment of a relationship between the structural parameters of the tetrahedral lattice and its density. The basic structure of each tetrahedral lattice, which consists of six cylinders with the same radius and spheres distributed at the four nodes, is shown in Figure 4-10. Namely, the construction of a tetrahedral lattice structure can be converted to operations that generate a sphere with the corresponding radius at each node and a cylinder with the corresponding radius between two adjacent nodes. Therefore, as long as the radius of the cylinder corresponding to the element density is known, the tetrahedral lattice structure can be automatically generated in the CAD software through a parameterized language, for instance, the automatic construction of the tetrahedral lattice is implemented using the python script in SCDM 2019R1 in this study. The relationship between the element density and the radius of the cylinder is derived as follows.

The density of the tetrahedron lattice is given by:

$$\rho_e = V_s / V_e \quad (4-20)$$

where V_e is the element volume and V_s is the volume of the solid part. V_e can be calculated as

$$V_e = \begin{vmatrix} 1 & x_1 & y_1 & z_1 \\ 1 & x_2 & y_2 & z_2 \\ 1 & x_3 & y_3 & z_3 \\ 1 & x_4 & y_4 & z_4 \end{vmatrix} \quad (4-21)$$

where x_Q, y_Q and z_Q ($Q = 1, 2, 3, 4$) are the coordinates of the four nodes.

The volume of the solid part is composed of the six cylinders that completely belong to the element. The volume of the solid part of the tetrahedral lattice can be obtained by calculating the volume of the part of each cylinder that belongs to the element and adding them. Since each cylinder is shared by adjacent elements, the volume belonging to the element is determined by the angle between the two faces with the cylinder axis as the common side. The volume calculation of the solid part of the tetrahedral lattice is explained by taking the volume calculation of a cylinder with the edge OA as an axis as an example. As shown in [Figure 4-10](#), let $\angle BOC = \alpha$, $\angle AOC = \beta$, $\angle AOB = \gamma$ and $\angle C'A'B' = \varphi$, in which φ is the angle between the two faces with OA as the common side. Through geometric calculations, the angle φ can be calculated by

$$\cos\varphi = \frac{\cos\alpha - \cos\beta\cos\gamma}{\sin\beta\sin\gamma} \quad (4-22)$$

Since the volume of cylinder with the edge OA as its axis is shared by several adjacent elements, the volume belonging to the element $OABC$ is proportional to the angle between face OAB and face OAC . More specifically, the ratio of the volume of the cylinder belonging to the element $OABC$ to the volume of the entire cylinder is $\varphi/2\pi$, where φ is the angle between surface OAB and surface OAC and can be calculated by [Eq. \(4-22\)](#). Thus, the volume of a cylinder with the edge OA as its axis completely belonging to this element is:

$$V_{L_1} = r^2 L_1 \varphi / 2 \quad (4-23)$$

where L_1 is the distance between nodes O and A , and r is the radius of the cylinder.

Similarly, the volume of other cylinders belonging to the element can be calculated. Finally, the relationship between the density and beam radius of the tetrahedral lattice structure can be obtained from the following equation

$$\rho_e = \left(\sum_{i=1}^6 V_{L_i} \right) / V_e = \left(\sum_{i=1}^6 (r^2 L_i \varphi_i / 2) \right) / V_e \quad (4-24)$$

The homogenization-based topology optimization and the subsequent construction of lattice structures can be used to generate ultralight and ultrastiff structures. As an example, a hexahedral unit with different volume fractions composed of a given tetrahedral lattice was constructed as shown in Figure 4-11.

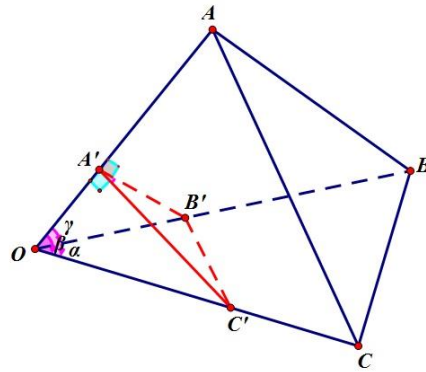


Figure 4-10. Illustration of the basic structure of tetrahedral lattice.

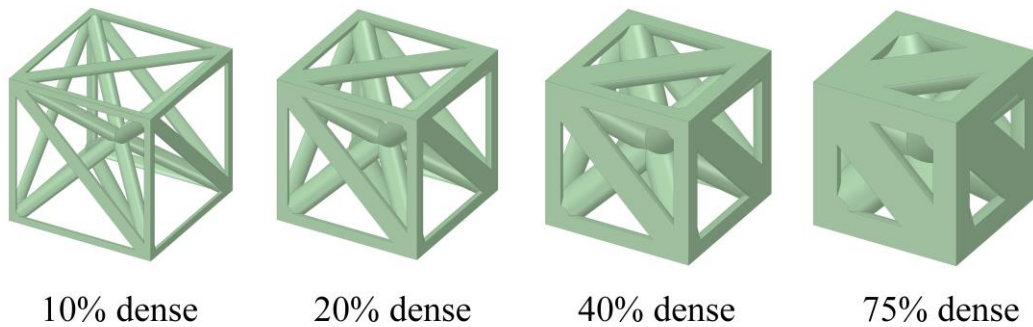


Figure 4-11. Hexahedral unit with different volume fractions generated using the proposed construction method.

4.1.5.2 Constructed 3D models

Figure 4-12 shows the constructed compression models with different cell sizes before and after topology optimization under the overall volume fraction constraint of 0.5. Note that the cells of the unoptimized model have a uniform density of 0.5. It is found that the beam radius of a model with a large cell size is larger than that of a model with a small cell size. To easily distinguish their structural differences, their top views are compared as shown in Figure 4-13. It is found that the beam radius of the elements in the middle region of the variable-

density model is smaller than that of the elements in the edge region, which is consistent with the optimal density distribution after topology optimization, as shown in Figure 4-8. The beam radius of each area of the unoptimized uniform density model is basically the same, indicating that the microlattice has a uniform density distribution.

The constructed three-point bending models with different cell sizes before and after topology optimization with the overall volume fraction constraint of 0.5 are shown in Figure 4-14. The beam radius distribution of the optimized variable-density model closely matches the density distribution map obtained by topology optimization shown in Figure 4-9, and the beam radius is larger in the area with higher density.

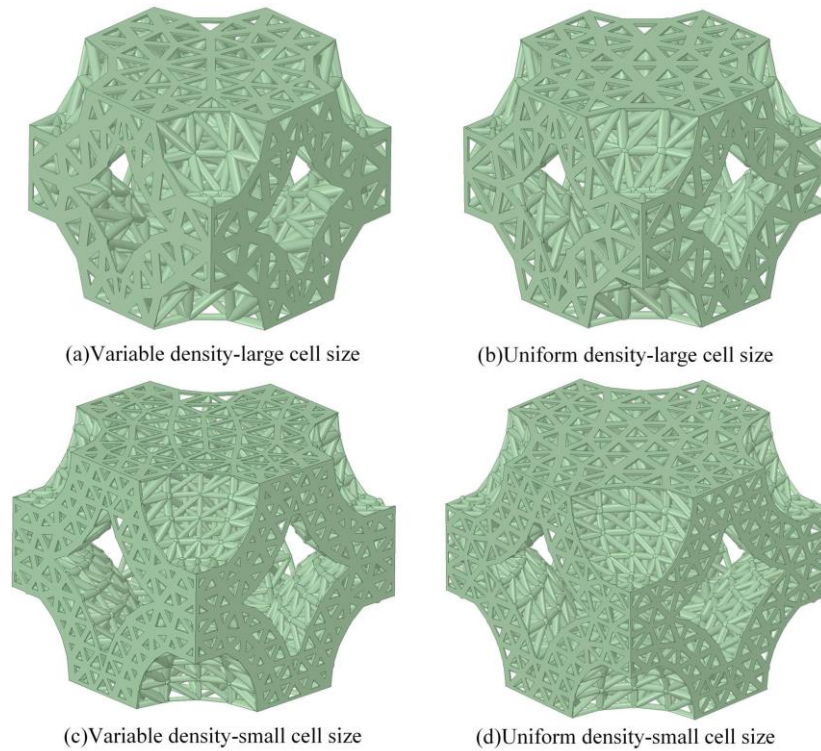


Figure 4-12. Constructed compression models with different cell sizes before and after topology optimization.

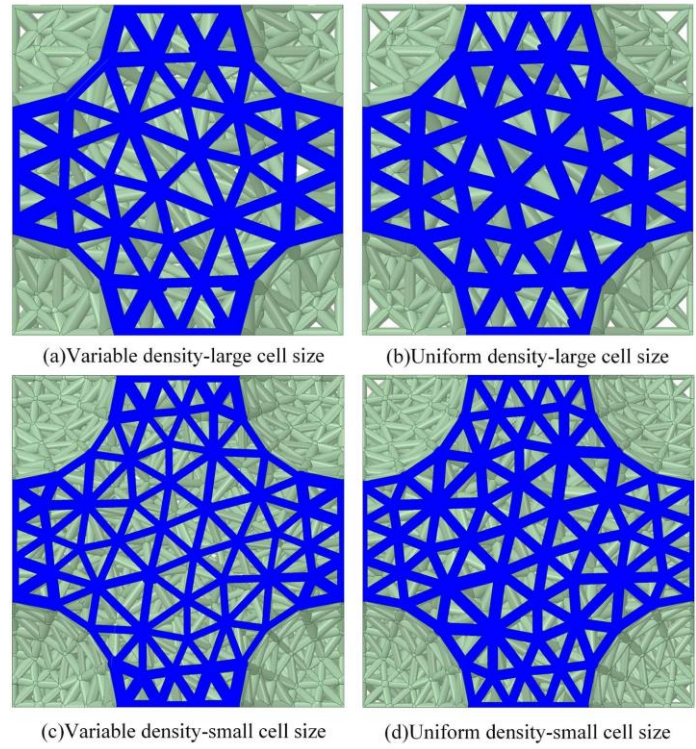


Figure 4-13. Comparison of top views of constructed compression models.

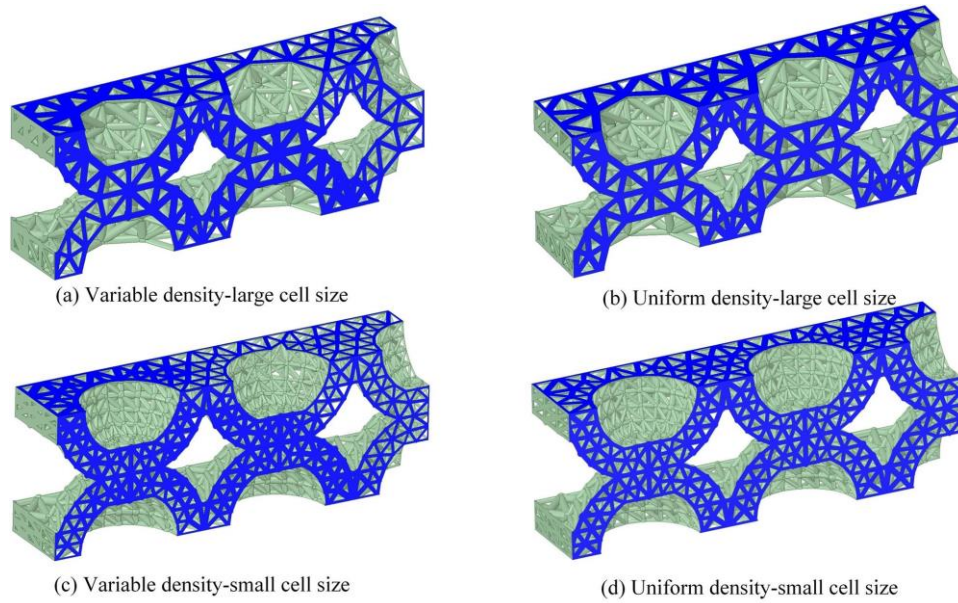


Figure 4-14. Constructed three-point bending models with different cell sizes before and after topology optimization.

4.1.6 Numerical and experimental validation

To validate the proposed design method, both numerical simulation and experiments are

conducted on the microlattice dome before and after minimum compliance optimization with the overall volume fraction constrained to 50% of the original solid dome. Furthermore, the compression and bending characteristics of the solid dome were also numerically simulated and experimentally tested, then compared with those of the microlattice dome.

4.1.6.1 CAE simulation

The material properties of 3D-printed polylactic acid (PLA) were required to build FEA models for CAE validation, which were obtained by conducting uniaxial tensile tests following the ASTM D638-14 standard. The standard tensile specimen with dimensions shown in [Figure 4-15\(a\)](#) are printed using Guider II (Flashforge Inc), a machine that adopts fused deposition modelling (FDM) technology. The process parameters are listed in [Table 4-2](#). The build orientation is along the thickness direction of the sample with a printing speed of 50 mm/s. The infill density is set as 100% to make a full solid inner structure of the specimen. The tensile test configuration is shown in [Figure 4-15\(b\)](#), where the tensile rate is set as 3 mm/min (the recommended range in the ASTM D638-14 standard is 1-5 mm/min). To avoid the influence of accidental factors and reduce the relative error, three sets of tensile tests were performed and the average values of the experimental results were taken as the material parameters of PLA for the CAE simulation. The material properties used for the simulation are consistent with those used in the topology optimization, as shown in [Table 4-3](#).

[Table 4-2](#). Process parameters.

Parameter	Value
Build orientation	Thickness direction
Infill density (%)	100
Layer thickness (mm)	0.12
Feed rate (mm/s)	50
Nozzle/Platform temperature (°C)	220/50

[Table 4-3](#). Material properties of 3D-printed PLA.

Property	Modulus (GPa)	Yield strength (MPa)	Poisson's ratio
Specimen 1	2.84	38.33	0.22
Specimen 2	2.72	36.81	0.22
Specimen 3	2.88	37.63	0.22
Average	2.81	37.59	0.22

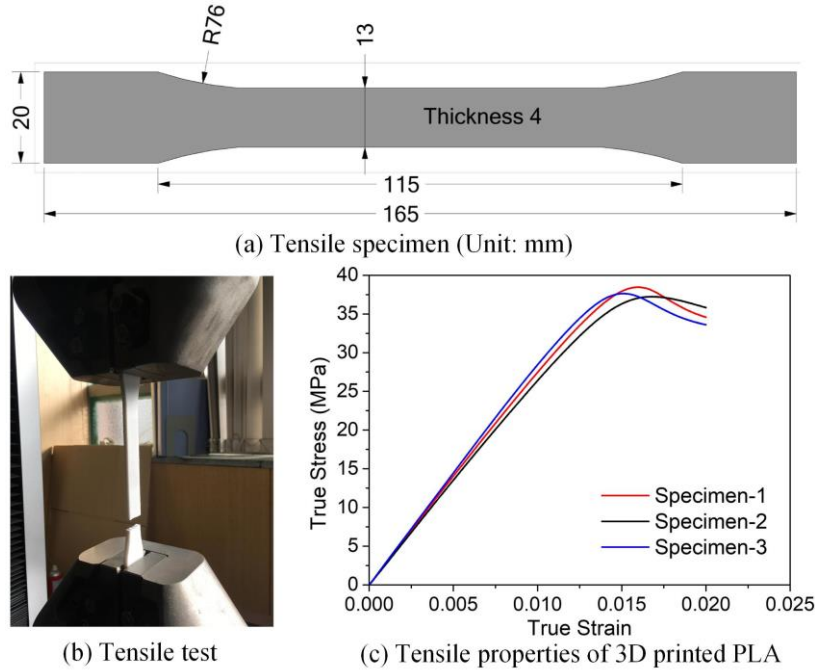


Figure 4-15. Tensile test configuration and results.

The constructed microlattice dome models in SCDM R1 were directly imported to ANSYS Workbench, where the static structural algorithm was selected to conduct the compression and three-point bending simulation. The numbers of elements and nodes of each model are listed in Table 4-4. To capture the stiffness of the 3D model and simultaneously reduce the computational time, the linear elastic material model was assumed for both the compression and three-point bending models. The boundary conditions for the compression simulation models are illustrated in Figure 4-16(a), where the top and bottom plates were modeled as rigid bodies and a vertical displacement of 2 mm was applied to the top plate while the bottom plate was fixed. For the three-point bending simulation models, as shown in Figure 4-16(b), to be consistent with the boundary conditions of topology optimization, symmetrical boundary conditions ($U_{x/y/z}$ and $U_{R_{x/y/z}}$ represent translation and rotation degrees of freedom in each direction, respectively) were applied to the two symmetry planes (black and blue regions) of the 1/4 model, and a vertical displacement of 3 mm was applied onto the middle of the upper surface. For consistency with the three-point bending test, the radii of rollers were set as 10 mm. For both the compression and three-point bending simulation models, the contact between the rigid plates with the dome structure was set as the frictional type with a friction coefficient

of 0.15.

Table 4-4. The numbers of elements and nodes of CAE models.

Model	Number of nodes/elements	
	Compression	Three-point bending
Variable density–large cell size	280537/155340	495975/260001
Variable density–small cell size	750551/418888	804846/450453
Uniform density–large cell size	284981/156289	283938/155683
Uniform density–small cell size	749443/414294	695984/383156
Solid	11925/6279	7832/3815

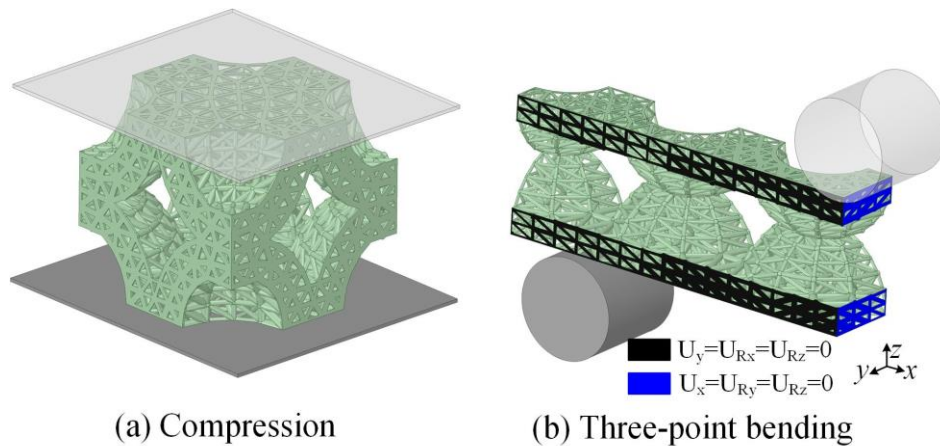


Figure 4-16. Illustration of boundary conditions for CAE models.

4.1.6.2 additive manufacturing and experimental setup

The constructed microlattice domes including optimized variable-density models, unoptimized uniform density models and solid domes, were printed adopting the same process parameters as those used to print the tensile samples. The printed microlattice dome structures for compression and three-point bending experiments are shown in Figure 4-17 and Figure 4-18, respectively.

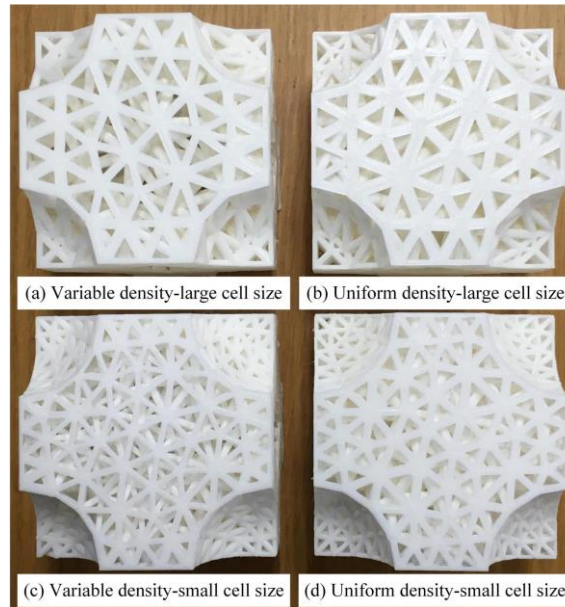


Figure 4-17. Additively manufactured optimized and unoptimized microlattice domes for compression tests.

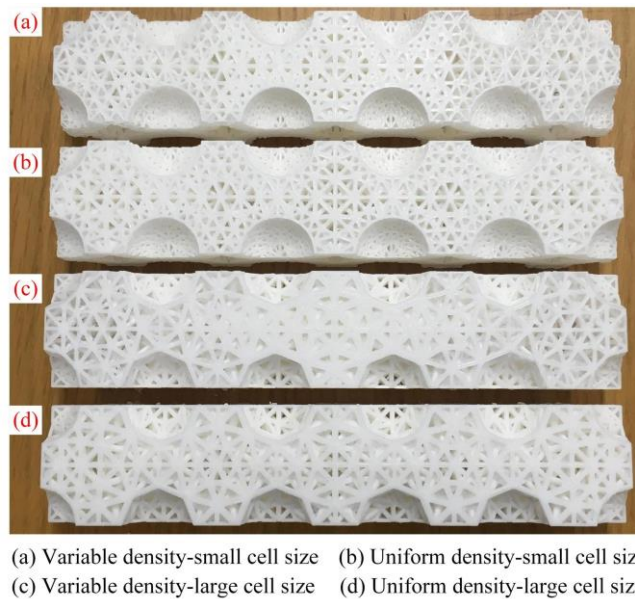


Figure 4-18. Additively manufactured optimized and unoptimized microlattice domes for three-point bending tests.

The experimental processes at the initial stage and during the compression test are shown in Figure 4-19, where the compression test was conducted using a 50 kN hydraulic servo press (Thermecmaster-Z, Fujidempa, Japan) with a load rate of 3 mm/min. The experimental configuration of the three-point bending test is shown in Figure 4-20, where the span length is 120 mm and the roller radius is 10 mm. The three-point bending was conducted using a 20 kN

material testing machine (Servopulser, Shimadzu, Japan) and the load speed was 3 mm/min.

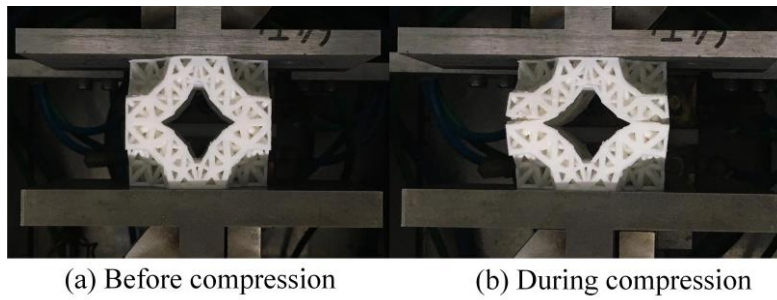


Figure 4-19. Experimental configuration for compression test.

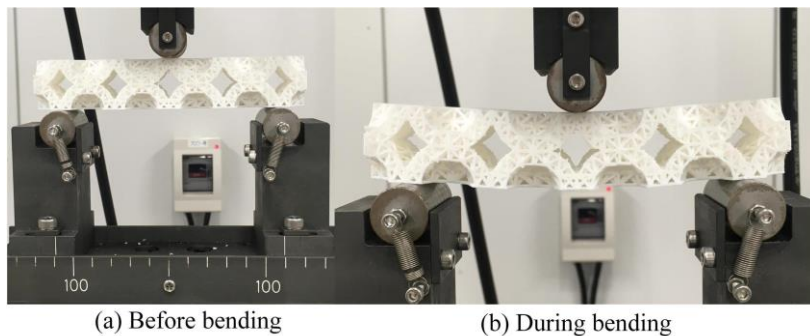


Figure 4-20. Experimental configuration for three-point bending test.

4.1.7 Results and discussion

4.1.7.1 Comparison between optimal density map with stress distribution contour

The stress distribution maps obtained from the compression simulation and three-point bending simulation are shown in Figure 4-21 and Figure 4-22, respectively. By comparing the density distribution map obtained by topology optimization and the stress distribution contours of FEA models, it is found that there is higher stress in the region with high density, while in the region with low density the stress is lower, which is an effective strategy to reduce material use by increasing the amount of material in high-stress areas and reducing the amount of material in low-stress areas. The above results are consistent with nature's awe-inspiring designs, such as the human bones. Bones that bear little weight, such as shoulder blades, tend to have a more open internal lattice, while strong load-bearing bones such as femurs have a much denser inner structure. In addition, comparing the stress distribution map of the variable-density model obtained by topology optimization with the unoptimized uniform-density model,

it is found that the maximum stress of the variable-density model is lower than that of the uniform density model, which indicates that the variable-density model has a more reasonable material distribution, enabling a more uniform stress distribution.

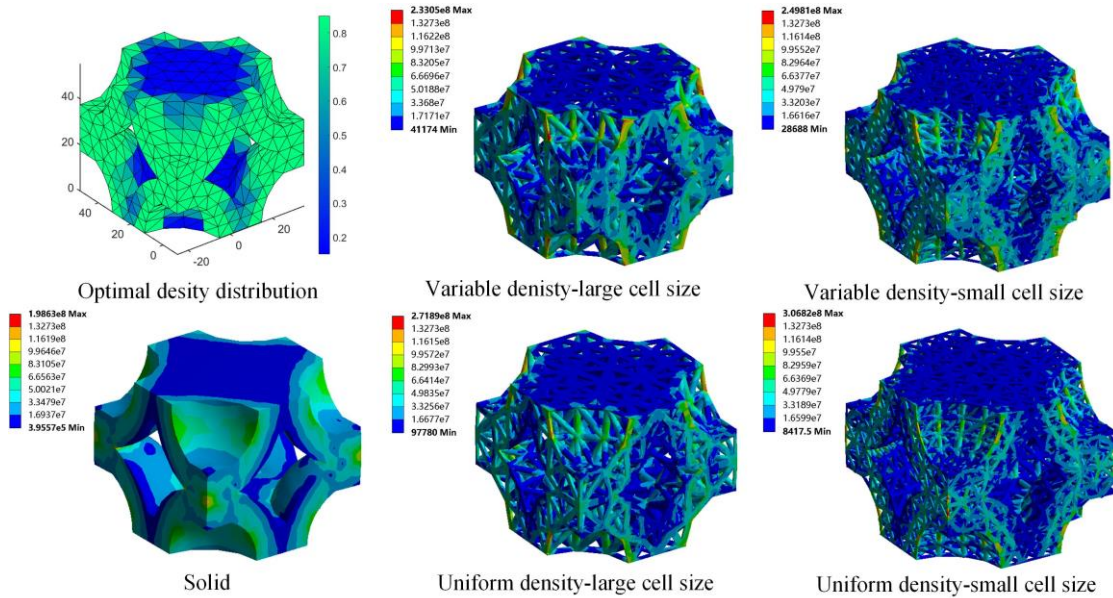


Figure 4-21. Stress distribution maps obtained from the compression simulation.

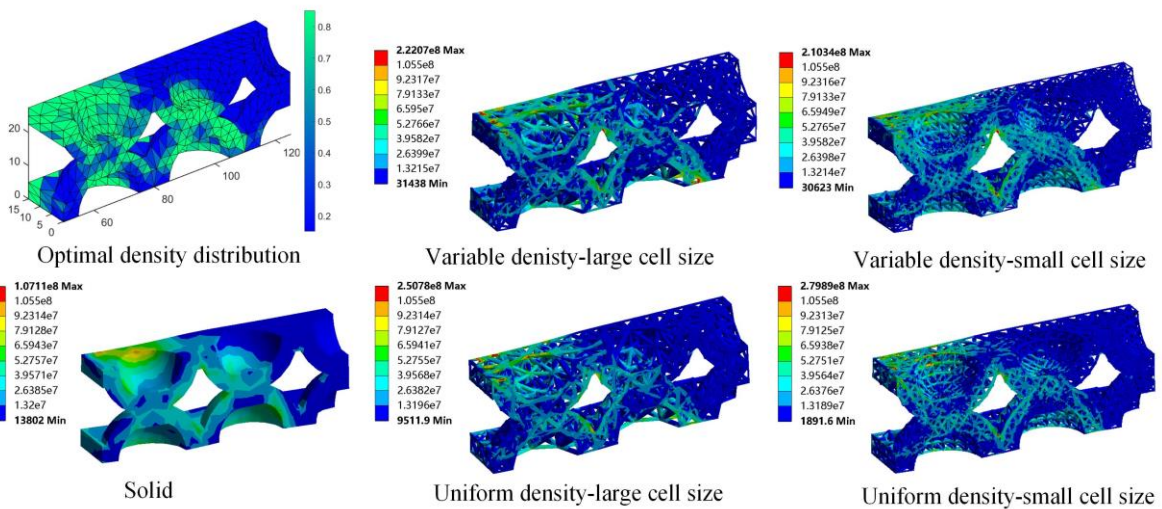


Figure 4-22. Stress distribution maps obtained from the three-point bending simulation.

4.1.7.2 Stiffness and energy absorption

The fractured microlattice domes and solid dome after compression and bending experiments are shown in Figure 4-23 and Figure 4-24, respectively. As shown in Figure 4-23, microlattice domes and solid dome structures show very similar deformation mode, where the bilayer dome breaks into two single layer domes from the central symmetric plane as indicated

by the red dash line. Besides, the same fracture faces were observed as indicated by the green dash lines for the solid dome and the unoptimized uniform-density microlattice dome with small cells, indicating the same fracture behaviour during compression test. Figure 4-24 shows the samples after bending experiments, microlattice domes and solid dome structures show the same deformation mode and break in half along the plane of symmetry in the middle, as indicated in the black dashed box.

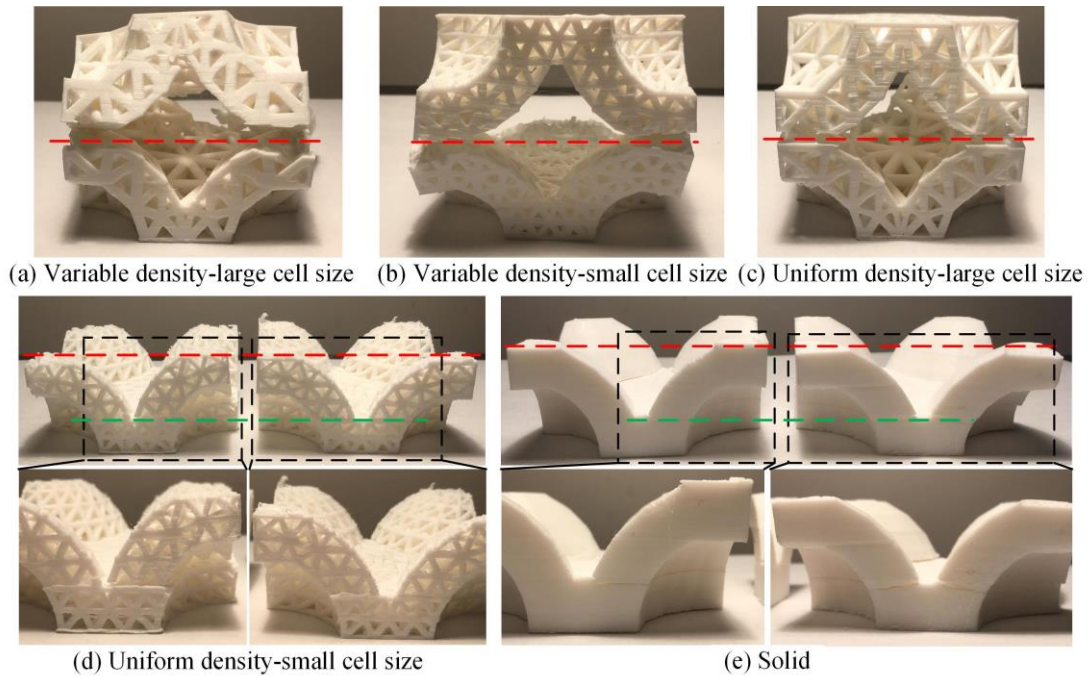


Figure 4-23. Fractured microlattice domes and solid dome after compression tests.

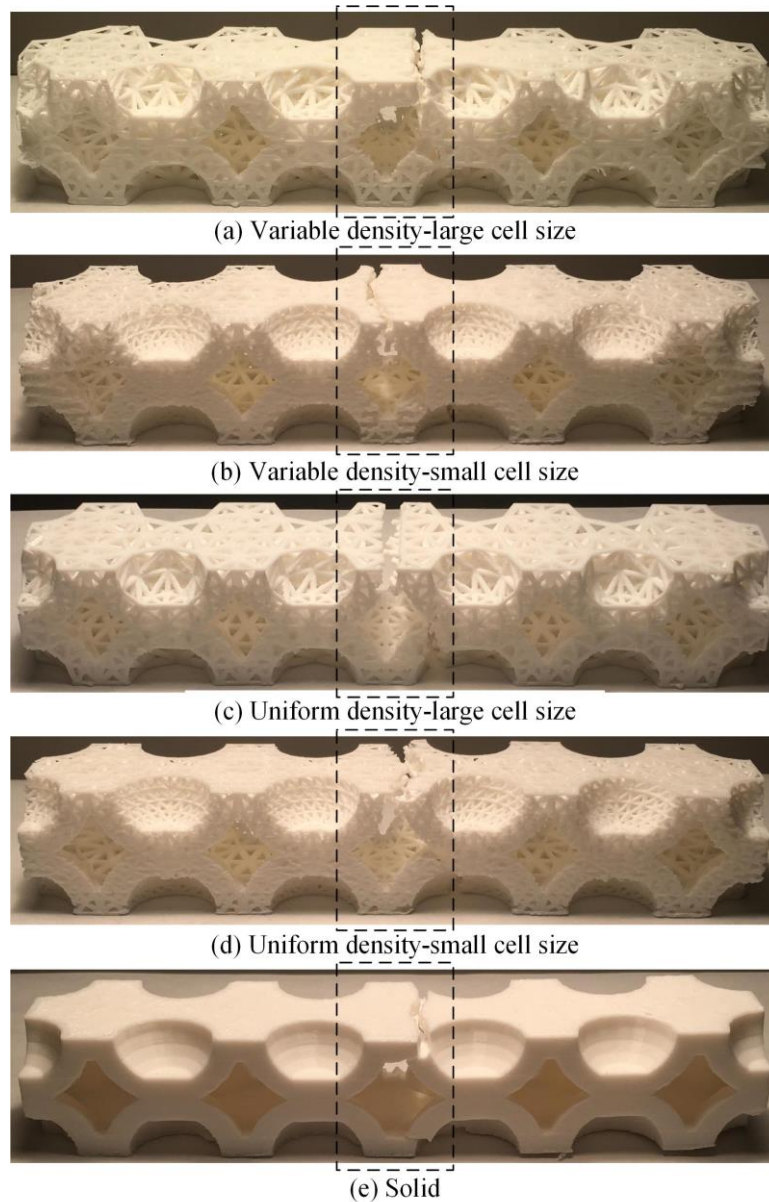


Figure 4-24. Fractured microlattice domes and solid dome after three-point bending tests.

The compressive and three-point bending load–displacement curves obtained through numerical simulation and experiments are shown in Figure 4-25 and Figure 4-26, respectively, where the load is divided by the mass of the corresponding model to acquire the specific load. The specific compressive and bending stiffnesses can be obtained by calculating the slope of the load–displacement curves within the elastic range, as shown in Figure 4-27. The specific energy absorption for the compression and bending models calculated by integrating the area enclosed by the experimental load–displacement curves and the X -axis is shown in Figure 4-28.

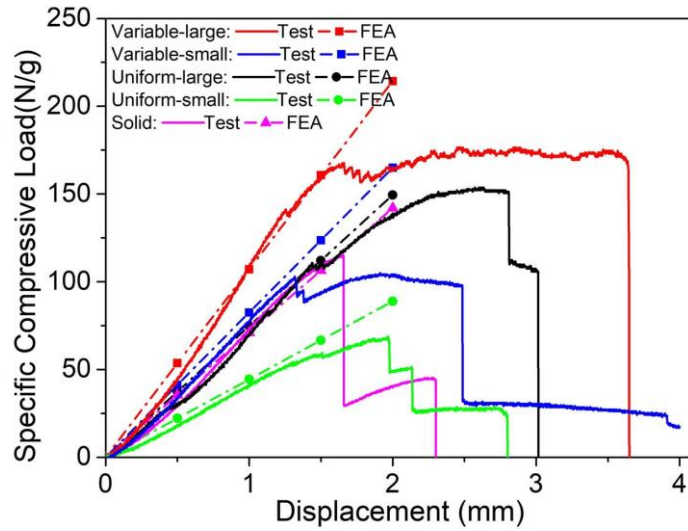


Figure 4-25. Compressive load–displacement curves obtained from numerical simulation and experiments.

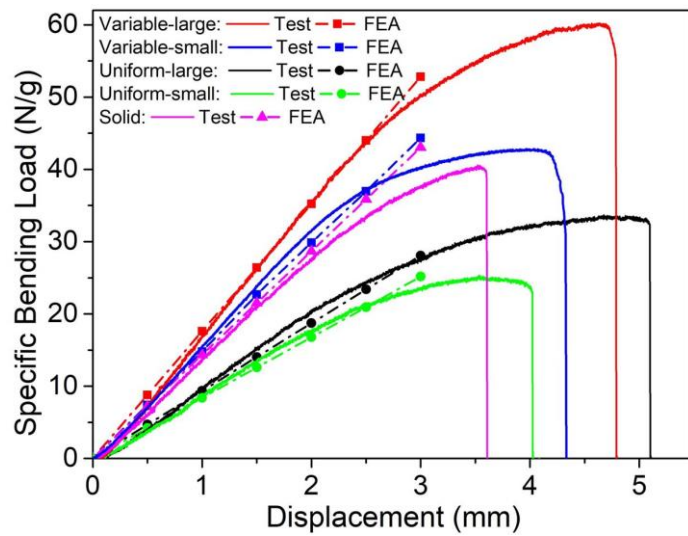


Figure 4-26. Three-point bending load–displacement curves obtained from numerical simulation and experiments.

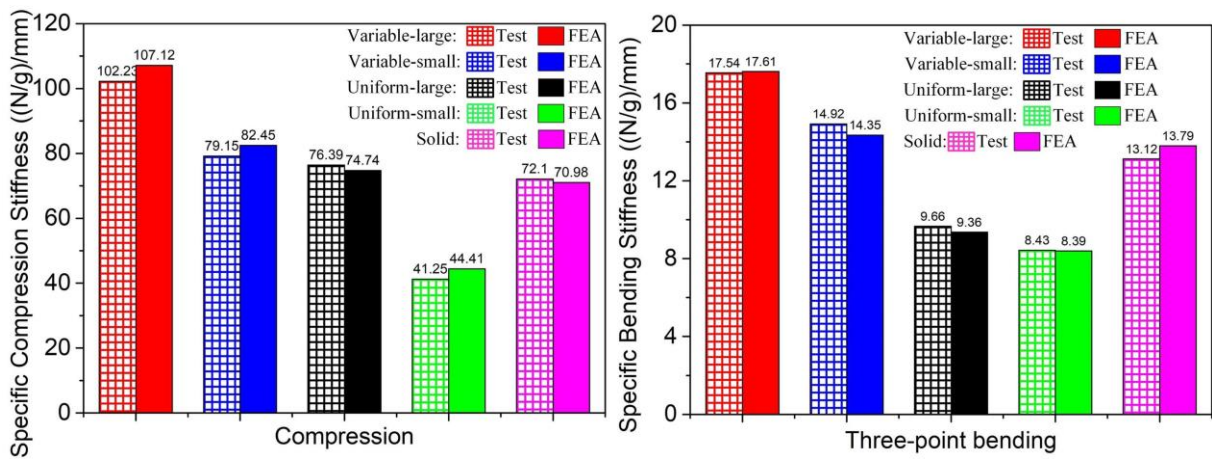


Figure 4-27. Specific compressive and bending stiffnesses obtained from FEA and experiments.

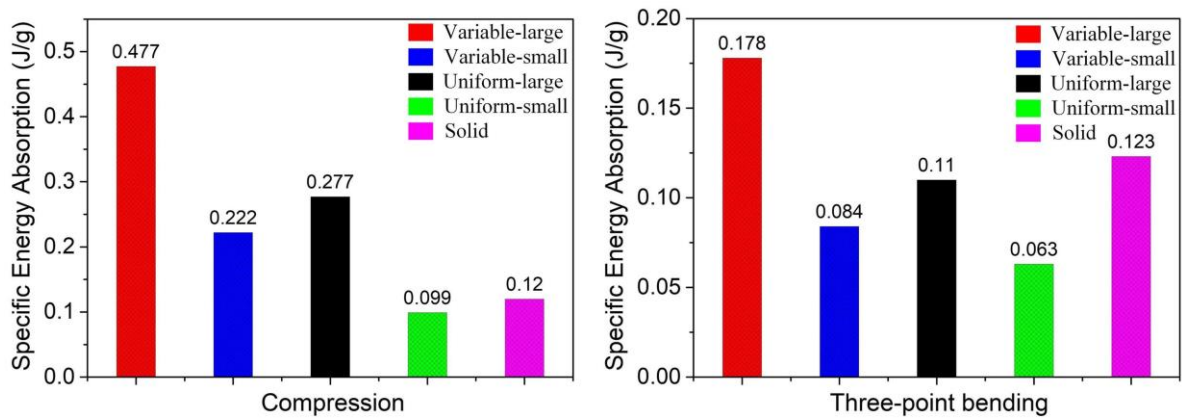


Figure 4-28. Specific energy absorption obtained from experiments.

It is found that the specific compressive stiffnesses of the optimized variable-density models with large and small cell sizes were improved by 33.8% and 91.8%, respectively, compared with the unoptimized uniform-density models. Compared with the unoptimized uniform-density models, the bending stiffnesses of the optimized variable-density models with large and small cells are increased by 81.6% and 76.9%, respectively. One interesting phenomenon is that the unoptimized uniform density model shows abrupt failure during the compression process, while the optimized variable-density structure exhibits a plateau load, which greatly improves the energy absorption capacity of the variable-density model. For the compression models, the energy absorption of the optimized variable-density structures with the large and small cells was improved by 72.2% and 124.2%, respectively. The energy absorption of the optimized variable-density models with the large and small cells is increased by 61.8% and 33.3%, respectively, during the three-point bending process. The above numerical and experimental results validate that the proposed topology optimization method effectively increases the stiffness and energy absorption of the microlattice dome.

Moreover, the compressive and bending stiffnesses of the optimized variable-density microlattice dome have been demonstrated to be 41.8% and 33.7% higher than that of the conventional solid dome. As shown in Figure 4-27, the numerical and experimental compressive stiffness of the unoptimized uniform-density microlattice dome is almost identical

or lower than that of the solid dome. This is consistent with the findings about the compressive stiffness of the 2nd order pyramidal-pyramidal lattice concept proposed by Wu et al. (2019), where the compressive stiffness of the 2nd order pyramidal-pyramidal lattice is found to be lower than that of the 1st order pyramidal lattice. Different from the unoptimized uniform-density microlattice dome and the 2nd order pyramidal-pyramidal lattice, the density distribution of the lattices has been optimized to achieve the optimal structural efficiency based on the applied load and boundary conditions, enabling a higher specific stiffness of the optimized variable-density microlattice dome owing to its highly improved utilization ratio of materials. Compared with the conventional solid dome, the energy absorption of the microlattice dome during compression and three-point bending is increased by 297.5% and 85%, respectively. The above results validate the superiority of the proposed microlattice dome to the conventional solid dome in terms of the stiffness and energy absorption. Furthermore, the microlattice dome with large cells has a higher compression, bending stiffness and energy absorption than the one with small cells, indicating that, under the same overall volume fraction constraint, a larger cell size improves the structural stiffness and energy absorption capability.

4.1.8 Conclusion of section 4.1

A new microlattice dome structure has been proposed, in which the solid part of the conventional dome structure is replaced by less dense and less brittle stretch-dominated tetrahedral microlattices. By integrating homogenization-based topology optimization with a tetrahedral microlattice, the optimal distribution of the microlattice was determined under compression and three-point bending loads to maximize the stiffness and energy absorption of the microlattice dome. The specific compressive stiffnesses of the optimized variable-density models with large and small cell sizes were improved by 33.8% and 91.8%, respectively, compared with the unoptimized uniform-density models. Compared with the unoptimized uniform-density models, the bending stiffnesses of the optimized variable-density models with large and small cells are increased by 81.6% and 76.9%, respectively. For the compression models, the energy absorption of the optimized variable-density structures with the large and small cells was improved by 72.2% and 124.2%, respectively. The energy absorption of the

optimized variable-density models with the large and small cells is increased by 61.8% and 33.3%, respectively, during the three-point bending process. The compressive and bending stiffnesses of the optimized variable-density microlattice domes are proved to be 41.8% and 33.7% higher than those of the conventional solid domes, while the energy absorption of the microlattice dome during compression and three-point bending is increased by 297.5% and 85%, respectively. Investigation of the cell size effect on the mechanical properties of the microlattice dome reveals that a larger cell size contributes more to the weight-specific stiffness and energy absorption capability at a given overall volume fraction constraint. The above significant findings prove that a microlattice dome with high weight-specific stiffness and energy absorption can be designed by integrating topology optimization and lattice structures. The homogenization-based topology optimization and construction methods described in this paper are universal and can be used to optimize and design structures with arbitrary macro shapes with microlattices as constituent units, which is of great significance for the development of ultralight and ultrastiff structures.

4.2 Homogenization-based topology optimization integrated with elastically isotropic lattices for additive manufacturing of ultralight and ultrastiff structures

The integration of topology optimization with lattice structures has shown great potential for the additive manufacturing (AM) of lightweight structures with superior mechanical properties and multifunctional characteristics. To further improve the design manufacturability, structural efficiency, structural isotropy and computational efficiency, the homogenization-based topology optimization (HMTO) method was proposed to integrate with plate–lattices exhibiting superior mechanical properties and excellent elastic isotropy. The validity of the proposed method was demonstrated by comparing the optimized models with conventional models composed of truss–lattices and solid materials. Results show that the proposed method highly improves stiffness and energy absorption capability.

4.2.1 Research background and literature review

Lattice structures have received considerable attention over the past two decades owing to their distinctive mechanical performance and wide multifunctional applications including conformal cooling channels, optimized fluid panels, acoustic damping and energy absorption devices as reviewed by [Thompson et al. \(2016\)](#). The unique layer-by-layer building paradigm of additive manufacturing (AM) enables the fabrication of such lattice structures with variable size, topology and space distribution, thus tailoring the mechanical properties and functionality of structural components.

The synergy of AM with topology optimization has shown much potential for further improvement of the structural efficiency and functionality of lattice structures used in biomedical devices, aerospace components, automotive parts and consumer applications as reviewed by [Vaneke et al. \(2020\)](#). The conventional homogenization-based topology optimization (HMTO) method proposed by [Bendsøe and Kikuchi \(1988\)](#) is capable of providing the optimal design with theoretical bounds on structural efficiency, but has limited computational efficiency as it is quite cumbersome to evaluate and determine the complex geometric parameters of optimal microstructures, and furthermore, the resulting optimal

designs cannot be manufactured due to lack of definite length–scale of the microstructures. For the improvement of computational efficiency and design manufacturability, the solid isotropic material with penalization (SIMP) method has been proposed by [Bendsøe \(1989\)](#) and incorporated in various commercial software packages. However, the optimal design generated by the SIMP method generally requires further post-processing before it can be additively manufactured, resulting in low design efficiency and manufacturability. To further improve manufacturability, the HMTO has been proposed to be integrated with lattice structures such as tetrahedral truss proposed by [Wang et al. \(2018\)](#), hexahedral truss proposed by [Cheng et al. \(2017\)](#) and certain two-dimensional truss–lattices introduced by [Groen and Sigmund \(2018\)](#). The integration of the HMTO method with lattice structures enables elements with intermediate densities in the SIMP method to be manufactured by replacing them with the corresponding lattice structures. Furthermore, lattice structures provide natural internal supports to overhangs during AM build, thus reducing the use of support structures. The computational efficiency of the HMTO method has also been highly improved by integrating the HMTO method with lattice structures as the cumbersome evaluation of microstructures in each iteration step is avoided.

However, the existing investigations on the integration of the HMTO method with lattice structures are limited to the use of truss–lattices of which mechanical properties are much lower than Hashin–Shtrikman’s upper bounds as stated by [Berger et al. \(2017\)](#), resulting in the limited structural efficiency as compared with the parent solid material. In addition, the significant anisotropy exhibited by these truss–lattices, coupled with the AM process-induced anisotropy discussed by [Stanković et al. \(2017\)](#), makes the properties of additively manufactured products more unpredictable and uncontrollable, which is undesirable for engineering materials for mass production. Moreover, an isotropic lattice is easier to be integrated with the HMTO method as fewer independent elastic constants are included in the material stiffness matrix, thereby reducing the computational complexity. To improve the structural efficiency and isotropy, the lattice structures with superior mechanical properties and excellent elastic isotropy are expected to be integrated with the HMTO method. In contrast to the conventional truss–lattices composed of beams or struts, novel plate–lattices composed of closed-cell sheets have been

reported to exhibit superior mechanical properties and can potentially achieve isotropic elastic properties as found by Berger et al. (2017). If such elastically isotropic plate–lattices with superior mechanical properties are integrated with the HMTO method, the structural efficiency and isotropy can be expected to be enhanced.

The aforementioned topology optimization methods are comprehensively evaluated using some indicators including design manufacturability, structural efficiency, structural isotropy and computational efficiency, as shown in Figure 4-29, in which the darker colored box represents better corresponding performance. Compared with other methods, the proposed HMTO method integrated with elastically isotropic plate–lattices can be expected to have the highest manufacturability, structural efficiency, structural isotropy and computational efficiency, which is undoubtedly of great significance for the AM of ultralight and ultrastiff structures. Therefore, in this study, the lattice structure with the excellent structural efficiency and elastic isotropy was integrated with the HMTO method to optimize two typical structures subjected to three-point bending and compression. The stiffness and energy absorption capability of the topologically optimized models were compared with those of the unoptimized model and conventional models composed of truss–lattices and solid materials to evaluate the validity of the proposed method.











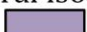









Indicator	Conventional HMTO ^[4]	SIMP ^[5]	HMTO with anisotropic truss-lattices ^[6-8]	HMTO with isotropic plate-lattices
Design manufacturability 	 --	 -	 ++	 ++
Structural efficiency 	 ++	 -	 +	 ++
Structural isotropy 	 -	 ++	 --	 ++
Computational efficiency 	 --	 ++	 +	 ++

Figure 4-29. Comprehensive evaluation of some representative topology optimization methods.

4.2.2 Evaluation of mechanical properties and elastic isotropy

4.2.2.1 Selection of lattice structures

Two classes of lattice structures including truss–lattices and plate–lattices were investigated. As shown in Figure 4-30(a), each type of lattice is categorized into three basic topologies including simple cubic (SC), body-centred cubic (BCC) and face-centred cubic (FCC), through combinations of which various lattice structures can be obtained such as SC–BCC–FCC truss–lattice, SC–BCC and SC–FCC plate–lattices shown in Figure 4-30(b). Here, the mechanical properties and elastic isotropy of six representative lattice structures including two truss–lattices (SC–BCC–FCC and octet truss–lattices) and four plate–lattices (BCC, FCC, SC–BCC and SC–FCC plate–lattices) were evaluated, as shown in Figure 4-30(b). It has been deduced by Tancogne-Dejean et al. (2018) that the topology constraints for achieving elastic isotropy in a combined SC–BCC–FCC lattice should satisfy

$$\rho_{SC}/3 + \rho_{BCC}/6 + \rho_{FCC}/9 = \rho/5 \quad (4-25a)$$

$$\rho_{SC} + \rho_{BCC} + \rho_{FCC} = \rho \quad (4-25b)$$

where ρ_{SC} , ρ_{BCC} and ρ_{FCC} represent the relative densities of elementary SC, BCC and FCC lattices, respectively, and ρ is the relative density of the combined lattice. By solving Eqs. (4-25a) and (4-25b), one can determine the relative density ratio of the SC plate to the BCC plate (ρ_{SC}/ρ_{BCC}) and that of the SC plate to the FCC plate (ρ_{SC}/ρ_{FCC}) in the combined SC–BCC and SC–FCC plate–lattices to be 1/4 and 2/3, respectively.

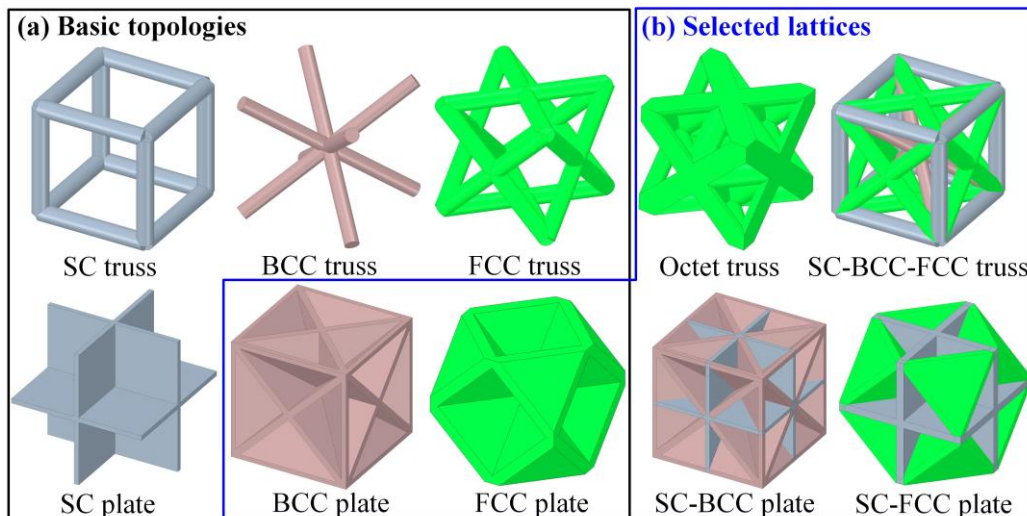


Figure 4-30. Basic topologies of truss–lattices and plate–lattices and their combinations.

4.2.2.2 Effective mechanical properties and elastic isotropy

Uniform macroscopic strains characterizing axial compression and simple shear were applied to the FEM models for the evaluation of equivalent mechanical properties including the elastic modulus E , shear modulus G and Poisson's ratio ν , as shown in Figure 4-31. The elastic modulus E and shear modulus G can be determined as

$$E = \sigma_{yy} / \varepsilon_{yy} \quad (4-26)$$

$$G = \tau_{xy} / \gamma_{xy} \quad (4-27a)$$

$$\gamma_{xy} = 2\varepsilon_{xy} = 2\varepsilon_{yx} \quad (4-27b)$$

where σ_{yy} and ε_{yy} denote the axial compression stress and strain, and τ_{xy} and γ_{xy} are the shear stress and strain, respectively. The macroscopic shear strains applied to the x and y directions are ε_{xy} and ε_{yx} , respectively. Poisson's ratio ν was deduced by dimensions of axial compression models before and after deformation.

The obtained equivalent mechanical properties were normalized by the respective mechanical properties of the parent solid material (E_s and ν_s) and plotted against relative density (ρ) as shown in Figure 4-32, from which, for further integration with the HMTO method, the relationship between effective mechanical properties (E/E_s , G/E_s and ν/ν_s) and relative density can be formulated by polynomial fitting.

The effective elastic modulus was further normalized by the relative density to highlight the structural efficiency as plotted in Figure 4-33(a), from which it can be seen that the plate–lattices exhibit much higher elastic moduli than the truss–lattices especially at low relative densities. The SC–BCC and SC–FCC plate–lattices display superior elastic moduli to other lattices.

The elastic isotropy was evaluated using the Zener anisotropy ratio defined as

$$a = E / [2G(1 + \nu)] \quad (4-28)$$

where a is the Zener anisotropy ratio, which is equal to 1 for an isotropic material. The calculated Zener anisotropic ratio is plotted against relative density as shown in Figure 4-33(b),

which clearly indicates that the SC–BCC and SC–FCC plate–lattices have good elastic isotropy, whereas the octet truss–lattice and FCC plate–lattice are relatively more anisotropic. By comprehensively considering the superior structural efficiency and excellent elastic isotropy, we find that the SC–BCC and SC–FCC plate–lattices are ideal options to be integrated with the HMT0 method.

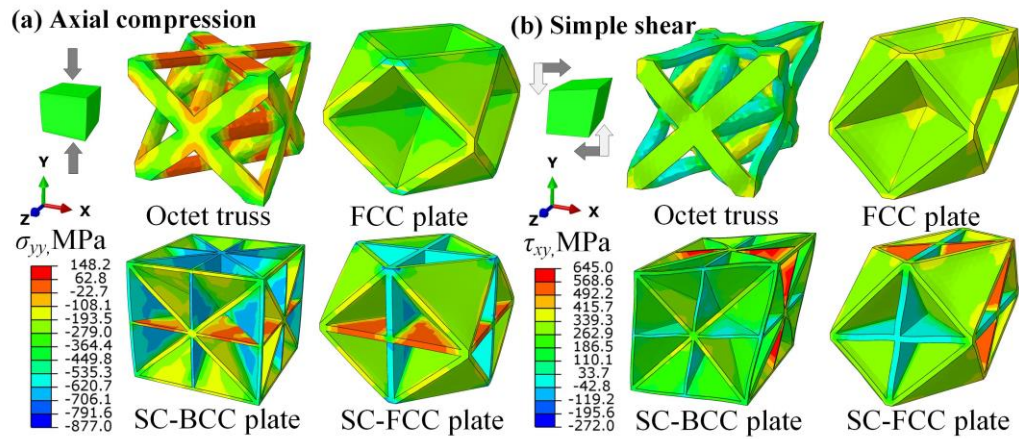


Figure 4-31. Stress distribution of truss–lattices and plate–lattices with relative density of 30% under axial compression strain of 0.2 and shear strain of 0.4.

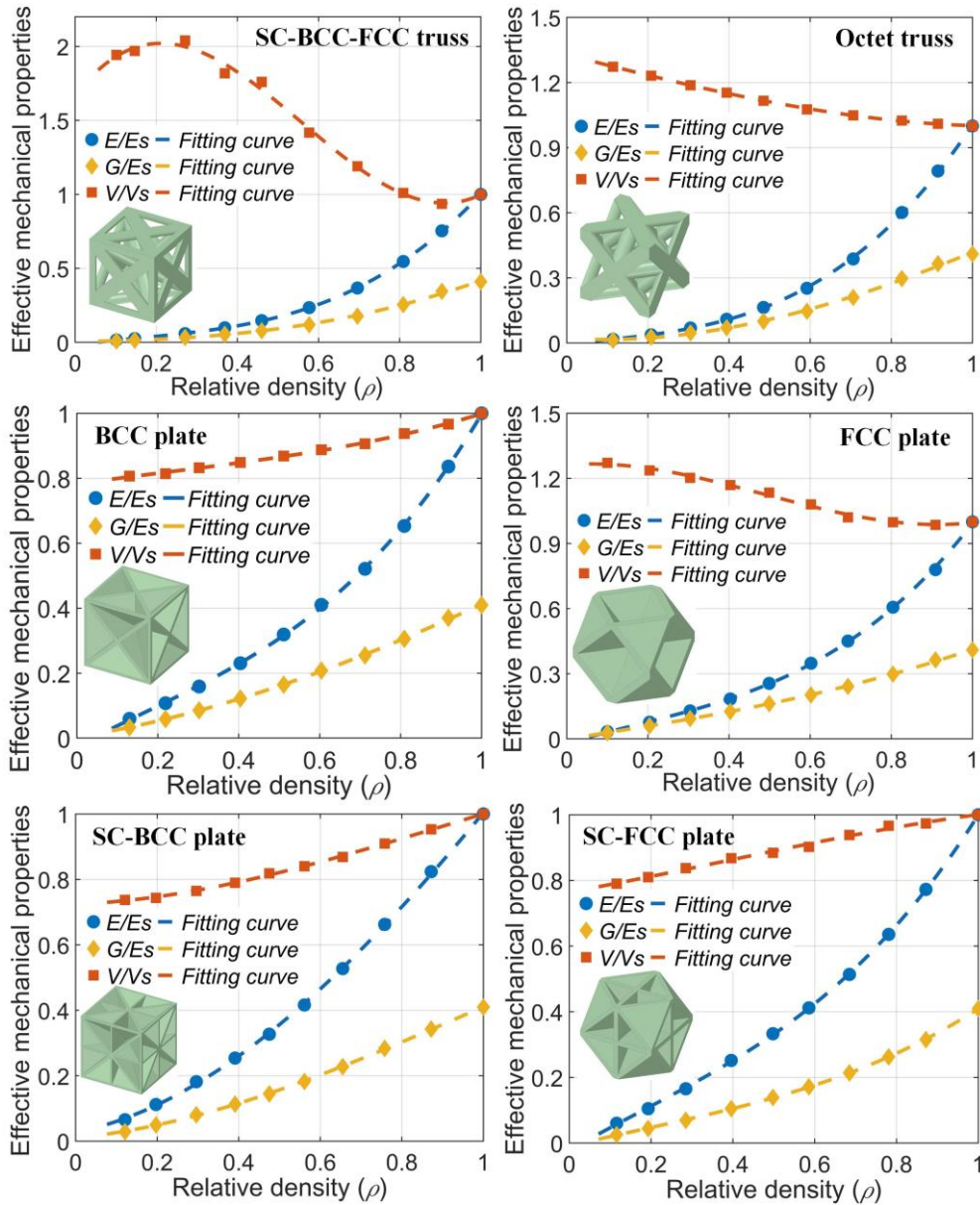


Figure 4-32. Effective mechanical properties at different relative densities for representative truss-lattices and plate-lattices.

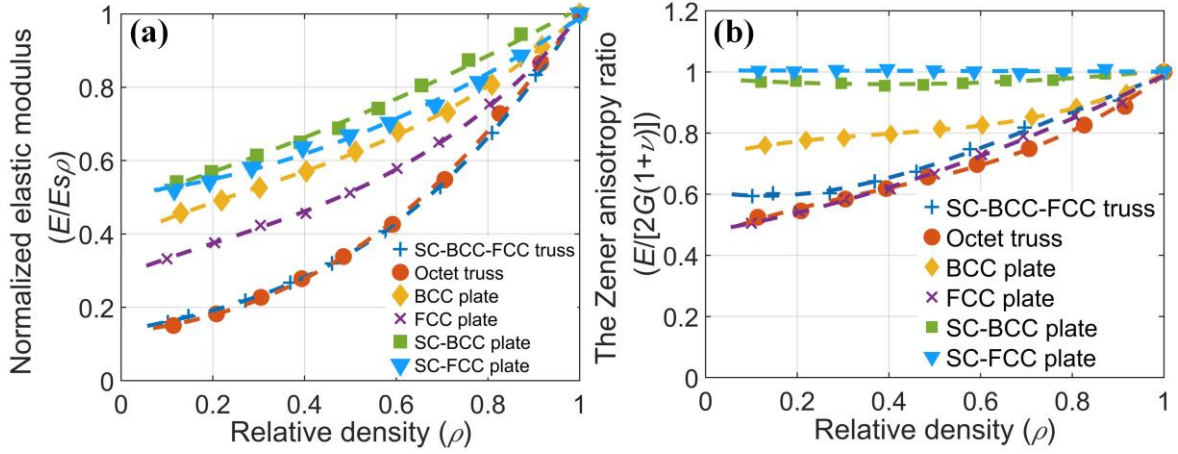


Figure 4-33. Elastic moduli and Zener anisotropy ratios of lattice structures: (a) normalized elastic moduli and (b) Zener anisotropy ratios.

4.2.3 Topology optimization

4.2.3.1 Integration of isotropic lattices with HMTO

The topology optimization procedure has been introduced in detail in **section 4.1**, following the same topology optimization thought, the elastically isotropic lattices were integrated with the HMTO method. In the conventional HMTO method, the microstructure with complex geometric features is explicitly modelled in each optimization step, resulting in high computational cost. As an alternative, the complex lattice structure is equivalent to a homogeneous solid material of which effective mechanical properties are formulated with relative density. Recall that SC-BCC and SC-FCC plate-lattices are better options for integration with HMTO owing to their superior mechanical properties and excellent elastic isotropy. As an example, the relationship between the effective mechanical properties and relative density of the SC-FCC plate-lattice was obtained by polynomial fitting, as given by Eqs. (4-29a)–(4-29c), which were substituted into Eqs. (4-4) and (4-14) for the efficient calculation of c and $\partial c / \partial \rho$ in each iteration step.

$$E = (0.6499\rho^3 - 0.3483\rho^2 + 0.7206\rho - 0.02265)E_s \quad (4-29a)$$

$$G = (0.2614\rho^3 - 0.1467\rho^2 + 0.3035\rho - 0.009393)E_s \quad (4-29b)$$

$$\nu = (-0.08154\rho^3 + 0.09356\rho^2 + 0.2244\rho + 0.7643)\nu_s \quad (4-29c)$$

4.2.3.2 Topology optimization examples

A rectangular beam subjected to three-point bending and a pyramidal structure subjected to out-of-plane compression were selected to evaluate the proposed method. Dimensions and boundary conditions of topology optimization models are shown in Figure 4-34. As the side length of the elementary cubic lattice was 10 mm, 100 and 384 unit cells were included in the rectangular beam and pyramidal structure, respectively. Owing to the symmetry of the pyramidal structure, only a 1/4 model was used.

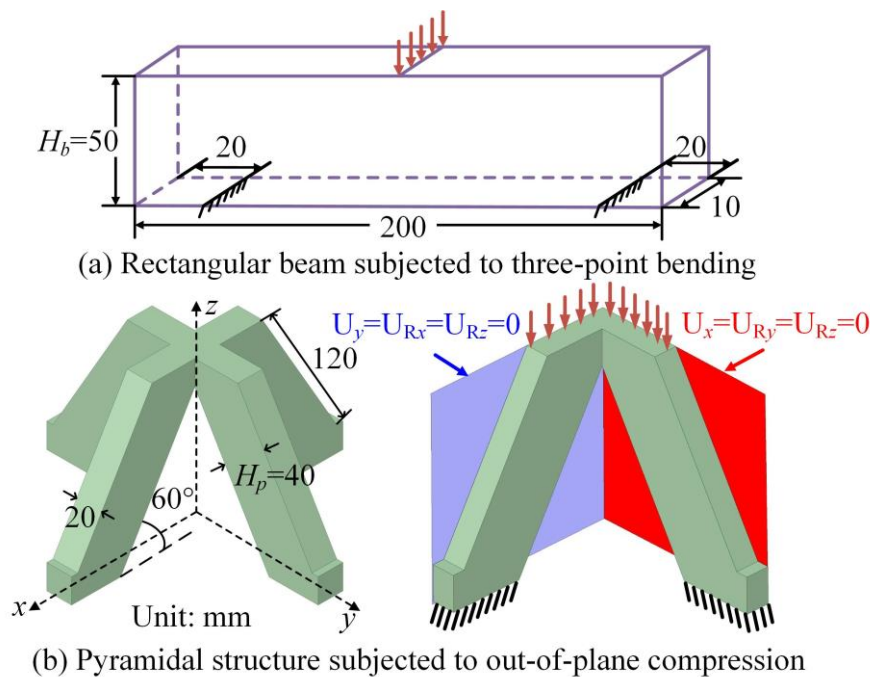


Figure 4-34. Dimensions and boundary conditions of topology optimization models subjected to three-point bending and out-of-plane compression.

4.2.3.3 Numerical validation and experimental tests

The 3D models were automatically constructed based on topology optimization results for numerical validation and AM, which was implemented by the Python script incorporated in the CAD software SCDM. Numerical simulation and experiments were conducted on the optimized and unoptimized models for the validation of topology optimization results. Furthermore, conventional models composed of uniform octet truss–lattices (unoptimized octet) and solid materials (solid model) with the same weight were also investigated for comparison. Note that H_b and H_p (shown in Figure 4-34) were set to 27.5 and 22 mm for the rectangular

beam and pyramidal solid models, respectively. All the models were printed by fused deposition modelling machine *Flashforged's GuilderII* using a polylactic acid (PLA) material. The same process parameters in **section 4.1** were adopted and the printed PLA has an elastic modulus of 2.8 GPa, a yield strength of 37.6 MPa and Poisson's ratio of 0.22. The constructed models were imported into Abaqus 6.14-2, in which the boundary conditions were consistent with the topology optimization models.

4.2.4 Results and discussion

4.2.4.1 Topology optimization results

The optimal density distribution maps of SC-FCC plate-lattices obtained through topology optimization are shown in [Figure 4-35\(a\)](#). The relative densities of elements in the design zone were constrained between 25 and 85% with an overall volume fraction of 55%. The highlighted blue region of the pyramidal structure was set as the solid part as it cannot be fully filled by the cubic SC-FCC plate-lattices owing to its irregular shape. The constructed optimized 3D models are shown in [Figure 4-35\(b\)](#), in which the highlighted black regions of the optimized 3D models are in accordance with the density distribution maps of topology optimization results. Printed optimized and unoptimized rectangular beams are shown in [Figure 4-36](#) to highlight the difference.

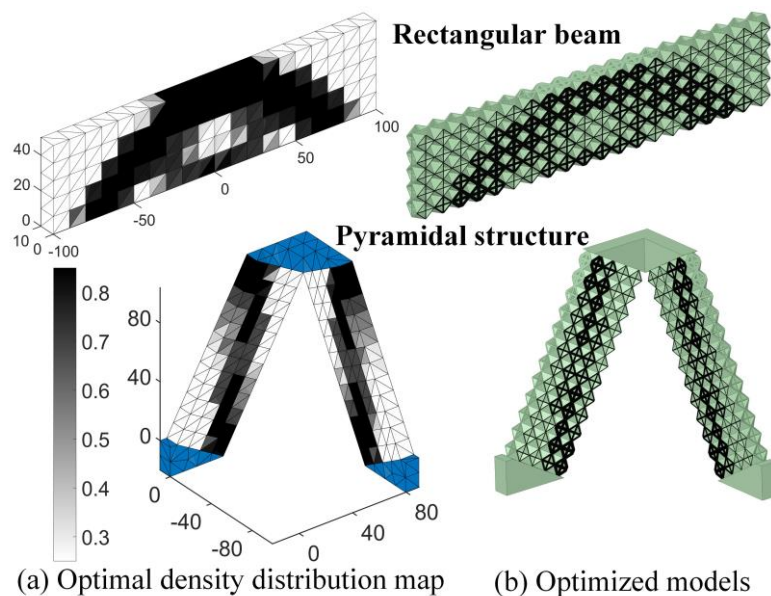


Figure 4-35. Topology optimization results and constructed 3D models.

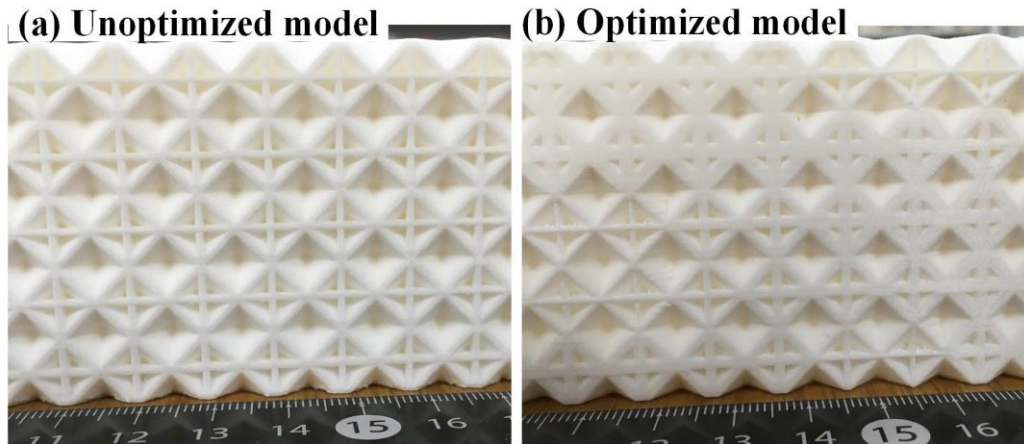


Figure 4-36. Optimized and unoptimized rectangular beams obtained by AM.

4.2.4.2 Stiffness and energy absorption capability

The load–displacement curves obtained from three-point bending and compression simulation and experiments are respectively shown in Figure 4-37(a) and (c), from which the corresponding stiffness and absorbed energy were obtained as shown in Figure 4-37(b) and (d). Note that the material properties assumed in the numerical simulation were ideally elastoplastic; therefore, the numerically predicted and experimental loads show large discrepancy after fracture. Although experimental stiffness is generally lower than the numerically predicted results owing to the deterioration of material properties during AM build, both of them display the same trend.

For the rectangular beam, the stiffness values of the optimized SC–FCC model are 103.5%, 127.2% and 24.9% higher than those of the solid, unoptimized octet and SC–FCC models, while the absorbed energies are 19.2% and 44.7% higher than those of the solid and unoptimized octet models, respectively. For the pyramidal structure, the optimized SC–FCC model exhibits 6.5%, 117.5% and 28.3% higher stiffness than the solid, unoptimized octet and SC–FCC models, respectively, while the absorbed energy is respectively improved by 53.3%, 120.7% and 26.0%. Both examples show highly improved stiffness and energy absorption capability of optimized models obtained by the proposed method.

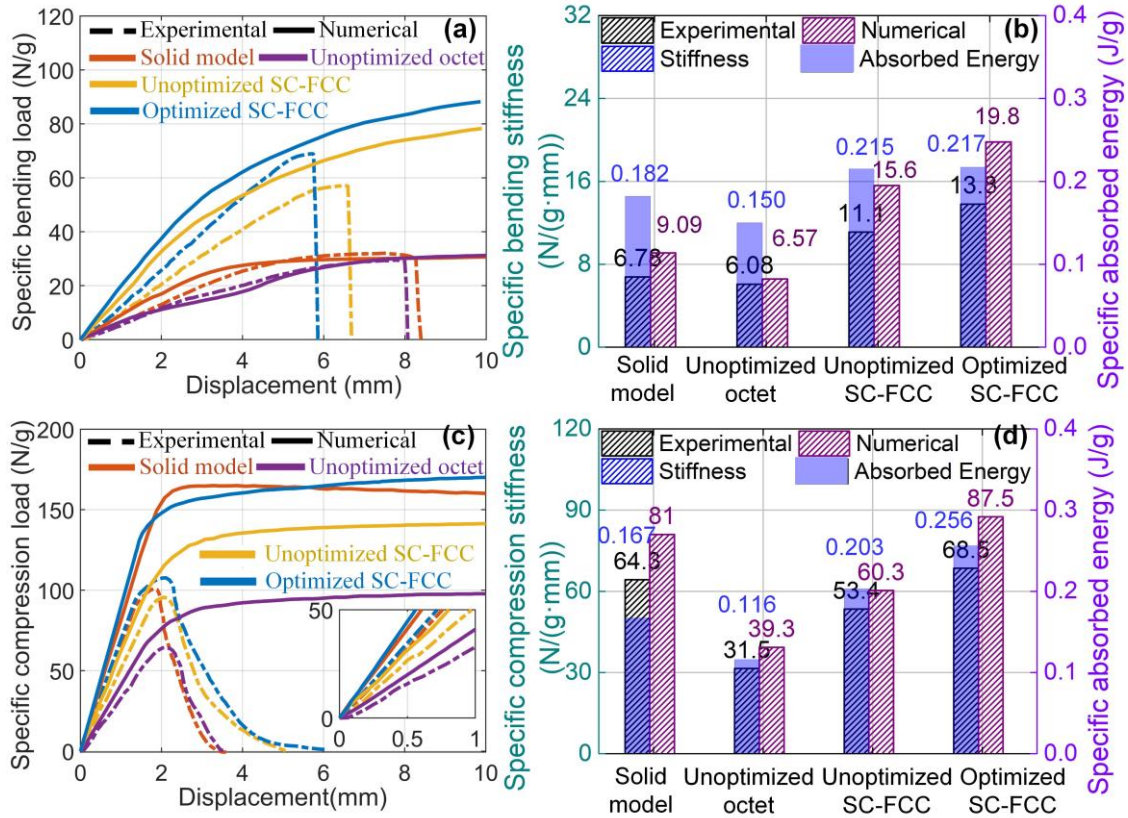


Figure 4-37. Three-point bending and out-of-plane compression results.

4.2.5 Conclusion of section 4.2

Elastically isotropic plate-lattices with superior mechanical properties were firstly proposed to be integrated with the HMTO method to improve design manufacturability, structural efficiency, structural isotropy and computational efficiency. The mechanical properties and elastic isotropy of representative truss-lattices and plate-lattices were investigated, after which the SC-FCC plate-lattice with excellent structural efficiency and elastic isotropy was integrated with the HMTO method to optimize two typical examples. The results indicate the proposed method can significantly improve structural efficiency including stiffness and energy absorption capability. Together with more advantages that this approach is easily implementable and generates designs suitable for AM, the proposed method can be expected to promote the development of ultralight and ultrastiff structures.

4.3 Summary

Although conventional manufacturing processes allow some control over shape and size of the inner core structure, they remain limited to producing a certain type of specially designed structures and thus the mechanical property, formability and functionality of inner core structures may still be restricted. In addition, the incapability of manufacturing precise complex structures, the high manufacturing cost and the discrepancy in the properties of produced structures also limit the applications of the conventional fabrication methods. The layer-by-layer fabrication paradigm of AM enables the build of lattice materials with extremely intricate external geometries and high control of the internal architecture, overcoming the limitations of conventional fabrication methods. The topology optimization enables the optimal material layout of the core structure at a given set of load and boundary conditions, and thus it can be relied on to optimize the core structure for the pursuit of higher structural efficiency and better formability. The synergy of topology optimization and additive manufacturing could be a perfect tool for the design and production of sandwich sheets with improved mechanical performance, formability and functionality. Therefore, the topology optimization is used to design optimal core structures with superior stiffness and formability in this chapter.

A new microlattice dome structure has been proposed, in which the solid part of the conventional dome structure is replaced by less dense and less brittle stretch-dominated tetrahedral microlattices. By integrating homogenization-based topology optimization with a tetrahedral microlattice, the optimal distribution of the microlattice was determined under compression and three-point bending loads to maximize the stiffness and energy absorption of the microlattice dome. The specific compressive stiffnesses of the optimized variable-density models with large and small cell sizes were improved by 33.8% and 91.8%, respectively, compared with the unoptimized uniform-density models. Compared with the unoptimized uniform-density models, the bending stiffnesses of the optimized variable-density models with large and small cells are increased by 81.6% and 76.9%, respectively. For the compression models, the energy absorption of the optimized variable-density structures with the large and small cells was improved by 72.2% and 124.2%, respectively. The energy absorption of the

optimized variable-density models with the large and small cells is increased by 61.8% and 33.3%, respectively, during the three-point bending process. The compressive and bending stiffnesses of the optimized variable-density microlattice domes are proved to be 41.8% and 33.7% higher than those of the conventional solid domes, while the energy absorption of the microlattice dome during compression and three-point bending is increased by 297.5% and 85%, respectively. Investigation of the cell size effect on the mechanical properties of the microlattice dome reveals that a larger cell size contributes more to the weight-specific stiffness and energy absorption capability at a given overall volume fraction constraint. The above significant findings prove that a microlattice dome with high weight-specific stiffness and energy absorption can be designed by integrating topology optimization and lattice structures. The homogenization-based topology optimization and construction methods described in this paper are universal and can be used to optimize and design structures with arbitrary macro shapes with microlattices as constituent units, which is of great significance for the development of ultralight and ultrastiff structures.

Elastically isotropic plate-lattices with superior mechanical properties were firstly proposed to be integrated with the HMTO method to improve design manufacturability, structural efficiency, structural isotropy and computational efficiency. The mechanical properties and elastic isotropy of representative truss-lattices and plate-lattices were investigated, after which the SC-FCC plate-lattice with excellent structural efficiency and elastic isotropy was integrated with the HMTO method to optimize two typical examples. The results indicate the proposed method can significantly improve structural efficiency including stiffness and energy absorption capability. Together with more advantages that this approach is easily implementable and generates designs suitable for AM, the proposed method can be expected to promote the development of ultralight and ultrastiff structures.

4.4 References

- Arabnejad, S., Pasini, D., 2013. Mechanical properties of lattice materials via asymptotic homogenization and comparison with alternative homogenization methods. *International Journal of Mechanical Sciences* 77, 249-262.
- Atwater, M.A., Guevara, L.N., Darling, K.A., Tschopp, M.A., 2018. Solid state porous metal production: a review of the capabilities, characteristics, and challenges. *Advanced Engineering Materials* 20, 1700766.
- Bendsøe, M.P., 1989. Optimal shape design as a material distribution problem. *Structural optimization* 1, 193-202.
- Bendsøe, M.P., Kikuchi, N., 1988. Generating optimal topologies in structural design using a homogenization method. *Computer methods in applied mechanics and engineering* 71, 197-224.
- Bendsoe, M.P., Sigmund, O., 2003. *Topology optimization: theory, methods, and applications*. Springer Science & Business Media.
- Bendsøe, M.P., Sigmund, O., 1995. *Optimization of structural topology, shape, and material*. Springer.
- Berger, J., Wadley, H., McMeeking, R., 2017. Mechanical metamaterials at the theoretical limit of isotropic elastic stiffness. *Nature* 543, 533-537.
- Besse, C.C., Mohr, D., 2012. Plasticity of formable all-metal sandwich sheets: Virtual experiments and constitutive modeling. *International Journal of Solids and Structures* 49, 2863-2880.
- Cheng, L., Zhang, P., Biyikli, E., Bai, J., Robbins, J., To, A., 2017. Efficient design optimization of variable-density cellular structures for additive manufacturing: theory and experimental validation. *Rapid Prototyping Journal*.
- Dumas, M., Terriault, P., Brailovski, V., 2017. Modelling and characterization of a porosity graded lattice structure for additively manufactured biomaterials. *Materials & Design* 121, 383-392.
- Groen, J.P., Sigmund, O., 2018. Homogenization-based topology optimization for high-resolution manufacturable microstructures. *International Journal for Numerical Methods in Engineering* 113, 1148-1163.
- Hussein, A., Hao, L., Yan, C., Everson, R., Young, P., 2013. Advanced lattice support structures for metal additive manufacturing. *Journal of Materials Processing Technology* 213, 1019-1026.
- Karlsson, J., Snis, A., Engqvist, H., Lausmaa, J., 2013. Characterization and comparison of materials produced by Electron Beam Melting (EBM) of two different Ti-6Al-4V powder fractions. *Journal of materials processing technology* 213, 2109-2118.
- Lingham-Soliar, T., 2014. Feather structure, biomechanics and biomimetics: the incredible lightness of being. *Journal of ornithology* 155, 323-336.
- Mahmoud, D., Elbestawi, M.A., 2017. Lattice structures and functionally graded materials applications in additive manufacturing of orthopedic implants: a review. *Journal of Manufacturing and Materials Processing* 1, 13.
- Maskery, I., Aboulkhair, N., Aremu, A., Tuck, C., Ashcroft, I., Wildman, R.D., Hague, R.,

2016. A mechanical property evaluation of graded density Al-Si10-Mg lattice structures manufactured by selective laser melting. *Materials Science and Engineering: A* 670, 264-274.

Meyers, M.A., McKittrick, J., Chen, P.-Y., 2013. Structural biological materials: critical mechanics-materials connections. *science* 339, 773-779.

Panesar, A., Abdi, M., Hickman, D., Ashcroft, I., 2018. Strategies for functionally graded lattice structures derived using topology optimisation for additive manufacturing. *Additive Manufacturing* 19, 81-94.

Seki, Y., Schneider, M.S., Meyers, M.A., 2005. Structure and mechanical behavior of a toucan beak. *Acta Materialia* 53, 5281-5296.

Sigmund, O., 1997. On the design of compliant mechanisms using topology optimization. *Journal of Structural Mechanics* 25, 493-524.

Sigmund, O., 2001. A 99 line topology optimization code written in Matlab. *Structural and multidisciplinary optimization* 21, 120-127.

Stanković, T., Mueller, J., Shea, K., 2017. The effect of anisotropy on the optimization of additively manufactured lattice structures. *Additive Manufacturing* 17, 67-76.

Tancogne-Dejean, T., Diamantopoulou, M., Gorji, M.B., Bonatti, C., Mohr, D., 2018. 3D Plate-Lattices: An Emerging Class of Low-Density Metamaterial Exhibiting Optimal Isotropic Stiffness. *Advanced Materials* 30, 1803334.

Thompson, M.K., Moroni, G., Vaneker, T., Fadel, G., Campbell, R.I., Gibson, I., Bernard, A., Schulz, J., Graf, P., Ahuja, B., 2016. Design for Additive Manufacturing: Trends, opportunities, considerations, and constraints. *CIRP annals* 65, 737-760.

Vaneker, T., Bernard, A., Moroni, G., Gibson, I., Zhang, Y., 2020. Design for additive manufacturing: Framework and methodology. *CIRP Annals* 69, 578-599.

Wang, Y., Arabnejad, S., Tanzer, M., Pasini, D., 2018. Hip implant design with three-dimensional porous architecture of optimized graded density. *Journal of Mechanical Design* 140, 111406.

Wu, Q., Vaziri, A., Asl, M.E., Ghosh, R., Gao, Y., Wei, X., Ma, L., Xiong, J., Wu, L., 2019. Lattice materials with pyramidal hierarchy: systematic analysis and three dimensional failure mechanism maps. *Journal of the Mechanics and Physics of Solids* 125, 112-144.

Yang, W., Chao, C., McKittrick, J., 2013. Axial compression of a hollow cylinder filled with foam: A study of porcupine quills. *Acta biomaterialia* 9, 5297-5304.

Yap, C.Y., Chua, C.K., Dong, Z.L., Liu, Z.H., Zhang, D.Q., Loh, L.E., Sing, S.L., 2015. Review of selective laser melting: Materials and applications. *Applied physics reviews* 2, 041101.

Zegard, T., Paulino, G.H., 2016. Bridging topology optimization and additive manufacturing. *Structural and Multidisciplinary Optimization* 53, 175-192.

Zhu, C., Han, T.Y.-J., Duoss, E.B., Golobic, A.M., Kuntz, J.D., Spadaccini, C.M., Worsley, M.A., 2015. Highly compressible 3D periodic graphene aerogel microlattices. *Nature communications* 6, 1-8.

Chapter 5 Concurrent topology optimization of formability and bending stiffness of sandwich sheets

To expand the application ranges of sandwich sheets from conventional 2D flat panel types to 3D complex shapes and simultaneously improve the specific bending stiffness, a novel topology optimization strategy that can optimize the bending stiffness while maintaining good formability was proposed. In the proposed approach, the density-based topology optimization was integrated with the multi-stage genetic algorithm (GA) to optimize the repeatable unit cell of the core structure of sandwich sheets. Two optimization schemes were adopted, in which one optimizes the formability and the other one optimizes the bending stiffness while fulfilling potential failure constraints. The failure constraints on core shear failure and face buckling were theoretically deduced to mathematically formulate the topology optimization problem, which was solved by the adaptive multi-stage GA to increase the possibility of generating physically meaningful and additively manufacturable topologies. For the experimental evaluations of mechanical properties and formability, the final optimal topologies under volume fraction constraints of 50% and 62.5% were additively manufactured using carbon fibre reinforced nylon. Comparing the sandwich topologies obtained by two optimization schemes, the bending stiffness of sandwich topologies with the core density of 50% and 62.5% are improved by 41.58% and 41.49%, while the energy absorption capabilities are improved by 13.60% and 29.40% respectively. L-bending and draw-bending tests indicate the improved formability of topologically optimized sandwich sheets. The proposed approach is capable of designing formable sandwich sheets with improved bending stiffness, which is expected to expand the application envelope of sandwich sheets with better mechanical properties.

5.1 Research background and literature review

Sandwich structures have been widely employed in many engineering areas especially in the aerospace and automotive industries owing to their superior weight-specific mechanical properties and multifunctional characteristics. However, the complex failure behaviours such as the core-face sheet delamination, face fracture, face buckling and core shear failure tend to cause poor formability of sandwich sheets, and thus limiting their applications to flat panel types. The conventional fabrication of three-dimensional sandwich structures involves the separate forming of face sheets and core into curved shapes followed by joining them together, which results in a high production cost and a low manufacturing efficiency. The design of sandwich sheets that can be formed by conventional sheet forming processes such as bending or drawing could be the key to expanding the application ranges to complex three-dimensional shapes. For this purpose, the formability of metal-polymer-metal sandwich sheets has been extensively investigated by Carradò et al. (2011) and Jackson et al. (2008). Formability of AA5182/polypropylene/AA5182 sandwich sheets has been comprehensively investigated by experimental tests for the establishment of forming limit diagram (FLD) as reported by Liu et al. (2013). Bending and deep drawing tests disclose good formability of steel/polymer/steel sandwich sheets with solid and mesh steel inlays as presented by Sokolova et al. (2011).

To further improve the structural efficiency in terms of weight-specific stiffness and strength, formable sandwich sheets with a hollow 3D core have been designed. Compared with sandwich sheets with the 2D core, it is more difficult to form sandwich sheets with the 3D hollow core as core shear failure and face buckling can be more easily caused owing to insufficient core shear strength and large gap between attachment points. The failure mechanism of thin metallic sandwich sheets during draw-bending was investigated by Mohr (2005), in which the core shear failure is revealed to be the main failure mode. A sheared dimple core was designed by Seong et al. (2010) for metallic sandwich sheets as it can provide sufficient core shear strength and effectively suppress the core shear failure during bending. The feasibility of plastic forming of sandwich sheets with egg-box-like (EBL) cores is revealed to be limited by face sheet buckling, face sheet dimpling and core cell fracture as reported by

Cai et al. (2018). The metal-based composite sheets with a 3D CFRP core were designed by Zhang and Yanagimoto (2019) and their forming behaviours under cold and warm forming conditions have been extensively examined by Zhang et al. (2021b). The effects of sandwich geometries and forming tool geometries on formability have been clarified by Zhang et al. (2020).

Although the sandwich sheets designed in aforementioned investigations may display good bendability or formability to a certain extent, their designs are mainly based on empirically parametric or shape optimizations and thus the structural topologies may not be the optimal. Moreover, only the formability of sandwich sheets is considered during the design process in aforementioned investigations and the bending stiffness of sandwich sheets is neglected. Different from the empirically parametric or shape designs, topology optimization is an intelligent structural design strategy which can generate optimal material distribution in the design space under given boundary constraints and objective functions. For lightweight functional designs, numerous topology optimization methods have been proposed, which can be mainly classified into the density-based method proposed Bendsøe (1989) and Zhou and Rozvany (1991), the level-set approach proposed by Allaire et al. (2002) and Wang et al. (2003), the topological derivative method proposed by Sokolowski and Zochowski (2003), the phase field method proposed by Bourdin and Chambolle (2003), evolutionary approach proposed by Xie and Steven (1993) and moving morphable components (MMC) proposed by Guo et al. (2014). Recently, with the rapid development of additive manufacturing technology, complex structures generated based on topology optimization can be actually produced and thus the integration of topology optimization and additive manufacturing has become a powerful tool in designing lightweight structures as adopted by Zhang et al. (2021a), heat exchanger as proposed by Cheng et al. (2018), vibrating structures as presented by Li et al. (2021), biomedical devices as reviewed by Cucinotta et al. (2019), magnetic actuators as produced by Sundaram et al. (2019) and soft robots as developed by Zhang et al. (2017).

Inspired by the conventional density-based topology optimization concept, an intelligent topology optimization approach was proposed to design the sandwich sheets that can not only withstand potential failure modes but also have the optimal bending stiffness in this study.

Based on the density-based topology optimization approach proposed by [Bendsøe \(1989\)](#), the repeatable unit cell of the core structure is taken as the design domain that is discretized into micro-design elements, in which the element of density 1 represents the solid part while the density of 0 is the void. Then the topology optimization problem with the element density as the design variable, the failure modes as the constraint conditions and the bending stiffness as the objective function is solved by the multi-stage genetic algorithm (GA) proposed by [Kim and De Weck \(2005\)](#). In the present study, the constraint conditions on failure modes including core shear failure and face buckling were firstly theoretically deduced to mathematically formulate the topology optimization problem. To improve the computational efficiency and structural resolution, the multi-stage GA was adopted to solve the topology optimization problem with massive design elements. Then, the optimal topologies were converted to 3D models that were additively manufacturable, after which the prototypes were additively manufactured using carbon fibre reinforced nylon. Finally, the produced sandwich sheets were subjected to three-point bending tests to validate the bending stiffness and energy absorption abilities, while the L-bending and draw-bending tests were employed to check the formability of designed sandwich sheets.

5.2 Topology optimization method

5.2.1 Introduction of topology optimization strategy

In the present study, the objective is to find the optimal topology of the unit cell of core structure so that the sandwich sheets can be bent without failure. Taking the unit cell of core structure as the design domain, as shown in Figure 5-1, inspired by the density-based topology optimization method, the design domain was discretized into micro design elements, in which each element is either a solid element indicated by the black colour or a void element represented by the white colour. The solid element has a density of 1, namely, the material properties of the solid element are the same as the basis core material, while the void element has a density of 0 and its material properties are 0. The mechanical characteristics of core unit cell depend on the number and distribution of solid elements in the design domain, which in turn affects the failure resistance of sandwich sheets during bending. Therefore, the topology optimization of core unit cell for bendable sandwich sheets is actually to find the optimal density distribution of elements in the design domain so that potential failure modes of sandwich sheets during bending can be suppressed. To achieve this, the constraints on potential failure modes should be mathematically formulated to solve the topology optimization problem, which will be discussed in the following sections.

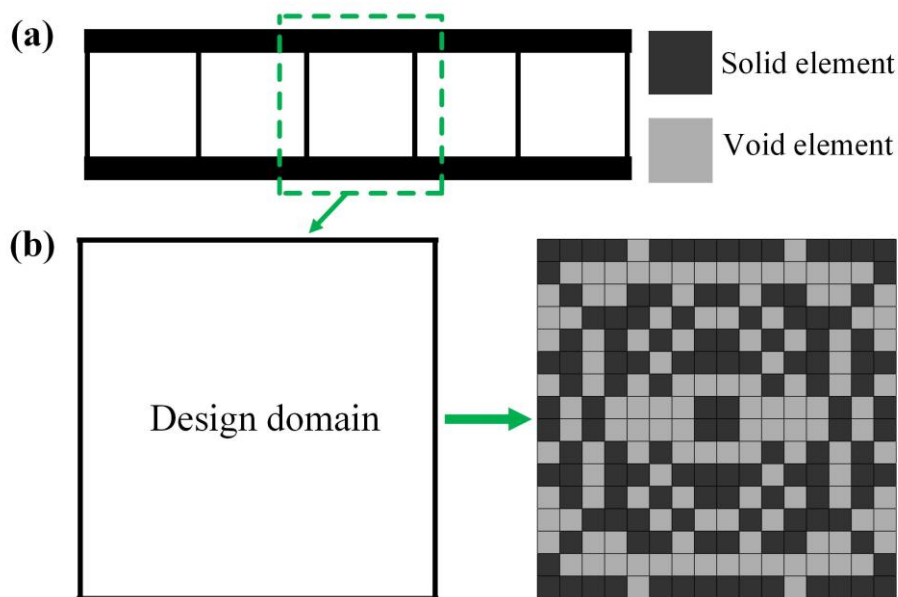
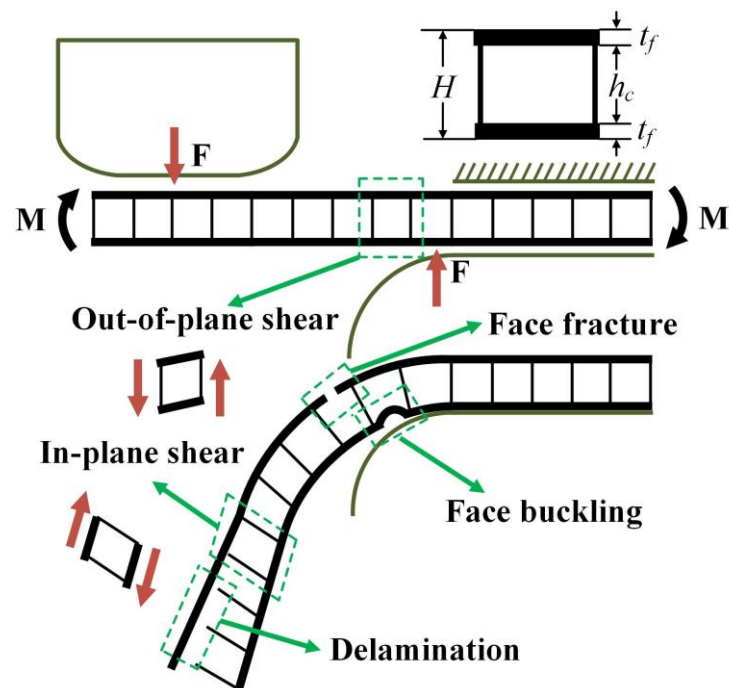


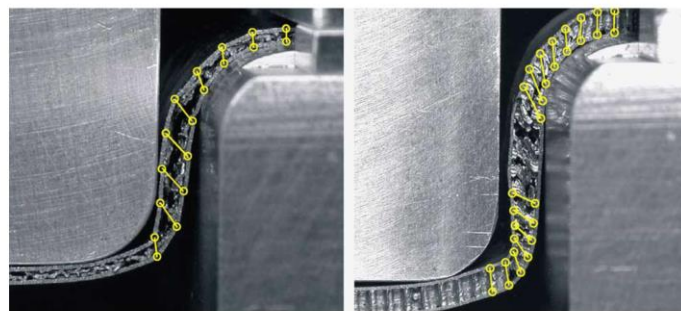
Figure 5-1. Illustration of topology optimization strategy.

5.2.2 Potential failure modes and corresponding constraints

Different from conventional monolithic sheets of which sheet buckling and sheet fracture are main failures, potential failure modes of sandwich sheets are more complicated during bending. As illustrated in Figure 5-2, typical failure modes of sandwich sheets include shear failure of core material, face buckling, face fracture and core-face sheet delamination. To formulate the topology optimization problem for bendable sandwich sheets, failure constraints should be obtained. Therefore, in this section, the constraints on failure modes were firstly deduced.



(a) Illustration of potential failure modes



(b) Experimentally observed failures

Figure 5-2. Illustration of typical failure modes of sandwich sheets during bending: (a) typical failure modes including core shear failure, face buckling, face fracture and core-face sheet

delamination and (b) experimentally observed failure modes of sandwich sheets during bending [Mohr \(2005\)](#).

5.2.2.1 Core shear failure constraint

Shear failure of core material is commonly seen in forming of sandwich sheets with a hollow core owing to its insufficient core shear strength. As shown in [Figure 5-2\(a\)](#), the unit cell near the shoulder of the lower die tends to be subjected to out-of-plane shear, while the one close to the fillet of the upper die mainly withstands the in-plane shear deformation. The experimental observations by [Mohr \(2005\)](#), as shown in [Figure 5-2\(b\)](#), indicate the same shear deformation modes of unit cells as described above. Since a hollow core is generally lack of sufficient core shear strength, the shear failure of core material has been revealed to be the main failure mode for sandwich sheets with a hollow core. For bendable sandwich sheets, the core shear strength should not be lower than the required core shear strength expressed by [Eq. \(2-15\)](#). The core shear strength will be obtained by FEM during the optimization process, which will be described in the following section.

5.2.2.2 Face buckling constraint

For sandwich sheets with a hollow core, as the gap between attachment points is generally too large for the face sheets to receive sufficient support from the core, the face buckling can be easily caused during bending as shown in [Figure 5-2\(a\)](#). To suppress face buckling, the gap between attachment points (d) should not be higher than the critical gap between attachment points (d_{cr}).

As described in [section 2.2.2](#), during bending, the maximum compressive strain in the face sheet is:

$$\varepsilon_c^{\max} = \frac{1}{2 + \varepsilon^*} \left[\frac{\sigma_f}{E_T} \varepsilon^* - \ln(1 + \varepsilon^*) \right] \quad (5-1)$$

where ε^* is given by [Eq. \(2-3\)](#).

With the maximum compressive strain, the maximum compressive stress is known. The face buckling can be suppressed if the magnitude of the maximum compressive stress is lower than the buckling strength σ_{cr} that is expressed by [Hibbeler \(2003\)](#):

$$\sigma_{cr} = \frac{k_c \pi^2 E t_f^2}{12(1-\nu^2)d^2} \quad (5-2)$$

where ν is Poisson's ratio and k_c is compressive buckling coefficient. E is the elastic modulus of the face sheet and d is the gap between attachment points. As both ends of the face member are fixed by attachment points, k_c can be determined to be 4. Note that, since the buckling mode here is different from those in **chapter 3**, so the value of k_c is 4 rather than 2.

The critical gap between attachment points d_{cr} can be determined based on the constraint that the buckling strength should be over the maximum compressive stress:

$$d \leq t_f \sqrt{\frac{k_c \pi^2}{12(1-\nu^2)|\varepsilon_c^{\max}|}} = d_{cr} \quad (5-3)$$

During the topology optimization process, since the design domain was discretized into randomly distributed solid and void elements, the gap between attachment points is dependent on distributions of elements bonded to the face sheets. More specifically, the gap between attachment points is determined by the maximum length of continuously aligned void elements. As shown in [Figure 5-3\(a\)](#), there are two possible distributions. In distribution 1, the continuously aligned void elements are not located at the end of the row, then the gap between attachment points is the length of the continuously aligned void elements calculated by:

$$d = n_v \times L_e \quad (5-4)$$

where n_v is the maximum number of continuously aligned void elements bonded to face sheets and L_e is the side length of each element as illustrated in [Figure 5-3\(b\)](#). In distribution 2 as indicated in [Figure 5-3\(a\)](#), in which the continuously aligned void elements lie at the end of the row, the gap between attachment points is twice the length of continuously aligned void elements as the unit cell is connected with the adjacent one. In this situation, the gap between attachment points is determined by:

$$d = 2n_v \times L_e \quad (5-5)$$

The gap between attachment points calculated by [Eqs. \(5-4\)](#) or [\(5-5\)](#) was set to be lower than the critical gap determined by [Eq. \(5-3\)](#) to meet the face buckling constraint.

5.2.2.3 Core–face sheet delamination constraint

Core–face sheet delamination is another typical failure mode owing to insufficient effective bonding strength. To suppress delamination, the minimum bonding length limit was set to ensure a certain bonding area between core and face sheets. As shown in Figure 5-3(b), the bonding length L_b can be determined by the number of solid elements bonded to face sheets as given by:

$$L_b = n_s \times L_e \quad (5-6)$$

where n_s is the number of solid elements bonded to face sheets. Here, the minimum bonding length ratio (L_b/L) was set to 0.25 as defined by:

$$L_b/L \geq 0.25 \quad (5-7)$$

where L is the side length of unit cell and L_b is the bonding length.

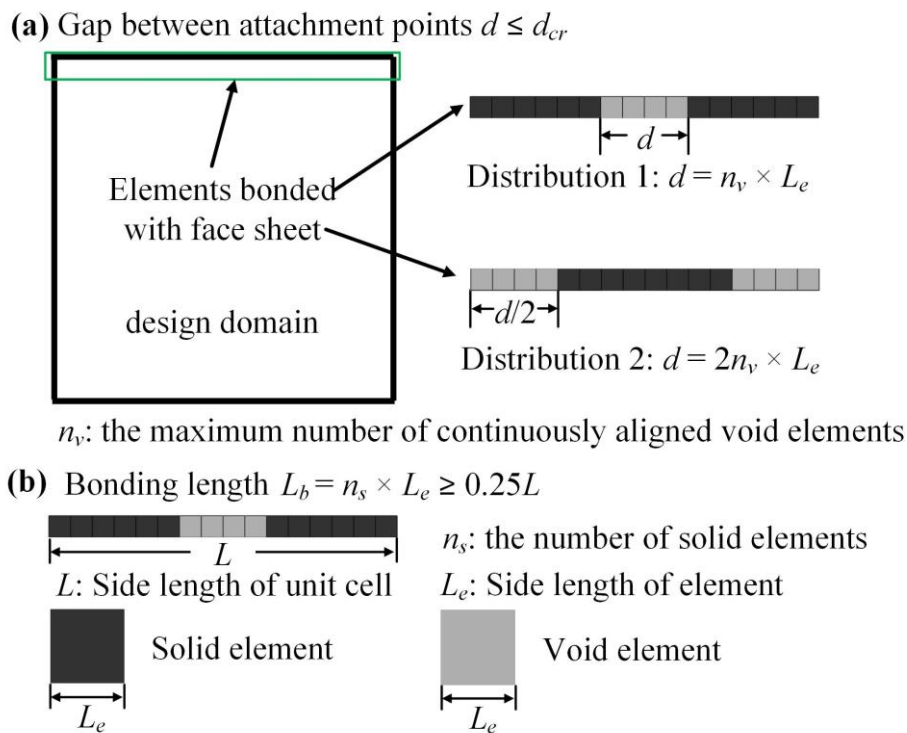


Figure 5-3. Determination of gap between attachment points and bonding length: (a) Calculation of gap between attachment points and (b) Determination of bonding length.

5.2.3 FEM simulation of macroscopic core shear strength and equivalent bending stiffness

The macroscopic core shear strength τ_c can be obtained by the shear analysis as shown in Figure 5-4(a), in which the shear strain was imposed by applying equal displacements to boundary planes of the unit cell. Here, both in-plane and out-of-plane shear modes were included. Through the shear analysis, the shear stress τ_{xy} at a given shear strain ε_{xy} can be calculated by:

$$\tau_{xy} = \frac{F}{LW} \quad (5-8)$$

$$\varepsilon_{xy} = \frac{2u_{sx}}{L} + \frac{2u_{sy}}{L} \quad (5-9)$$

where F is the shear force extracted from simulation results. L and W are the side length of unit cell and the unit width (along z direction), respectively. The applied displacements along x and y directions are denoted as u_{sx} and u_{sy} , respectively. Through the FEM analysis, the macroscopic core shear strength defined as the shear stress level at the intersection of the linear extrapolations of the elastic and elasto-plastic parts of the stress–strain curve as shown in Figure 5-4(a) can be determined.

As shown in Figure 5-4(b), the equivalent bending stiffness of the unit cell was determined by the pure bending analysis, in which the periodic boundary conditions deduced in the Appendix A was employed by adopting the MPC user subroutine incorporated in ABAQUS/CAE 6.14-2. Two equal bending angles $\varphi/2$ and $-\varphi/2$ were applied to two boundary planes of the unit cell and the equivalent bending stiffness can be deduced by:

$$(EI)_{eq} = \frac{M}{\kappa} \quad (5-10)$$

$$\kappa = \frac{\varphi}{L} \quad (5-11)$$

where M is the bending moment and the κ is the bending curvature within the elastic range.

A shear strain of 20% was imposed by applying a displacement of 0.3 mm to each edge of the unit cell for the shear analysis and a bending curvature of 0.001 rad/mm was applied by imposing a bending angle of 0.003 rad to each boundary plane for pure bending analysis. As

shown in Figure 5-4(c), the elastic modulus and yield strength of the solid element were set to 1.4 GPa and 36 MPa ($E_s=1.4$ GPa and $\sigma_s=36$ MPa), respectively, while those of the void element were set close to 0 ($E_v=10^{-9}$ GPa and $\sigma_v=10^{-9}$ MPa).

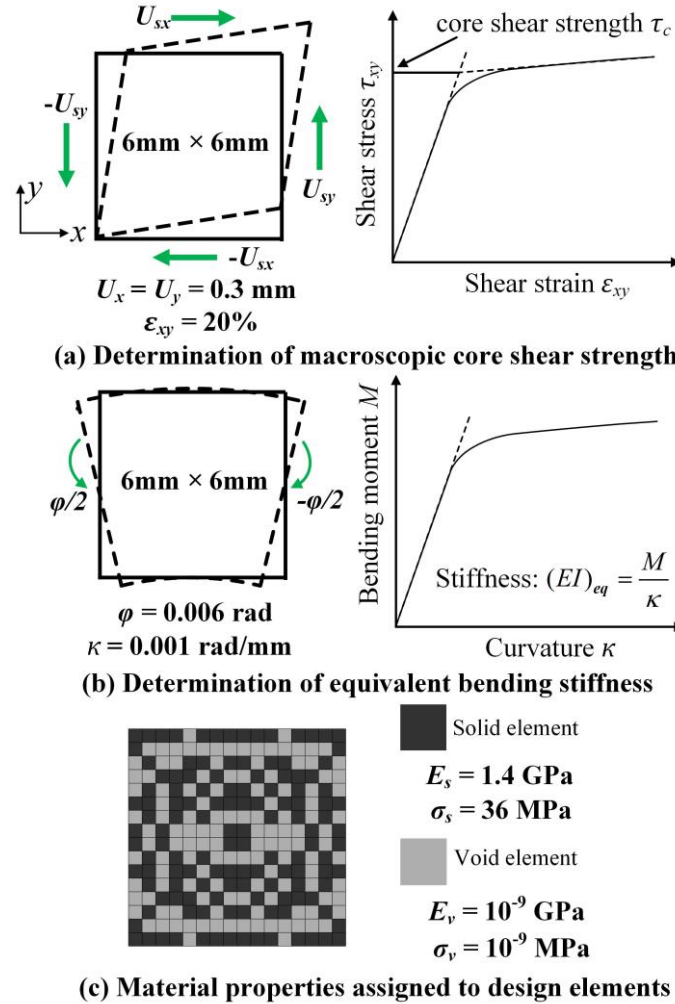


Figure 5-4. Setup of FEM models: (a) Determination of macroscopic core shear strength and (b) Determination of equivalent bending stiffness and (c) Material properties assigned to design elements.

5.2.4 Formulation of topology optimization problem

5.2.4.1 Topology optimization schemes

Two topology optimization schemes were adopted to optimize the core structure for formable sandwich sheets, in which the optimization scheme 1 (case 1) optimizes the formability while the optimization scheme 2 (case 2) optimizes the bending stiffness while

simultaneously maintaining good formability. The constraint conditions including volume fraction, face buckling and delamination constraints, given by Eqs. (5-12)-(5-14) were applied in both case 1 and case 2. The objective function in case 1 was defined by Eq. (5-15), in which the value of the objective function was set to be inversely proportional to the core shear strength. In this way, to minimize the value of the objective function is actually to maximize the core shear strength so that the formability is optimized. The flowchart of the optimization scheme 1 is shown in Figure 5-5.

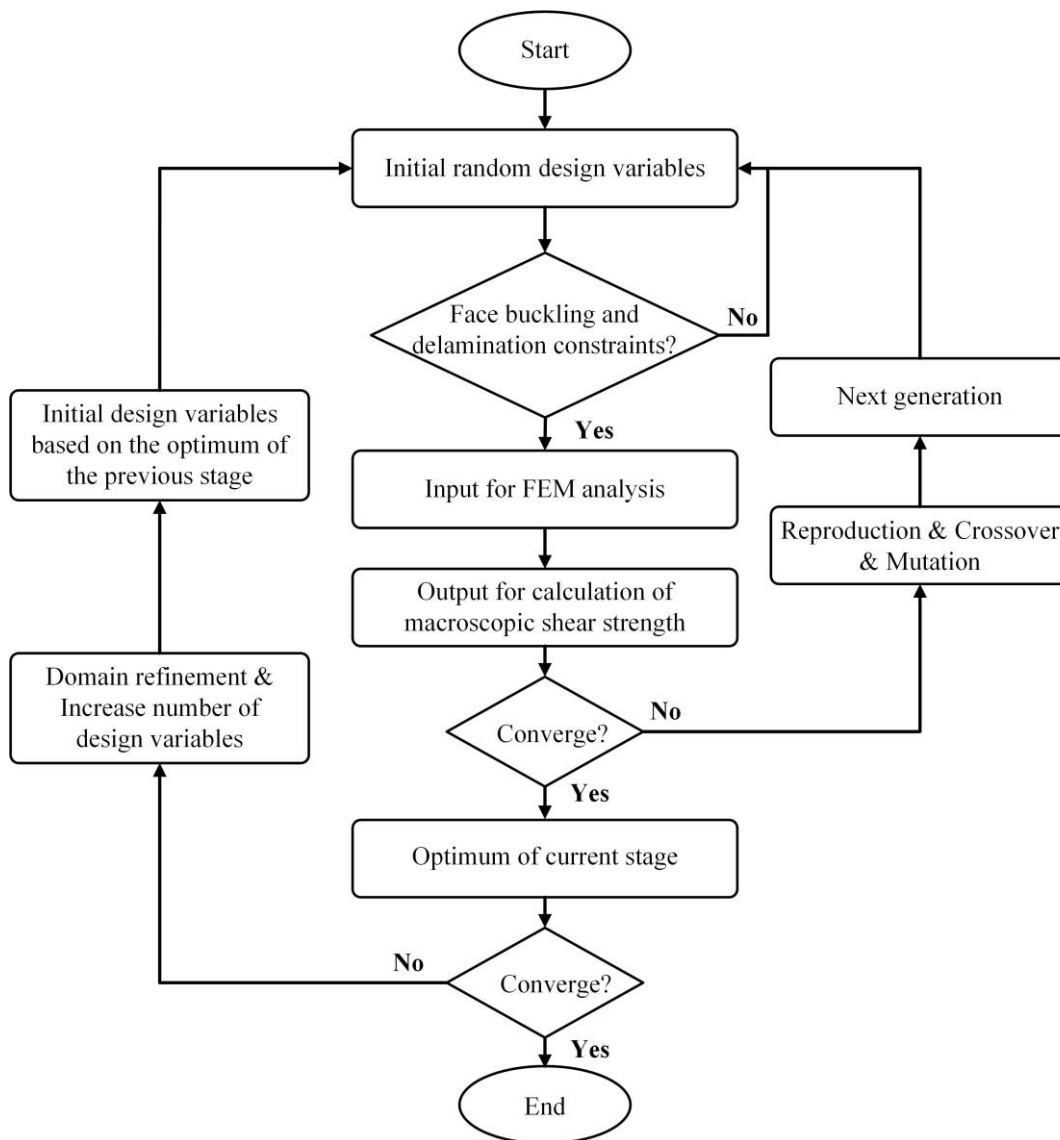


Figure 5-5. Flowchart of the optimization scheme 1 (case 1).

In case 2, the objective was to optimize the bending stiffness while keeping the formability constraint. As massive repetitive judgments will be made on topologies that do not meet the

core shear failure constraint in the optimization loop if the core shear failure constraint is directly applied, the core shear failure constraint was converted to objective function with the optimization priority to avoid such massive repetitive judgments for the improvement of computational efficiency. Therefore, two objective functions were adopted, in which one was used to optimize formability and the other one was to optimize the bending stiffness and an optimization priority was set between these two objective functions. The optimization priority was set by keeping the value of one objective function higher than that of the other objective function so that the objective function with a higher value will be optimized first. The value of the objective function optimizing the formability (Eq. (5-16)) was always greater than 1 while the value of the objective function optimizing the bending stiffness (Eq. (5-17)) was less than 1, so that the formability will be optimized first until the switch was triggered (when $\tau_c \geq \tau_{re}$) after which the bending stiffness will be optimized. Note that in Eq. (5-17), the $(EI)_s$ is the equivalent bending stiffness of the full-solid core structure with the same weight. The flowchart of the optimization scheme 2 is shown in Figure 5-6.

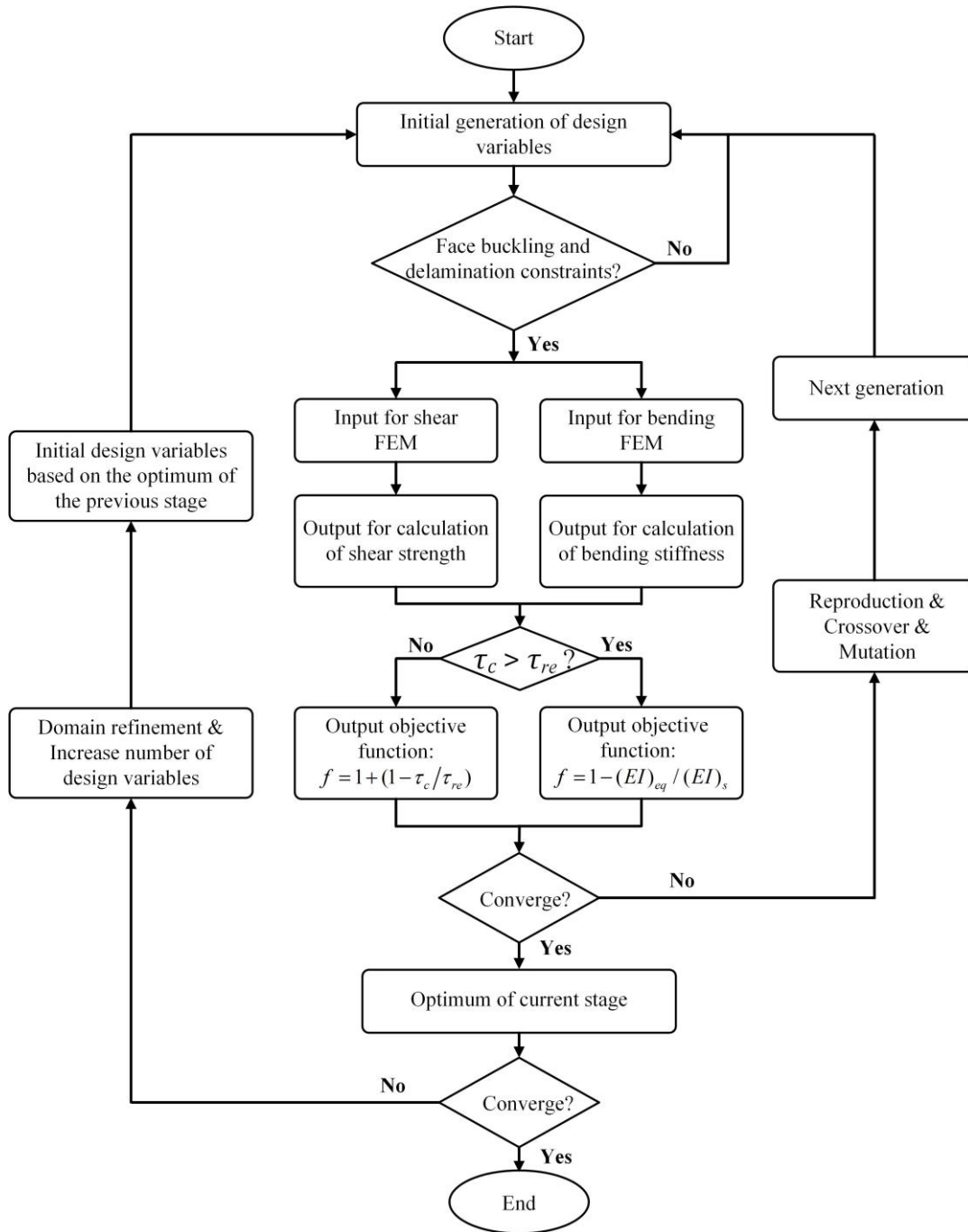


Figure 5-6. Flowchart of the optimization scheme 2 (case 2).

The constraint and objective functions in two topology optimization schemes are as follows:

Constraint functions in optimization schemes 1 and 2 (case 1 and 2):

$$\text{Volume fraction constraint: } \rho = N_s / N \quad (5-12)$$

$$\text{Face buckling constraint: } d \leq d_{cr} \quad (5-13)$$

$$\text{Delamination constraint: } L_b/L \geq 0.25 \quad (5-14)$$

where N_s and N are the number of solid elements and all elements in the design domain, respectively. The relative density, that is, the volume fraction of the unit cell is denoted as ρ .

Objective function in optimization scheme 1 (case 1):

$$f = 1 - \tau_c / \tau_{re} \quad (5-15)$$

Objective functions in optimization scheme 2 (case 2):

$$f = 1 + (1 - \tau_c / \tau_{re}) \text{ when } \tau_c < \tau_{re} \quad (5-16)$$

$$f = 1 - (EI)_{eq} / (EI)_s \text{ when } \tau_c \geq \tau_{re} \quad (5-17)$$

In conventional density-based topology optimization methods, in which the relative density of the design element is continuously changed from 0 to 1, the sensitivity of the objective function can be theoretically solved and thus gradient based approach such as the conventional optimality criteria is generally adopted to solve the optimization problem. However, the drawback of gradient based approaches or optimality criteria methods is that often intermediate densities are obtained, which are not physically meaningful and cannot be practically produced. In the present study, the relative density of the design element is either 0 or 1, which enables better manufacturability of the optimal design. But as the sensitivity of the objective function cannot be theoretically solved, the gradient based approach cannot solve the optimization problem. As an alternative, the GA with variable chromosome lengths proposed by [Kim and De Weck \(2005\)](#) was employed, in which the design domain was progressively refined by a multi-stage search strategy to reduce the number of design variables and increase the possibility of generating physically meaningful designs. [Figure 5-7](#) illustrates the design map of the density-based topology optimization integrated with the multi-stage GA. Considering the symmetric boundary conditions of shear and bending analyses, the design zone will naturally have two symmetry planes as indicated by the two dashed lines in [Figure 5-7](#). To reduce the size of the search space for exploration of problems with many design variables and also increase the likelihood of approaching the global optimum, it is better to optimize only one quarter of the design zone. The design domain was discretized into coarse 16×16 cells in the 1st stage and the optimum was then transferred to the 2nd stage to generate the initial input, in which the design domain was refined to 32×32 cells and the number of design variables

was increased. The optimal solution of the 2nd stage was used to generate the initial input in the 3rd stage, in which the design domain was further refined into 64×64 cells and the number of design variables was further increased. This multi-stage search strategy, in which the rough optimum in the early stage searched by a low computational cost was used as a starting point in the following stage, can significantly improve the computational efficiency compared with the brute-force GA as the exploration of the entire design space with massive design variables can be avoided. The population sizes set for three optimization stages were 200, 300 and 500, respectively. More detailed setups such as mutation rate and crossover possibility of the multi-stage GA can be referred to the approach presented by [Kim and De Weck \(2005\)](#).

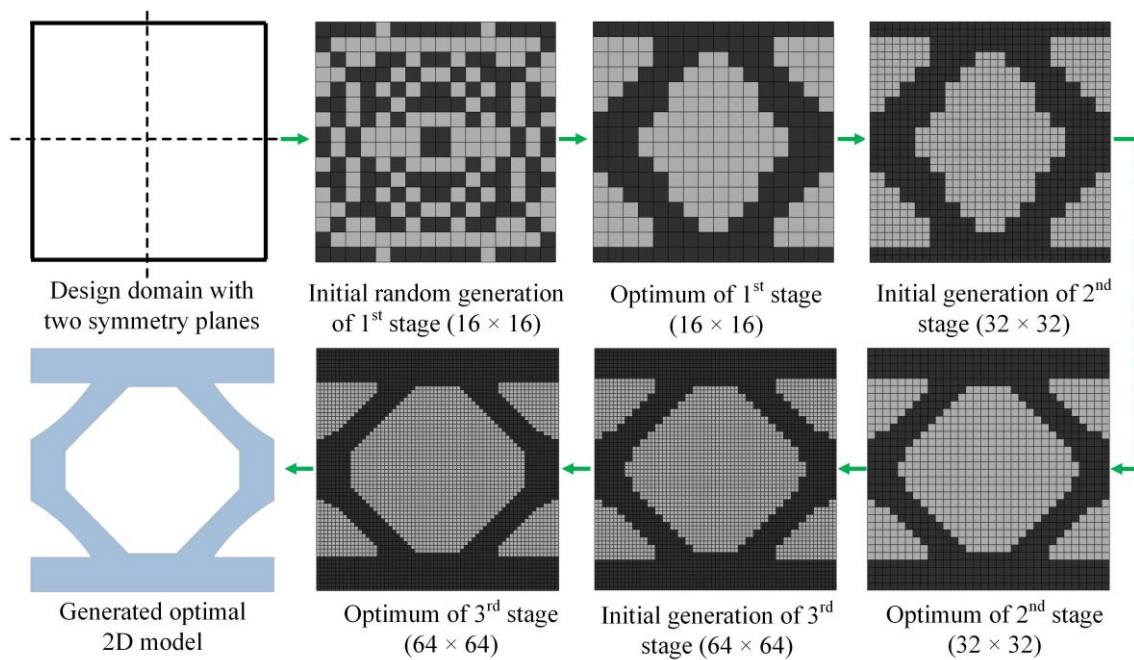


Figure 5-7. Design map of the density-based topology optimization integrated with multi-stage GA.

5.3 Materials and experiments

5.3.1 Materials and fabrication of prototypes

The face sheet was stainless steel (SUS304) sheet of thickness 0.5 mm. The core material was carbon fibre reinforced nylon (Onyx), which can be used for fusion deposition modelling type 3D printer *MarkTwo* (Markforged, USA) to produce the prototypes with complex geometries. The material properties of SUS304 and Onyx are listed in [Table 5-1](#).

[Table 5-1](#). Mechanical properties of SUS304 and Onyx.

Property	Onyx	SUS304
Density (g/cm ³)	1.2	7.85
Young's modulus (GPa)	1.4	200
Poisson's ratio	0.3	0.29
Yield strength (MPa)	36	215
Linear hardening modulus (GPa)	None	2.3

The optimized core structures were fabricated using *MarkTwo* (Markforged, USA) printer with the process parameters listed in [Table 5-2](#). The nozzle temperature and layer thickness were 275 °C and 0.1 mm, respectively. The printed core structures were then bonded to SUS304 face sheets using an adhesive IW2460 (3M, USA) in an autoclave (Hanyuda, Japan). The bonding temperature was 120 °C, the holding time was 75 minutes and the applied pressure was 0.3 MPa. The adhesive IW2460 was selected owing to its high bonding strength, high heat resistance and high moisture resistance, which enables the use of produced sandwich sheets in various environments. The tensile shear strengths of aluminium alloy joints (A2024–A2024) and steel joints (SPCC–SPCC) bonded by IW2460 at room temperature have been provided by the manufacturer, which are 30 and 19 MPa, respectively.

[Table 5-2](#). Process parameters for additive manufacturing.

Description	Value
Material	Carbon fibre reinforced nylon (Onyx)
Nozzle temperature (°C)	275
Bed temperature (°C)	Room temperature
Fill pattern	Solid
Fill density (%)	100
Wall layers	2
Layer thickness (mm)	0.1

5.3.2 Experimental tests of mechanical properties and formability

Mechanical properties including bending stiffness and energy absorption capabilities were checked by the three-point bending test using a 50-kN hydraulic servo press (Fujidempa, Japan). The load rate was set to 3 mm/min and span length was 50 mm. The radii of supports and load rollers were 5 mm. FEM simulation was also carried out to model the bending stiffness, in which an ideal bonding condition between core and face sheets was modelled by a tie contact and elastoplastic properties were assumed for both face sheet and core materials to save simulation time. The simulation was conducted using the dynamic explicit solver incorporated in ABAQUS/6.14-2 and the friction coefficient between dies and specimen was set to 0.15.

L-bending and draw-bending tests were employed to examine the formability using a mechanical servo press (H1F110, Komatsu, Japan). As shown in Figure 5-8, for the L-bending test, the radii of upper punch and lower die were 40 and 60 mm, while those of used for the draw-bending test were 20 and 30 mm, respectively. For both L-bending and draw-bending tests, the clearance between punch and die was 15 mm and a clearance of 9 mm between the blank holder and the lower die was set to fix the specimen during forming. The forming rate was set to 1 mm/s for both L-bending and draw-bending tests.

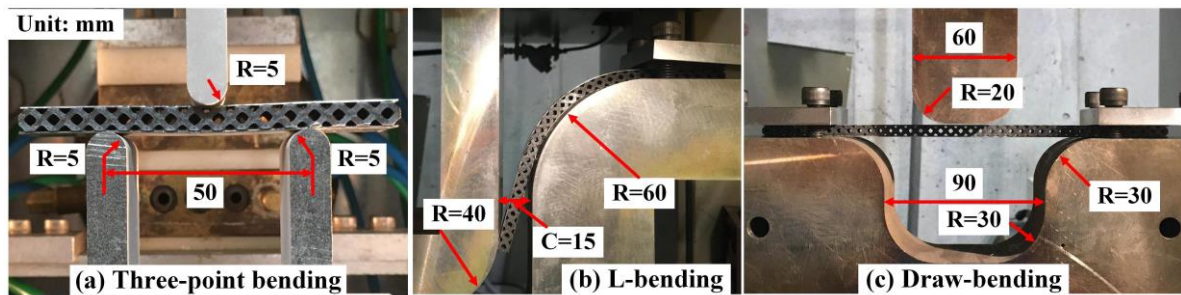


Figure 5-8. Experimental setups for three-point bending, L-bending and draw-bending tests.

5.4 Results and discussion

5.4.1 Topology optimization results

5.4.1.1 Evolution of objective functions

The relative densities (ρ), that is, the volume fractions of the core structures were constrained to be 50% and 62.5% during the topology optimization process. In case 1, the objective function value and core shear strength with the update of the iteration step are shown in [Figure 5-9](#), in which three optimization stages are included. The required core shear strength of SUS304/Onyx/SUS304 sandwich sheets can be calculated to be 4.8468 MPa, note that the actual bending radius is 68 mm as the clearance (15 mm) between punch and die is 8 mm larger than the thickness (7 mm) of sandwich sheets. The core shear strengths of the final optimal topologies under the volume fraction constraints of 50% and 62.5% are 7.4878 and 9.3693 MPa, respectively, which are higher than the required core shear strength of 4.8468 MPa, indicating that the core shear failure can be expected to be successfully suppressed at given bending conditions.

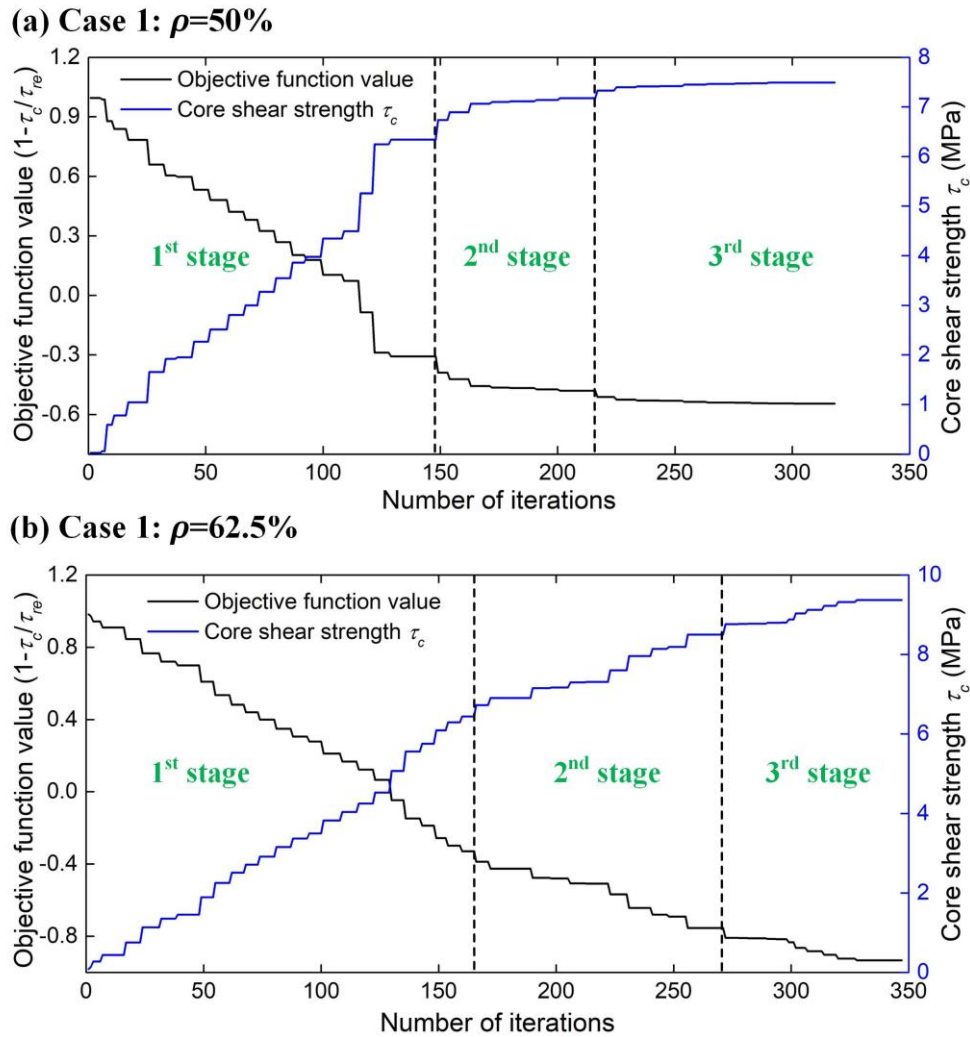
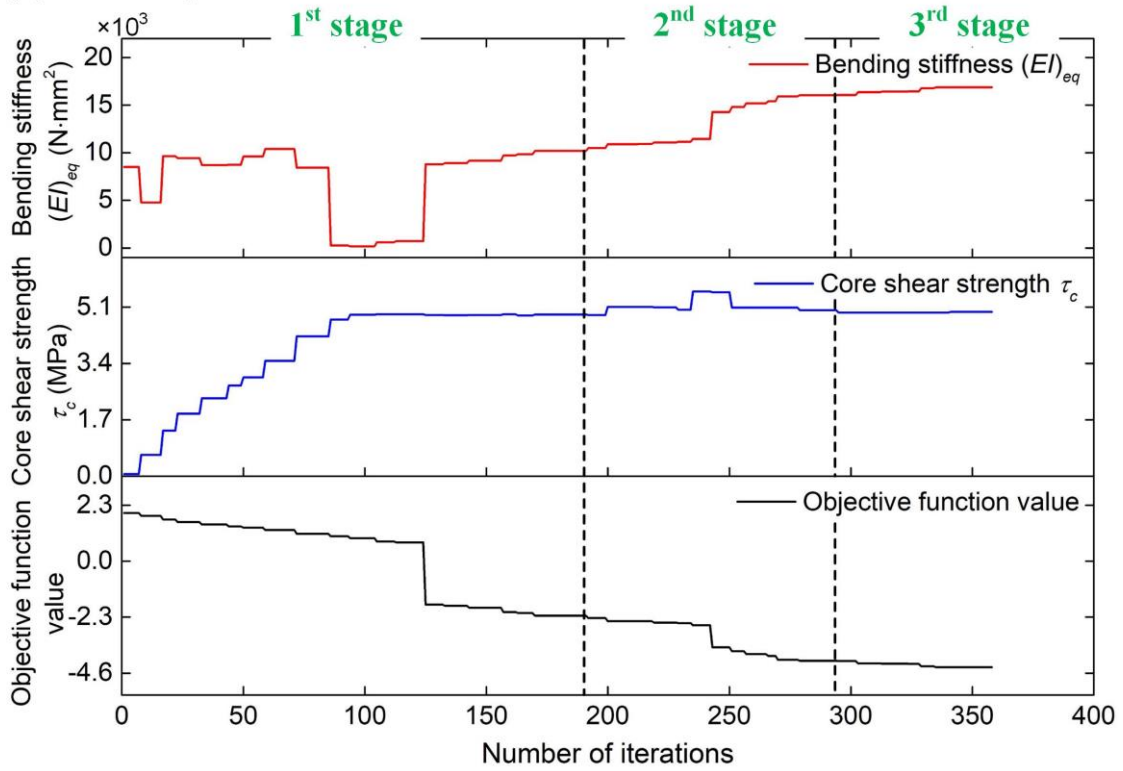


Figure 5-9. The objective function value and core shear strength with the update of the iteration step in case 1: (a) Volume fraction constraint of 50% and (b) Volume fraction constraint of 62.5%.

In case 2, the evolution of objective function value, core shear strength and bending stiffness under volume fraction constraints of 50% and 62.5% are shown in [Figure 5-10](#), from which it can be seen that the core shear strength is firstly optimized in the early stages until the formability constraint is satisfied and then the bending stiffness is optimized in later stages until the final optimal topology is found. The core shear strengths of the final optimal topologies at relative densities of 50% and 62.5% are respectively 4.9559 and 4.9074 MPa, which are above the required core shear strength of 4.8468 MPa, demonstrating that the formability constraint is satisfied. The equivalent bending stiffness of the optimal topologies

obtained in case 1 and case 2 under the volume fraction constraint of 50% are 1910 and 16885 $\text{N} \cdot \text{mm}^2$, respectively. The bending stiffness of the topologically optimized core structure in case 2 is 8.84 times of that of the optimized core structure in case 1. At relative density of 62.5%, the bending stiffness of optimized core structures in case 1 and case 2 are 4278 and 21848 $\text{N} \cdot \text{mm}^2$, respectively. The bending stiffness of the optimal core structure in case 2 is 5.11 times of that of the optimized core structure in case 1. The above results indicate that the optimal core topologies obtained in case 2 can be expected to be well bent without failure and simultaneously display superior bending stiffness than those optimized in case 1.

(a) Case 2: $\rho=50\%$



(b) Case 2: $\rho=62.5\%$

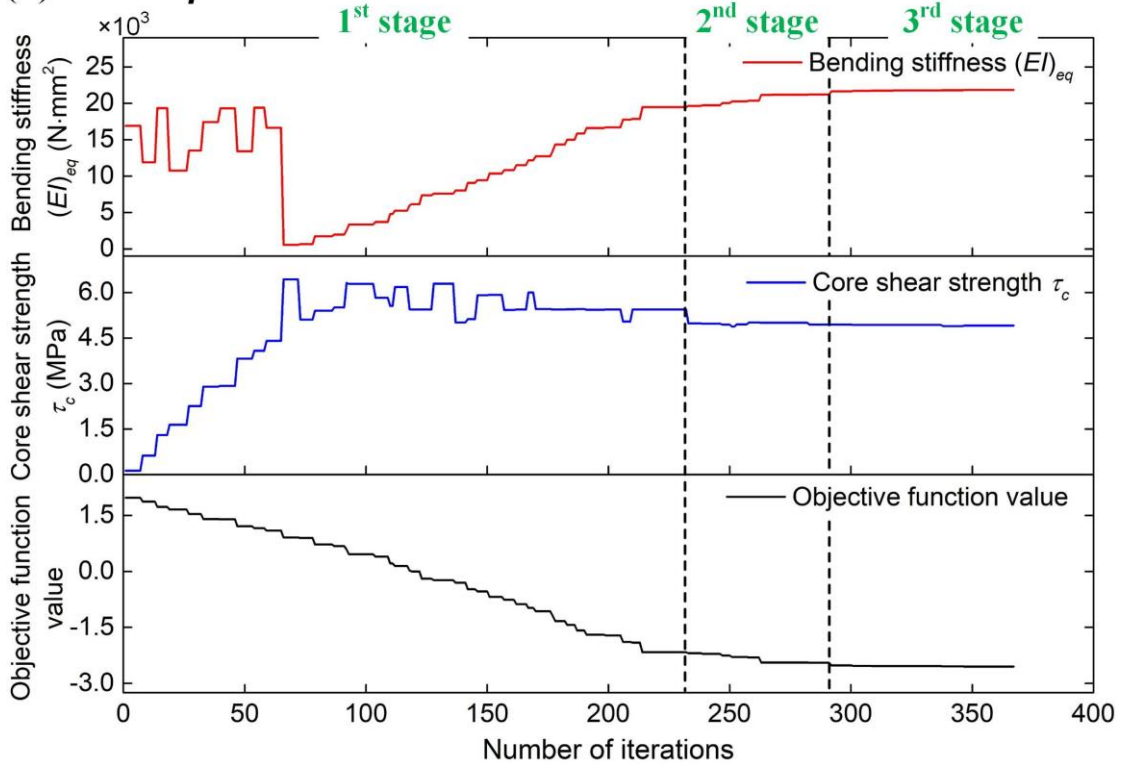


Figure 5-10. The objective function value, core shear strength and bending stiffness with the update of the iteration step in case 2: (a) Volume fraction constraint of 50% and (b) Volume

fraction constraint of 62.5%.

5.4.1.2 Evolution of core topology

The detailed evolution processes of core topologies at relative densities of 50% and 62.5% in case 1 are shown in [Figure 5-11](#) and [5-12](#), in which dark and light colours represent the solid and void elements, respectively. It can be seen that the design domain was discretized into coarse 16×16 cells in the 1st optimization stage and the core shear strength increased with the evolution of topology until the optimal topology was found. Then, the optimal topology obtained in the 1st stage was transferred to the 2nd optimization stage to generate the starting point, in which 32×32 design cells were included. Similarly, the optimal topology of the 2nd stage was used as the initial input in the 3rd stage and the design domain was further refined to 64×64 cells. Eventually, the optimum in the 3rd stage was determined to be the final optimal topology. Although more optimization stages may generate better topologies with a higher resolution, much higher computational cost is needed. Therefore, three optimization stages were adopted in this study for the consideration of computational efficiency. The change of core topologies under different volume fraction constraints in case 2 are shown in [Figure 5-13-5-14](#). It can be clearly seen that the core shear strength increased in the initial optimization stages until it was higher than the required core shear strength after which the bending stiffness increased in later optimization stages until the final optimal topology was found.

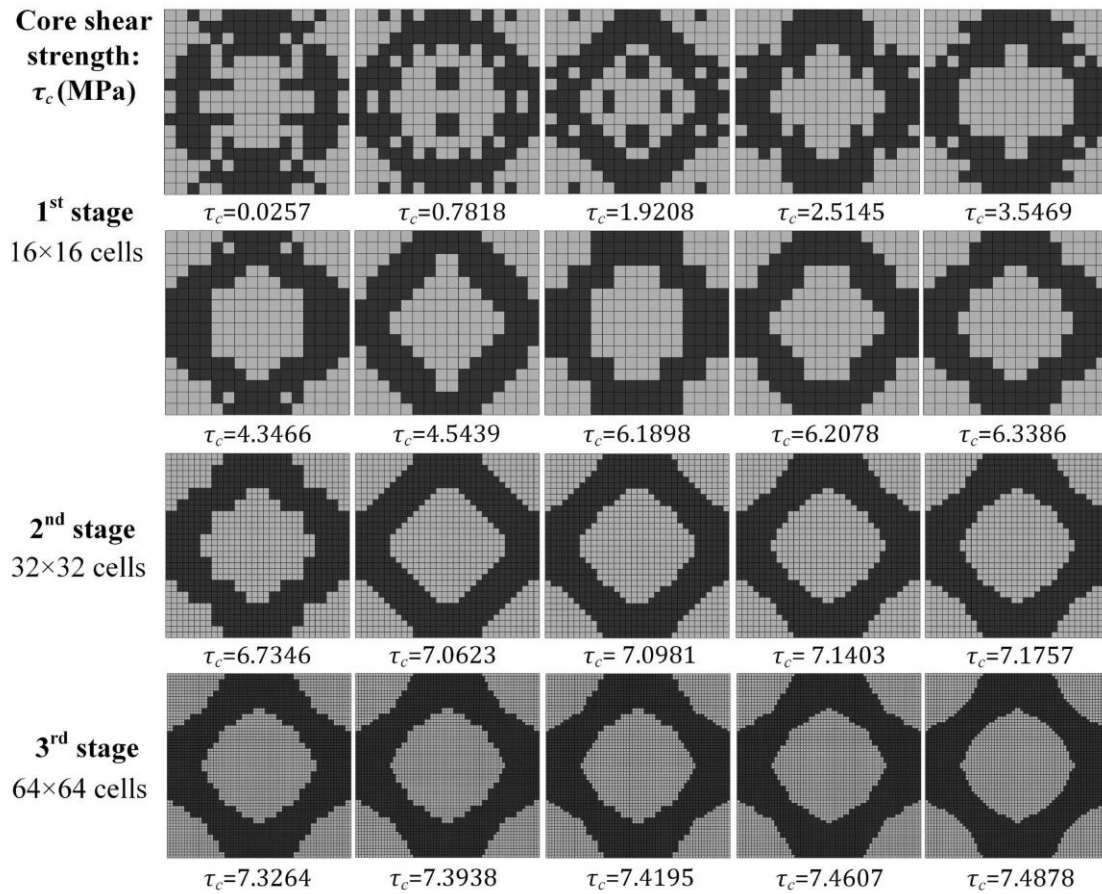


Figure 5-11. Evolution processes of core topologies under volume fraction constraint of 50% in case 1.

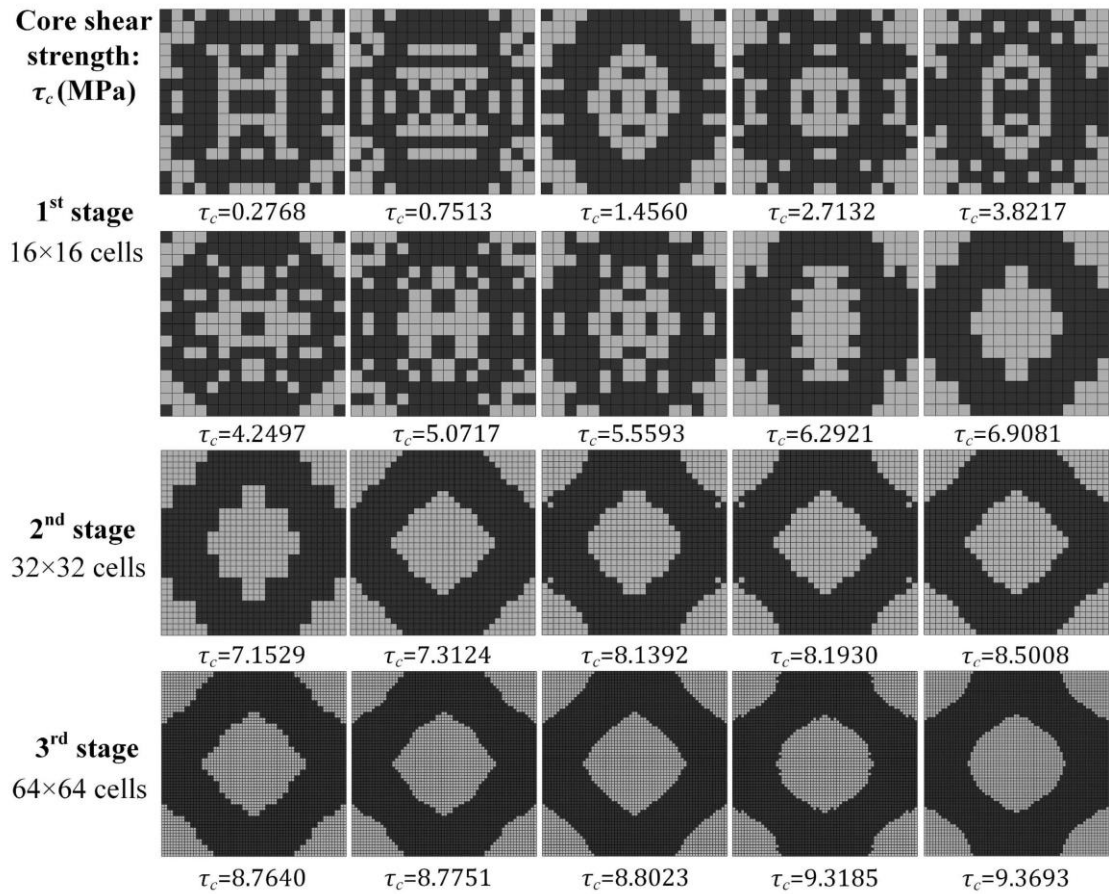


Figure 5-12. Evolution processes of core topologies under volume fraction constraint of 62.5% in case 1.

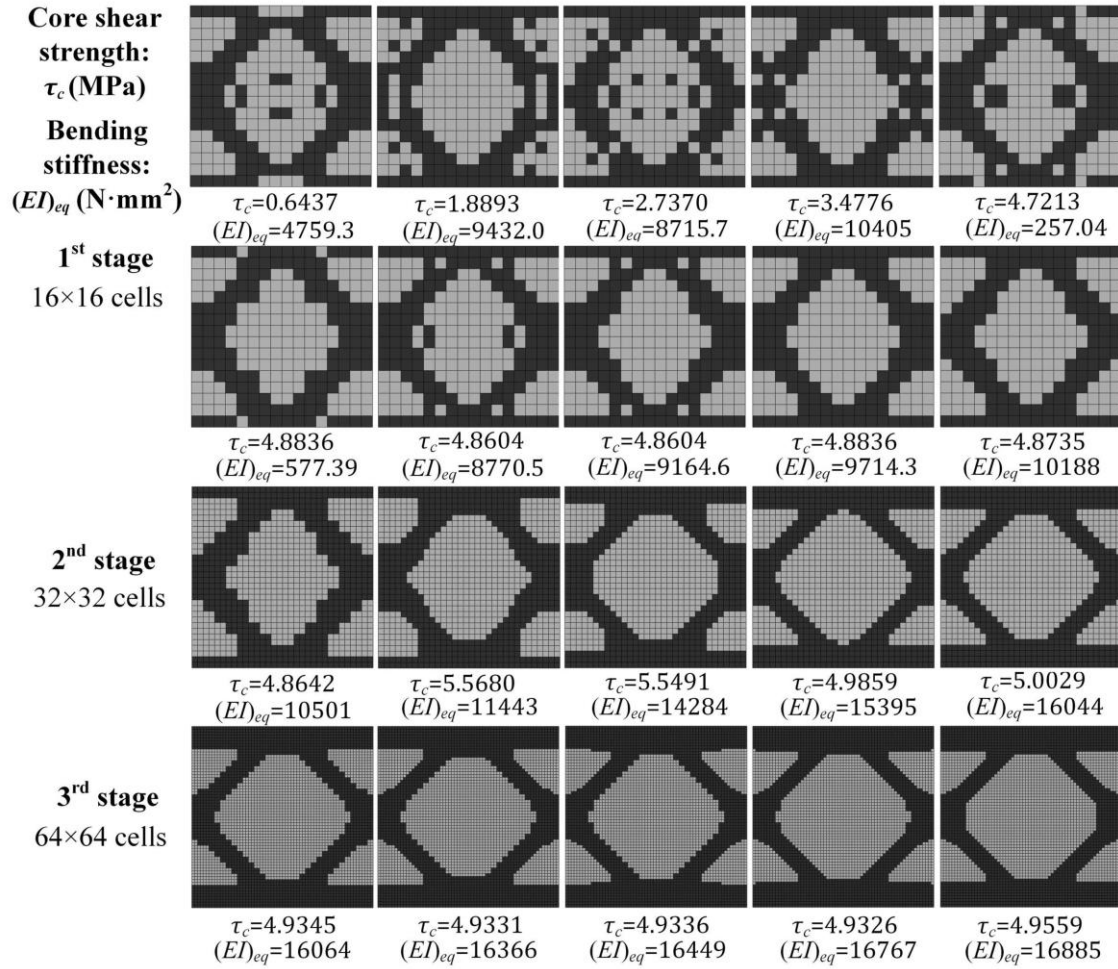


Figure 5-13. Evolution processes of core topologies under volume fraction constraint of 50% in case 2.

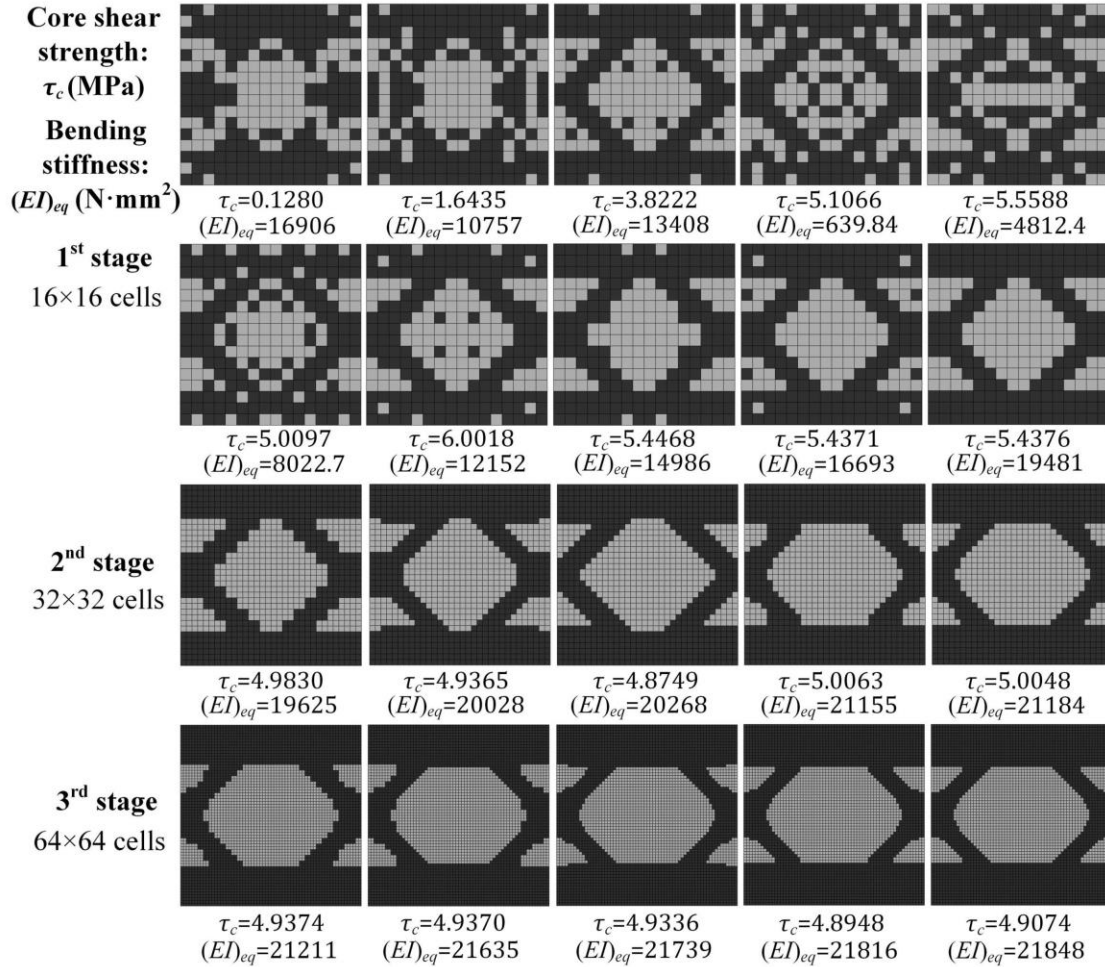


Figure 5-14. Evolution processes of core topologies under volume fraction constraint of 62.5% in case 2.

The optimal topologies obtained in two cases under volume fraction constraints of 50% and 62.5% are shown in Figure 5-15. The core shear strength, gap between attachment points and bonding length ratio of optimal topologies were listed in Table 5-3, in which they were compared with the prescribed values to verify the failure constraints. The core shear strengths of optimal topologies are all above the required value of 4.8468 MPa. The gaps between attachment points of optimal topologies are all lower than the critical gap calculated to be 4.79 mm. The bonding length ratios (L_b/L) of optimal topologies are all higher than the prescribed minimum value of 0.25. The above results indicate that the failure constraints including core shear failure, face buckling and delamination constraints are well satisfied.

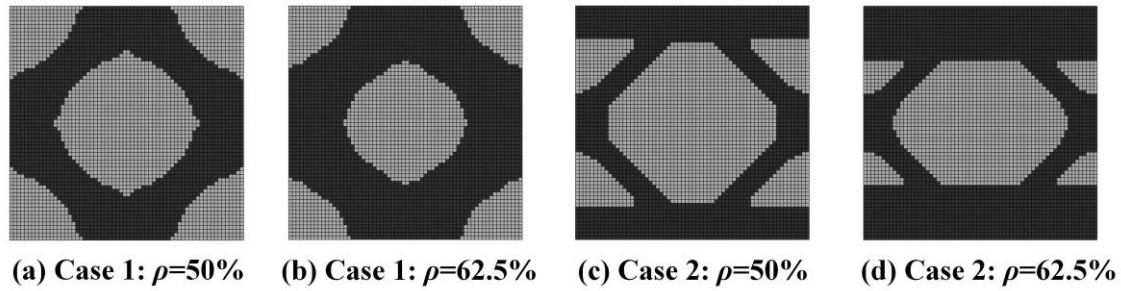


Figure 5-15. The optimal topologies obtained by proposed topology optimization schemes.

Table 5-3. Core shear strength, gap between attachment points and bonding length ratio of optimal topologies.

Core relative density ρ	Core shear strength τ_c (MPa)		Required core shear strength τ_{re} (MPa)	Gap between attachment points d (mm)		Critical gap between attachment points d_{cr} (mm)	Bonding length ratio L_b/L	
	Case 1	Case 2		Case 1	Case 2		Case 1	Case 2
	50%	7.4878	4.9559	4.8468	3.75	0	4.79	0.3750
62.5%	9.3693	4.9074	4.8468	3.1875	0	4.79	0.4687	1

5.4.1.3 Generation of 3D models for additive manufacturing

As shown in Figure 5-16, the optimal topologies were firstly converted to 2D models by smoothing the edges after which the 2D models were extruded to the 3D models for additive manufacturing. The accuracy of the converted 2D models was firstly checked. The total areas of the solid elements were kept unchanged while smoothing the edges of the TO models and thus the areas of the 2D and TO models are equivalent. To keep conditions consistent in the FEM analysis, the mesh type and size of the 2D and TO models were kept the same. The stress distributions at a shear strain of 5% for the topologically optimized models (TO models) and 2D models obtained in case 1 are shown in Figure 5-17, in which the stress distributions of the TO models are very similar to those of the 2D models. Figure 5-18 shows the stress distributions at a bending curvature of 0.001 rad/mm and a shear strain of 5% for TO and 2D models obtained in case 2, in which similar stress distributions can also be found. It is clearly indicated in Figure 5-17 and Figure 5-18 that the void elements in the TO models show stresses of 0 and thus their contribution to the shear strength and bending stiffness can be neglected. The stress distributions of the solid elements in TO models are well consistent with the stress

contours in the 2D models, which explains why the 2D and TO models show similar shear strengths and bending stiffness. The core shear strength and bending stiffness of TO and 2D models are compared in Table 5-4, in which TO and 2D models have very close core shear strength and bending stiffness and the errors are within 2%. The sufficient accuracy of the 2D models is verified by the above comparisons.

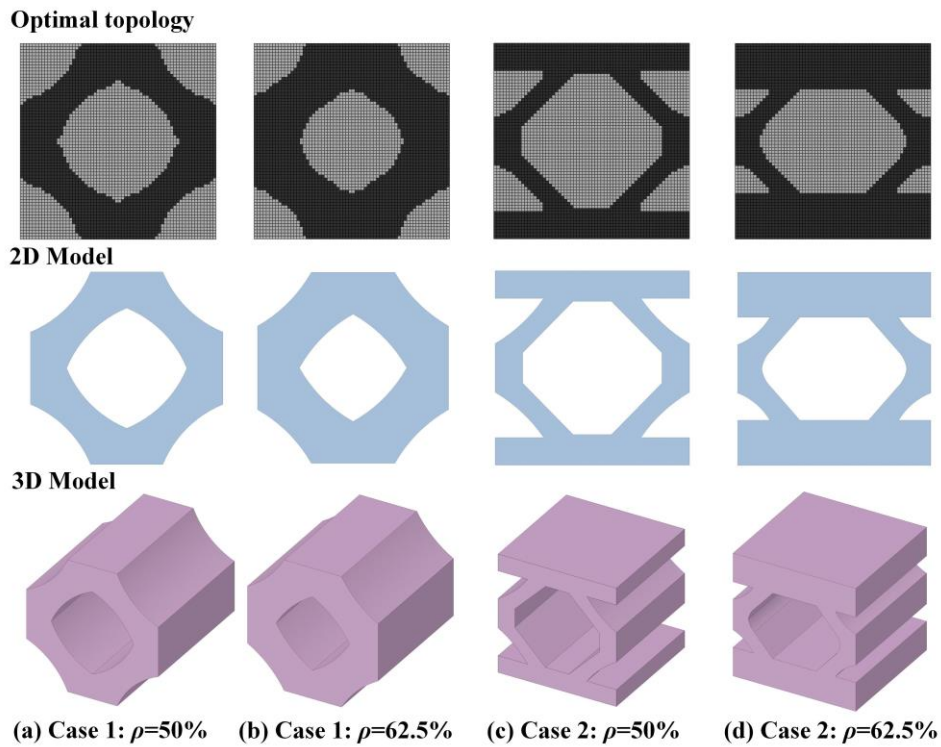


Figure 5-16. 2D and 3D models converted from optimal topologies for additive manufacturing.

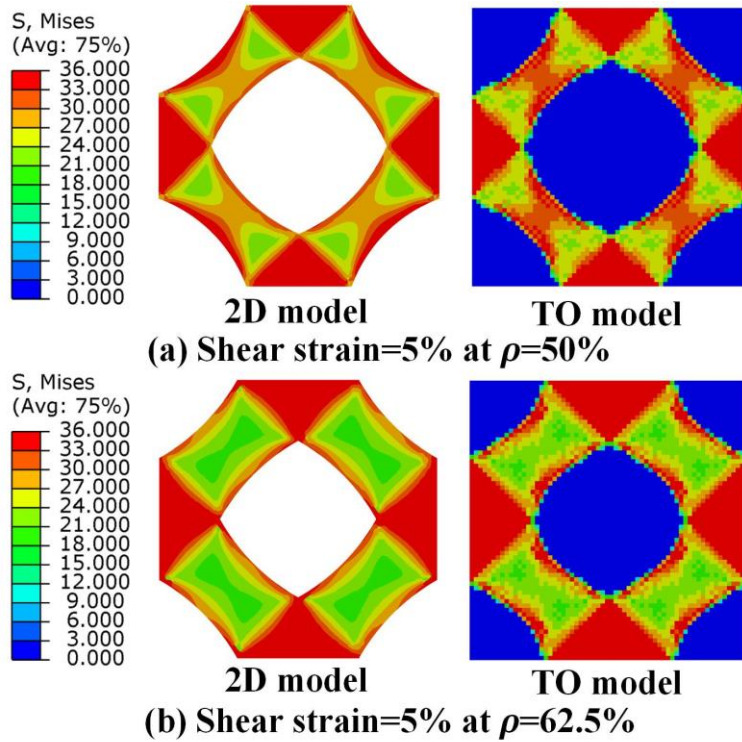


Figure 5-17. Stress distributions of the optimal topologies (TO models) and converted 2D models in case 1: (a) Relative density of 50% and (b) Relative density of 62.5%.

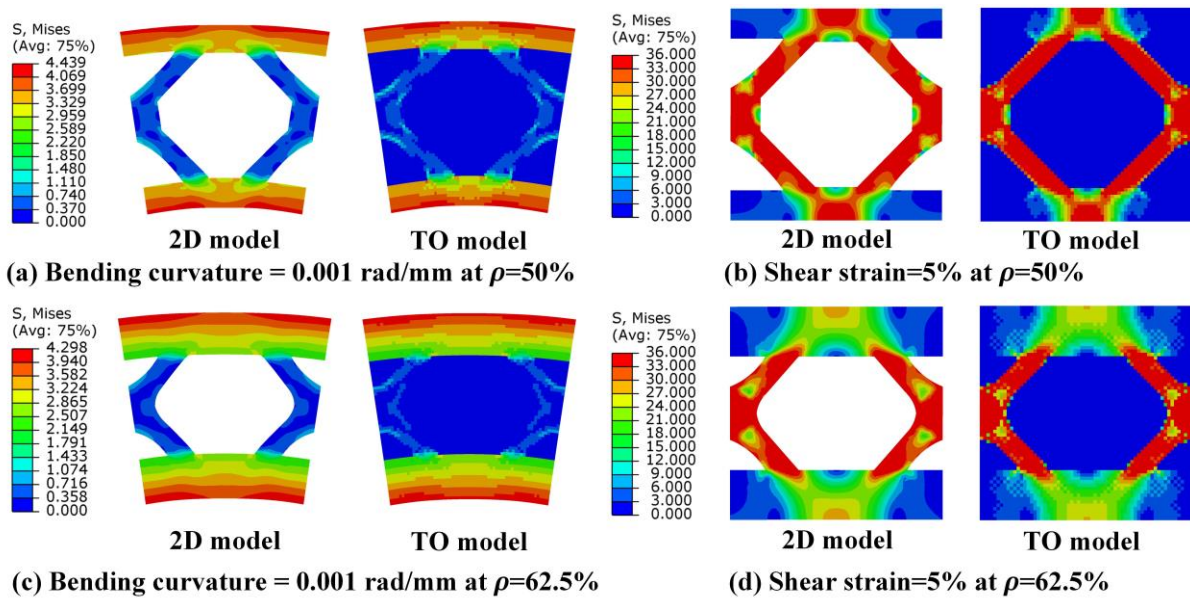


Figure 5-18. Stress distributions at a bending curvature of 0.001 rad/mm and a shear strain of 5% for TO and 2D models in case 2: (a) Pure bending at relative density of 50%; (b) Shear at relative density of 50%; (c) Pure bending at relative density of 62.5% and (d) Shear at relative density of 62.5%.

Table 5-4. Comparison of TO and 2D models in terms of core shear strength and bending stiffness.

Properties	Case 1: $\rho=50\%$		Case 1: $\rho=62.5\%$		Case 2: $\rho=50\%$		Case 2: $\rho=62.5\%$	
	TO model	2D model	TO model	2D model	TO model	2D model	TO model	2D model
Core shear strength τ_c (MPa)	7.4878	7.4025	9.3693	9.4556	4.9559	4.9012	4.9074	4.9323
Bending stiffness $(EI)_{eq}$ (N·mm ²)	1909.81	2049.71	4277.86	4177.36	16885	17147	21848	21466

5.4.2 Experimental validation

5.4.2.1 Additively manufactured prototypes

Printed CFRP core structures are shown in Figure 5-19, in which Figure 5-19(a) and (b) are optimized core structures in case 1 and 2, respectively. The use of support structures during 3D printing can be avoided by setting the build direction to be the extrusion direction. Consider the build direction illustrated in Figure 5-19 is perpendicular to the principal bending plane as shown in Figure 5-8 and 3D printed onyx is isotropic in the plane perpendicular to the build direction, it is reasonable to treat onyx as an isotropic material in this study. SUS304 face sheets were adhesively bonded to core structures to produce the sandwich sheets as shown in Figure 5-20. To highlight the differences of sandwich topologies, a wide-area 3D measurement system controller (Keyence VR-5000) was employed to observe the topologies as shown in Figure 5-21, where a magnification on a 15" monitor 12× was used.

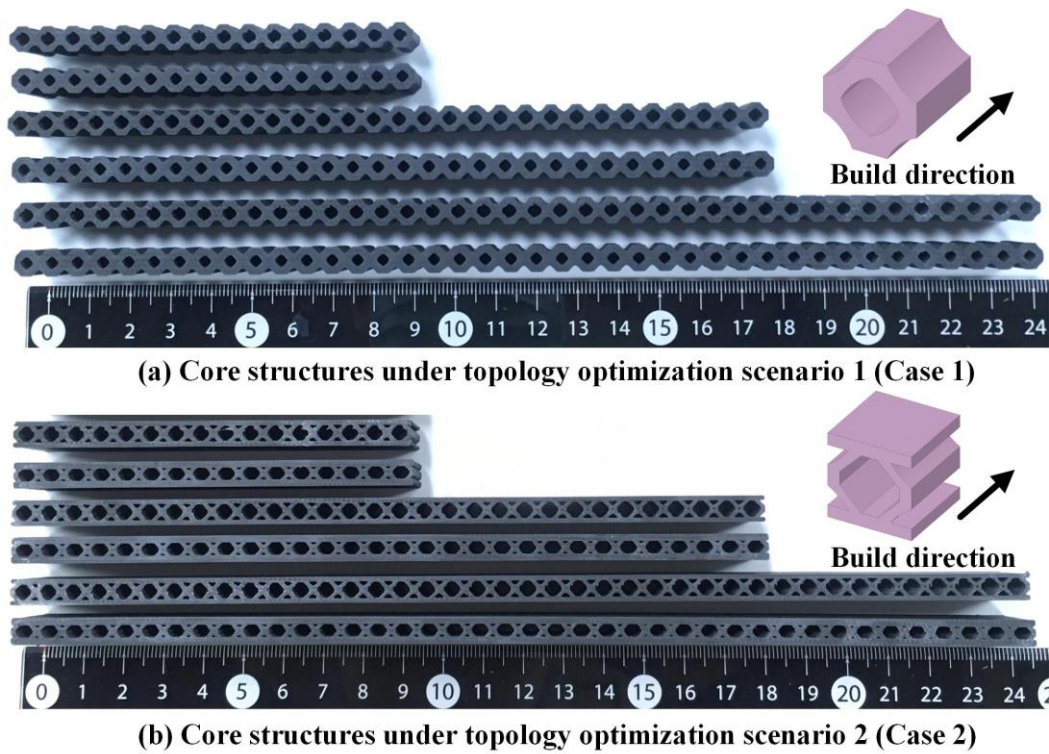
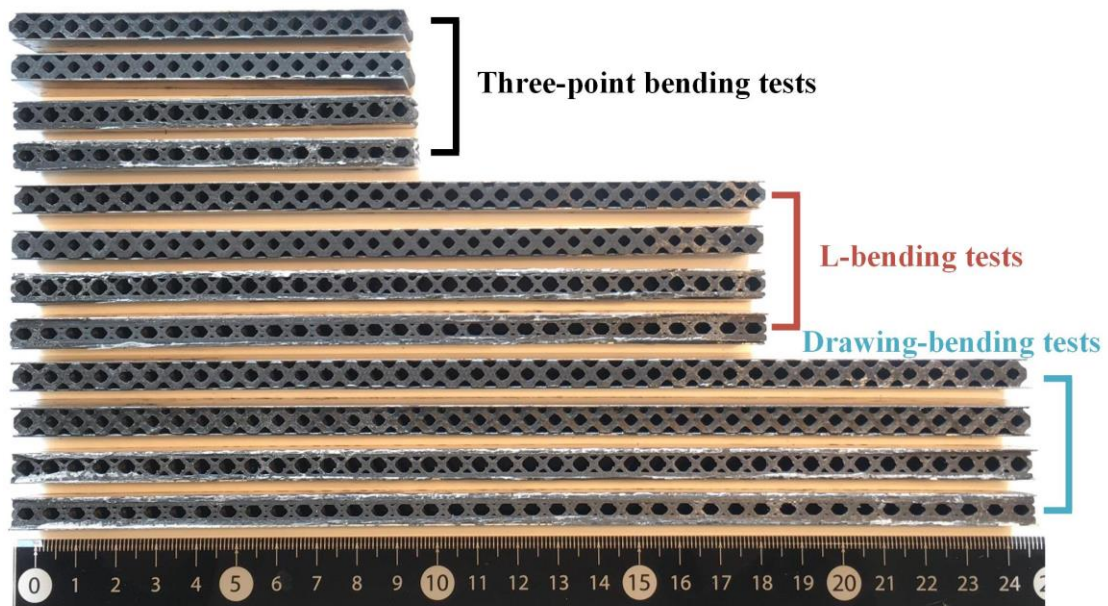


Figure 5-19. Additively manufactured prototypes: (a) Core structures optimized in case 1 and (b) Core structures optimized in case 2.



Fabricated sandwich sheets for stiffness and formability tests

Figure 5-20. Produced sandwich sheets after adhesive bonding.

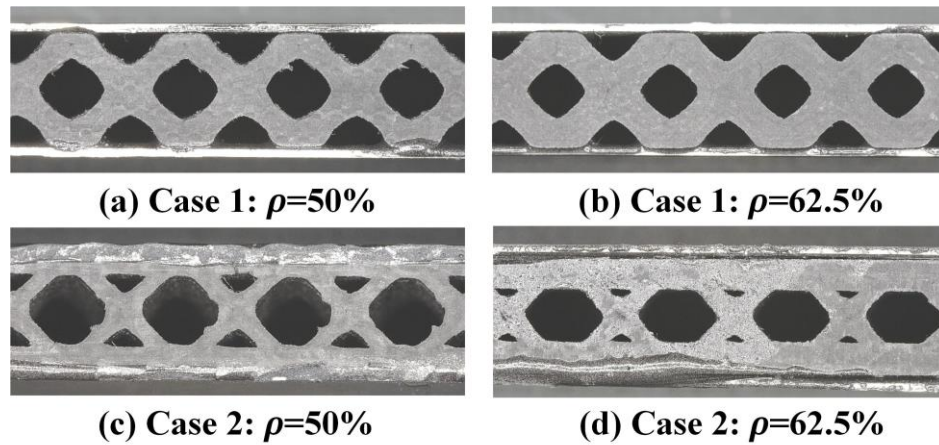


Figure 5-21. Sandwich topologies observed by a wide-area 3D measurement system controller with a magnification on a 15" monitor 12 \times .

5.4.2.2 Three-point bending results

Deformation processes during three-point bending experiments and simulations are shown in Figure 5-22 and Figure 5-23, in which only sandwich sheets with the core density of 50% were presented. It can be seen that the core fracture and delamination are the main failure modes for sandwich topologies in case 1 while the core indentation is the main deformation mode for those in case 2. Since ideal bonding conditions and elastoplastic material properties were assumed in FEM, delamination and core fracture for case 1 cannot be captured in the simulation. Nevertheless, the core indentation for case 2 can be well predicted as shown in Figure 5-23. The bending load–displacement curves are shown in Figure 5-24(a). The abrupt drop of the bending load for case 1 is due to the core fracture or delamination while the core indentation leads to the progressive decrease of the bending load for case 2. Although the simulated load curves show certain discrepancies to the experimental load curves owing to the ideal assumptions on bonding conditions and material properties in FEM, the simulated bending stiffness are quite close to the experimental results. The calculated specific bending stiffness and absorbed energy are shown in Figure 5-24(b) and Table 5-5. It can be found that at the same core density the bending stiffness and energy absorption capability in case 2 are improved compared with those in case 1. When the core relative density is 50%, the bending stiffness and energy absorption capability are improved by 41.58% and 13.60%, respectively, while they are respectively enhanced by 41.49% and 29.40% at core density of 62.5%. These

results indicate improved structural efficiencies including higher bending stiffness and energy absorption capabilities of sandwich topologies optimized in case 2. As the absorbed energy is calculated by integrating the area enclosed by the load–displacement curve, the energy absorption capability is thus mainly determined by the stiffness and formability, namely, higher stiffness and better formability tend to improve the energy absorption capability. Therefore, although the energy absorption capability was not directly optimized in this study, the optimized bending stiffness can be expected to enhance the energy absorption capability as the good formability is simultaneously maintained. This explains why the structures optimized in case 2 display higher energy absorption capability over those in case 1.

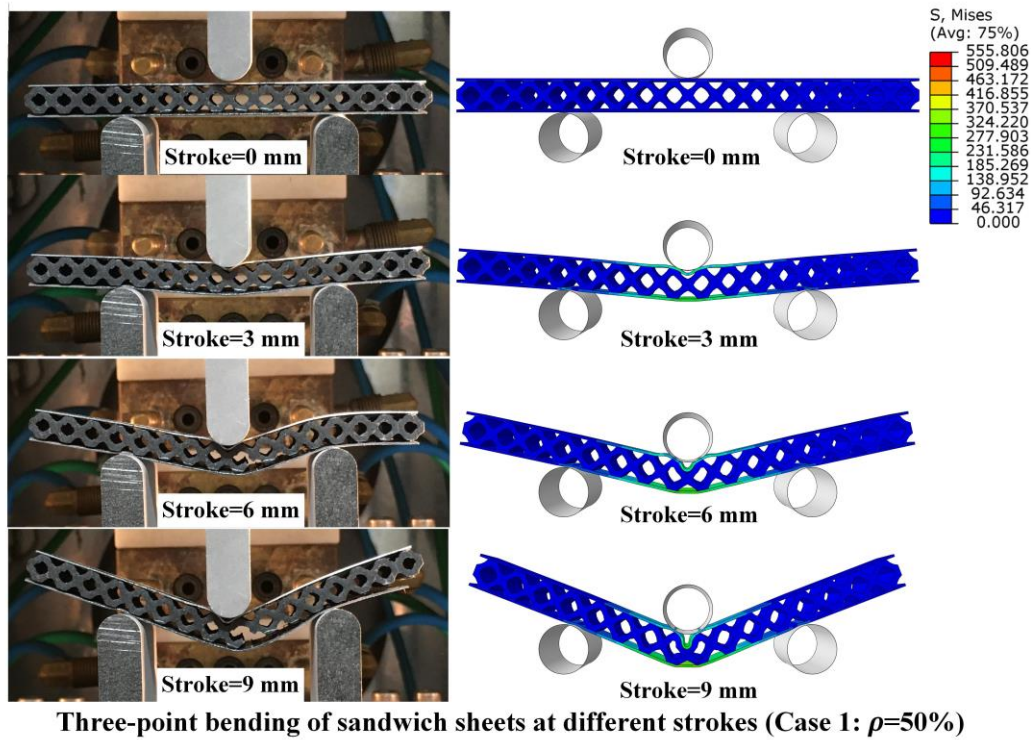


Figure 5-22. Deformation processes during three-point bending experiments and simulations for sandwich sheets with the core density of 50% in case 1.

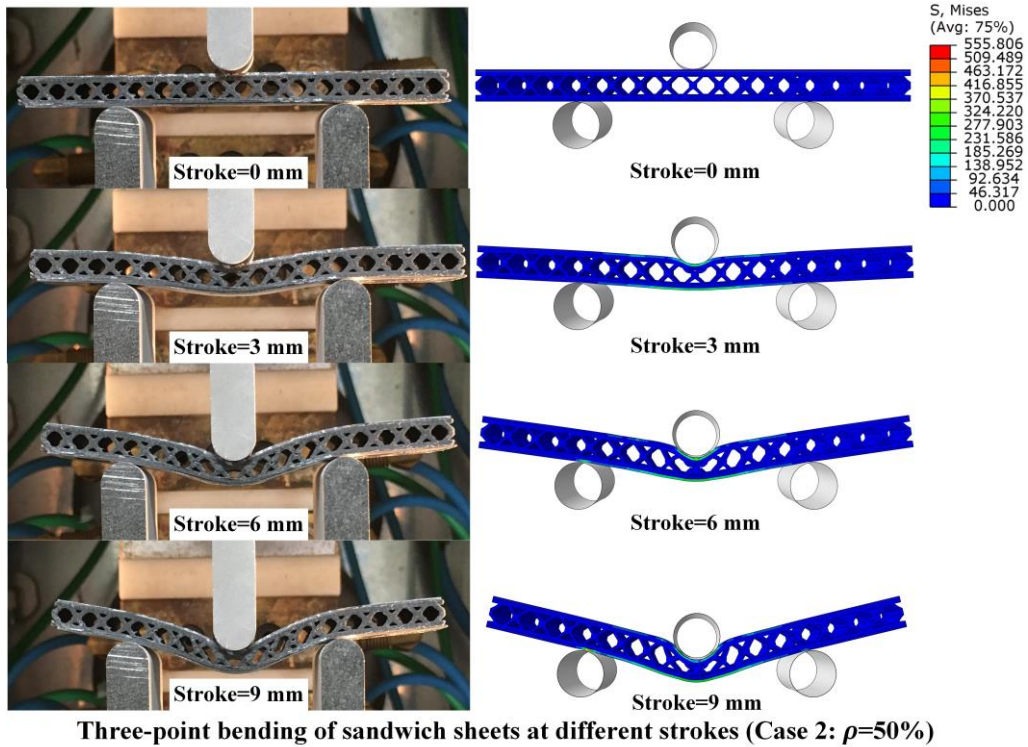


Figure 5-23. Deformation processes during three-point bending experiments and simulations for sandwich sheets with the core density of 50% in case 2.

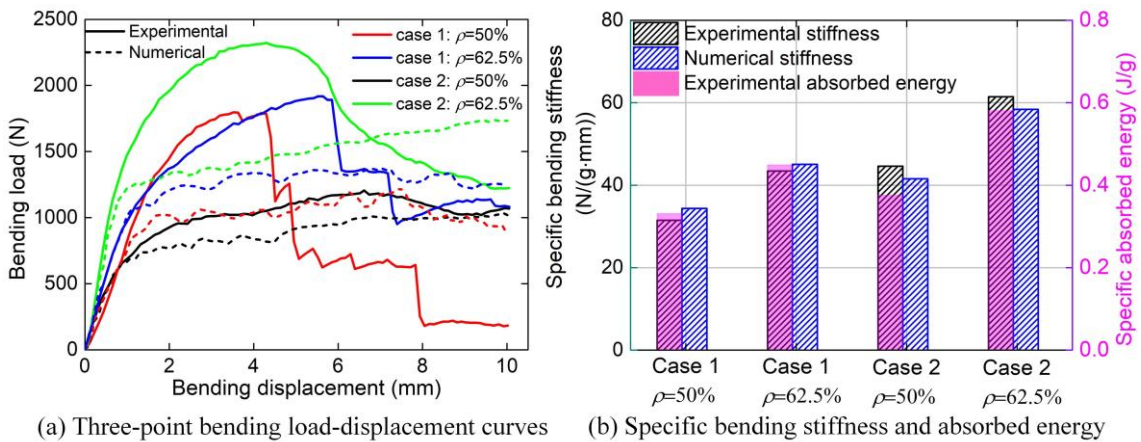


Figure 5-24. Three-point bending properties: (a) Load-displacement curves and (b) Specific bending stiffness and absorbed energy.

Table 5-5. Specific bending stiffness and absorbed energy for different sandwich topologies.

Properties	Case 1: $\rho=50\%$	Case 1: $\rho=62.5\%$	Case 2: $\rho=50\%$	Case 2: $\rho=62.5\%$
Experimental bending stiffness (N/(g·mm))	31.491	43.428	44.586	61.448
Numerical bending stiffness (N/(g·mm))	34.367	45.048	41.558	58.411
Experimental absorbed energy (J/g)	0.331	0.449	0.376	0.581

5.4.2.3 L-bending results

The deformation processes during L-bending are shown in [Figure 5-25](#). The deformed sandwich sheets are presented in [Figure 5-26](#), in which the clamped region between blank holder and die as well as the bent regions are magnified to highlight the failure modes. Except for the sandwich topology with the core density of 50% in case 2, other sandwich sheets can be well bent without any failure. Note that the core shear failure is caused mainly in the clamped region between the blank holder and die while the bent region is good without failure. The predicted core shear strength of the optimal topology with the core density of 50% in case 2 is 4.9559 MPa, which is above the required core shear strength of 4.8468 MPa, and should be capable of suppressing the core shear failure. However, the insufficient in-plane shear strength may lead to the core shear failure as the main deformation mode in the clamped region is restricted to be the in-plane shear. Nevertheless, in the other 3 situations, the potential failure modes including core shear failure, face buckling and delamination are successfully suppressed, which demonstrates the validity of the topology optimization schemes. It should be pointed out that the bending stiffness of deformed sandwich sheets is very important in the practical applications although it was not evaluated in this study. As the bending stiffness after deformation could be affected by many factors such as potential defects and residual stresses caused during deformation, the optimization of bending stiffness after bending could be very difficult. Nevertheless, higher bending stiffness of the intact sandwich sheets generally gives higher bending stiffness of deformed sandwich sheets if they can be bent without failure.

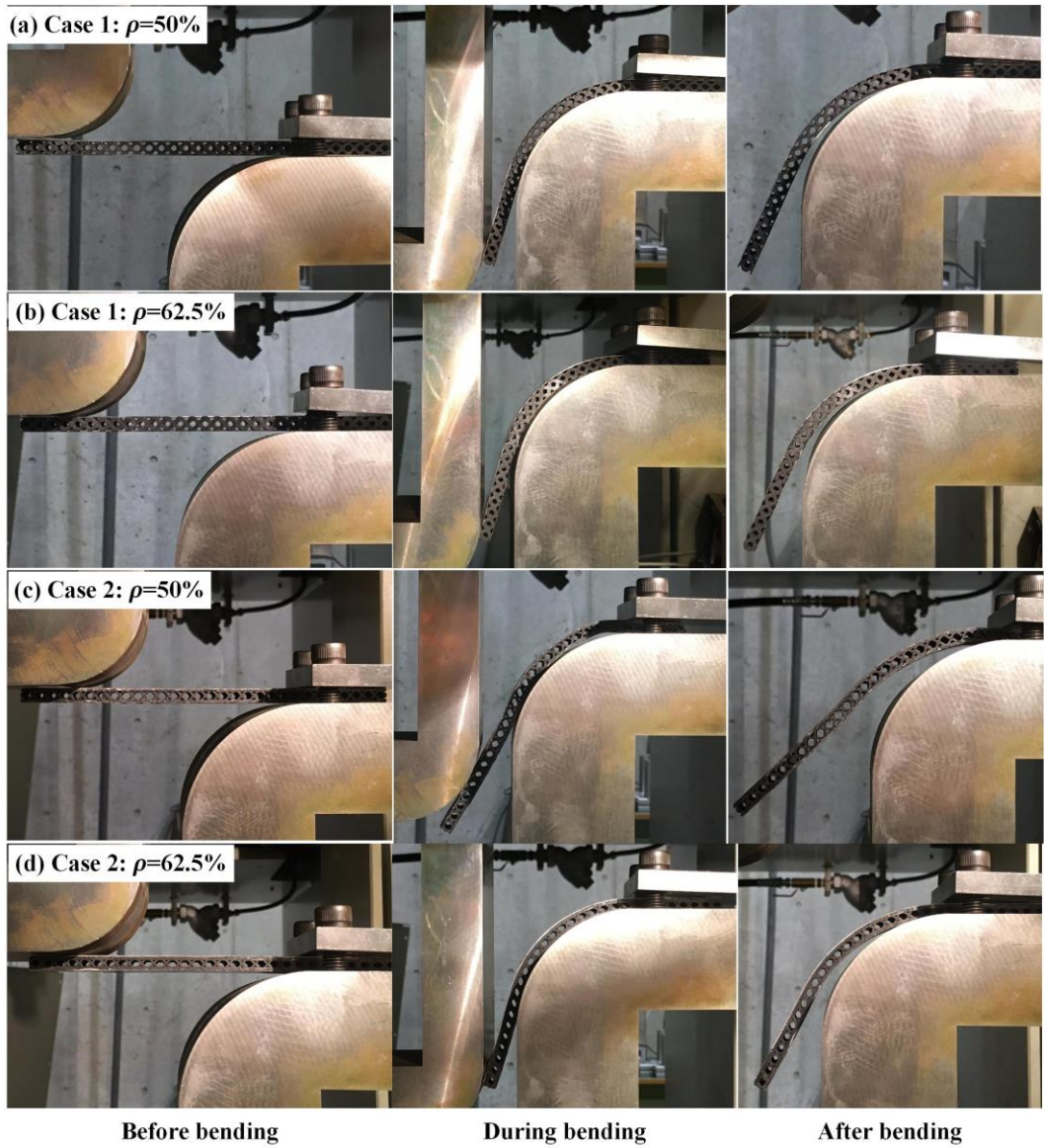


Figure 5-25. Deformation processes of sandwich sheets during L-bending tests.

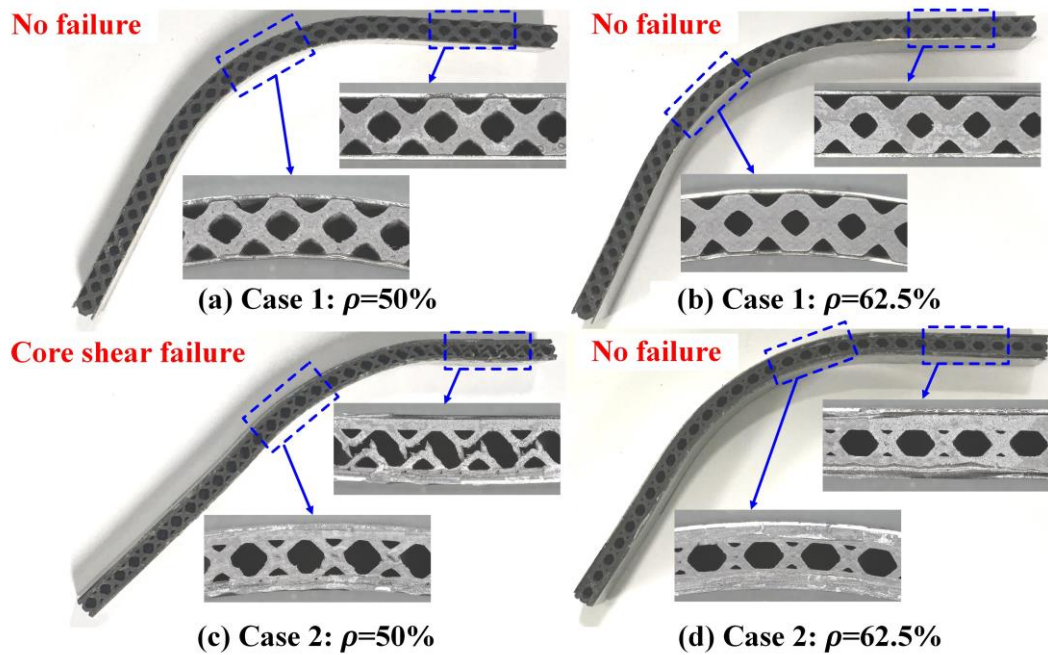


Figure 5-26. Deformed sandwich sheets and highlighted failure modes after L-bending.

5.4.2.4 Draw-bending results

The deformation processes during draw-bending are shown in Figure 5-27. The maximum drawable depths before the initiation of failures were recorded for different sandwich topologies during draw-bending tests. The maximum drawable depths are 30 and 35 mm for sandwich topologies optimized in case 1 with core densities of 50% and 62.5%, respectively, while maximum drawable depths are respectively 20 and 30 mm for those in case 2. The better formability of sandwich topologies optimized in case 1 is proved as the maximum drawable depths in case 1 are higher than those in case 2, which attributes to the higher core shear strengths. The failure modes during draw-bending are highlighted in Figure 5-28. The main failure mode of sandwich topologies in case 1 is delamination, which is due to smaller bonding areas compared with sandwich sheets optimized in case 2. Owing to the lower core shear strengths, the core shear failure is the dominant failure mode for sandwich topologies optimized in case 2. The above failure modes observed in the draw-bending tests are consistent with the topological characteristics.

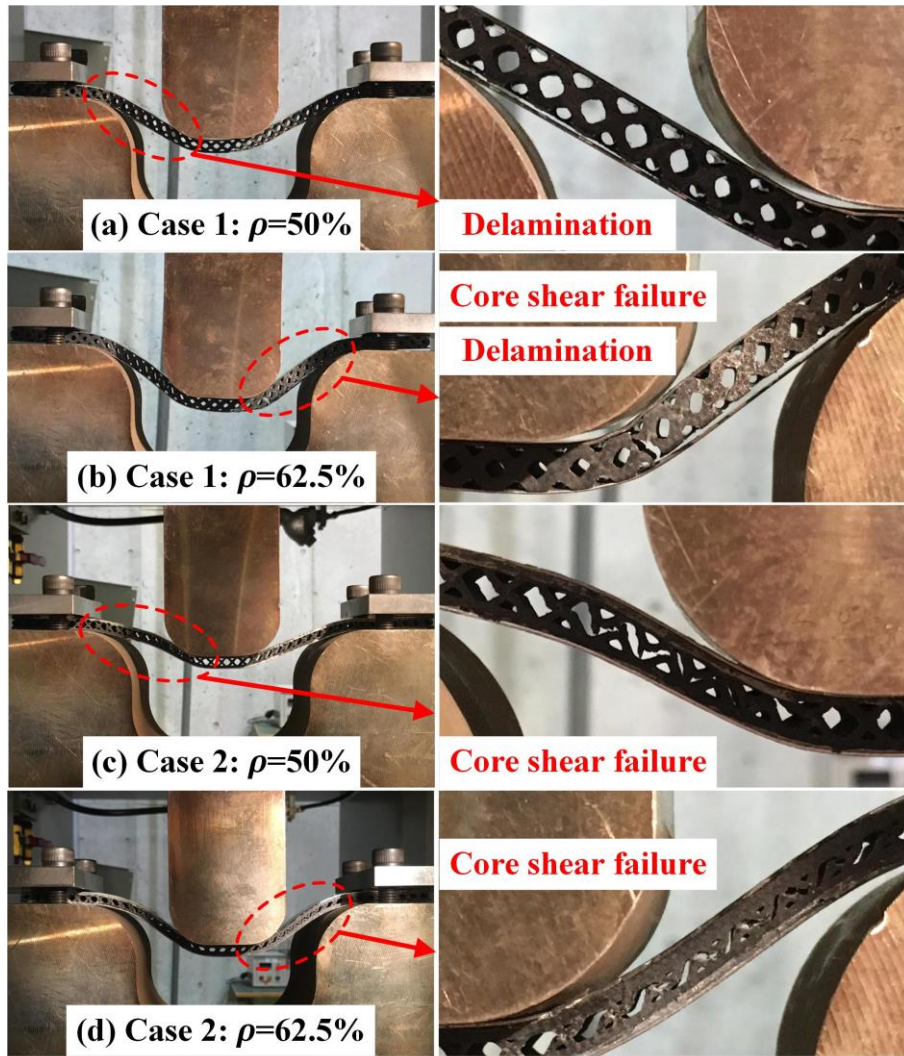


Figure 5-27. Deformation processes and failure modes of sandwich sheets during draw-bending tests.

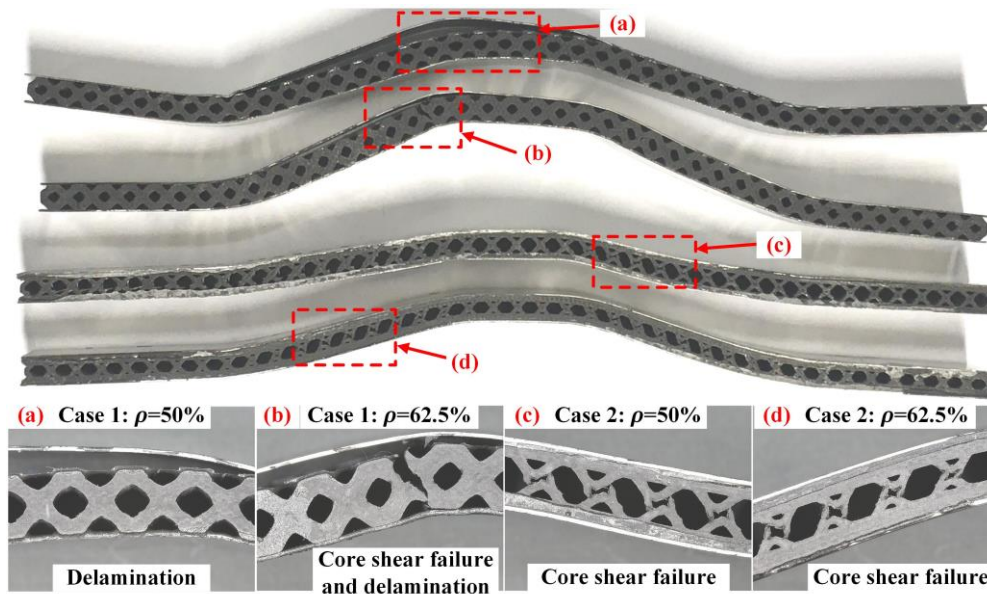


Figure 5-28. Deformed sandwich sheets and highlighted failure modes after draw-bending.

However, two major limitations of the proposed method need to be pointed out. First one is that the computational efficiency of the multi-stage GA is much lower than that of the conventional gradient-based method, in which the optimization problem can be solved within minutes by the conventional gradient-based optimization while it takes days for the multi-stage GA. A feasible means to improve the computational efficiency is to decrease the number of design variables by discretizing the design domain into morphable surfaces (2D) or plates (3D) instead of into single microscopic points, which remains to be investigated in future. Second, as the objective functions are not theoretically solved, the optimal design found by the multi-stage GA may not be the theoretically optimal. To find the mathematically optimal solutions by the gradient-based scheme, the relationships between objective functions (the shear strength and bending stiffness) and design variables (element density) need to be theoretically solved in future.

5.5 Summary

A new topology optimization method, in which the density-based topology optimization was integrated with multi-stage GA, was proposed for the design of sandwich sheets with optimal bending stiffness while maintaining good formability. The theoretical core shear failure and face buckling constraints were deduced and incorporated in two topology optimization schemes to design the inner core topology for formable sandwich sheets, in one of which the formability of the sandwich sheets was optimized and in the other one the bending stiffness was optimized while fulfilling potential failure constraints. Three-point bending tests indicate that the bending stiffness and energy absorption capability of sandwich topologies obtained by the proposed optimization scheme can be effectively improved. Comparing the structures obtained by two optimization schemes, the bending stiffness of sandwich topologies with the core density of 50% and 62.5% are improved by 41.58% and 41.49%, while the energy absorption capabilities are improved by 13.60% and 29.40% respectively. L-bending tests show that potential failures including core shear failure, core–face sheet delamination and face buckling of most optimized sandwich topologies can be well suppressed. Draw-bending tests indicate that the formability of optimized sandwich topologies can be effectively improved, and corresponding failure modes are consistent with the sandwich topological characteristics. The validity of the design strategy is demonstrated, that is, through the proposed topology optimization approach, the sandwich sheets with good formability and improved bending stiffness can be designed, which is expected to expand the applications of sandwich sheets with better formability and superior mechanical properties.

5.6 References

- Allaire, G., Jouve, F., Toader, A.-M., 2002. A level-set method for shape optimization. *Comptes Rendus Mathématique* 334, 1125-1130.
- Bendsøe, M.P., 1989. Optimal shape design as a material distribution problem. *Structural optimization* 1, 193-202.
- Bourdin, B., Chambolle, A., 2003. Design-dependent loads in topology optimization. *ESAIM: Control, Optimisation and Calculus of Variations* 9, 19-48.
- Cai, Z.-Y., Zhang, X., Liang, X.-B., 2018. Multi-point forming of sandwich panels with egg-box-like cores and failure behaviors in forming process: analytical models, numerical and experimental investigations. *Materials & Design* 160, 1029-1041.
- Carradò, A., Faerber, J., Niemeyer, S., Ziegmann, G., Palkowski, H., 2011. Metal/polymer/metal hybrid systems: Towards potential formability applications. *Composite Structures* 93, 715-721.
- Cheng, L., Liu, J., Liang, X., To, A.C., 2018. Coupling lattice structure topology optimization with design-dependent feature evolution for additive manufactured heat conduction design. *Computer Methods in Applied Mechanics and Engineering* 332, 408-439.
- Cucinotta, F., Guglielmino, E., Longo, G., Risitano, G., Santonocito, D., Sfravara, F., 2019. Topology optimization additive manufacturing-oriented for a biomedical application, *Advances on Mechanics, Design Engineering and Manufacturing II*. Springer, pp. 184-193.
- Guo, X., Zhang, W., Zhong, W., 2014. Doing topology optimization explicitly and geometrically—a new moving morphable components based framework. *Journal of Applied Mechanics* 81.
- Hibbeler, R.C., 2003. *Mechanics of materials*. ed. Upper Saddle River New Jersey: Prentice Hall.
- Jackson, K., Allwood, J., Landert, M., 2008. Incremental forming of sandwich panels. *Journal of Materials Processing Technology* 204, 290-303.
- Kim, I.Y., De Weck, O., 2005. Variable chromosome length genetic algorithm for progressive refinement in topology optimization. *Structural and Multidisciplinary Optimization* 29, 445-456.
- Li, Q., Wu, Q., Liu, J., He, J., Liu, S., 2021. Topology optimization of vibrating structures with frequency band constraints. *Structural and Multidisciplinary Optimization* 63, 1203-1218.
- Liu, J., Liu, W., Xue, W., 2013. Forming limit diagram prediction of AA5052/polyethylene/AA5052 sandwich sheets. *Materials & Design* 46, 112-120.
- Mohr, D., 2005. On the role of shear strength in sandwich sheet forming. *International Journal of Solids and Structures* 42, 1491-1512.
- Seong, D., Jung, C.G., Yang, D.-Y., Kim, J., Chung, W., Lee, M., 2010. Bendable metallic sandwich plates with a sheared dimple core. *Scripta materialia* 63, 81-84.
- Sokolova, O.A., Carradò, A., Palkowski, H., 2011. Metal–polymer–metal sandwiches with local metal reinforcements: A study on formability by deep drawing and bending. *Composite Structures* 94, 1-7.
- Sokolowski, J., Zochowski, A., 2003. Optimality conditions for simultaneous topology and

shape optimization. *SIAM journal on control and optimization* 42, 1198-1221.

Sundaram, S., Skouras, M., Kim, D.S., van den Heuvel, L., Matusik, W., 2019. Topology optimization and 3D printing of multimaterial magnetic actuators and displays. *Science advances* 5, eaaw1160.

Wang, M.Y., Wang, X., Guo, D., 2003. A level set method for structural topology optimization. *Computer methods in applied mechanics and engineering* 192, 227-246.

Xie, Y.M., Steven, G.P., 1993. A simple evolutionary procedure for structural optimization. *Computers & structures* 49, 885-896.

Zhang, H., Wang, M.Y., Chen, F., Wang, Y., Kumar, A.S., Fuh, J.Y., 2017. Design and development of a soft gripper with topology optimization, 2017 IEEE/RSJ International Conference on Intelligent Robots and Systems (IROS). IEEE, pp. 6239-6244.

Zhang, J., Sato, Y., Yanagimoto, J., 2021a. Homogenization-based topology optimization integrated with elastically isotropic lattices for additive manufacturing of ultralight and ultrastiff structures. *CIRP Annals*.

Zhang, J., Taylor, T., Kizaki, T., Yanagimoto, J., 2020. Bendable metal-based composite sheets with a truncated dome core made of carbon fibre reinforced thermoplastics. *Composite Structures* 236, 111918.

Zhang, J., Taylor, T., Yanagimoto, J., 2021b. Mechanical properties and cold and warm forming characteristics of sandwich sheets with a three-dimensional CFRTP core. *Composite Structures* 269, 114048.

Zhang, J., Yanagimoto, J., 2019. Design and fabrication of formable CFRTP core sandwich sheets. *CIRP Annals* 68, 281-284.

Zhou, M., Rozvany, G., 1991. The COC algorithm, Part II: Topological, geometrical and generalized shape optimization. *Computer methods in applied mechanics and engineering* 89, 309-336.

Chapter 6 Concluding remarks

The design and fabrication of lightweight hybrid structures with optimal mechanical performance, production efficiency and improved functionality has always been driven by the pursuit of further reduction of energy consumption and greenhouse gas emissions. However, the technical issues associated with the design and production processes, such as the low manufacturing efficiency and high production cost, the limited formability and restricted mechanical performance and functionality, severely hindered the widespread use of such lightweight multifunctional hybrid structures. This doctoral thesis aims to overcome these engineering challenges by proposing a new type of metal face/3D CFRP core hybrid structure with enhanced mechanical performance productivity and formability achieved by more effective design strategies and efficient production processes.

Two main strategies were proposed for the design and fabrication of lightweight formable metal face/3D CFRP core hybrid structures, in which the shape design and conventional production processes were firstly proposed in the first strategy while the second strategy relies on topology optimization and additive manufacturing. To be specific, the suitable inner core structure with superior mechanical property was designed and efficiently produced by warm stamping of CFRTP sheet. The effects of material properties of face sheets and core, sandwich geometries, forming tool geometries, core shapes, forming processes and forming temperatures on formability of sandwich sheets were systematically investigated by experiments and theoretical analyses. The homogenization-based topology optimization (HMTO) method was firstly integrated with the tetrahedral truss-based lattice structure to optimize the stiffness and later the elastically isotropic plate-based lattices with superior structural efficiency was further proposed to integrate with HMTO to improve the design efficiency, manufacturability, structural isotropy and computational efficiency. The stiffness and formability of sandwich sheets were simultaneously optimized by integrating the density-based topology optimization method with the multi-stage genetic algorithm. The feasibility of effective design and efficient fabrication of hybrid metal face/CFRP core composite sheets with superior mechanical property, formability as well as productivity is demonstrated by a series of investigations

presented in this thesis.

To gain insight into the future development direction, as shown in [Figure 6-1](#), most common structures are comprehensively evaluated in terms of specific shear modulus characterizing the shear failure resistance or formability, flexural stiffness representing the bending mechanical performance and production methods revealing the productivity. It can be seen that the dome-like structures proposed in **Chapter 2** have limited specific shear modulus and flexural stiffness compared to the microlattice dome designed in **section 4.1**. These properties are further improved by proposing the truss-lattice and plate-lattice in **section 4.2**. In **Chapter 5**, the 2D topology optimization method, in which the density-based TO is integrated with genetic algorithm, is proposed to further enhance the flexural stiffness and simultaneously maintain relatively good formability. Since the method proposed in **Chapter 5** is limited to the 2D optimization, the formability is still restricted. Therefore, the future development route is to find the core structure with better formability and excellent stiffness by 3D topology optimization approach. To achieve this, however, the computational efficiency must be improved. A feasible means to improve the computational efficiency is to decrease the number of design variables by discretizing the design domain into morphable surfaces (2D) or plates (3D) instead of into single microscopic points, which remains to be investigated in future. The other way is to find the mathematically optimal solutions by the gradient-based scheme, the relationships between objective functions (the shear strength and bending stiffness) and design variables (element density) need to be theoretically solved in future.

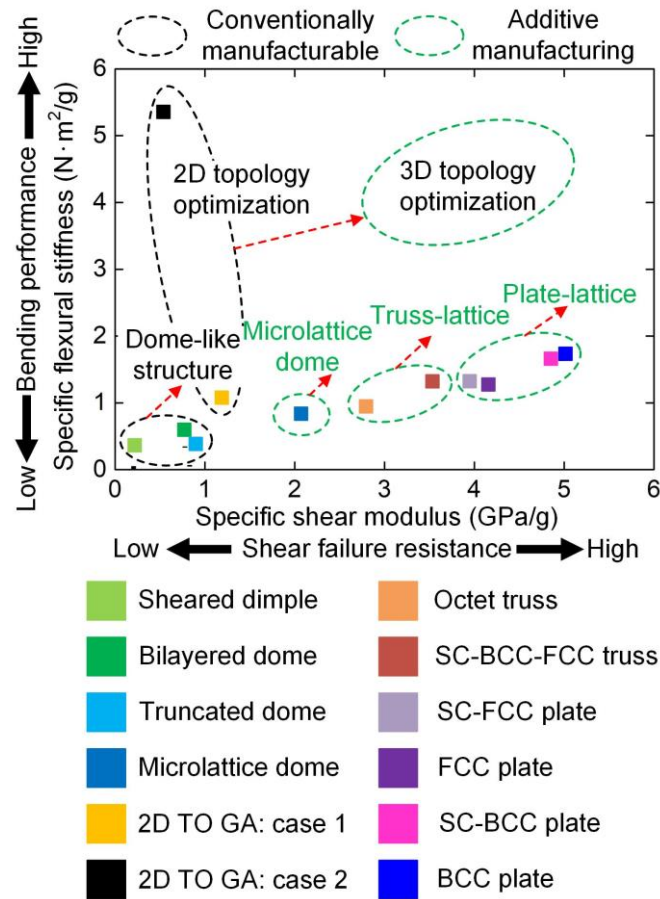


Figure 6-1. Core structures characterized with ‘specific shear modulus’ and ‘specific flexural stiffness’ as well as manufacturable methods, made of basis material CFRTP with a modulus of 13.5 GPa and density of 1.8 g/cm³.

Chapter 2 Shape design and conventional fabrication of formable sandwich sheet

Sandwich structures have had remarkable success in engineering applications, but their applications are mostly limited to flat panel types because of their poor formability. To expand the range of applications of sandwich structures, new metal face/CFRP core sandwich sheets are proposed, where a CFRP core structure is designed to increase formability and structural performance. This chapter first introduces the design methods followed by the fabrication processes and finally reports the flexural properties and formability of the proposed sandwich sheets.

Comprehensively considering the mechanical property, manufacturability and failure resistance ability, a truncated dome core made of carbon fiber reinforced thermoplastics

(CFRTP) was determined to be the inner macrostructure of sandwich sheets. The proposed truncated dome core structure was composed of a periodic array of domes which were introduced into an initially flat CFRTP sheet through warm stamping. The numerical investigation shows that the optimal relative density of the truncated dome core is 0.22 in terms of comprehensive consideration of bending stiffness, shear modulus and face buckling degree. The optimal forming conditions of CFRTP sheet were investigated prior to the continuous fabrication process of long CFRTP core by piecewise sectional forming technology. The flexural properties were tested by three-point bending, and formability of sandwich sheets was evaluated experimentally by cold and warm L-bending and draw-bending tests. The results indicate that the sandwich sheets composed of metallic face sheets and CFRTP core have better formability when cold formed, while the sandwich sheets composed of CFRTP face sheets and CFRTP cores have superior formability when warm formed. The development of formable metal face/CFRP core sandwich sheets is expected to expand the application range of sandwich structures and promote the use of lightweight parts in engineering fields. More detailed conclusions can be drawn as follows:

- (i) Rapid continuous manufacturing of a three-dimensional core structure can be achieved by warm stamping an initially flat CFRP sheet at a forming temperature of 200°C, demonstrating the feasibility of mass production of metal face/CFRP core sandwich sheets.
- (ii) The specific bending stiffness and shear modulus of the sandwich sheet with the truncated dome core are 5 and 2 times larger than those of the sandwich sheet with the conventional flat core, respectively, which proves the structural superiority of the sandwich sheet with the truncated dome core.
- (iii) Forming tests indicate that the failure mode and maximum drawing depth of sandwich sheets are closely related to forming temperature, and good formability can be achieved by adjusting forming temperature.
- (iv) The sandwich sheets composed of metallic face sheets and CFRTP core have better formability when cold formed, while the sandwich sheets composed of CFRTP face sheets and CFRTP cores have superior formability when warm formed.

- (v) Sandwich sheets composed of metallic face sheets and CFRTP core can be subjected to shallow drawing without failure under ambient temperature, while the sandwich sheets composed of CFRTP face sheet and CFRTP core can be well formed at a forming temperature of 150°C.
- (vi) The investigations in this chapter demonstrate feasibility of rapid production and of secondary forming by conventional forming methods, which is expected to expand the commercial application of sandwich structures.

Chapter 3 Investigation on influence factors on forming behaviors of sandwich sheet

Previous investigations on the forming characteristics of sandwich sheets with various inner macrostructures have revealed that failure modes such as core-face sheet delamination, face buckling and core shear failure are highly related to material properties of sandwich constituents, the sandwich geometries, forming tool geometries, core shapes, forming processes, forming temperatures, etc. Therefore, the relation between formability and these influence factors is clarified by systematical experimental tests and theoretical analyses for effective design and efficient fabrication process. In addition, the functional lattice structures are embraced in the core structure for the improvement of mechanical performance and potential functionality of sandwich sheets. The effects of lattice core topologies and relative densities on the mechanical property and forming behavior are extensively investigated.

Firstly, for the sandwich sheets with a truncated dome core designed in the previous chapter, theoretical analyses were conducted to determine the conditions required for successfully forming these sandwich sheets into curved shapes. Experimental results of formability tests agree well with the theoretical predictions, which demonstrates the validity of the theoretical models. Sandwich sheets with both A2017P and SUS304 face sheets of a thickness of 0.5 mm can be bent without any failure at a bending radius of 60 mm. To further improve structural performance, bendability and potential functionality of metal-based sandwich sheets, the 3D lattice cores were sandwiched between thin metallic face sheets. The bending properties of sandwich sheets with 3D printed CFRP lattice cores originating from basic topologies of

spherical shell, tetrahedral truss and tetrahedral plate were systematically investigated. The effects of core topologies, core relative densities, core heights, face sheet thicknesses on structural properties were clarified. The common failure modes during bending of sandwich sheets, such as face buckling and shear failure of core, were deeply investigated by theoretical models and experimental tests. At a prescribed radius of 60 mm, the sandwich sheets with the bilayered dome, octet truss and plate lattice cores of relative density of 50%, height of 6 mm and face sheet thickness of 0.5 mm are bendable. The feasibility of design and production of bendable sandwich sheets with 3D lattice cores is demonstrated based on the theoretical and experimental validations. The designed bendable sandwich sheets can be adopted to replace conventional heavy monolithic metal sheets in various engineering applications, which is anticipated to fulfill the high demand for lightweight functional materials.

Chapter 4 Design and fabrication of inner macrostructure with enhanced stiffness via topology optimization and additive manufacturing

Although conventional manufacturing processes allow some control over shape and size of the inner core structure, they remain limited to producing a certain type of specially designed structures and thus the mechanical property, formability and functionality of inner core structures may still be restricted. In addition, the incapability of manufacturing precise complex structures, the high manufacturing cost and the discrepancy in the properties of produced structures also limit the applications of the conventional fabrication methods. The layer-by-layer fabrication paradigm of AM enables the build of lattice materials with extremely intricate external geometries and high control of the internal architecture, overcoming the limitations of conventional fabrication methods. The topology optimization enables the optimal material layout of the core structure at a given set of load and boundary conditions, and thus it can be relied on to optimize the core structure for the pursuit of higher structural efficiency and better formability. The synergy of topology optimization and additive manufacturing could be a perfect tool for the design and production of sandwich sheets with improved mechanical performance, formability and functionality. Therefore, the topology optimization is used to design optimal core structures with superior stiffness and formability in this chapter.

A new microlattice dome structure has been proposed, in which the solid part of the conventional dome structure is replaced by less dense and less brittle stretch-dominated tetrahedral microlattices. By integrating homogenization-based topology optimization with a tetrahedral microlattice, the optimal distribution of the microlattice was determined under compression and three-point bending loads to maximize the stiffness and energy absorption of the microlattice dome. The specific compressive stiffnesses of the optimized variable-density models with large and small cell sizes were improved by 33.8% and 91.8%, respectively, compared with the unoptimized uniform-density models. Compared with the unoptimized uniform-density models, the bending stiffnesses of the optimized variable-density models with large and small cells are increased by 81.6% and 76.9%, respectively. For the compression models, the energy absorption of the optimized variable-density structures with the large and small cells was improved by 72.2% and 124.2%, respectively. The energy absorption of the optimized variable-density models with the large and small cells is increased by 61.8% and 33.3%, respectively, during the three-point bending process. The compressive and bending stiffnesses of the optimized variable-density microlattice domes are proved to be 41.8% and 33.7% higher than those of the conventional solid domes, while the energy absorption of the microlattice dome during compression and three-point bending is increased by 297.5% and 85%, respectively. Investigation of the cell size effect on the mechanical properties of the microlattice dome reveals that a larger cell size contributes more to the weight-specific stiffness and energy absorption capability at a given overall volume fraction constraint. The above significant findings prove that a microlattice dome with high weight-specific stiffness and energy absorption can be designed by integrating topology optimization and lattice structures. The homogenization-based topology optimization and construction methods described in this paper are universal and can be used to optimize and design structures with arbitrary macro shapes with microlattices as constituent units, which is of great significance for the development of ultralight and ultrastiff structures.

Elastically isotropic plate–lattices with superior mechanical properties were firstly proposed to be integrated with the HMTO method to improve design manufacturability, structural efficiency, structural isotropy and computational efficiency. The mechanical

properties and elastic isotropy of representative truss–lattices and plate–lattices were investigated, after which the SC–FCC plate–lattice with excellent structural efficiency and elastic isotropy was integrated with the HMTO method to optimize two typical examples. The results indicate the proposed method can significantly improve structural efficiency including stiffness and energy absorption capability. Together with more advantages that this approach is easily implementable and generates designs suitable for AM, the proposed method can be expected to promote the development of ultralight and ultrastiff structures.

Chapter 5 Concurrent topology optimization of formability and bending stiffness of sandwich sheet

A new topology optimization method, in which the density-based topology optimization was integrated with multi-stage GA, was proposed for the design of sandwich sheets with optimal bending stiffness while maintaining good formability. The theoretical core shear failure and face buckling constraints were deduced and incorporated in two topology optimization schemes to design the inner core topology for formable sandwich sheets, in one of which the formability of the sandwich sheets was optimized and in the other one the bending stiffness was optimized while fulfilling potential failure constraints. Three-point bending tests indicate that the bending stiffness and energy absorption capability of sandwich topologies obtained by the proposed optimization scheme can be effectively improved. Comparing the structures obtained by two optimization schemes, the bending stiffness of sandwich topologies with the core density of 50% and 62.5% are improved by 41.58% and 41.49%, while the energy absorption capabilities are improved by 13.60% and 29.40% respectively. L-bending tests show that potential failures including core shear failure, core–face sheet delamination and face buckling of most optimized sandwich topologies can be well suppressed. Draw-bending tests indicate that the formability of optimized sandwich topologies can be effectively improved, and corresponding failure modes are consistent with the sandwich topological characteristics. The validity of the design strategy is demonstrated, that is, through the proposed topology optimization approach, the sandwich sheets with good formability and improved bending stiffness can be designed, which is expected to expand the applications of sandwich sheets with

better formability and superior mechanical properties.

Offers for future work

As discussed in the beginning of this chapter, to seek a better balance between the mechanical performance and formability of lightweight inner macrostructures is still a challenge, which relies on the development of new design strategies. One approach has been provided and discussed in the beginning of this chapter, that is, to extend the integration of density-based topology optimization and genetic algorithm to 3D optimization problem. To achieve this, however, the computational efficiency must be improved. A feasible means to improve the computational efficiency is to decrease the number of design variables by discretizing the design domain into morphable surfaces (2D) or plates (3D) instead of into single microscopic points, which remains to be investigated in future. The other way is to find the mathematically optimal solutions by the gradient-based scheme, the relationships between objective functions (the shear strength and bending stiffness) and design variables (element density) need to be theoretically solved in future.

In this dissertation, the material and structural models are considered ideal, that is, the geometry inaccuracy and material anisotropy that may be introduced by the additive manufacturing process are not considered in the topology optimization model. However, the actual layer-by-layer manufacturing process of additive manufacturing will cause geometry errors and material anisotropy. For example, the greater the thickness of the build-up layer, the greater the geometry error, and the material properties along the build-up direction and perpendicular to the build-up direction are usually different. Therefore, it is necessary to consider the structural errors and material anisotropy introduced by the additive manufacturing process to obtain a topology optimization result closer to the actual production. To address this problem, we propose a design and production strategy that integrates material property-structure-performance for the synergy of topology optimization and additive manufacturing, as shown in [Figure 6-2](#). To be specific, compared with the conventional and serial design mode in [Figure 6-2\(a\)](#) based on AM incorporating ideal conditions, this strategy establishes the as-fabricated stair-step model of unit lattices based on AM, and the homogenization theory and

TO algorithm are adopted to estimate the mechanical performance of microstructures and macro-structures. Initially, ideal 3D unit cells are transformed into sliced models with stair-step features. Then elements are generated in sliced and ideal CAD models, and the periodic boundary conditions are applied to FE models to perform the finite element analysis (FEA). The effective mechanical properties of ideal and sliced lattices can be obtained from the FEA results. Finally, these effective parameters are delivered into TO formulation to optimize macro-structural topology. This research is currently underway, and the computed results are expected to provide a reference for the designer and manufacturer to select rational parameters.

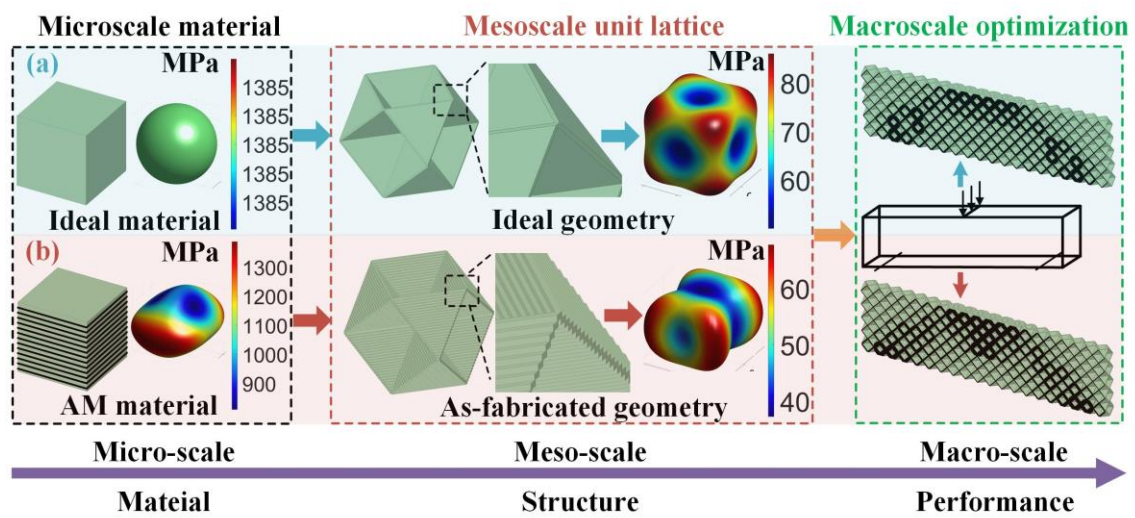


Figure 6-2. Material-structure-performance integrated design and production strategy for the synergy of topology optimization and additive manufacturing.

In addition, in this dissertation, only one material is used in the design and manufacturing process. To further improve mechanical properties and functionality, multi-material design strategies and production methods can be considered. Now, additive manufacturing technology makes it possible to produce structures with multiple materials. Compared with the structures made of a single material component, those composed of multiple materials can be expected to achieve better mechanical property and functionality. Furthermore, topology optimization strategies based on multi-materials and multi-structures have also been extensively studied. Therefore, by combining the multi-material topology optimization method with multi-material additive manufacturing technology, the design and production of multi-functional structures can be realized. For example, by combining the soft and hard characteristics and structural

design of different materials, functional products such as origami structures and soft robots can be manufactured. In future, the combination of multi-material topology optimization and multi-material additive manufacturing technology deserves to be investigated for the further improvement of mechanical performance and functionality of lightweight structures.

Appendix

Appendix A Periodic boundary conditions for pure bending

Consider the unit cell of length L subjected to pure bending as shown in [Figure A-1](#), where the principal bending plane is on the xoy plane and the xoz plane coincides with neutral plane of bending. Assuming that the bending angle is φ and $x=0$ is at the center plane of the unit cell, the displacement at right boundary face (S^+) of the unit cell after pure bending can be expressed by:

$$u_x = -[x - (\beta + y) \sin(\varphi/2)] \quad (\text{A-1})$$

$$u_y = -(\beta + y)(1 - \cos(\varphi/2)) \quad (\text{A-2})$$

where displacements in x and y directions are denoted as u_x and u_y , respectively, and β is the radius of curvature given by:

$$\beta = \frac{L}{\varphi} \quad (\text{A-3})$$

As the deformed unit cell after pure bending is an arc-like shape, it is more convenient to analyse the pure bending problem under cylindrical coordinates. Therefore, as illustrated in [Figure A-2](#), the displacements in Cartesian coordinates ([Eqs. \(A-1\)-\(A-2\)](#)) are converted to those in cylindrical coordinates through coordinate transformation:

$$u_r = u_x \sin(\varphi/2) + u_y \cos(\varphi/2) \quad (\text{A-4})$$

$$u_\theta = u_x \cos(\varphi/2) - u_y \sin(\varphi/2) \quad (\text{A-5})$$

where u_r and u_θ are displacements along r and θ directions, respectively.

Combining [Eqs. \(A-1\)-\(A-2\)](#) and [Eqs. \(A-4\)-\(A-5\)](#), displacements at the right boundary face in cylindrical coordinates are given by:

$$u_r|^{S^+} = [-x \sin(\varphi/2) + (\beta + y)(1 - \cos(\varphi/2))] \quad (\text{A-6})$$

$$u_\theta|^{S^+} = [-x \cos(\varphi/2) + (\beta + y) \sin(\varphi/2)] \quad (\text{A-7})$$

Respectively replacing $\varphi/2$ and x with $-\varphi/2$ and $-x$, the displacements at the left boundary

face (S^-) are:

$$u_r|^{S^-} = [-x \sin(\varphi/2) + (\beta + y)(1 - \cos(\varphi/2))] \quad (\text{A-8})$$

$$u_\theta|^{S^-} = [x \cos(\varphi/2) - (\beta + y) \sin(\varphi/2)] \quad (\text{A-9})$$

Then the periodic boundary conditions of the unit cell under pure bending can be expressed in cylindrical coordinates by:

$$\begin{aligned} u_r|^{S^+} - u_r|^{S^-} &= 0 \\ u_\theta|^{S^+} - u_\theta|^{S^-} &= 2(\beta + y) \cdot \sin(\varphi/2) - 2x \cdot \cos(\varphi/2) \\ u_z|^{S^+} - u_z|^{S^-} &= 0 \end{aligned} \quad (\text{A-10})$$

Since the implementation of periodic boundary conditions through FEM is easier in Cartesian coordinates, periodic boundary conditions in cylindrical coordinates (Eq. (A-10)) are converted back to those in Cartesian coordinates through coordinate transformation:

$$\begin{aligned} u_x|^{S^+} \cdot \cos(\varphi/2) - u_y|^{S^+} \cdot \sin(\varphi/2) - u_x|^{S^-} \cdot \cos(\varphi/2) \\ - u_y|^{S^-} \cdot \sin(\varphi/2) &= 2(\beta + y) \cdot \sin(\varphi/2) - 2x \cdot \cos(\varphi/2) \\ u_x|^{S^+} \cdot \sin(\varphi/2) + u_y|^{S^+} \cdot \cos(\varphi/2) + u_x|^{S^-} \cdot \sin(\varphi/2) \\ - u_y|^{S^-} \cdot \cos(\varphi/2) &= 0 \\ u_z|^{S^+} - u_z|^{S^-} &= 0 \end{aligned} \quad (\text{A-11})$$

At a given bending angle φ , pure bending FEM analysis is conducted by applying Eq. (A-11) to each pair of corresponding nodes that have the same y and z coordinates on left and right boundary faces (S^- and S^+), which can be implemented by the MPC user subroutine incorporated in FEM software ABAQUS 6.14-2.

The specific bending moment can be extracted from the simulation results and then the specific pure flexural rigidity $(EI)_{eq}$ can be calculated according to Eq. (A-12).

$$(EI)_{eq} = \frac{1}{m} \frac{ML}{\varphi} \quad (\text{A-12})$$

in which m is the mass of the repeated unit cell.

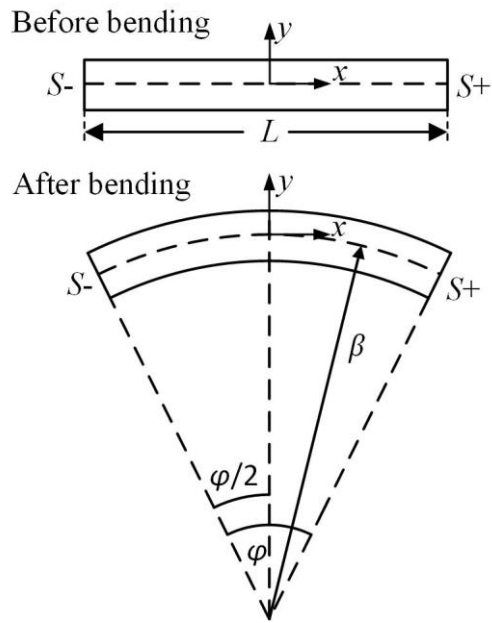


Figure A-1. Free body diagram during pure bending.

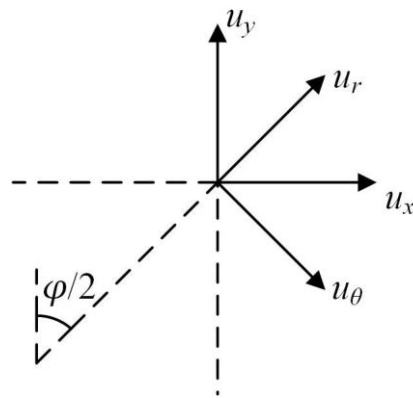


Figure A-2. Illustration of coordinate transformation between Cartesian and cylindrical coordinate systems.

Appendix B Implementation of periodic boundary conditions for pure bending by MPC User Subroutine incorporated in ABAQUS

```
SUBROUTINE MPC(UE,A,JDOF,MDOF,N,JTYPE,X,U,UNIT,MAXDOF,LMPC,KSTEP,
```

```
  * KINC,TIME,NT,NF,TEMP,FIELD,LTRAN,TRAN)
```

C

```
  INCLUDE 'ABA_PARAM.INC'
```

C

```
  DIMENSION UE(MDOF),A(MDOF,MDOF,N),JDOF(MDOF,N),X(6,N),
```

```
  * U(MAXDOF,N),UNIT(MAXDOF,N),TIME(2),TEMP(NT,N),
```

```
  * FIELD(NF,NT,N),LTRAN(N),TRAN(3,3,N)
```

C

```
  REAL angle,AAA,BBB,t
```

```
  IF (KSTEP .EQ. 1) THEN
```

```
  IF (JTYPE .EQ. 1) THEN
```

```
    angle = 0.05*TIME(1) !bending angle increases linearly
```

```
    AAA=SIN(angle)
```

```
    BBB=COS(angle)
```

```
    CCC=TAN(angle)
```

C

```
UE(1)=CCC*U(2,1)+U(1,2)+CCC*U(2,2)+2*X(2,2)*CCC+2*X(1,2)*CCC/angle
```

```
  &-2*X(1,2)
```

```
UE(2)=-AAA/BBB*U(1,1)-AAA/BBB*U(1,2)+U(2,2)
```

```
UE(3)=U(3,2) ! value of eliminated degree of freedom
```

C

```
  A(1,1,1) = BBB
```

```
  A(1,2,1) = -AAA
```

```
  A(2,1,1) = AAA
```

A(2,2,1) = BBB

A(3,3,1) = 1

A(1,1,2) = -BBB

A(1,2,2) = -AAA

A(2,1,2) = AAA

A(2,2,2) = -BBB

A(3,3,2) = -1 !submatrices of coefficients of the

linearized constraint function

C

JDOF(1,1) = 1

JDOF(2,1) = 2

JDOF(3,1) = 3 !eliminated degree of freedom of first

node

JDOF(1,2) = 1

JDOF(2,2) = 2

JDOF(3,2) = 3 !involved degree of freedom of second

node

END IF

END IF

C

RETURN

END

Publications

International journals

* = Corresponding Author

Papers included in this dissertation

1. **J. Zhang***, J. Yanagimoto. "Design and fabrication of formable CFRTP core sandwich sheets." *CIRP Annals* 68.1 (2019): 281-284. <https://doi.org/10.1016/j.cirp.2019.04.060> (Chapter 2)
2. **J. Zhang***, T. Taylor, J. Yanagimoto. "Mechanical properties and cold and warm forming characteristics of sandwich sheets with a three-dimensional CFRTP core." *Composite Structures* (2021): 114048. <https://doi.org/10.1016/j.compstruct.2021.114048> (Chapter 2)
3. **J. Zhang***, T. Taylor, T. Kizaki, J. Yanagimoto. "Bendable metal-based composite sheets with a truncated dome core made of carbon fibre reinforced thermoplastics." *Composite Structures* 236 (2020): 111918. <https://doi.org/10.1016/j.compstruct.2020.111918> (Chapter 3)
4. **J. Zhang***, Sheng Ding, J. Yanagimoto. "Bending properties of sandwich sheets with thin metallic face sheets and additively manufactured 3D CFRP lattice cores" *Journal of Materials Processing Technology* (2021), <https://doi.org/10.1016/j.jmatprotec.2021.117437>. (Chapter 3)
5. **J. Zhang***, Y. Sato, J. Yanagimoto. "Homogenization-based topology optimization integrated with elastically isotropic lattices for additive manufacturing of ultralight and ultrastiff structures." *CIRP Annals* 70.1 (2021): 111-114. <https://doi.org/10.1016/j.cirp.2021.04.019> (Chapter 4)

6. **J. Zhang***, J. Yanagimoto. "Topology optimization of CFRP hierarchical pyramidal structures fabricated by additive manufacturing." *Composites Part B: Engineering* 224 (2021). <https://doi.org/10.1016/j.compositesb.2021.109241> (Chapter 4)
7. **J. Zhang***, J. Yanagimoto. "Topology optimization of microlattice dome with enhanced stiffness and energy absorption for additive manufacturing." *Composite Structures* 255 (2021): 112889. <https://doi.org/10.1016/j.compstruct.2020.112889> (Chapter 4)
8. **J. Zhang***, J. Yanagimoto. "Density-based topology optimization integrated with genetic algorithm for optimizing formability and bending stiffness of 3D printed CFRP core sandwich sheets." *Composites Part B: Engineering* 225 (2021). <https://doi.org/10.1016/j.compositesb.2021.109248> (Chapter 5)
9. **J. Zhang***, J. Yanagimoto. "Design of bendable sandwich sheets with 3D printed CFRP cores via multi-stage topology optimization." *Composite Structures* (2022). <https://doi.org/10.1016/j.compstruct.2022.115372> (Chapter 5)

Papers NOT included in this dissertation

10. T. Kizaki, **J. Zhang***, Q. Yao, J. Yanagimoto. "Continuous manufacturing of CFRP sheets by rolling for rapid fabrication of long CFRP products." *Composites Part B: Engineering* 189 (2020): 107896. <https://doi.org/10.1016/j.compositesb.2020.107896>
11. **J. Zhang***, T. Taylor, L. Shukla, J. Yanagimoto. "Rapid fabrication of 3D CFRP parts by hot forming of pre-cured CFRP sheets." *Composite Structures* (2021): 113942. <https://doi.org/10.1016/j.compstruct.2021.113942>
12. **J. Zhang***, J. Yanagimoto. "Integrated material-structure-performance topology optimization strategy for additive manufacturing of carbon fibre reinforced lattice structures." *To be submitted*.

13. Y. Shibuya, **J. Zhang***, Y. Sato, J. Yanagimoto. "Integration of material and structural anisotropies in design for additive manufacturing of carbon fibre reinforced plastic structures." *CIRP Annals* (2022), *Under Review*.
14. S. Ding, **J. Zhang***, SA. Khan, Y. Sato, J. Yanagimoto. "Metadynamic recrystallization in A5083 aluminum alloy with homogenized and as-extruded initial microstructures." *Materials Science and Engineering A* (2022). <https://doi.org/10.1016/j.msea.2022.142789>
15. S. Ding, **J. Zhang**, SA. Khan, J. Yanagimoto. "Static recovery of A5083 aluminum alloy after a small deformation through various measuring approaches." *Journal of Materials Science & Technology* (2021). <https://doi.org/10.1016/j.jmst.2021.06.053>
16. T. Taylor, K. Kim, **J. Zhang**, D. Penney, J. Yanagimoto. "TRIP assisted press hardened steel by the anisothermal bainitic ferrite transformation." *Journal of Materials Processing Technology* 289 (2021): 116950. <https://doi.org/10.1016/j.jmatprotec.2020.116950>
17. Y. Shibuya, **J. Zhang**, Y. Sato, J. Yanagimoto. "Evaluation of the Mechanical Properties and Formability of Metal-Based Composite Sheets made of Thin Stainless-Steel Sheets and Carbon Fiber Reinforced Plastics." *International Journal of Material Forming*. Accepted, in press.
18. T. Taylor, **J. Zhang**, J. Yanagimoto. "Evaluation of a concept out-of-autoclave process for manufacturing carbon fibre reinforced polymer automotive parts." *Procedia CIRP* 86 (2019): 162-166. <https://doi.org/10.1016/j.procir.2020.01.030>

International conferences

19. **J. Zhang*** and J. Yanagimoto: Design and fabrication of formable CFRTP core sandwich sheets, 2019 CIRP General Assembly, CIRP Annals - Manufacturing Technology, Vol.68/1

(2019), 281-284, Birmingham, UK.

20. **J. Zhang*** and J. Yanagimoto: Homogenization-based topology optimization integrated with elastically isotropic lattices for additive manufacturing of ultralight and ultrastiff structures, 2021 CIRP General Assembly, CIRP Annals - Manufacturing Technology, Vol.70/1 (2021), 111-114, Munich, Germany.

Domestic conferences

21. **J. Zhang*** and J. Yanagimoto: Design and Fabrication of Formable CFRTP Core Metal Sandwich Sheet, The Proceedings of the 2018 Japanese Spring Conference for the Technology of Plasticity, (2018-6), 87-88, Tokyo, Japan.
22. **J. Zhang*** and J. Yanagimoto: Effects of sandwich sheet geometry and forming tool geometry on the formability of the CFRTP core sandwich sheet, The Proceedings of the 2019 Japanese Spring Conference for the Technology of Plasticity, (2019-6), 129-130, Kyoto, Japan.
23. **J. Zhang*** and J. Yanagimoto: Homogenization-based topology optimization integrated with elastically isotropic lattices for the design of inner core for metal face/CFRP core hybrid structure, The Proceedings of the 72nd Japanese Joint Conference for the Technology of Plasticity, (2021-10), Online, Japan.

Acknowledgement

The life experience in Yanagimoto Laboratory for more than five years left me with precious memories that will never be forgotten. What I learned and felt here far exceeded what I could express. When I realized that I was about to graduate and might leave Yanagimoto Laboratory one day in the future, I felt very sad and unwilling to give up. No matter when and where I am in the future, I believe that these bits and pieces of my experience in Yanagimoto Laboratory will be connected in some way in the future and bring me life-long impact.

First of all, I would like to express my sincere gratitude to my supervisor, Professor Jun Yanagimoto, for his encouragement, help, understanding and tolerance during my studies and research at the University of Tokyo. I am very grateful to him for giving me the right to freely choose and explore research topics, which allows me to do research that I am interested in, and also cultivates my independent research ability. With his professional and patient guidance and help, I became a more independent and confident person step by step. I am very grateful to him for supporting me to present the results of this research at many international conferences, especially for taking me to participate in CIRP general assembly, where I was deeply inspired by outstanding scientists, which strengthened my determination to be an excellent academic citizen. Words alone cannot express how grateful I am for him. I believe that in the long career in the future, I will often think of what I learnt from him and strive to become a researcher who lives up to his expectations.

In addition, I am very grateful to Prof. Yoshikawa, Prof. Takahashi, Prof. Izumi and Prof. Okabe for taking the time out of their busy schedule to serve as members of the review committee for my doctoral dissertation. Their constructive and insightful comments are very helpful to the doctoral dissertation.

The research work presented in this dissertation was financially supported by JSPS Grants-in-Aid for Scientific Research – (JSPS KAKENHI Grant Number JP 21J11337) and JSPS Grants-in-Aid for Scientific Research (A) – (Contract No. 20H00300). I would like to express sincere thanks to JSPS for their financial supports.

I sincerely thank Dr. Sumio Sugiyama in Yanagimoto Laboratory for his patient help,

useful discussions and invaluable friendship. Sugiyama-sensei is a famous researcher on semi-solid forming in Japan and has a kind-hearted and tolerant attitude towards this world. I also appreciate the kind help, understanding and concerns from Secretary Matsunaga-san, Assistant professor Sato-san and Sabrina-san, Technician Ishikawa-san and Komine-san in Yanagimoto Laboratory.

I am very grateful to all the members of Yanagimoto Lab. Dr. Sheng Ding gave me a lot of guidance and help on many experimental techniques and insightful suggestions. With his friendly support, I quickly became familiar with the Yanagimoto laboratory. I am also very grateful to Dr. Tom Taylor for his countless help, companion, discussion, encouragement and everything. Thanks very much for the funny and unforgettable hang-out time together with Dr. Tom and Dr. Ding. Thank Assistant Professor Park, Higuchi-san, Dr. Wu, Dr. Ho, Dr. Wang, Dr. Lin, Park-san, Hsieh-san, Love-san, Kim-san, Kobayashi-san, Uebayashi-san, Yoshimura-san, Zhong-san, Keigo Uchida-san, Nakashima-san, Dani-san, Suzuki-san, Shibuya-san, Uji-san, Otaku-san, Tomotaku Uchida-san, Takatori-san and others for their companion, encouragement, help and sharing have made my time in Yanagimoto laboratory so enjoyable and joyful. I would also like to thank Professor Meng Yi from Chongqing University, Professor Li Jingyuan from University of Science and Technology Beijing and Professor Wang Jian from Yanshan University for their help, encouragement and inspiration during their visit to Yanagimoto Lab.

I also would like to thank the University of Tokyo for providing me with such good study and living conditions, as well as the scholarship provided by the Graduate School of Engineering. Thank the staff of the Mechanical Office for their support and help.

Finally, I would like to thank my family, my parents, my loved ones and friends for their support, companionship, encouragement and love. I would also like to thank my motherland, and I am looking forward to returning to her embrace and making my own contributions to her prosperity. I am also very grateful to Shanghai Jiao Tong University for providing me with a fantastic platform to continue my research.

Thank you very much.

Jingwei Zhang